

2

**PIEZOELECTRIC AND ELECTROSTRICTIVE MATERIALS  
FOR TRANSDUCERS APPLICATIONS**

Period February 1, 1991 to January 31, 1992

**DTIC**  
**SELECT**  
**JUN 3 1992**  
**C D**

**AD-A250 889**

**Final Report**



**VOLUME I**

**OFFICE OF NAVAL RESEARCH**  
Contract No. N00014-89-J-1689

**APPROVED FOR PUBLIC RELEASE - DISTRIBUTION UNLIMITED**

Reproduction in whole or in part is permitted for any purpose  
of the United States Government

**L. E. Cross**  
**R. E. Newnham**  
**A. S. Bhalla**  
**J. P. Dougherty**  
**J. H. Adair**  
**V. K. Varadan**  
**V. V. Varadan**

**PENNSTATE**



**92-14491**



**THE MATERIALS RESEARCH LABORATORY**  
**UNIVERSITY PARK, PA**

92 6 01 156

**Best  
Available  
Copy**

# REPORT DOCUMENTATION PAGE

Form Approved  
OAS No. 0704-0188

1a. REPORT SECURITY CLASSIFICATION		1b. RESTRICTIVE MARKINGS	
2a. SECURITY CLASSIFICATION AUTHORITY		3. DISTRIBUTION/AVAILABILITY OF REPORT Reproduction in whole or in part is permitted for any purpose of the United States Government	
2b. DECLASSIFICATION/DOWNGRADING SCHEDULE			
4. PERFORMING ORGANIZATION REPORT NUMBER(S) N00014-89-J-1689		5. MONITORING ORGANIZATION REPORT NUMBER(S)	
6a. NAME OF PERFORMING ORGANIZATION MATERIALS RESEARCH LABORATORY	6b. OFFICE SYMBOL (If applicable)	7a. NAME OF MONITORING ORGANIZATION	
6c. ADDRESS (City, State, and ZIP Code) THE PENNSYLVANIA STATE UNIVERSITY UNIVERSITY PARK, PA 16802		7b. ADDRESS (City, State, and ZIP Code)	
8a. NAME OF FUNDING/SPONSORING ORGANIZATION	8b. OFFICE SYMBOL (If applicable)	9. PROCUREMENT INSTRUMENT IDENTIFICATION NUMBER	
8c. ADDRESS (City, State, and ZIP Code)		10. SOURCE OF FUNDING NUMBERS	
		PROGRAM ELEMENT NO.	PROJECT NO.
		TASK NO.	WORK UNIT ACCESSION NO.
11. TITLE (Include Security Classification) PIEZOELECTRIC AND ELECTROSTRICTIVE MATERIALS FOR TRANSDUCER APPLICATIONS			
12. PERSONAL AUTHOR(S) L. E. Cross, R. E. Newnham, A. S. Bhalla, J. P. Dougherty, J. H. Adair, V.K. Varadan, V.V. Varadan			
13a. TYPE OF REPORT FINAL	13b. TIME COVERED FROM 2/1/91 TO 1/31/92	14. DATE OF REPORT (Year, Month, Day)	15. PAGE COUNT
16. SUPPLEMENTARY NOTATION			
17. COSATI CODES		18. SUBJECT TERMS (Continue on reverse if necessary and identify by block number)	
FIELD	GROUP	SUB-GROUP	
19. ABSTRACT (Continue on reverse if necessary and identify by block number)  SEE REVERSE SIDE OF PAGE.			
20. DISTRIBUTION/AVAILABILITY OF ABSTRACT <input type="checkbox"/> UNCLASSIFIED/UNLIMITED <input type="checkbox"/> SAME AS RPT. <input type="checkbox"/> DTIC USERS		21. ABSTRACT SECURITY CLASSIFICATION	
22a. NAME OF RESPONSIBLE INDIVIDUAL		22b. TELEPHONE (Include Area Code)	22c. OFFICE SYMBOL

## ABSTRACT

This report documents work carried out in the Materials Research Laboratory of The Pennsylvania State University on the third and final year of the program on "Piezoelectric and Electrostrictive Materials for Transducers Applications" sponsored by the Office of Naval Research (ONR) under grant No. N00014-89-J-1689. This marks the termination of a very long and highly productive sequence of contracts and grants focusing on the development of new materials for Piezoelectric and Electrostrictive transducer applications carried through under core ONR funding. Fortunately many elements of the work will be continuing on a new University Research Initiative (URI) program under ONR sponsorship.

Highlights of the past year's activities include: An increased emphasis upon the flexensional (moonie) type actuators, modelling both the internal stress distribution as a function of geometry, and the very interesting resonant mode structure of the composites; A more refined focus upon the performance of piezoelectric ceramic transducers, particularly under high drive levels is developing with concern for the extrinsic domain and phase boundary contributions to response. Measurement and modelling are being used to explore the nonlinearity and the frequency response and to examine the phase partitioning at the rhombohedral : tetragonal morphotropic phase boundary in the PZT system. Phenomena limiting lifetime in polarization and phase switching actuators are being explored to separate surface and volume effects and those due to grain size and flaw population differences. New work has been initiated to examine Acoustic Emission as a technique, in combination with Barkhausen current pulse analysis, to separate and evaluate domain switching and microcracking in polarization switching systems.

From work on this program it has now become clear that the relaxor ferroelectrics are in fact close analogues of the magnetic spin glasses, so that the spin glass formalism can be used to explain the very wide range of dielectric, elastic and electrostrictive properties. The remaining outstanding fundamental problem is that of the detailed interrelationship between the known nano-heterogeneity in the structure and chemistry and the nanopolar regions which contribute the electrical response.

Of very high practical interest is the manner in which the relaxor can be field biased into extremely strong piezoelectric response. Work is going forward to examine this response in detail and to explore the possibility that such "super-responses" can be induced by chemical (solid solution) means.

Processing studies have focused upon new lower temperature consolidations for relaxors, and upon new compositions for high temperature piezoelectric ceramics.

In parallel with the ONR Transducer Program the Laboratory has extensive DARPA sponsored research on ferroelectric thin films. Since the films structures frequently involve materials like the PZT, PMN : PT, PLT and PLZT families of compositions and do explore piezoelectric effects and applications, a small group of the most relevant papers from this program are appended to the report.



**PIEZOELECTRIC AND ELECTROSTRICTIVE MATERIALS  
FOR TRANSDUCERS APPLICATIONS**

Period February 1, 1991 to January 31, 1992

Final Report

**VOLUME I**

**OFFICE OF NAVAL RESEARCH**  
Contract No. N00014-89-J-1689

**APPROVED FOR PUBLIC RELEASE -- DISTRIBUTION UNLIMITED**

Reproduction in whole or in part is permitted for any purpose  
of the United States Government

**L. E. Cross  
R. E. Newnham  
A. S. Bhalla  
J. P. Dougherty  
J. H. Adair  
V. K. Varadan  
V. V. Varadan**



Accession For	
Dist	Special
Dist	Special
Availability Codes	
Dist	Special
Special	

**PENNSSTATE**



**THE MATERIALS RESEARCH LABORATORY**  
UNIVERSITY PARK, PA

## TABLE OF CONTENTS

ABSTRACT.....	5
INTRODUCTION.....	7
1.0 GENERAL SUMMARY PAPERS.....	9
2.0 COMPOSITE MATERIALS.....	9
3.0 PIEZOELECTRIC CERAMICS.....	10
4.0 PHENOMENOLOGICAL STUDIES.....	11
5.0 RELAXORS AND RELATED SYSTEMS.....	12
6.0 PROCESSING STUDIES.....	13
7.0 FERROELECTRIC THIN FILMS.....	14
8.0 APPRENTICE PROGRAM.....	15
9.0 PAPERS PUBLISHED IN REFEREED JOURNALS.....	17
10.0 INVITED PAPERS PRESENTED AT NATIONAL AND INTERNATIONAL MEETINGS.....	18
11.0 CONTRIBUTED PAPERS AT NATIONAL AND INTERNATIONAL MEETINGS.....	19
12.0 HONORS TO MRL FACULTY AND STUDENTS.....	24
13.0 REFERENCES .....	24

## APPENDICES

### *General Summary Papers*

1. L. Eric Cross. "Ferroelectric Ceramics Tailoring Properties for Specific Applications."
2. R. E. Newnham and T. R. Shrout. "Advanced Ceramics," Electronic Ceramics 1, 601-620.

### *Composite Materials*

3. R. E. Newnham "Tunable Transducers: Nonlinear Phenomena in Electroceramics," National Institute of Standards and Technology Special Publication 804, Chemistry of Electronic Ceramic Materials, Proceedings of the International Conference held in Jackson, WY, August 17-22, 1990, issued January 1991.
4. R. E. Newnham. "Composite Electroceramics," International Encyclopedia of Composites, Vol. 6, 158-173.

TABLE OF CONTENTS  
(continued)

*Composite Materials (continued)*

5. M. Blaszkiewicz, R. E. Newnham and Q. C. Xu. "Tunable Transducers as Smart Materials," *Transducers 91*, 6th International Conference Solid State Sensors and Actuators, San Francisco, CA (June 24-28, 1991).
6. Q. C. Xu, S. Yoshikawa, J. R. Belsick and R. E. Newnham. "Piezoelectric Composites with High Sensitivity and High Capacitance for Use at High Pressure," *IEEE Transactions on Ultrasonics, Ferroelectrics, and Frequency Control* 38 (6), 634-639 (November 1991).
7. Q. C. Xu, A. Dogan, J. Tressler, S. Yoshikawa and R. E. Newnham. "Ceramic-Metal Composite Actuator."

*Piezoelectric Ceramics*

8. Q. Y. Jiang, W. Cao and L. E. Cross. "Effects of Surface Layers on the Physical Properties of Lanthanum Doped Lead Zirconate Titanate Ceramic."
9. Qiyue Jiang, Wenwu Cao and L. E. Cross. "The Influence of Surface Contamination on Electric Fatigue of Ferroelectrics."
10. L. E. Cross and Q. Jiang. "Fatigue Effects in High Strain Actuators."
11. V. Srikanth and E. C. Subbarao. "Acoustic Emission in Ferroelectric Lead Titanate Ceramics: Origin and Recombination of Microcracks," *Acta Metall. Mater.* (received February 11, 1991)
12. M. Fukuhara, A. S. Bhalla and R. E. Newnham. "Morphotropic Phase Boundary in the  $\text{Pb}(\text{Zr}_x\text{Ti}_{1-x})\text{O}_3$  System," *Phys. Stat. Sol. (a)* 122, 677 (1990)
13. Wenwu Cao and L. E. Cross. "Theory of Tetragonal Twin Structure in Ferroelectric Perovskites with a First-Order Phase Transition," *Physical Review B* 44 (1), 5-12 (1 July 1991-I).
14. Shaoping Li, Wenwu Cao and L. E. Cross. "The Extrinsic Nature of Nonlinear Behaviour Observed in Lead Zirconate Titanate Ferroelectric Ceramic," *J. Appl. Phys.* 69 (10), 7219-7224 (15 May 1991).
15. Shaoping Li, Wenwu Cao, R. E. Newnham and L. E. Cross. "Electromechanical Nonlinearity of Ferroelectric Ceramics and Related Non-180° Domain Wall Motions."
16. Shaoping Li, Wenwu Cao and L. E. Cross. "Stress and Electric Displacement Distribution Near Griffith's type III Crack Tips in Piezoceramics," *Materials Letters* 10 (6), 219-222 (December 1990).

*Phenomenological Studies*

17. George A. Rossetti, Jr., L. E. Cross and Keiko Kushida. "Stress Induced Shift of the Curie Point in Epitaxial  $\text{PbTiO}_3$  Thin Films," *Appl. Phys. Lett.* 59 (20), 2524-2526 (11 November 1991).

TABLE OF CONTENTS  
(continued)

*Phenomenological Studies (continued)*

18. G. A. Rossetti, Jr., T. Nishimura and L. E. Cross. "X-ray and Phenomenological Study of Lanthanum-Modified Lead Zirconate-Titanates in the Vicinity of the Relaxor Phase Transition Region," *J. Appl. Phys.* **70** (3), 1630-1637 (1 August 1991).
19. Wenwu Cao and L. Eric Cross. "Distribution Functions of Coexisting Phases in a Complete Solid Solution System."

*Relaxors and Related Systems*

20. Dwight D. Viehland. "The Glassy Behaviour of Relaxor Ferroelectrics," Abstract from A Thesis in Solid State Science, The Pennsylvania State University, The Graduate School (May 1991).
21. Dwight Viehland, S. Jang, L. Eric Cross and Manfred Wuttig. "The Dielectric Relaxation of Lead Magnesium Niobate Relaxor Ferroelectrics," *Philosophical Magazine B* **64** (3), 335-344 (1991).
22. Dwight Viehland, S. J. Jang, L. Eric Cross and Manfred Wuttig. "Anelastic Relaxation and Internal Strain in Lead Magnesium Niobate Relaxors," *Philosophical Magazine A* **64** (4), 835-849 (1991).
23. Dwight Viehland, S. J. Jang, L. Eric Cross and Manfred Wuttig. "Local Polar Configurations in Lead Magnesium Niobate Relaxors," *J. Appl. Phys.* **69** (1), 414-419 (1 January 1991).
24. Dwight Viehland, J. F. Li, S. J. Jang, L. Eric Cross and Manfred Wuttig. "Dipolar-Glass Model for Lead Magnesium Niobate," *Physical Review B* **43** (10), 8316-8320 (1 April 1991).
25. Ruyan Guo. "Ferroelectric Properties of Lead Barium Niobate Compositions Near the Morphotropic Phase Boundary," Abstract from A Thesis in Solid State Science, The Pennsylvania State University, The Graduate School (December 1990).
26. R. Guo, A. S. Bhalla and L. E. Cross. "Pyroelectric Properties of Lead Barium Niobate Single Crystals," *Ferroelectrics* **118**, 77-83 (1991).
27. C. A. Randall, R. Guo, A. S. Bhalla and L. E. Cross. "Microstructure-Property Relations in Tungsten Bronze Lead Barium Niobate,  $Pb_{1-x}Ba_xNb_2O_6$ ," *J. Mater. Res.* **6** (8), 1720-1728 (August 1991).
28. Jayne R. Gliniewicz. "An Investigation of the Lead Scandium Tantalate-Lead Titanate Solid Solution System," Abstract from A Thesis in Solid State Science, The Pennsylvania State University, The Graduate School (December 1991).
29. J. R. Gliniewicz, A. S. Bhalla and L. E. Cross. "Pyroelectric Response and Depolarization Behaviour of  $(1-x)Pb(Sc_{1/2}Ta_{1/2})O_3$ - $(x)PbTiO_3$  Materials," *Ferroelectrics* **118**, 157-164 (1991).
30. D. J. Tyalor, D. Damjanovic and A. S. Bhalla. "Pyroelectric and Dielectric Properties of PMN-Based Ceramics Under DC Bias," *Ferroelectrics* **118**, 143-155 (1991).

TABLE OF CONTENTS  
(continued)

***Processing Studies***

31. V. Srikanth and E. C. Subbarao. "Chemical Reactions of Lead Magnesium Niobate Titanate in the Presence of a Glass," *J. Mater. Res.* **6** (6), 1-16 (June 1991).
32. Paul A. Fuierer and Robert E. Newnham. "La<sub>2</sub>Ti<sub>2</sub>O<sub>7</sub> Ceramics," *J. Am. Ceram. Soc.* **74** (11), 2876-2881 (1991).
33. G. R. Fox, J. H. Adair and R. E. Newnham. "Effects of pH and H<sub>2</sub>O<sub>2</sub> Upon Coprecipitated PbTiO<sub>3</sub> Powders," *J. Mater. Sci.* **26**, 1187-1191 (1991).
34. G. A. Rossetti, Jr., D. J. Watson, R. E. Newnham and J. H. Adair. "Kinetics of the Hydrothermal Crystallization of the Perovskite Lead Titanate," *J. Crystal Growth* **116**, 251-259 (1992).
35. A. Srivastava, A. Bhalla and L. E. Cross. "A Study of Y<sub>1</sub>Ba<sub>2</sub>Cu<sub>3</sub>O<sub>7-x</sub> Thick Films on Ferroelectric Substrates."
36. A. Srivastava, A. Bhalla and L. E. Cross. "Y<sub>1</sub>Ba<sub>2</sub>Cu<sub>3</sub>O<sub>7-x</sub> As An Electrode Materials for Ferroelectric Devices," *Ferroelectrics* **123**, 243-251 (1991).

***Ferroelectric Thin Films***

37. K. R. Udayakumar, J. Chen, P. J. Schuele, L. E. Cross, V. Kumar and S. B. Krupanidhi. "Polarization Reversal and High Dielectric Permittivity in Lead Magnesium Niobate Titanate Thin Films," *Appl. Phys. Lett.* **60** (10), 1187-1189 (9 March 1992).
38. K. R. Udayakumar, P. J. Schuele, J. Chen, K. G. Brooks and L. E. Cross. "Ferroelectric Switching in Lead Zirconate-Lead Zinc Niobate Thin Films,"
39. Keith G. Brooks, Jiyu Chen, K. R. Udayakumar and L. Eric Cross. "Lead Zirconate Titanate Stannate Thin Films for Large Strian Microactuator Applications."
40. K. R. Udayakumar, S. F. Bart, A. M. Flynn, J. Chen, L. S. Tavrow, L. E. Cross, R. A. Brooks, D. J. Ehrlich. "Ferroelectric Thin Film Ultrasonic Micromotors," *IEEE*, 109-113 (1991).
41. Anita M. Flynn, Lee S. Tavrow, Stephen F. Bart, Rodney A. Brooks, Daniel J. Ehrlich, K. R. Udayakumar and L. Eric Cross. "Piezoelectric Micromotors for Microrobots," *J. Microelectromechanical Systems* **1** (1) 47-50 (1992).

## ABSTRACT

This report documents work carried out in the Materials Research Laboratory of The Pennsylvania State University on the third and final year of the program on "Piezoelectric and Electrostrictive Materials for Transducers Applications" sponsored by the Office of Naval Research (ONR) under grand No. N00014-89-J-1689. This marks the termination of a very long and highly productive sequence of contracts and grants focusing on the development of new materials for Piezoelectric and Electrostrictive transducer applications carried through under core ONR funding. Fortunately many elements of the work will be continuing on a new University Research Initiative (URI) program under ONR sponsorship.

Highlights of the past year's activities include: An increased emphasis upon the flexensional (moonie) type actuators, modeling both the internal stress distribution as a function of geometry, and the very interesting resonant mode structure of the composites; A more refined focus upon the performance of piezoelectric ceramic transducers, particularly under high drive levels is developing with concern for the extrinsic domain and phase boundary contributions to response. Measurement and modelling are being used to explore the nonlinearity and the frequency response and to examine the phase partitioning at the rhombohedral : tetragonal morphotropic phase boundary in the PZT system. Phenomena limiting lifetime in polarization and phase switching actuators are being explored to separate surface and volume effects and those due to grain size and flaw population differences. New work has been initiated to examine Acoustic Emission as a technique, in combination with Barkhausen current pulse analysis, to separate and evaluate domain switching and microcracking in polarization switching systems.

From work on this program it has now become clear that the relaxor ferroelectrics are in fact close analogues of the magnetic spin glasses, so that the spin glass formalism can be used to explain the very wide range of dielectric, elastic and electrostrictive properties. The remaining outstanding fundamental problem is that of the detailed interrelationship between the known nano-heterogeneity in the structure and chemistry and the nanopolar regions which contribute the electrical response.

Of very high practical interest is the manner in which the relaxor can be field biased into extremely strong piezoelectric response. Work is going forward to examine this response in detail and to explore the possibility that such "super-responses" can be induced by chemical (solid solution) means.

Processing studies have focused upon new lower temperature consolidations for relaxors, and upon new compositions for high temperature piezoelectric ceramics.

In parallel with the ONR Transducer Program the Laboratory has extensive DARPA sponsored research on ferroelectric thin films. Since the films structures frequently involve materials like the PZT, PMN : PT, PLT and PLZT families of compositions and do explore piezoelectric effects and applications, a small group of the most relevant papers form this program are appended to the report.

## **INTRODUCTION**

This report documents work carried out in the Materials Research Laboratory of The Pennsylvania State University over the third and final year of the program on "Piezoelectric and Electrostrictive Materials for Transducer Applications" sponsored under grant no. N00014-89-J-1689 from the Office of Naval Research. In general the change of emphasis which was initiated last year (ONR Report for 1990) has continued and intensified, with the group studies moving away from purely sensing systems and toward a more balanced approach to both sensing and actuating functions for ceramic, ceramic polymer, and ceramic metal composite systems.

For reporting purposes, the activities have been grouped under the following topics.

1. GENERAL SUMMARY PAPERS.
2. COMPOSITE MATERIALS.
3. PIEZOELECTRIC CERAMICS.
4. PHENOMENOLOGICAL STUDIES.
5. RELAXORS AND RELATED SYSTEMS.
6. PROCESSING STUDIES
7. FERROELECTRIC THIN FILMS.

Following precedent established over more than fifteen earlier reports, the report will present a brief narrative description of the work making reference for details to the published studies which are appended as technical appendices and form the bulk of the document.

Over the past year we have combined a continuing emphasis on the research topics and advances necessary to maintain leadership in the area of Transducers with the need to bolster the educational background for people who will soon be driven to using active mechanical systems to maintain a competitive position. In the Second International Summer School on Ferroelectrics, L. Eric Cross gave the opening address summarizing many of the techniques in Ferroelectric Ceramics for tailoring properties to specific application and R. E. Newnham gave the closing address on Smart Ceramics. For the ADPA/AIAA/ASME/SPIE Conference on Active Materials and Adaptive Structures the Penn State Group (Cross, Newnham and Uchino) gave a full one day tutorial on piezoelectricity in crystal and ceramics and the application of piezoelectrics to Actuator Structures. The Gordon Conference on Ceramics was organized around the possibility for engineering super response, with Cross opening the proceedings. Perhaps a rather clear indication of the dominant position which the Penn State Group has achieved in electric ceramics is the fact that at the upcoming 94th Annual Meeting of the American Ceramic Society, Cross will give the Orton Lecture and at the same meeting



Newnham will follow with the Sossman Lecture. These educational ventures are of course a subsidiary but important contribution enabled by the continuing ongoing ONR support.

In the technical area, the continuing trend has been to increase activity relevant to the material systems most important for Actuation both for single phase and composite families. For larger strains at lower forces than bulk ceramics, the flextensional (moonie) offers an almost ideal intermediate between solid ceramic and current bimorph structures and the combination of the Moonie with a multilayer co-fired element offers 50  $\mu$  meter strain at low control voltages.

For the 1 : 3 composites which are becoming increasingly important for large area actuation, new exact solutions for the strain behaviour are being formulated but these are not yet published and will be reported next year.

Concern for the behaviour of both piezoelectrics and electrostrictors at the high continuous drive levels necessary for many actuation functions is being addressed by studies to separate surface and volume effects, grain size related effects and the role of the flaw populations in limiting cycle lifetime. New work has been started to compliment these approaches by using acoustic emission analysis in conjunction with Barkhausen pulse analysis to attempt distinction between noise associated with domain switching and that associated with micro-cracking. Extrinsic contributions from domain wall and phase boundary motion which become important in all piezoceramics at high drive levels are being explored both experimentally and theoretically, measuring nonlinearity and frequency dispersion and by extending Arlt's<sup>1</sup> model for the domain contribution into the nonlinear regime.

Work on the relaxor ferroelectrics continues to further substantiate the analogue to spin glass behaviour in magnetic systems, and the full panoply of the spin glass formalism is being used to describe the material properties. A major developing interest is in the detailed origin of the exceedingly large induced piezoelectric effects in polarization biased electrostrictors and in the exploration of systems combining end members with relaxor and ferroelectric properties.

Processing studies continue to explore different techniques for generating fine powders of conventional perovskite ferroelectrics. More recently however the ultra high Curie temperature strontium pyroniobate family is being examined and hot forged grain oriented samples of  $\text{La}_2\text{Ti}_2\text{O}_7$  have been produced. The objective is to develop piezoelectric materials with very wide working temperature range.

The ferroelectrics group in MRL is also involved in a significant program under DARPA sponsorship to produce thin films of ferroelectric materials. The composition of interest

embrace the perovskite PZTs, PTs, PLTs and PLZTs and though the emphasis is upon generating switchable compositions for nonvolatile semiconductor memory, it is necessary to know the piezoelectric response and its potential problems and applications. For completeness a small selection of the papers most relevant to the piezoelectric behaviour is also appended.

## **1.0 GENERAL SUMMARY PAPERS**

In a very broad ranging survey (Appendix 1). Eric Cross explored dielectric, piezoelectric, pyroelectric and electro-optic applications of ferroelectric ceramic, introducing the week long deliberations of the Second International Summer School on Ferroelectrics in Ascona, Switzerland. The primary focus was on dielectric and piezoelectric systems and introduced much of the effort ongoing in MRL, particularly on this ONR program to tailor properties for these specific applications.

For Advanced Ceramics (Electronic) Newnham (Appendix 2) covers a wider range of topics including magnetics and semiconductors, however the focus on techniques for multilayer systems is important in the context of the actuator studies.

## **2.0 COMPOSITE MATERIALS**

Tuneable Transducers (Appendix 3) by R. E. Newnham highlights the possible application of nonlinear properties to smart and very smart systems. The focus is upon the relaxor ferroelectric and the tuning of the piezoelectric response under DC field bias.

The article on Composite Electroceramics (Appendix 4) by R. E. Newnham gives a general introduction to the important controlling parameters, highlighting the roles of connectivity, symmetry and scale in determining a wide range of properties. For systems involving transport, the importance of percolation and the percolation threshold are introduced and polychromatic percolation is briefly discussed.

Tuneable Transducer for Smart Materials (Appendix 5) by Michael Blaszkiewicz and R. E. Newnham deals with the possibility of using an elastomer under mechanical stress to control compliance in a composite, and thus to tune the resonant frequency of a composite resonator. Electrical tuning was introduced by incorporating a piezoelectric actuator stack to generate the modulating stress.

The paper on Piezoelectric Composite with High Sensitivity and High Capacitance for Use at High Pressure, by Xu, Yoshikawa, Belsick and Newnham (Appendix 6) underscores the advantages of the flextensional (Moonie) structure in providing high  $d_h$ , high  $g_h$ , high  $d_h g_h / \tan \delta$  large capacitance and low tangents  $\delta$  in combination with the robustness

required for deep submergence. Ceramic Metal Composite Actuators by Xu, Dogan, Tressler, Yoshikawa and Newnham (Appendix 7) examines the flexensional moonie as an actuator and points up the excellent motion amplification which can be achieved in this system.

### **3.0 PIEZOELECTRIC CERAMICS**

From dielectric measurements the work by Q. Y. Jiang, W. Cao and L. E. Cross on the "Effects of Surface Layers on Physical Properties of Lanthanum Doped Lead Zirconate Titanate Ceramics" (Appendix 8) uses the effects of changing sample thickness to delineate clearly a nonferroelectric layer on conventional ground and polished samples, the manner in which this layer can be removed by etching and through post annealing the separation of the effects of pure capacitance padding and of the two dimensional stress generated by the processing.

The importance of the electrode sample interface is further stressed in the paper on "The Influence of Surface Contamination on Electrical Fatigue of Ferroelectrics" by Jiang, Cao and Cross (Appendix 9) which shows the importance of an exceedingly clean ferroelectric surface in relieving the switching fatigue for polarization reversal and large strain switching in 7 : 68 : 32 PLZT.

These fatigue effects are summarized in the paper by Cross and Jiang on Fatigue Effects in High Strain Actuators (Appendix 10) which underscores also the importance of small grain size and pore free character (optical transparency) in reducing fatigue effects so that saturated polarization switching may be extended to  $\sim 10^9$  cycles.

Our intention is to use Acoustic Emission to explore polarization switching in PZTs. In preparation for this study more conventional AE has been explored in the paper Acoustic Emission in Ferroelectric Lead Titanate Ceramics : Origin and Recombination of Microcracks by V. Srikanth and E. C. Subbarao (Appendix 11). Here heating and cooling through  $T_c$  has been used to initiate the cracking in Niobium modified lead titanate. The method was also used to confirm the healing of microcracks as had been postulated much earlier by Buessem.<sup>2</sup>

The following six papers deal with aspects of the behaviour of Lead zirconate titanate ceramics. In the discussion of the MPB in the PZT system M. Fukuhara, A. S. Bhalla and R. E. Newnham look at the general considerations which suggest that the phase change is driven by polarizability differences and by the coupling to the elastic strain field (Appendix 12).

A three dimensional Landau-Ginsburg model is constructed by Cao and Cross to develop a "Theory of Tetragonal Twin Structures in Ferroelectric Perovskite with First-Order Phase Transition" (Appendix 13) and a quasi one dimensional solution obtained for 180° and for change neutral 90° twin walls. The elastic deformations and dimensional changes associated

with the twin structures are delineated in the parameters of the model and the implications for piezoelectric effects in ceramic ferroelectrics are discussed.

In the two papers of Appendices 14 and 15 Shaoping Li, W. Cao, R. E. Newnham and L. E. Cross examine the extrinsic nonlinearity in lead zirconate titanate ferroelectric ceramics. Appendix 14 presents preliminary experimental evidence to confirm that the nonlinearity of the poled ceramic is extrinsic and uses an extension of the model by Arlt and co-workers<sup>3</sup> to describe the nonlinearity. Appendix 15 gives a more complete treatment of the problem. The analysis traces in more detail the origins of the loss and explores the influence of high driving fields upon the resonant frequency of the poled ceramic.

The inhomogeneous stress and field distribution in the vicinity of a Griffiths type III crack tip in a piezoceramic is explored by Li, Cao and Cross in Appendix 16. The paper tackles the rather straightforward problem of a type III crack along the  $x_1$  axis extending through the ceramic in  $x_3$  which is the poling direction. Stress intensify factors are worked out for fields applied along  $x_2$  and for shear stress applied  $\sigma_{32}$ . Clearly in this configuration the effects of stress and field can add or subtract depending on the sign of the field.

#### 4.0 PHENOMENOLOGICAL STUDIES

In observations on thin films structures carried out in Hitachi Laboratories for epitaxial  $\text{PbTiO}_3$  films, a rather massive ( $50^\circ\text{C}$ ) shift of the apparent Curie temperature was observed for certain preparation conditions. Appendix 17 describes a straightforward application of Devonshire Theory by Rossetti and Cross using values for  $\text{PbTiO}_3$  delineated in this Laboratory to suggest that the origin may be in a two dimensional effective compressive stress  $\sim 400$  MPa, which has little effect upon the room temperature values of piezoelectric or dielectric properties.

From a very careful x-ray and phenomenological study in the  $\text{Pb}_{1-x}\text{La}_x(\text{Zr}_{0.65}\text{Ti}_{0.35})_{1-x/4}\text{O}_3$  system Rossetti, Nishimura and Cross (Appendix 18) came to the very important conclusion that in this PLZT system the  $T_c$  as determined from Landau-Ginsburg-Devonshire Theory is independent of the lanthanum concentration, and that the apparent shift of the dielectric permittivity maximum is associated with a freezing in of dynamical nanopolar regions which originate at this interpreted LGD Curie temperature. The analysis gives additional support to the earlier assertion by Burns et al. that the onset of polar micro regions in PLZT is not affected by the Lanthanum content but does suggest that the so called Burns temperature is not associated with a static dipole, but with the onset of conventional ferroelectric ordering in regions which are of a size to be unstable against thermal vibrations.

A problem which has not here-to-fore been effectively considered is that of how the rhombohedral and tetragonal phases at the morphotropic phase boundary should proportion themselves. In Appendix 19 Cao and Cross show that the lever rule which is frequently used is completely invalid for the PZT case and that in fact the width of the co-existence region is a function of the domain (crystallite) size, going to zero for macroscopic dimension.

### **5.0 RELAXORS AND RELATED SYSTEMS**

An excellent account of the complete experimental data which forces the conclusion that the relaxor ferroelectrics are spin glass systems is summarized in the thesis in Solid State Science by D. D. Viehland. The abstract for the thesis is included as Appendix 20, the full thesis is now available through University Microfilms.

The papers published on the analysis of dielectric relaxation in Lead Magnesium niobate in terms of the Vogel-Fulcher relations is given in Appendix 21, the anelastic relaxation and its close correlation with the dielectric response in Appendix 22 the bias field dependence of the dielectric response and its relevance to the local polar configurations is discussed in Appendix 23 and the analysis leading to the conclusion that lead magnesium niobate is a spin glass is detailed in Appendix 24. In several senses this work does we believe put the capstone upon more than 20 years of continuous study of the dielectric response in what have come to be called the relaxor ferroelectrics.

The Tungsten Bronze structure family is an important group of oxide ferroelectrics with structures based on corner sharing oxygen octahedra and the frequent occurrence of interesting ferroelectric and relaxor ferroelectric properties. The structure is more complex than the perovskite and of lower symmetry (tetragonal 4/mmm prototype) but again the crystals have high permittivity and strong piezoelectric effects. A composition family of special interest is the solid solution between Lead metaniobate and barium metaniobate (PBN). Appendix 25 reproduces the abstract from the PhD thesis in Solid State Science by Dr. Ruyan Guo which involved a very comprehensive study of the PBN solid solution family. The work was submitted to the Penn State Campus wide Xerox awards committed and judged to be the best PhD thesis submitted in 1991.

PBN is one of the most interesting bronze solid solution systems since it embraces a morphotropic phase boundary at the composition  $\text{Pb}_{0.63}\text{Ba}_{0.37}\text{Nb}_2\text{O}_6$  separating a phase with orthorhombic and a phase with tetragonal ferroelectric domain state symmetry.

Ruyan's studies have clearly delineated the nature of the MPB and the orientations of the polar vector in the tetragonal and in the orthorhombic ferroelectric phases (Appendix 26). It is most interesting to note that both tetragonal and orthorhombic phases show relaxor

ferroelectric character for directions perpendicular to the dominant polar vector direction so that one must conclude that in these solid solutions there is a nanostructure within which the true symmetry is monoclinic and the polar vector tilted slightly away from the high symmetry direction in the domain. A further complexity in the PBN system is the occurrence of incommensurate ferroelastic displacement structures (Appendix 27) which can have lock in phase transitions even above the ferroelectric Curie temperature.

The relaxor  $\text{PbSc}_{1/2}\text{Ta}_{1/2}\text{O}_3$  in the perovskite structure family is unique in that by ordering the Sc/Ta cations on the B site of the  $\text{ABO}_3$  structure using thermal annealing it is possible to go continuously from well defined relaxor response to a sharp first order ferroelectric phase change. Extensive studies by Dr. Jayne Giniewicz of the system  $\text{PbSi}_{1/2}\text{Ta}_{1/2}\text{O}_3 : \text{PbTiO}_3$  are summarized in the abstract of her PhD thesis in Solid State Science which is included as Appendix 28. It is interesting to note that the region in which ordering may be changed by annealing only extends up to 7.5% lead titanate in the solid solution, but that for compositions between 0.4 and 0.45 mole%  $\text{PbTiO}_3$  a morphotropic phase boundary occurs to a tetragonal ferroelectric region.

Pyroelectric studies of compositions in the variable order region up to 7.5 mole% lead titanate (Appendix 29) show very high sensitivity and properties which may be most advantageous for thermal imaging systems. It is evident that combinations of relaxor ferroelectrics with strong ferroelectric phase can give both interesting piezoelectric and high sensitivity pyroelectric properties. Studies of the polarization behaviour in lead magnesium niobate : lead titanate solid solutions shows that high figures of merit can be achieved (Appendix 30).

## 6.0 PROCESSING STUDIES

For the lead magnesium niobate : lead titanate solid solution system it is interesting to explore how the processing temperatures can be modified by glass additives (Appendix 31). Studies by Srikanth and Subbarao suggest that high density perovskite structure compositions can be densified at 800°C to yield dielectric properties which could be most interesting for thick film capacitors.

To expand the range of ferroelectric properties to higher temperature, exploratory studies are being carried out upon the Strontium Pyroniobate family of ferroelectrics. The production of powders and of grain oriented ceramics of  $\text{La}_2\text{Ti}_2\text{O}_7$  is reported in Appendix 32. Excellent low loss dielectric response is achieved and there is clear evidence of strong grain orientation. Studies are now being extended to explore possible poling methods to achieve piezoelectric response.

Two studies relevant to the production of ultra fine Lead titanate powders by hydrothermal methods have been accomplished. In Appendix 33 the effects of pH and of  $H_2O_2$  upon the crystallization of Lead titanate in a hydrothermal environment are delineated and in Appendix 34 the kinetics of the hydrothermal crystallizations are explored and conditions delineated which permit the growth of uniform crystallites in the size range from 750 down to 20 nanometers.

Two studies have examined the possible use of the new Yttrium barium cuprate superconductor in its metallic phase above  $T_c$  as an electrode material for ferroelectric transducers. Appendix 35 reports studies of thick films of YBCO on PZT, PMN : PT and Barium titanate using conventional firing. In all cases there was evidence of interaction between electrode and ceramic with the minimum adverse effect in the PZT family. Extension of these studies using rapid thermal processing improved matters significantly (Appendix 36) yielding strongly adhering coatings with performance identical to gold electrodes on PZT, but still some adverse reaction with PMN : PT compositions.

To improve the performance of the oxide electrodes a new search was initiated for sintering aids which could lower the temperature for densification of PZT. Based on these studies a new family of fluxes has been discovered which permit densification at 950°C without loss of properties. These fluxes are now the subject of a patent disclosure and the publication is held up whilst this is being processed.

## **7.0 FERROELECTRIC THIN FILMS**

Five short papers which stem from work outside the ONR contract are included because of their potential interest and relevance to transducing structures.

In Appendix 37 it is shown that high permittivity PMN : PT solid solutions can be deposited by sol-gel spin on techniques onto platinum electrodes on silicon, which would have interesting potential as field switchable piezoelectric micro-actuators.

In the  $PbZrO_3$  -  $Pb(Zn_{1/3}Nb_{2/3})O_3$  solid solution system compositions close to, but on the ferroelectric side, of the antiferroelectric : ferroelectric morphotropic phase boundary have been fabricated in thin film form by sol-gel spin on processing (Appendix 38). The excellent hysteresis and low coercivity suggest strong piezoelectric response and the possibility of high strains in antiferroelectric : ferroelectric switching. Such switching compositions have been realized in the  $Pb_{0.97}La_{0.02}(Zr_{1-x-y}Ti_xSn_y)O_3$  perovskite (Appendix 39) and do show the expected high strain associated with induction of the ferroelectric phase.

Use of the piezoelectric response in conventional PZT thin films to produce micro-versions of the flexure surface wave piezoelectric motor are discussed in Appendix 40, and the possible application of such motors, to microrobots in Appendix 41.

## 8.0 APPRENTICE PROGRAM

### 1991 ONR APPRENTICE PARTICIPANTS

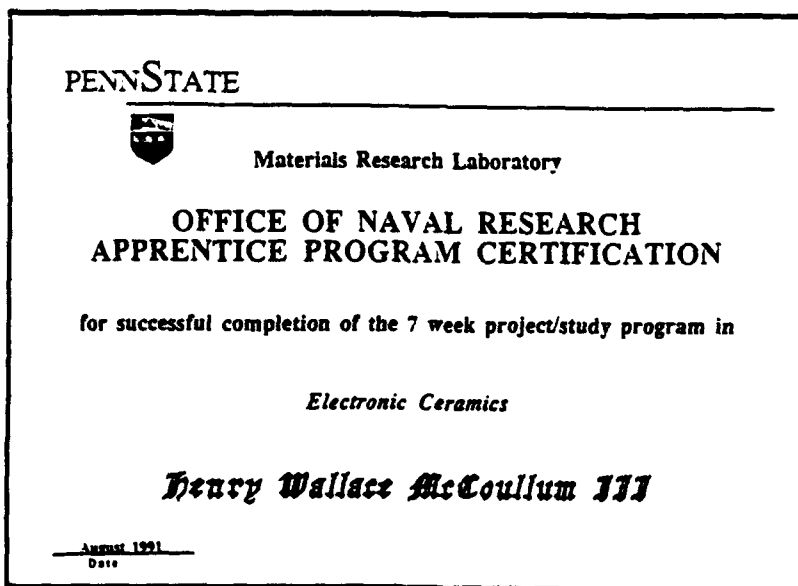
1.   Name:                               Henry Wallace McCoullun III  
     Home Address:                   3130 North Park Avenue  
                                     Philadelphia, PA 19132  
     High School:                    High School of Engineering and Science
2.   Name:                               Corey B. Bryant  
     Home Address:                   2201 W. Ruffner Street  
                                     Philadelphia, PA 19140  
     High School:                    George Washington
3.   Name:                               Shawn M. Bryant  
     Home Address:                   1537 W. Orland Street  
                                     Philadelphia, PA 19126  
     High School:

---

Henry McCoullun, III performed literature review studies in the area of bio-mimetics particularly in relation to sensor and actuation utilized by fish. He worked closely with the graduate students, and compiled his data into a nice working document.

Corey B. Bryant assisted graduate students in the fabrication and characterization of polymer filled composites for microwave absorption.

Shawn M. Bryant aided graduate students in computer simulated graphics and data formatting. He also performed literature searches in the area of sensors and actuators.





PENNSTATE



Materials Research Laboratory

OFFICE OF NAVAL RESEARCH  
APPRENTICE PROGRAM CERTIFICATION

for successful completion of the 7 week project/study program in

*Electronic Ceramics*

***Corey B. Bryant***

August 1991  
Date

PENNSTATE



Materials Research Laboratory

OFFICE OF NAVAL RESEARCH  
APPRENTICE PROGRAM CERTIFICATION

for successful completion of the 7 week project/study program in

*Electronic Ceramics*

***Shawn M. Bryant***

August 1991  
Date

## 9.0 PAPERS PUBLISHED IN REFEREED JOURNALS

1. R. E. Newnham. *Advanced Ceramics (Electronic)* 1, 601 (1991).
2. R. E. Newnham. *Tunable Transducers: Nonlinear Phenomena in Electroceramics*, NIST Publ. 804 (January 1991).
3. M. Blaskiewicz, R. E. Newnham, Q. C. Xu. *Tunable Transducers as Smart Materials*, Proc. 6th Int. Conference on Solid State Sensors and Actuators, San Francisco (June 24-25, 1991).
4. R. E. Newnham. *Composite Electroceramics*, International Encyclopedia of Composites Vol. 6, VCH, New York (1991).
5. Q. C. Xu, S. Yoshikawa, J. R. Belsick and R. E. Newnham. "Piezoelectric Composites with High Sensitivity and High Capacitance for Use at High Pressure," *IEEE Trans. UFFC* 38 (6), 634 (1991).
6. V. Srikanth and E. C. Subbarao. "Acoustic Emission in Ferroelectric Lead Titanate Ceramics: Origin and Recombination of Microcracks," *Acta Met.*
7. M. Fukuhara, A. S. Bhalla and R. E. Newnham. "Morphotropic Phase Boundary in the  $\text{Pb}(\text{Zr}_x\text{Ti}_{1-x})\text{O}_3$  System," *Phys. Stat. Sol (a)* 122, 677 (1990).
8. W. Cao and L. E. Cross. "Theory of Tetragonal Twin Structures in Ferroelectric Perovskites with First Order Phase Transition," *Phys. Rev. B* 44, 5 (1991).
9. S. Li, W. Cao and L. E. Cross. "The Extrinsic Origin of Nonlinear Behaviour Observed in Lead Zirconate Titanate Ferroelectric Ceramics," *J. Appl. Phys.* 69 (10), 7219 (1991).
10. S. Li, W. Cao and L. E. Cross. "Stress and Electric Displacement Distribution near Griffiths Type III Crack Tips in Piezoceramics," *Mat. Letters* 10 (6), 219 (1990).
11. G. A. Rossetti, Jr and L. E. Cross. "Stress Induced Shift of the Curie Point in Epitaxial  $\text{PbTiO}_3$  Thin Films," *J. Appl. Phys.* 59 (20), 2524 (1991).
12. G. A. Rossetti, Jr., T. Nishinura and L. E. Cross. "X-ray and Phenomenological Study of Lanthanum-Modified Lead Zirconate-Titanates in the Vicinity of the Relaxor phase transition Region," *J. Appl. Phys.* 70 (3), 1630 (1991).
13. J. R. Giniewicz, A. S. Bhalla and L. E. Cross. "Pyroelectric Response and Depolarization Behaviour of  $(1-x)\text{PbSc}_{1/2}\text{Ta}_{1/2}\text{O}_3 - x\text{PbTiO}_3$  Materials," *Ferroelectrics* 118, 157 (1991).
14. D. J. Taylor, D. Damjanovic and A. S. Bhalla. "Pyroelectric and Dielectric Properties of PMN-Based Ceramics under DC Bias," *Ferroelectrics* 118, 143 (1991).
15. V. Srikanth and E. C. Subbarao. "Chemical Reactions of Lead Magnesium Niobate Titanate in the Presence of a Glass," *J. Mat. Res.* 6, 1 (1991).
16. P. A. Fuierer and R. E. Newnham. " $\text{La}_2\text{Ti}_2\text{O}_7$  Ceramics," *J. Am. Ceram. Soc.* 74 (11), 2876 (1991).
17. G. R. Fox, J. H. Adair and R. E. Newnham. "Effects of pH and  $\text{H}_2\text{O}_2$  Upon Coprecipitation of  $\text{PbTiO}_3$  Powders," *J. Mat. Sci.* 26, 1187 (1991).

## **9.0 PAPERS PUBLISHED IN REFEREED JOURNALS (continued)**

18. G. A. Rossetti, Jr., D. A. Watson, R. E. Newnham and J. H. Adair. "Kinetics of the Hydrothermal Crystallization of the Perovskite Lead Titanate," *J. Crystal Growth* **116**, 251 (1991).
19. A. Srivastava, A. S. Bhalla and L. E. Cross. "A Study of  $Y_1Ba_2Cu_3O_{7-\delta}$  Thick Films on Ferroelectric Substrates," *J. Am. Ceram. Soc.*
20. A. Srivastava, A. S. Bhalla and L. E. Cross. " $Y_1Ba_2Cu_3O_{7-x}$  as an Electrode Material for Ferroelectric Devices," *Ferroelectrics* **123**, 243 (1991).
21. R. Guo, A. S. Bhalla and L. E. Cross. "Pyroelectric Properties of Lead Barium Niobate Single Crystals," *Ferroelectrics* **118**, 77 (1991).
22. C. A. Randall, R. Guo, A. S. Bhalla and L. E. Cross. "Microstructure-Property Relations in Tungsten Bronze Lead Barium Niobate  $Pb_{1-x}Ba_xNb_2O_6$ ," *J. Mat. Res.* **6**, 1720 (1991).
23. A. S. Bhalla, R. Guo, L. E. Cross, G. Burns, F. H. Dacol and R. R. Neurgaonkar. *J. Applied Phys.* **69** (6) (1992).
24. D. Viehland, S. Jang, L. E. Cross and M. Wuttig. "The Dielectric Relaxation of Lead Magnesium Niobate Relaxor Ferroelectrics," *Phil. Mag. B* **64**, 335 (1991).
25. D. Viehland, S. J. Jang, L. E. Cross and M. Wuttig. "Anelastic Relaxation and Internal Strain in Lead Magnesium Niobate Ceramics," *Phil. Mag. A* **64** (4), 835 (1991).
26. D. Viehland, S. J. Jang, L. E. Cross and M. Wuttig. "Local Polar Configurations in Lead Magnesium Niobate Relaxors," *J. Appl. Phys.* **69**, 414 (1991).
27. D. Viehland, J. F. Li, S. J. Jang, L. E. Cross and M. Wuttig. "Dipolar-Glass Model of Lead Magnesium Niobate," *Phys. Rev. B* **43**, 8316 (1991).
28. K. R. Udayakumar, J. Chen, P. L. Schuele, L. E. Cross, V. Kumar and S. B. Krupanidhi. "Polarization Reversal and High Dielectric-Permittivity in Lead Magnesium Niobate Titanate Thin Films," *Appl. Phys. Lett.* **9**, 1 (1991).

## **10.0 INVITED PAPERS PRESENTED AT NATIONAL AND INTERNATIONAL MEETINGS**

1. R. E. Newnham. "Size Effects in Ferroelectric Films," 5th International Congress on Ultra Structure Processing, Orlando, Florida (February 14, 1991).
2. R. E. Newnham. "Smart Materials," Sensors 1991, San Francisco (June 27, 1991).
3. R. E. Newnham. "Electroceramics in the 1990s and Beyond," Keynote Address European Ceramic Society, Augsburg, Germany (September 11, 1991).
4. R. E. Newnham. "Smart Ceramics," Centennial Meeting of the Japan Ceramic Society, Yokohama, Japan (October 16, 1991).
5. R. E. Newnham. "Biomimetic Sensors and Actuators," Materials Research Society, Boston (December 1991).
6. K. R. Udayakumar, A. M. Flynn, J. Chen and L. E. Cross. "Ferroelectric PZT Thin Films for Microelectromechanical Applications," MEMS 91, Nara, Japan (January 31, 1991).

## 10.0 INVITED PAPERS PRESENTED AT NATIONAL AND INTERNATIONAL MEETINGS (continued)

7. L. E. Cross. "A Dipolar Glass Model for Relaxor Ferroelectrics," EMF7 European Meeting on Ferroelectrics, Dijon, France (July 1991).
8. L. E. Cross. "Piezoelectric Ceramics and Composites for Advanced Sensors Actuators and Smart Materials," EPFL Lausanne Symposium on Matériaux pour les besoins de demain (June 6, 1991).
9. L. E. Cross. "High Strain Actuators for Optical Applications," SPIE Mtg., San Diego (July 24, 1991).
10. L. E. Cross. "Possibility of Super Responses in Ceramics," Gordon Conference on Ceramics, Holderness, Plymouth (July 29, 1991).
11. L. E. Cross. "Actuator Materials," ADPA/AIAA/ASME/SPIE Conference on Active Materials and Adaptive Structures (November 1991).
12. L. E. Cross and Q. Jiang. "Fatigue Effects in High Strain Actuators," 2nd US/Japan Conference on Adaptive Structures, Nagoya, Japan (November 12, 1991).

## 11.0 CONTRIBUTED PAPERS AT NATIONAL AND INTERNATIONAL MEETINGS

*93rd American Ceramic Society National Meeting, Cincinnati, Ohio (April 29, 1991).*

1. **The Extrinsic Contributions to Piezoelectric Effects in Ferroelectric Ceramic.** W. Cao and L. E. Cross, Pennsylvania State University, University Park, PA.
2. **Synthesis of  $\text{PbMg}_{1/3}\text{Nb}_{2/3}\text{O}_3$  (PMN) Using a Novel Peroxo-Citrate Process.** D. S. Applegate, J. J. Kingsley, G. L. Messing and W. Huebner, Pennsylvania State University, University Park, PA.
3. **Effect of Seeding on the Crystallization of Lead Magnesium Niobate (PMN) Gels.** P. Ravindranathan, S. Komarneni, A. S. Bhalla and R. Roy, Pennsylvania State University, University Park, PA.
4. **Particle/Grain Size Dependence of Ferro- and Antiferroelectricity (Invited Paper).** K. Uchino, Sophia University, Tokyo, Japan.
5. **Electrorheological Fibril Formation and Its Application to Electroceramic Composites (Invited Paper).** C. A. Randall, D. V. Miller, and A. S. Bhalla, Pennsylvania State University, University Park, PA; and J. H. Adair, University of Florida, Gainesville, FL.
6. **An Empirical Relationship for Predicting the Dielectric Constants of Oxides.** K. A. Markowski, V. Sundar and R. E. Newnham, Pennsylvania State University, University Park, PA.
7. **Microwave Properties of 0-3 and 1-3 Composite Materials.** F. G. Jones, C. A. Randall and S. J. Jang, Pennsylvania State University, University Park, PA.

## 11.0 CONTRIBUTED PAPERS AT NATIONAL AND INTERNATIONAL MEETINGS (continued)

*93rd American Ceramic Society National Meeting, Cincinnati, Ohio  
(April 29, 1991)[continued].*

8. **Process-Property Relations in PMN-Based Ceramics.** U Kumar, M. Megherhi and J. P. Dougherty, Pennsylvania State University, University Park, PA; and A. Halliyal, The DuPont Company, Wilmington, DE.
9. **High Temperature Thermal Expansion Mechanism of Perovskite Relaxor Ferroelectrics.** L. M. Kamdar, H. Takahara, A. S. Bhalla and R. E. Newnham, Pennsylvania State University, University Park, PA.
10. **Electrooptic Effects in the Ceramic  $\text{Pb}(\text{Mg}_{1/3}\text{Nb}_{2/3})\text{O}_3$ ,  $\text{PbTiO}_3$  System.** D. A. McHenry, S. J. Jang and A. S. Bhalla, Pennsylvania State University, University Park, PA.
11. **The Role of Lithium Nitrate in Lowering the Sintering Temperature of Lead Magnesium Niobate-Based Ceramics.** M. H. Megherhi, J. P. Dougherty and R. E. Newnham, Pennsylvania State University, University Park, PA; and G. O. Dayton, Vitramon, Inc. Bridgeport, Ct.
12. **Measurement of Piezoelectric Coefficients Using Laser Interferometry.** K. W. Gachigl, A. S. Bhalla and L. E. Cross, Pennsylvania State University, University Park, PA.
13. **Hydrothermal Synthesis of PZT ( $\text{Pb}(\text{Zr}_{0.52}\text{Ti}_{0.48})\text{O}_3$ ) Powders.** J. P. Witham, P. Ravindranathan and J. P. Dougherty, Pennsylvania State University, University Park, PA.
14. **Electric Fatigue in Ferroelectric PLZT Ceramics.** Q. Y. Jiang, L. E. Cross and S. B. Krupanidhi, Pennsylvania State University, University Park, PA.
15. **Grain Size Effects in PZT Based Ceramics.** N. Kim, J. T. Fielding, S. J. Jang and T. R. Shrout, Pennsylvania State University, University Park, PA.
16. **Characterization of Ferroelectric Surfaces and Thin Films by Spectroscopic Ellipsometry.** S. E. Troler-McKinstry, P. Chindaudom and R. E. Newnham, Pennsylvania State University, University Park, PA.
17. **The Dielectric Dispersion of Relaxor Ferroelectrics.** D. Viehland, S. J. Jang and L. E. Cross, Pennsylvania State University, University Park, PA; and M. Wuttig, University of Maryland, College Park, MD.
18. **Ferroelectric Thin Films - Current Status and Future Prospects (Overview) (Invited Paper).** L. E. Cross, Pennsylvania State University, University Park, PA.
19. **Synthesis of  $\text{BaTiO}_3$  By a Modified Citrate Gel Method.** S. Kumar, G. L. Messing and W. Huebner, Pennsylvania State University, University Park, PA.
20. **Low Temperature Conventional Preparation of Ultra-Fine Grained  $\text{BaTiO}_3$  Ceramic.** U. Kumar and J. P. Dougherty, Pennsylvania State University, University Park, PA.

## 11.0 CONTRIBUTED PAPERS AT NATIONAL AND INTERNATIONAL MEETINGS (continued)

*93rd American Ceramic Society National Meeting, Cincinnati, Ohio  
(April 29, 1991)(continued).*

21. **Optical and Electrooptic Properties of Lead Barium Niobate (PBN) Single Crystals.** R. Guo, D. A. McHenry, A. S. Bhalla and L. E. Cross, Pennsylvania State University, University Park, PA.

*Papers Presented at the Materials Research Society Meeting, Boston (December 1991).*

1. **Crystallization Dynamics and Rapid Thermal Annealing of PZT Thin Films.** Jiayu Chen, Keith G. Brooks, K. R. Udayakumar and L. Eric Cross, Pennsylvania State University, Materials Research Laboratory, University Park, PA.
2. **Piezoelectric Thin Film Ultrasonic Micromotors.** K. R. Udayakumar, J. Chen, K. G. Brooks and L. E. Cross, Pennsylvania State University, Materials Research Laboratory, University Park, PA; A. M. Flynn, S. F. Bart, L. S. Tavrow, R. A. Books, Massachusetts Institute of Technology, AI Laboratory, Cambridge, MA; and D. J. Ehrlich, Massachusetts Institute of Technology, Lincoln Laboratory, Lexington, MA.
3. **Electron Cyclotron Resonance (ECR) Plasma Assisted Growth of Ferroelectric Thin Films.** John R. Belsick, Nick Maffei and S. B. Krupanidhi, Pennsylvania State University, Materials Research Laboratory, University Park, PA.
4. **Properties of PZT Thin Films with Glass Additives Prepared by the Sol-Gel Process.** Keith G. Brooks, Jiayu Chen, K. R. Udayakumar and L. Eric Cross, Pennsylvania State University, Materials Research Laboratory, University Park, PA.
5. **Ferroelectric Thin Films for Microactuator Applications.** Jiayu Chen, K. R. Udayakumar, Keith G. Brooks and L. Eric Cross, Pennsylvania State University, Materials Research Laboratory, University Park, PA.
6. **Ferroelectric Switching in Lead Zirconate-Lead Zinc Niobate Thin Films.** K. R. Udayakumar, Jiayu Chen, Keith G. Brooks and L. Eric Cross, Pennsylvania State University, Materials Research Laboratory, University Park, PA.
7. **Modified Tetragonal Lead Zirconate Titan Stannate Thin Films Prepared by Sol-Gel Process Large Strain Microactuator Applications.** Keith G. Brooks, Jiayu Chen, K. R. Udayakumar and L. Eric Cross, Pennsylvania State University, Materials Research Laboratory, University Park, PA.

*Invited Presentations at University, Industry and Government Laboratories.*

1. January 8, 1991. "Nanocomposites," R. E. Newnham, National Materials Advisory board Meeting on Hierarchical Materials, Washington, D.C.
2. February 14, 1991. "Smart Ceramics," R. E. Newnham, Alcoa Research Center Seminar, Alcoa Center, Pittsburgh, PA.
3. March 19, 1991. "Smart Materials," R. E. Newnham, IBM Research Laboratory Seminar, White Plains, NY.

## **11.0 CONTRIBUTED PAPERS AT NATIONAL AND INTERNATIONAL MEETINGS (continued)**

### *Invited Presentations at University, Industry and Government Laboratories (continued).*

4. March 21, 1991. "Smart Ceramics," R. E. Newnham, General Motors Research Laboratory Seminar, Detroit, MI.
5. April 8, 1991. "Smart Ceramics," R. E. Newnham, Dept. of Materials Science, University of Illinois, Champaign-Urbana, IL.
6. April 17, 1991. "Integrated Electroceramics," R. E. Newnham, Lubrizol Research Laboratory Seminar, Cleveland, OH.
7. April 22, 1991. "Flextensional Transducers and Actuators," R. E. Newnham, ONR Piezoelectric Transducer Meeting, Penn State.
8. April 27, 1991. "Smart Materials," R. E. Newnham, JASON D.A.R.P.A. Meeting, Washington D.C.
9. May 7, 1991. "Smart Materials," R. E. Newnham, Center for Dielectric Studies, Penn State.
10. May 24, 1991. "Composite Piezoelectrics," R. E. Newnham, United Technologies Research Center, e. Hartford, Connecticut.
11. June 4, 1991. "Ferroelectric Materials," R. E. Newnham, Materials Research Society, Arlington, TX (invited).
12. June 11-13, 1991. "Composite Sensors and Actuators" and "Smart Ceramics," R. E. Newnham. Two seminars at the Houldsworth School of Materials, Leeds University, Leeds, UK.
13. June 20, 1991. "Smart Ceramics," R. E. Newnham, G.E.C. Marconi Research Laboratory, UK.
14. July 18, 1991. "Smart Materials," R. E. Newnham, D.A.R.P.A Materials Meeting, San Diego, CA.
15. July 19, 1991. "Electrostriction," R. E. Newnham, JASON Meeting, San Diego, CA.
16. September 6, 1991. "Composite Ferroelectrics," R. E. Newnham, International Summer School on Ferroelectricity, Ascona, Switzerland (invited).
17. September 9, 1991. "Smart Ceramics," R. E. Newnham, Seminar at Asea, Brown, Boveri Research Laboratory (ABB), Baden, Switzerland (invited).
18. September 24, 1991. "Smart Ceramic Devices," R. E. Newnham, Electrical Engineering Department Seminar, Syracuse University.
19. October 9, 1991. "Ferroic Nanocomposites," R. E. Newnham, D.A.R.P.A. Annual Meeting, Alexandria, VA.

## **11.0 CONTRIBUTED PAPERS AT NATIONAL AND INTERNATIONAL MEETINGS (continued)**

### *Invited Presentations at University, Industry and Government Laboratories (continued).*

20. October 21, 1991. "Smart Ceramics," R. E. Newnham, Seminar at Kyocera Co., Kagoshima, Japan.
21. October 31, 1991. "Smart Ceramics," R. E. Newnham, Speech at Chemically Bonded Ceramics Center, Penn State.
22. November 3, 1991. "Smart Electroc ceramics," R. E. Newnham, ONR Workshop on Robotic Actuators, Alexandria, VA (invited).
23. November 4-8, 1991. International Symposium on Active Materials and Adaptive Structures, Alexandria, VA. Tutorial Workshop on Piezoelectricity and Electrostriction, L. E. Cross, R. E. Newnham and K. Uchino (invited). "Piezoelectric and Electrostrictive Composites Actuators," R. E. Newnham, Q. C. Xu and S. Yoshikawa.
24. November 13, 1991. "Smart Materials," R. E. Newnham, Materials Research Society, Pittsburgh Chapter (invited).
25. November 14, 1991. "Recent Advances in Packaging Materials," R. E. Newnham, Alcoa Research Seminar (invited).
26. February 3-5, 1991. "A Dipolar Glass Model for Relaxor Ferroelectrics," D. Viehland, S. J. Jang, M. Wuttig and L. E. Cross, Lehigh/ONR Workshop on Fundamental Experiments in Ferroelectricity, Williamsburg, VA.
27. "Twin Structures and Their Contributions to Piezoelectric Effects in Ferroelectric Ceramics," W. Cao and L. E. Cross.
28. February 19, 1991. "Relaxor Ferroelectrics," L. E. Cross, Arizona State University.
29. September 2, 1991. "Ferroelectric Ceramics: Tailoring Properties for Specific Applications," L. E. Cross, 2nd International Ferroelectric Summer School, Ascona, Switzerland (invited).
30. October 30, 1991. "Photorefractive Fibers," L. E. Cross, DARPA Eye and Sensor Protection Review, Arlington, VA.
31. March 26, 1991. "Sensor and Transducer Material at Penn State MRL," J. Dougherty, Ford Motor Co. Electronics Technical Center (invited).
32. August 7, 1991. J. Dougherty, Seminar at General Motor AC Rochester Technical Center.
33. September 4-5, 1991. J. Dougherty, ARO Workshop on Smart Materials for Resilient Structure, Research Triangle, NC.
34. September 6, 1991. "Piezoelectric Transducer Materials," J. Dougherty, EPRI Workshop, Washington, DC (invited).
35. October 14, 1991. "Electronic Ceramics at MRL," J. Dougherty, Seminar to Lord Corporation, State College, PA.



## 11.0 CONTRIBUTED PAPERS AT NATIONAL AND INTERNATIONAL MEETINGS (continued)

*Invited Presentations at University, Industry and Government Laboratories (continued).*

36. November 13, 1991. "Electronic Ceramics at MRL," J. Dougherty, Seminar at DSM Technical Center, Geleen, Netherlands (invited).

## 12.0 HONORS TO MRL FACULTY AND STUDENTS

<u>Name of Person Receiving the Award</u>	<u>Name of Award</u>	<u>Sponsor</u>
R. E. Newnham	John Jeppson Medal and Award	American Ceramic Society
R. E. Newnham	Centennial Award of Ceramic Society of Japan	Japan Ceramic Society
Ruyan Guo	Xerox Award for Best Materials PhD in 1991.	Xerox Corporation

## 13.0 REFERENCES

1. G. Arlt, "The Role of Domain Wall on the Dielectric, Elastic and Piezoelectric Properties of Ferroelectric Ceramics," *Ferroelectrics* **76**, 451-458 (1987); G. Arlt, "Microstructure and Domain Effects in Ferroelectric Ceramics," *Ferroelectrics* **91**, 3-7 (1989).
2. W. R. Buessem, N. R. Thielke and R. V. Sarakausakas, *Ceramic Age* **60**, 38 (1952); W. R. Buessem, in *Mechanical Properties of Engineering Ceramics* (edited by W. W. Kriegel and H. Palmour III), p. 127, Interscience, New York (1961); W. R. Buessem and F. F. Lange, *Interceram* **15**, 229 (1966).
3. G. Arlt, H. Dederichs, and R. Herbel, *Ferroelectrics* **74**, 37 (1987).

# **GENERAL SUMMARY PAPERS**

## **APPENDIX 1**

# **FERROELECTRIC CERAMICS TAILORING PROPERTIES FOR SPECIFIC APPLICATIONS**

**L. Eric Cross**

**Evan Pugh Professor of Electrical Engineering  
Materials Research Laboratory  
The Pennsylvania State University  
University Park, PA 16802-4801 USA**

## **1.0. INTRODUCTION**

Ferroelectric oxide ceramics are used in a very broad range of functional ceramics and form the materials base for the majority of electronic applications. These electronic applications account for more than 60% of the total high technology ceramics market worldwide.<sup>1</sup> It is the purpose of this tutorial paper to examine the range of physical properties which make the ferroelectrics attractive for electronic applications and the techniques which can be used to modify, control and optimize these families of properties.

Major applications can be divided into five distinct areas which draw upon different combinations of properties.

Dielectric applications make use of the very high dielectric permittivity  $\epsilon_{ij}$ , low dispersion and wide frequency range of response for compact capacitors in multilayers, thick and thin film forms.<sup>2</sup> Nonlinear hysteretic response is of interest also for thin film nonvolatile semiconductor memory,<sup>3</sup> and high permittivity films are of interest for local capacitance in high count DRAMs and both on and off chip in packaging.<sup>4</sup>

Piezoelectric and Electrostrictive responses in poled and unpoled ferroelectric and relaxor ferroelectric compositions are of importance in Transducers<sup>5</sup> for converting electrical to mechanical response,<sup>6</sup> and vice versa.<sup>7</sup> Sensor applications make use of the very high piezoelectric constants  $d_{ijk}$  of the converse effect, which also permit efficient conversion of electrical to mechanical response.<sup>8</sup> For Actuation the strong basic electrostrictive coupling can be exploited for very high precision position control<sup>9</sup> and the possibility of phase and domain switching with shape memory used in polarization controlled actuation.<sup>10</sup>

Pyroelectric systems rely upon the strong temperature sensitivity of electric polarization ( $dP_e/dT$ ).<sup>11</sup> the pyroelectric effect in ferroelectrics, for the bolometric detection of long wavelength infra red (IR) radiation.<sup>12</sup> Simple point detectors are widely used in domestic and industrial applications<sup>13</sup> and there is now a strong focus upon imaging systems which may be used for night vision<sup>14</sup> and for thermal-medical diagnostics.<sup>15</sup>

P.T.C. semiconductors are a specialized area of application in which the barrier to charge transport at the ceramic grain boundary in specially processed barium titanate based ceramics is controlled by the polarization state of the ferroelectric,<sup>16</sup> giving rise to an extremely strong positive temperature coefficient of resistivity (PTCR effect) controlled by the Curie point of the ferroelectric composition.<sup>17</sup>

In Electro-optic applications the properties of interest are the high quadratic<sup>18</sup> and linear<sup>19</sup> electro-optic coefficients ( $r_{ijk}$ ,  $g_{ijk}$ ) which occur in ferroelectrics and the

manner in which these can be controlled in modulators,<sup>20</sup> switches,<sup>21</sup> guided wave structures and photo-refractive devices.<sup>22</sup>

In this tutorial, the dielectric, piezoelectric and electrostrictive applications will be the focus, but the techniques examined to modify and improve properties will also be valid for many of the other material needs.

Considering the nature of the properties to be optimized two important features will be stressed. Firstly the interest is in bulk, lattice properties controlled largely by the crystal structure of the ceramic. Secondly in every case it is augmented compliance (softness) which is of interest, in contrast often to the structural ceramics where it is stiffnesses which must be augmented. It follows then that instability of the lattice will be of importance, since this engenders compliance, and thus phase changes which are the finger prints of instability will be of major importance. Frequently to improve properties then, we are looking to exploit and control solid state phase transitions.

Clearly a bounding condition is that the crystal structure must permit ferroelectricity in a useful region of temperature and pressure, and must be of a type which can be exploited in the simple polycrystal ceramic form. In fact, all of the structures of interest are based on regular arrays of oxygen octahedra, and the simple perovskite structure is certainly the most widely used.

## 2.0 STRUCTURE TYPES OF INTEREST

The interesting oxygen octahedron structures which show strong ferroelectric properties with high usable temperature ranges are all based upon corner linking of oxygen octahedra. The simplest arrangement is the very well known perovskite structure Fig. 2.1 where the octahedra are linked in a regular cubic array forming the high symmetry  $m3m$  prototype for many ferroelectric forms. The small 6 fold coordinated site in the center of the octahedron is filled by a small highly charged (3,4,5 or 6 valent) cation and the larger 12 fold coordinated 'interstitial' site between octahedra carries a larger mono, di or trivalent cation, or is empty as in  $\text{WO}_3$ .

The perovskite structure is a common stable form for many double oxides, but ferroelectricity was not discovered in the family until the early 1940s, when Wainer and Solomon<sup>23</sup> in the USA, Ogawa<sup>24</sup> in Japan and Wul and Goldman<sup>25</sup> in the USSR made almost simultaneous discovery of ferroelectricity in barium titanate  $\text{BaTiO}_3$ . The US study was part of a 'crash' program during World War II to discover a ceramic substitute for mica which was being exhausted by rapidly escalating military needs. It is perhaps interesting to note that  $\text{BaTiO}_3$  which was the highlight of these early studies is still the base for the composition of most of the world's ceramic capacitors. An interesting documentation of early work in Japan has been carried forward by Murata Company and is now available in book form<sup>26</sup> for those well versed in the language. Perhaps now it may be possible to catalogue more completely the Soviet contribution to complete the early history of the titanates. Structural information for a very broad range of perovskites is available in the early book by Galasso,<sup>27</sup> which is now being revised and updated. Certainly the most complete trustworthy cataloguing of ferroelectric oxide perovskites is given in the Landolt Bornstein Vol. 16a on oxide ferroelectrics.<sup>28</sup> This tabulates more than 100 perovskite compounds and innumerable solid solutions between compounds.

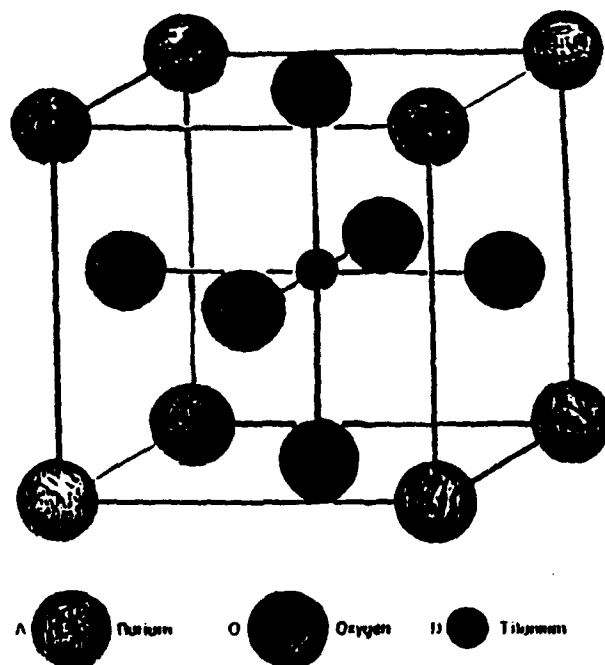


Fig. 2.1 The unit cell for a typical cubic perovskite barium titanate in the cubic  $Pm\bar{3}m$  prototypic phase above  $T_c$ .

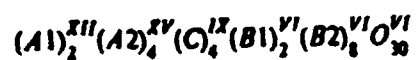
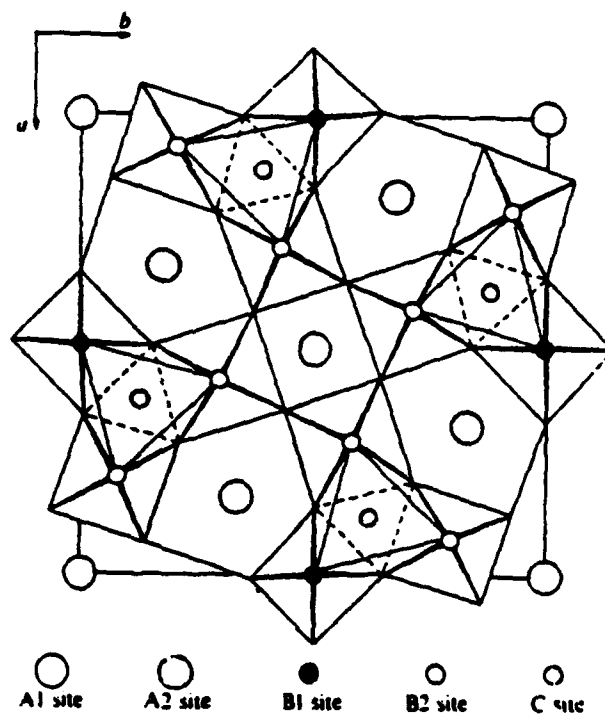
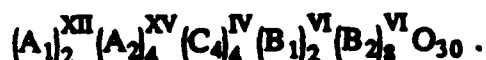


Fig. 2.2 Projection down the  $c(3)$  axis of a unit cell in the tungsten bronze structure. Site locations are marked and the structure related formula is given. Roman superscripts mark the coordination of the ions at each site location.

Of major importance in ceramic dielectric applications are  $\text{BaTiO}_3$  and solid solutions with  $\text{SrTiO}_3$ ,  $\text{PbTiO}_3$ ,  $\text{BaZrO}_3$ ,  $\text{BaSnO}_3$ ,  $\text{CaTiO}_3$ ..... and a range of bismuth oxide based modifiers. In piezoelectrics the higher Curie points in the  $\text{PbTiO}_3$ : $\text{PbZrO}_3$  solid solutions and the unusual ferroelectric phase makeup are vital and in both dielectric and electrostrictive application the  $\text{Pb}(\text{B}_1\text{B}_2)\text{O}_3$  mixed cation compositions are becoming of increasing interest where  $\text{B}_1$  may be Fe, Ni, Mg, Zn..... and  $\text{B}_2$ , Ti, Zr, Nb, Ta, W.... etc.

In current electronic ceramic applications only perovskite structure compositions are used, however with increasing sophistication in ceramic processing it is probably that strongly grain oriented structures may become practicable. The newer thin film structures also provide avenues for orientation using topotactic configurations on suitable substrates, so that ferroelectrics from lower prototypic symmetries may become of interest in ceramics.

The next most versatile structure family are the Tungsten Bronze structure ferroelectrics with the octahedron arrangement in fig. 2.2 . The rotations of the octahedra evident in the ab plane of the structure in 2.2 reduce the point symmetry to tetragonal (4/mmm) with layers stacked in regular sequence along the 4 fold (c) axis. The arrangement distinguishes two inequivalent 6 fold coordinated B sites at the centers of inequivalent octahedra with 5, 4 and 3 sided tunnels for the A site cations extending along the c axis giving the structure related formula for the bronzes.



The bronzes are a very rich family of oxide ferroelectrics with Curie temperatures reaching up to 560°C and more than 85 compounds in the most recent survey.<sup>29</sup> Again there is very extensive solid solution between end members<sup>30</sup> and the open nature of the structure as compared to the perovskite permits a very wide range of cation and anion substitutions without loss of ferroelectricity.

The bismuth oxide layer structures for which  $\text{Bi}_4\text{Ti}_3\text{O}_{12}$  is the prototype are depicted in fig. 2.3 and have structures based on corner linked perovskite like sheets, separated by bismuth oxide  $(\text{Bi}_2\text{O}_2)^{2+}$  layers.<sup>31</sup> Compositions with 1, 2, 3, 4 and 5 layers are known and there is limited mutual solid solubility.<sup>32</sup>

The lithium niobate structure is really a variant of the perovskite fig. 2.4 and a much more restrictive arrangement, so that only  $\text{LiNbO}_3$ ,  $\text{LiTaO}_3$  and a very limited range of solid solutions based on these compounds have this form.

In what follows, the discussion is centered on systems with the perovskite structure.

### 3.0 PHASE TRANSITIONS IN PEROVSKITES

Three different types of phase transitions are of interest in the perovskites, starting from the highest symmetry cubic form.

- Simple proper ferroelectric transitions leading to fully ferroelectric partially ferroelastic species.

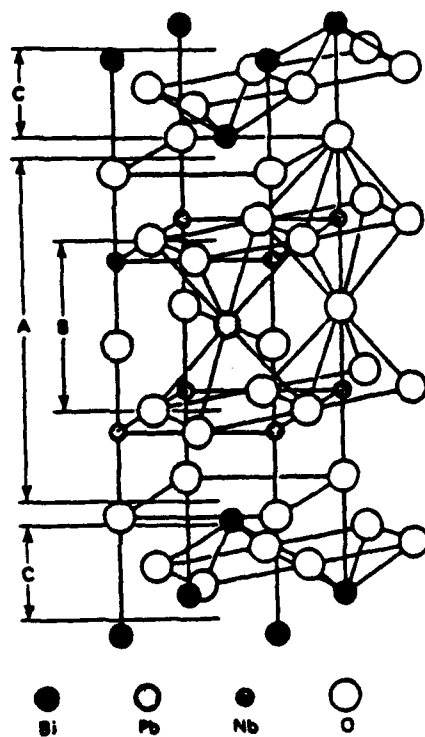


Fig. 2.3 One half of the tetragonal ( $4/\text{mmm}$ ) unit cell of  $\text{PbBi}_2\text{Nb}_2\text{O}_9$ .  $A$  denotes the perovskite double layer  $(\text{PbNb}_2\text{O}_7)^{2-}$ ;  $B$  denotes a hypothetical  $\text{PbNbO}_3$ ;  $C$  denotes the  $(\text{Bi}_2\text{O}_2)^{2+}$  layers.

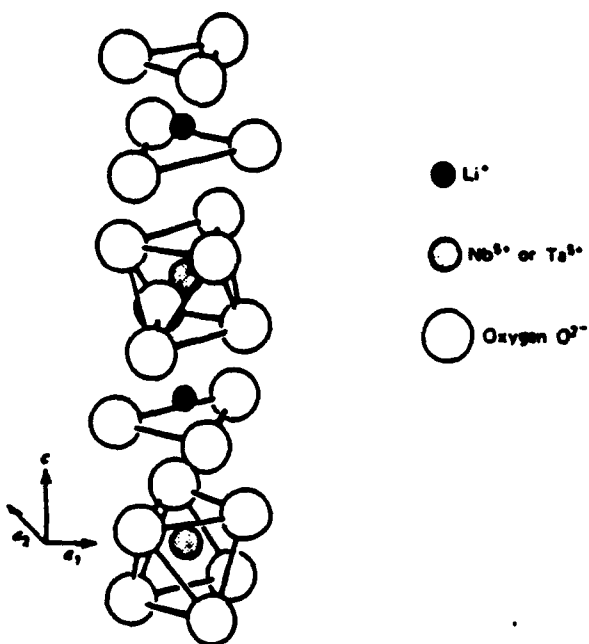


Fig. 2.4 Structure of ferroelectric  $\text{LiNbO}_3$  and  $\text{LiTaO}_3$  (40).



- Antiferroelectric transitions close in free energy to the ferroelectric forms, giving rise to interesting dielectric and to improper ferroelastic species.
- Oxygen octahedron tilting transitions which can occur independently, or in association with either ferroelectric or antiferroelectric forms.

### 3.1 Ferroelectric Phase Transitions

Most important for their profound influence on the dielectric polarizability and the resultant sequence of polar variants are the simple proper ferroelectric transitions. In the symmetry classification of Aizu<sup>33,34,35</sup> and of Shuvalov<sup>36</sup> the high symmetry cubic  $m3m$  prototype can give rise to six different polar species (Table 3.1). The vector directions of polarization which are specified with respect to elements of the prototype symmetry form the domain states of the ferroelectric form in each case giving 6, 12, 8, 24, 24 and 48 domain polarization directions respectively.

TABLE 3.1

Ferroelectric phase transitions possible from the cubic  $m3m$  prototype following the symbolism of Shuvalov.

Phase	Symmetry	Polarization Components	Shuvalov Species
Cubic	$m3m$	$P_1 = P_2 = P_3 = 0$	Prototype
Tetragonal	$4mm$	$P_1^2 \neq 0 \quad P_2^2 = P_3^2 = 0$	$m3m(3)D4F4mm$
Orthorhombic	$mm2$	$P_1^2 = P_2^2 \neq 0 \quad P_3^2 = 0$	$m3m(6)D2Fmm2$
Rhombohedral	$3m$	$P_1^2 = P_2^2 = P_3^2 \neq 0$	$m3m(4)D3F3m$
Monoclinic	$m$	$P_1^2 \neq P_2^2 \neq 0 \quad P_3^2 = 0$	$m3m(12)A4Fm$
Monoclinic	$m$	$P_1^2 = P_2^2 \neq 0 \quad P_3^2 \neq 0$ $P_1^2 \neq P_2^2$	$m3m(12)A2Fm$
Triclinic	1	$P_1^2 \neq P_2^2 \neq P_3^2 \neq 0$	$m3m(24)A1F$

Clearly for a randomly axed polycrystalline ceramic form, the more switchable domain states, the easier it will be to "thread" polarization through the sample. Surprisingly however, even though permitted by symmetry, there have been no cases reported of transitions into monoclinic or triclinic symmetries in the perovskites even though such states would be highly advantageous for ceramics.

In many instances the ferroelectric variant is not stable over the whole temperature range below the first ferroelectric Curie point transition and the structure may go successively into lower symmetry species. The sequence of transitions in barium titanate, which is the base composition for most dielectric applications is shown in fig. 3.1a. Successive transitions on cooling take the domain symmetry to tetragonal, orthorhombic and rhombohedral. A very simple Landau type theory has been given by Devonshire<sup>37,38</sup> which gives an elegant phenomenological description of the phase transitions, polarization states, dielectric and elastic properties and the shape changes depicted in fig. 3.1b.

### **3.2 Octahedral Tilting Phase Transitions**

In many perovskites, particularly those with smaller A site cations, the net of orthogonal corner linked oxygen octahedra "crumples" at lower temperatures. The octahedra remain corner linked and adjacent octahedra thus must contra rotate fig. 3.2. Rotations can take place around any of the three 4-fold axes so that formally the tilt structures may be treated phenomenologically (using the tilt angle  $\theta$  as the appropriate order parameter).<sup>39</sup> Since the tilts necessarily carry strongly coupled antipolar oxygen displacement effects on the polarizability of the lattice are not strong, however the displacements are shape changing and thus give rise to improper ferroelastic domain structures. Excellent compact classifications of the possible tilt system have been given by Glazer<sup>40</sup> (see fig. 3.3) and by Alexandrov.<sup>41</sup>

### **3.3 Antiferroelectric Phase Transitions**

In certain perovskites the dielectric "fingerprints" in the prototypic high temperature phase suggest increasing compliance with decreasing temperature, the signal for a lower temperature ferroelectricity. However the phase transition is into a nonpolar form with antipolar displacements of the normal ferroactive cations at the unit cell level. As with the polar forms, the antipolar displacements are strongly coupled to the crystal shape so that in symmetry, the domain states are a sub group of the improper ferroelastics. For electrical purposes only those antiferroelectrics which are close in free energy to alternative ferroelectric forms are of interest especially in the special case where the energy difference can be over ridden by a realizable electric field.

Sodium niobate and Lead zirconate are two well documented antiferroelectrics where high field switching to the ferroelectric form has been well authenticated.<sup>42,43</sup> However the list of "card carrying" perovskite antiferroelectrics is still short and the subject merits additional study. It would be indeed useful to remove some of the question marks which 'dog' current lists of antiferroelectric compositions (fig. 3.4).

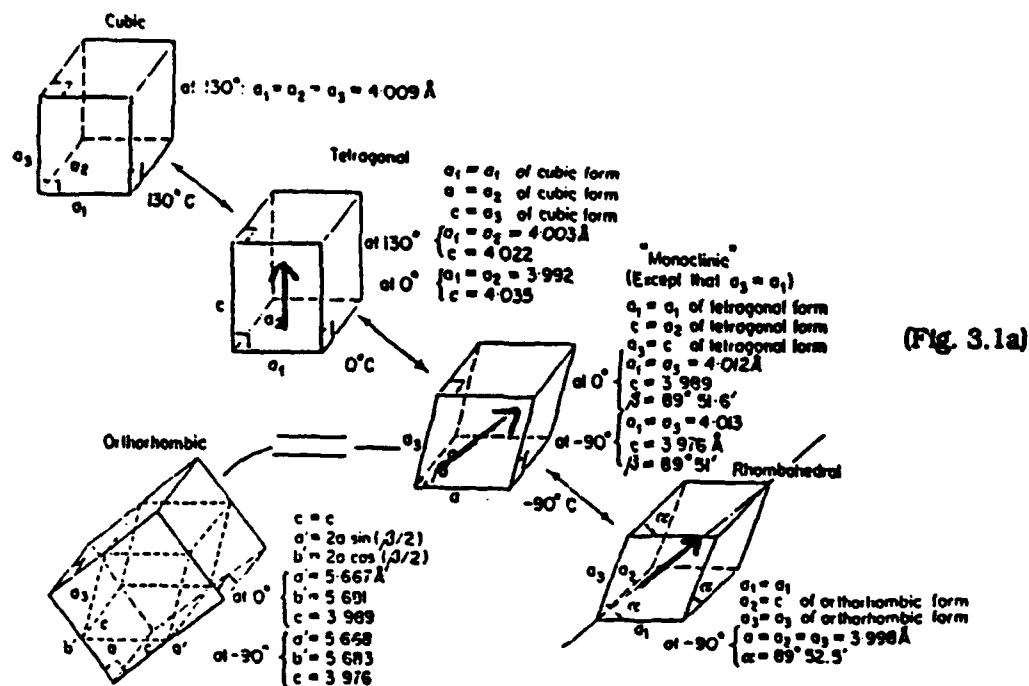


(Fig. 3.1a)

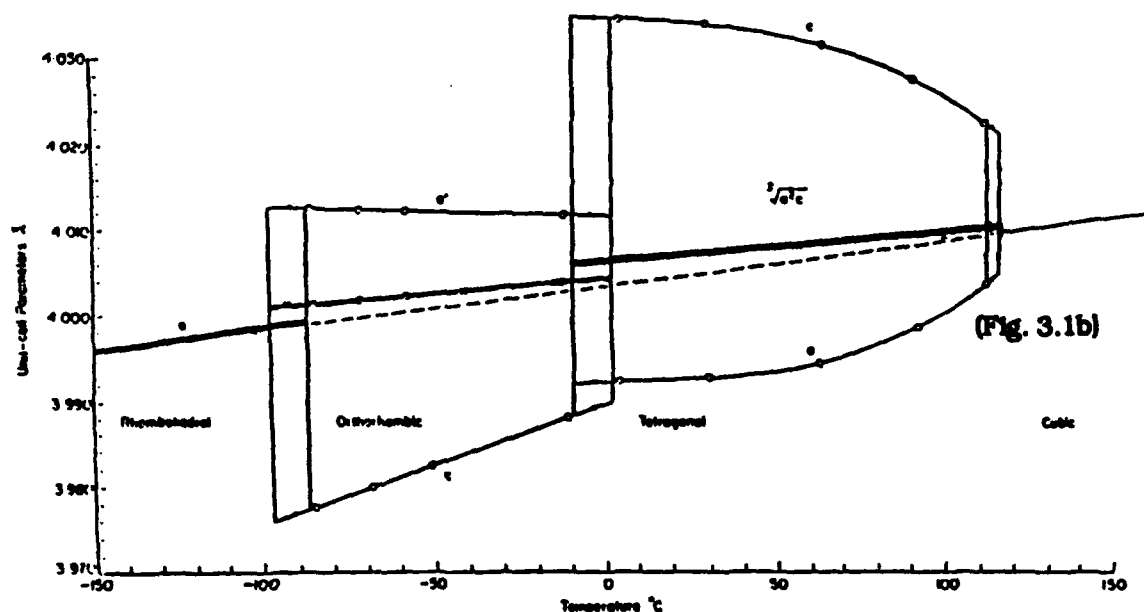


Fig. 3.1 Sequence of phases which occur on cooling a  $\text{BaTiO}_3$  crystal from high temperature. (Fig. 3.1a) Unit cell dimensions and orientation of  $\text{Ps}$  vector in each phase. (Fig. 3.1b) Unit cell dimensions as a function of temperature across the three ferroelectric phases.

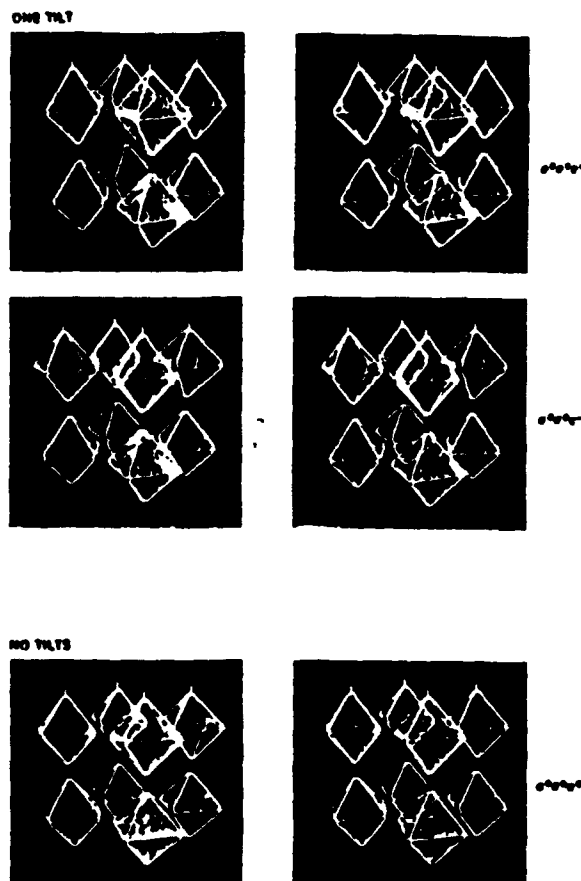


Fig. 3.2 Oxygen octahedral arrangements in an untilted structure  $a^0a^0a^0$ : Oxygen tilts in a co-tilted c axis rotated structure  $a^0a^0c^+$  and in a contra-rotated layer structure  $a^0a^0c^-$ . Notation due to A Glaser.

**Complete list of possible simple tilt systems**

Serial number	Symbol	Lattice centring	Multiple cell	Relative pseudocubic subcell parameters	Space group
<b>3-tilt systems</b>					
(1)	$a^+b^+c^+$	$I$	$2a_p \times 2b_p \times 2c_p$	$a_p \neq b_p \neq c_p$	$Immm$ (No. 71)
(2)	$a^+b^+h^+$	$I$		$a_p \neq b_p = c_p$	$Immm$ (No. 71)
(3)	$a^+a^+a^+$	$I$		$a_p = b_p = c_p$	$Im3$ (No. 204)
(4)	$a^+h^+c^-$	$P$		$a_p \neq b_p \neq c_p$	$Pmmn$ (No. 39)
(5)	$a^+a^+c^-$	$P$		$a_p = b_p \neq c_p$	$Pmmn$ (No. 39)
(6)	$a^+h^+h^-$	$P$		$a_p \neq b_p = c_p$	$Pmmn$ (No. 39)
(7)	$a^+a^+a^-$	$P$		$a_p = b_p = c_p$	$Pmmn$ (No. 39)
(8)	$a^+h^+c^-$	$A$		$a_p \neq b_p \neq c_p, \alpha \neq 90^\circ$	$A2_1/m11$ (No. 11)
(9)	$a^+a^+c^-$	$A$		$a_p = b_p \neq c_p, \alpha \neq 90^\circ$	$A2_1/m11$ (No. 11)
(10)	$a^+h^+b^-$	$A$		$a_p \neq b_p = c_p, \alpha \neq 90^\circ$	$Pmm2$ (No. 62) <sup>*</sup>
(11)	$a^+a^+a^-$	$A$		$a_p = b_p = c_p, \alpha \neq 90^\circ$	$Pmm2$ (No. 62) <sup>*</sup>
(12)	$a^+h^+c^-$	$F$		$a_p \neq b_p \neq c_p, \alpha \neq \beta \neq \gamma \neq 90^\circ$	$F\bar{1}$ (No. 2)
(13)	$a^+h^+h^-$	$F$		$a_p \neq b_p = c_p, \alpha \neq \beta \neq \gamma \neq 90^\circ$	$I2/a$ (No. 15) <sup>*</sup>
(14)	$a^+a^+a^-$	$F$		$a_p = b_p = c_p, \alpha = \beta = \gamma \neq 90^\circ$	$R\bar{3}c$ (No. 167)
<b>2-tilt systems</b>					
(15)	$a^+b^+c^+$	$I$	$2a_p \times 2b_p \times 2c_p$	$a_p < b_p \neq c_p$	$Immm$ (No. 71)
(16)	$a^+h^+h^+$	$I$		$a_p < b_p = c_p$	$I4/m$ (No. 78)
(17)	$a^+h^+c^-$	$B$		$a_p < b_p \neq c_p$	$Bmmh$ (No. 63)
(18)	$a^+h^+h^-$	$B$		$a_p < b_p = c_p$	$Bmmh$ (No. 63)
(19)	$a^+h^+c^-$	$F$		$a_p < b_p \neq c_p, \alpha \neq 90^\circ$	$F2/m11$ (No. 12)
(20)	$a^+b^+b^-$	$F$		$a_p < b_p = c_p, \alpha \neq 90^\circ$	$Imcm$ (No. 74) <sup>*</sup>
<b>1-tilt systems</b>					
(21)	$a^+a^+c^+$	$C$	$2a_p \times 2b_p \times c_p$	$a_p = b_p < c_p$	$C4/mmb$ (No. 127)
(22)	$a^+a^+c^-$	$F$	$2a_p \times 2b_p \times 2c_p$	$a_p = b_p < c_p$	$F4/mmc$ (No. 140)
<b>Zero-tilt system</b>					
(23)	$a^+a^+a^+$	$P$	$a_p \times b_p \times c_p$	$a_p = b_p = c_p$	$Pm\bar{3}m$ (No. 221)

\* These space group symbols refer to axes chosen according to the matrix transformation

$$\begin{pmatrix} 1 & 0 & 0 \\ \gamma & 1 & -1 \\ 0 & 1 & 1 \end{pmatrix}.$$

Fig. 3.3 Classification for zero, one, two and three tilt systems after A Glaser.

Compound	Formula	Phase-transition temperature °C
1	2	3
Displacive antiferroelectrics		
A. Perovskite structure		
Lead zirconate	PbZrO <sub>3</sub>	230, ~228
Sodium niobate	NaNbO <sub>3</sub>	~480, 354, -200
Lead hafnate	PbHfO <sub>3</sub>	215, 160
Bismuth ferrite?	BiFeO <sub>3</sub>	~850, ~400, ~200
Silver niobate?	AgNbO <sub>3</sub>	325, 550
Lead stannate?	PbSnO <sub>3</sub>	~400
Lead magnesium tungstate	PbMg <sub>1/2</sub> W <sub>1/2</sub> O <sub>3</sub>	~38
Lead nickel tungstate	PbNi <sub>1/2</sub> W <sub>1/2</sub> O <sub>3</sub>	17-160
Lead cobalt tungstate	PbCo <sub>1/2</sub> W <sub>1/2</sub> O <sub>3</sub>	~30, -20, -206
Lead cadmium tungstate?	PbCd <sub>1/2</sub> W <sub>1/2</sub> O <sub>3</sub>	~400, 100
Lead ytterbium niobate	PbYb <sub>1/2</sub> Nb <sub>1/2</sub> O <sub>3</sub>	~310, ~160
Lead ytterbium tantalate?	PbYb <sub>1/2</sub> Ta <sub>1/2</sub> O <sub>3</sub>	~290
Lead lutecium niobate?	PbLu <sub>1/2</sub> Nb <sub>1/2</sub> O <sub>3</sub>	~280
Lead lutecium tantalate?	PbLu <sub>1/2</sub> Ta <sub>1/2</sub> O <sub>3</sub>	~270
Lead indium niobate?	PbIn <sub>1/2</sub> Nb <sub>1/2</sub> O <sub>3</sub>	~90
Sodium bismuth titanate?	Na <sub>1/2</sub> Bi <sub>1/2</sub> TiO <sub>3</sub>	200, 320, 520
Lead ferrouanate?	PbFe <sub>2/3</sub> U <sub>1/3</sub> O <sub>3</sub>	~-100
Lead manganese tungstate?	PbMn <sub>1/2</sub> W <sub>1/2</sub> O <sub>3</sub>	~150
Lead manganese tungstate?	PbMn <sub>2/3</sub> W <sub>1/3</sub> O <sub>3</sub>	200, -70
Lead gallium niobate?	Pb <sub>2</sub> GaNbO <sub>6</sub>	~100
Lead bismuth niobate?	Pb <sub>2</sub> BiNbO <sub>6</sub>	~-235
Lead manganese rhoeate?	PbMn <sub>1/2</sub> Re <sub>1/2</sub> O <sub>3</sub>	~120, ~170
Lead cobalt rhoenate?	PbCo <sub>1/2</sub> Re <sub>1/2</sub> O <sub>3</sub>	~130

Fig. 3.4 Antiferroelectric perovskites.

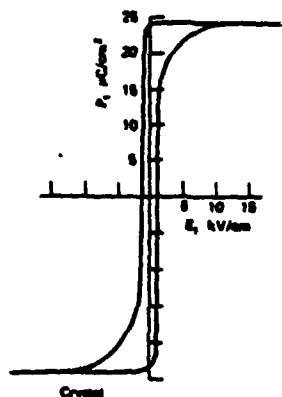


Fig. 4.1 Hysteresis in single crystal BaTiO<sub>3</sub> selected to be without 90° domains.

#### 4.0 ENGINEERING OF FERROELECTRIC PHASE TRANSITIONS

The extrema which occur in the dielectric, pyroelectric, elasto electric and opto-electric properties of ferroelectrics at temperatures close to the phase transitions take the properties into exceedingly interesting and practically important ranges. It is thus important to explore the mechanisms which can be used to modify and control the transition behaviour.

In the perovskite system, five types of control are important:

- For solid solutions, the phase transition temperatures often change continuously with composition so that in homogeneous compositions the transitions may be placed at optimum temperatures. Further, by controlling a deliberate heterogeneity a range of transitions can be engendered spreading and smoothing the sharp extrema.
- In some solid solutions, ferroelectric:ferroelectric phase transitions occur at fixed compositions and are nearly independent of temperature. These so called morphotropic phase boundaries are extremely important in piezoelectric ceramics.
- Elastic stress can have a marked effect on the transition behaviour and the property extrema near the transition so that self generated stresses in ceramics may be engineered to improve the properties.
- For ceramic compositions the grain:grain boundary heterogeneity can be invoked to modify extrema and to control the field distribution in the ceramic.
- Since ferroelectricity is a cooperative phenomenon the scale of the ferroelectric region is of critical importance. Nano-scale heterogeneity can engender completely new properties and give rise to spin glass behaviour which can be exploited in both capacitors and transducers.

#### 4.1 Engineering Transitions for Dielectric Applications

Many practical ferroelectric capacitor dielectrics are based upon barium titanate,  $\text{BaTiO}_3$ . The key feature of any ferroelectric is that in some accessible range of temperature and pressure it has a ferroelectric phase, and that in that phase a spontaneous electric polarization can be switched between two or more equilibrium orientations by a realizable electric field.

As has been shown in fig. 3.1  $\text{BaTiO}_3$  at room temperature is ferroelectric with six alternative domain states polarized along any one of the six equivalent  $\langle 100 \rangle$  directions of the original cubic prototypic form.

For a 100 oriented single crystal the hysteresis loop is very square fig. 4.1, the end states may be shown to be single domain yielding in the most perfect crystals a value  $P_s = 26 \mu\text{C}/\text{cm}^2$  at  $20^\circ\text{C}$ .<sup>44</sup> In a polycrystal ceramic, the domain structure is much more complex fig. 4.2 the hysteresis loop very rounded so that both maximum and remanent polarizations are much lower than the single crystal values fig. 4.3.<sup>45</sup>



Fig. 4.2 Microstructure of 90° twin domains in a coarse grained  $\text{BaTiO}_3$  ceramic.

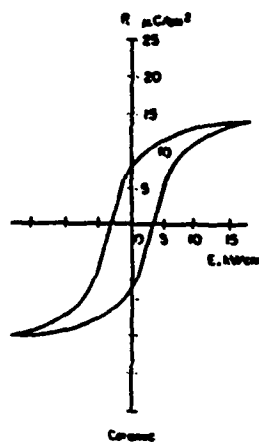


Fig. 4.3 Dielectric hysteresis in a coarse grain  $\text{BaTiO}_3$  ceramic.



For the more perfect crystal which can be converted to single domain state, the paraelectric and the single domain intrinsic polarizability can be measured fig. 4.4, 4.5. Unlike ferromagnets very high permittivity persists for a wide temperature range above the Curie Point  $T_c$  following a Curie Weiss law.

$$\epsilon = \frac{C}{T - \Theta} .$$

In this case however  $C \approx 1.5 \cdot 10^5 \text{ } ^\circ\text{K}$  as compared to  $C \sim 10^{-2} \text{ } ^\circ\text{K}$  in a corresponding ferro or ferri magnet (Fig. 4.6).

Above  $T_c$ , the cubic  $m3m$  symmetry dictates that the weak field dielectric susceptibility (permittivity) be spherically symmetrical so the  $\epsilon_w$  can be completely characterized.

$$\begin{array}{ccc} \epsilon_w & 0 & 0 \\ 0 & \epsilon_w & 0 \\ 0 & 0 & \epsilon_w \end{array}$$

In ceramic form, the first question must be whether the grain boundary acts as a high impedance layer strongly limiting utility as a capacitor. The cubic form above  $T_c$  permits an unequivocal answer. Extensive experiments on very carefully prepared  $\text{BaTiO}_3$  ceramics with average grain size from 0.75 to 53  $\mu$  meters by Yamagi et al.<sup>46</sup> show no significant change either in  $C$  or in  $\Theta$  as compared to the crystal (fig. 4.7), confirming that ceramics can be made with low impedance grain boundary structures

The absence of major grain boundary impedance suggests that the high permittivity near  $T_c$  could be exploited in capacitors if  $T_c$  could be moved near room temperature and the response broadened. In solid solutions, all of the phase transitions move continuously with composition as shown in fig. 4.8 for solutions with  $\text{PbTiO}_3$ ,  $\text{SrTiO}_3$ ,  $\text{BaZrO}_3$ ,  $\text{CaTiO}_3$  and  $\text{BaSnO}_3$ .

In both  $\text{BaZrO}_3$  and  $\text{BaSnO}_3$  systems there is an interesting "pinch off" region in the phase diagram where for temperatures close to room temperature tetragonal, orthorhombic and rhombohedral states are becoming of similar energy i.e., it becomes easy to thread the polarization vector through a randomly axed ceramic.

For the dielectric response, two desirable effects are evident as for example in the  $\text{Ba}(\text{T}_{1-x}\text{Zr}_x)\text{O}_3$  system. At low level additions the dielectric peak rises sharply (fig. 4.9) and with further addition broadens markedly. Broadening may be traced to macroscopic heterogeneity in the composition giving rise to a distribution of Curie temperatures and thus a broadened peak. This principle is widely used in commercial dielectrics, which often use several additives to trim the properties. Some commercial formulations taken from the book by Herbert<sup>47</sup> are shown in table 4.1.

To provide capacitors with high  $K$  but greater temperature stability two additional features are used to control and enhance permittivity in almost pure  $\text{BaTiO}_3$  ceramics:

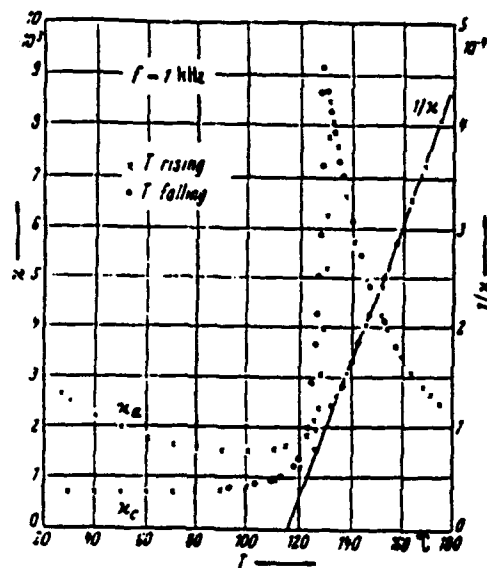


Fig. 4.4 Dielectric permittivity (weak field) near the Curie temperature in a single domain  $\text{BaTiO}_3$  crystal.

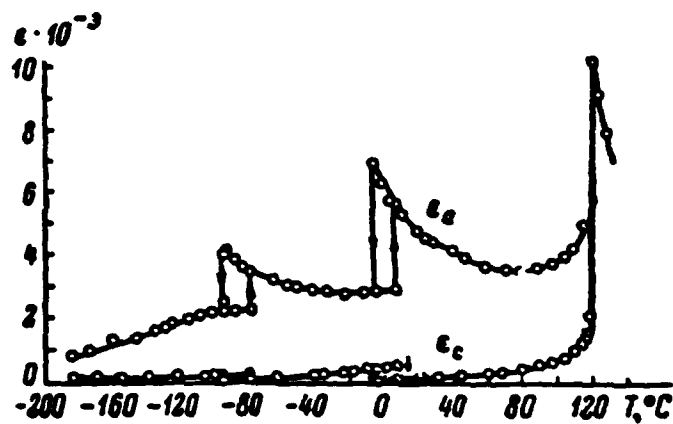
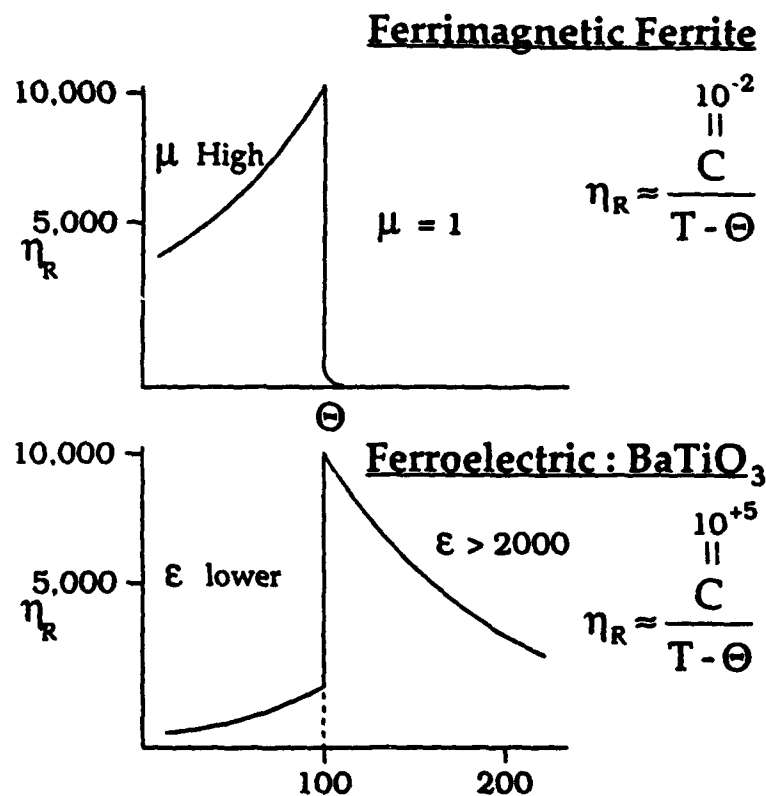


Fig. 4.5 Lower temperature weak field dielectric permittivity in a single domain  $\text{BaTiO}_3$  crystal.

- Note that below  $0^\circ\text{C}$  the crystal breaks up into domains and below  $-90^\circ\text{C}$  the domain structure imparts an anisotropy which should not occur in the single domain state.



**Spin 1/2 : Dipole:Dipole Coupling**

$$\eta_R \approx \frac{3 \Theta}{T - \Theta} \quad C \sim 10^{+3}$$

**MAGNETIC → Strong Exchange Coupling**

**DIELECTRIC → Soft Mode**

**Fig. 4.6** Contrast between the dielectric behaviour of a BaTiO<sub>3</sub> perovskite type ferroelectric and the magnetic behaviour of a normal soft ferrite ferrimagnet.

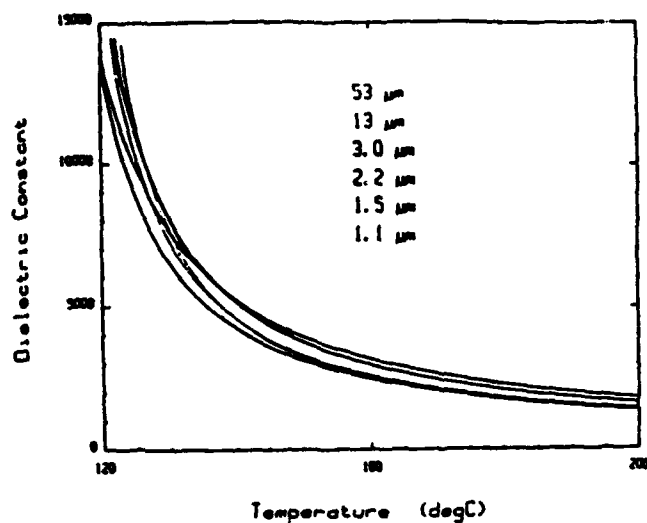


Fig. 4.7 Dielectric permittivity above the Curie temperature in very carefully prepared BaTiO<sub>3</sub> ceramics as a function of grain size. NOTE: there is no significant grain size dependence.

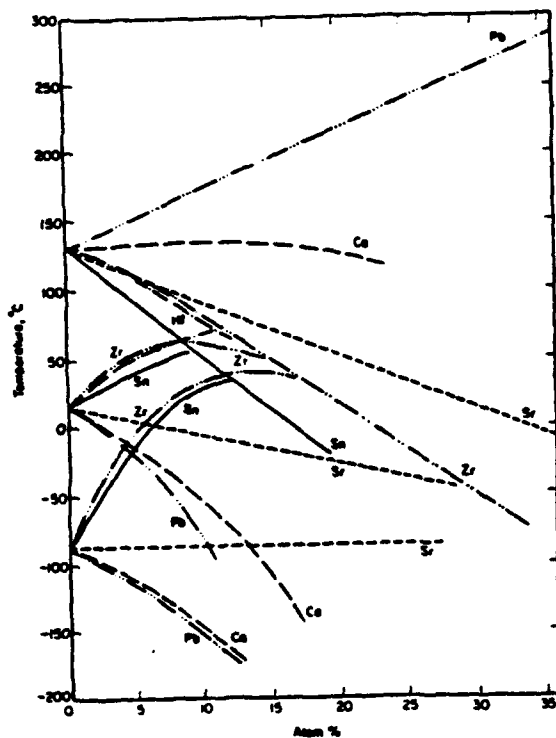


Fig. 4.8 Behaviour of the phase transitions as a function of composition in a sequence of BaTiO<sub>3</sub>:ABO<sub>3</sub> solid solutions.

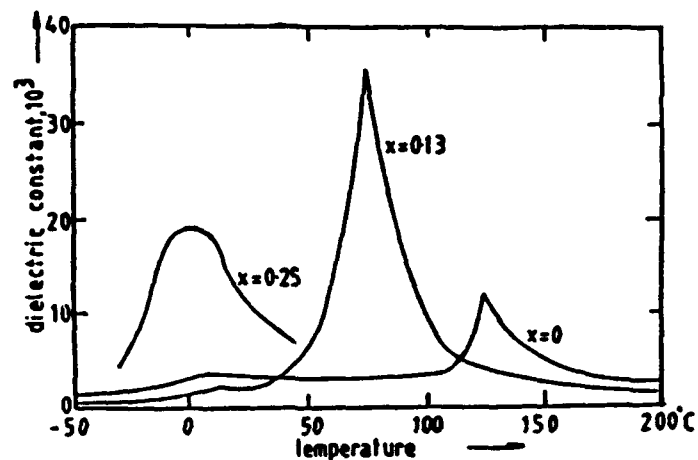


Fig. 4.9 Permittivity temperature curves for solid solutions in the  $\text{BaTiO}_3\text{:BaZrO}_3$  composition system.

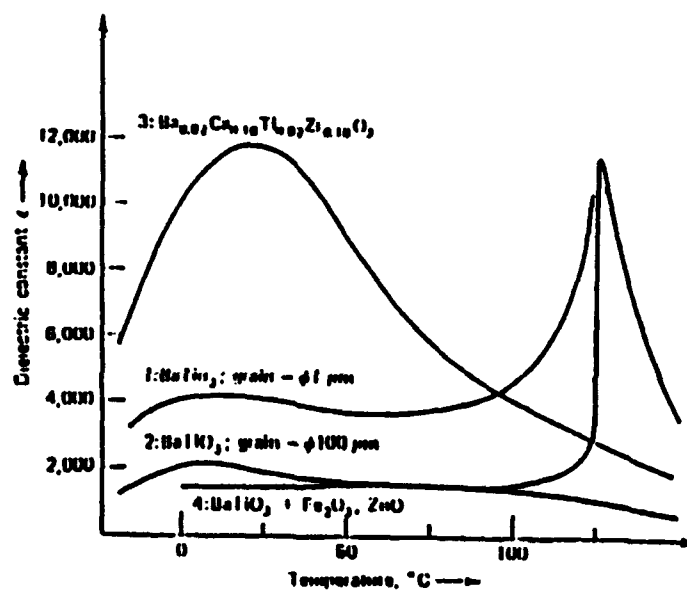


Fig. 4.10 Comparison of Curie point shifted high K dielectrics, with grain size and grain boundary controlled "pure"  $\text{BaTiO}_3$  compositions.

1. Control of the permittivity in fine grained  $\text{BaTiO}_3$  ceramic.
2. Control of the grain boundary impedance to suppress the Curie peak at  $T_c$ .

Both effects are illustrated in fig. 4.10 which contrasts this behaviour vis-a-vis the Curie point adjusted compositions.

#### 4.1.1 Grain Size Effects in $\text{BaTiO}_3$ Ceramics

It was known from the early 1950s, that small additions of  $\text{TiO}_2$  together with controlled firing could give rise to  $\text{BaTiO}_3$  ceramic capacitors with permittivity close to 3,000 over a broad temperature range. Over time the beneficial effects were traced to a liquid phase densification which inhibited grain growth in the ceramic and left a residual boundary phase, which reduced the Curie peak permittivity. More recently these effects have been achieved by other means and both effects studied separately.

Probably the best measurements of the pure grain size effect are due to Kinoshita<sup>46</sup> who used hot pressing of a weakly dysprosium doped  $\text{BaTiO}_3$  to produce samples with controlled grain size from 1.1  $\mu\text{m}$  to 53  $\mu\text{m}$  which showed no suppression of the Curie peak. In his samples there is a continuous increase of weak field permittivity  $\epsilon'$  near room temperature with reduction in grain size to values above 5,000 at 1.1  $\mu\text{m}$  (fig. 4.11).

Concomitant with the reduction in grain size, the group at NTT also observed a reduction in the frequency of occurrence of 90° domains with reducing grain size. Earlier, Buessem et al.<sup>49</sup> had suggested that a reduction in the twin density would give rise to internal stress of the type depicted in fig. 4.12 which would strongly enhance the intrinsic permittivity, markedly raising  $\epsilon'$  and shifting the orthorhombic tetragonal transition to higher temperature (fig. 4.12). Some additional support for this model come on studies of the mechanical strength in hot pressed  $\text{BaTiO}_3$  by Pohanka et al.<sup>49</sup> who measured the flexural strength above and below  $T_c$  and noted a reduction in strength in the ferroelectric phase which could be accounted for by the internal tensile stresses required in the Buessem model.

It must be noted however that an alternative model for the grain size effect has been proposed by Arit and co workers<sup>50</sup> which would require that the fine grain ceramic have a higher density of twins and some experimental evidence is advanced for this hypothesis. The advantage of the twin (domain) model is that it does account well for the higher  $\tan \delta$  in the fine grain system, but it does not explain the phase transition shift. Clearly more work is needed to resolve this important question.

One possible avenue for study would be to suppress the 0°C transition as for example by calcium titanate doping. For the internal stress model, the grain size effect should diminish rapidly as  $\epsilon_a$  intrinsic is lowered. For the domain wall model, the proximity of the tetragonal:orthorhombic transition is not necessary provided the lattice strain and wall energy are not too strongly effected.

#### 4.2 Manipulation of Grain Boundary Impedance

In  $\text{BaTiO}_3$  ceramics, it is remarkably easy to produce "dirty" grain boundaries, and most ceramics like the Siemens C40 material show Curie maximum suppression to greater or lesser degree, and it is often advantageous for practical application. To demonstrate the phenomenon quantitatively, and in the process to produce a useful

TABLE 4.1

Typical practical BaTiO<sub>3</sub> based dielectric formations taken from Herbert.

Item	K <sub>max</sub>	Temp. range for K <sub>max</sub> -20%	AO/B <sub>2</sub> O <sub>3</sub>	Ba	Sr	Ca	Mg	Ti	Zr	Sn
Composition in cation%										
A	2280	-20 to +100	0.98	48.5	0.73	-	-	49.5	-	0.73
B	1260	0 to 120	1.03	45.3	-	4.8	1.08	44.0	4.8	-
C	3450	-10 to 72	1.01	44.2	-	5.7	0.75	42.9	6.4	-
D	5000	12 to 75	1.02	47.6	2.3	-	0.45	45.3	0.45	3.38
E	8200	42 to 70	1.005	35.5	12.5	1.8	0.8	46.9	2.6	-

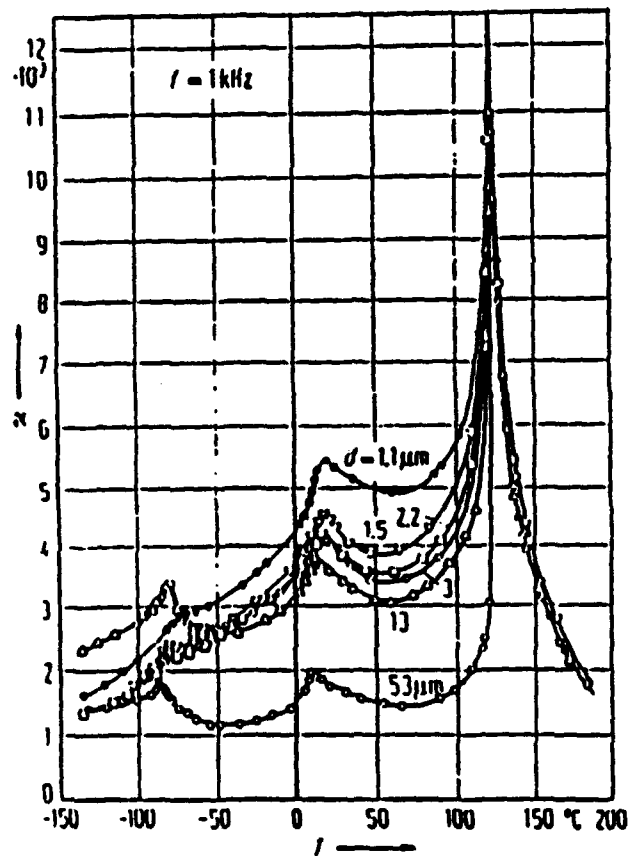
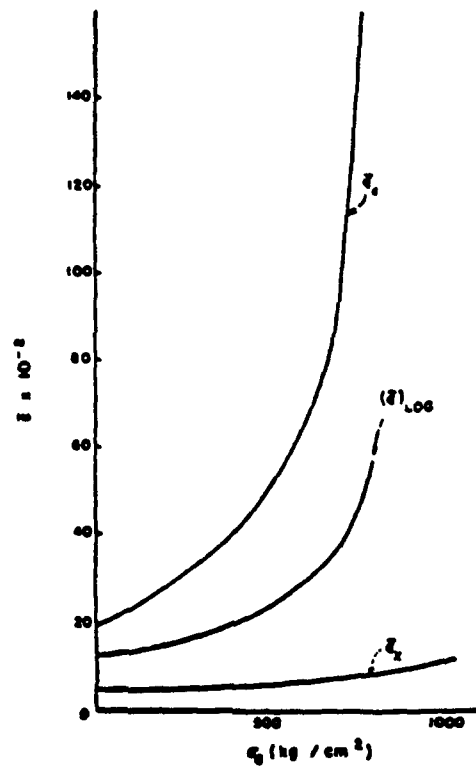
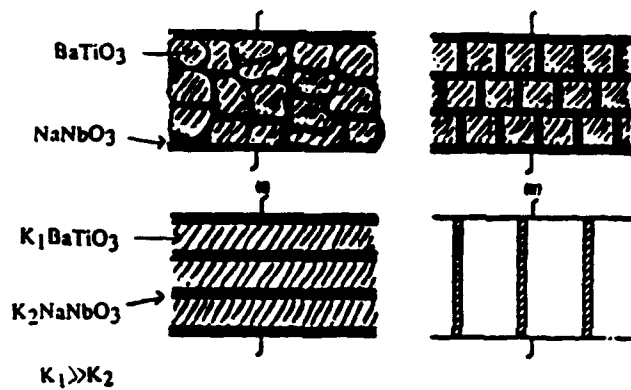


Fig. 4.11 Dielectric permittivity of BaTiO<sub>3</sub> as a function of grain size.

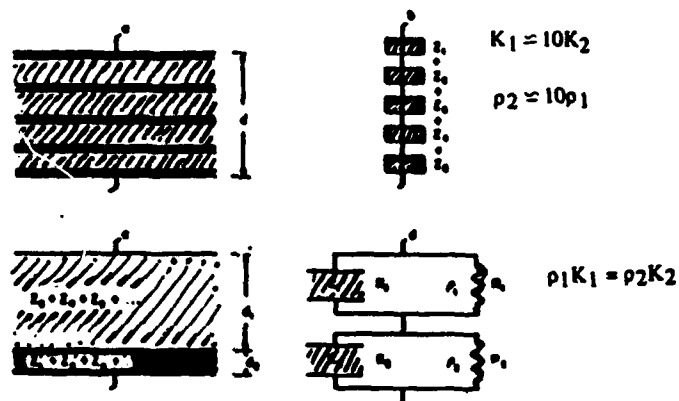


**Fig. 4.12** Calculated mean permittivity as a function of combined uniaxial compressive and orthogonal two dimensional tensile stress: the self generated stress system expected in untwinned fine grain  $\text{BaTiO}_3$ .





BRICK-WALL MODEL OF POLYCRYSTALLINE MICROSTRUCTURE



EQUIVALENT CIRCUIT FOR THE BRICK-WALL MODEL

Fig. 4.13 Derivation of the simple brick wall model for a diphasic ceramic and the reduction to a simple RC parallel circuit combination.

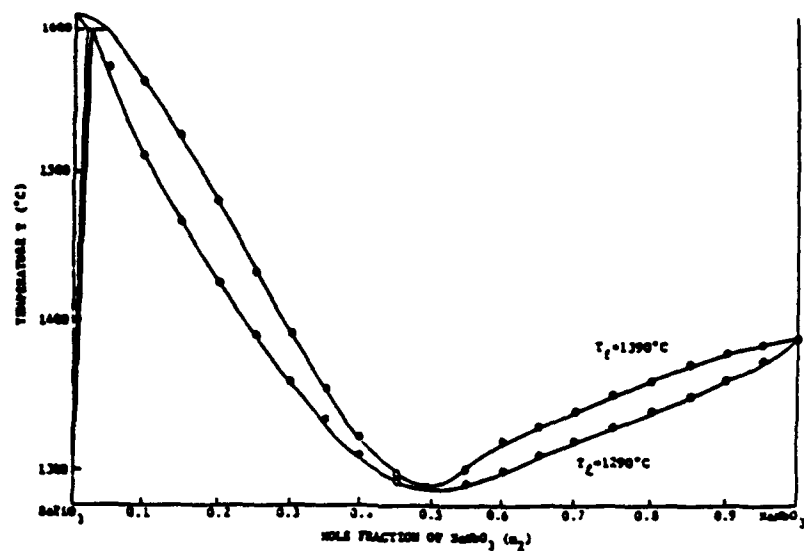


Fig. 4.14 Pseudo eutectic in the phase diagram of  $\text{BaTiO}_3\text{:NaNbO}_3$  solid solutions.

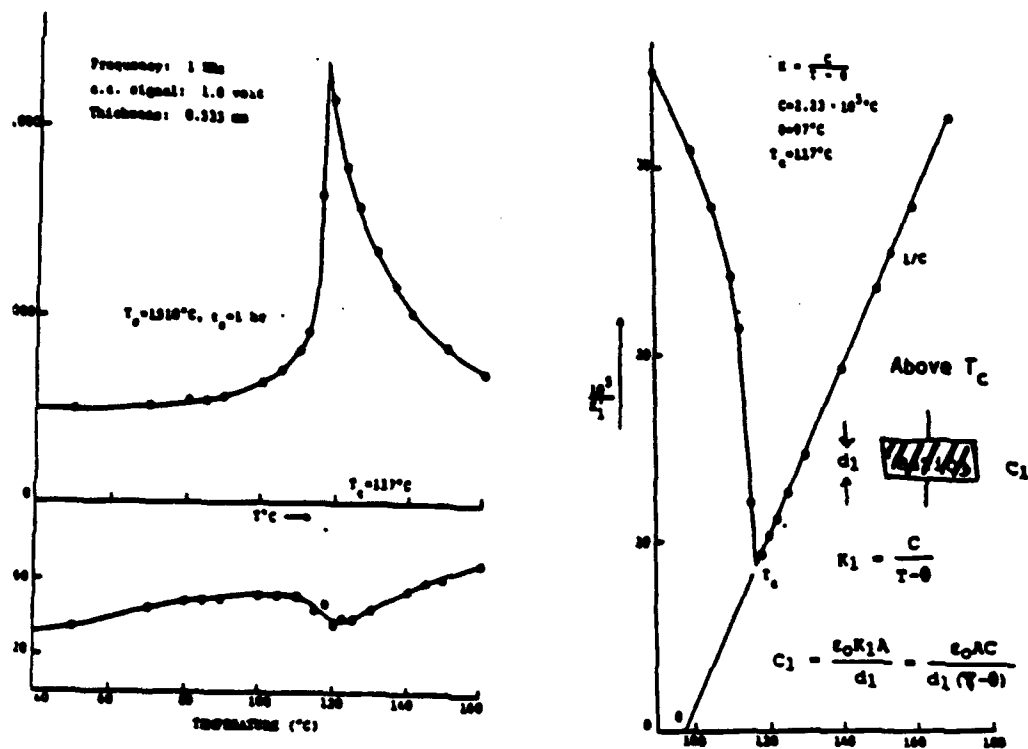


Fig. 4.15 Weak field dielectric permittivity of  $\text{BaTiO}_3$  as function of temperature.

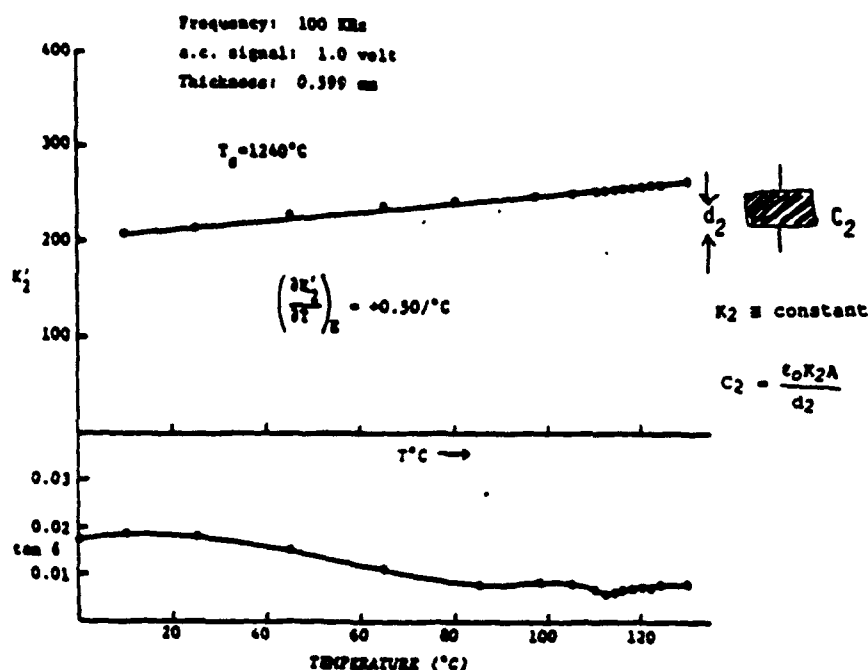


Fig. 4.16 Weak field permittivity of  $\text{NaNbO}_3$  as function of temperature showing near constant behaviour.

high voltage dielectric. Payne and Cross<sup>52,53</sup> explored fast fired  $\text{BaTiO}_3\text{:NaNbO}_3$  composites. Using the fact that there is a pseudo eutectic in the solid solution system, it is possible to generate a rapid liquid phase densification which leaves a thin  $\text{NaNbO}_3$  coating over the  $\text{BaTiO}_3$  grains whose thickness can be controlled by the volume of  $\text{NaNbO}_3$  used. Since  $\text{NaNbO}_3$  has a flat permittivity:temperature behaviour it is possible to use Curie Weiss analysis to derive the impedance of the boundary phase directly and to verify the predictions of the simple "brick wall" model for the ceramic. The argument is presented pictorially in figures 4.13, 4.14, 4.15, 4.16, 4.17, 4.18. A comparison of the characteristics of a 5%  $\text{NaNbO}_3\text{:BaTiO}_3$  versus a pure  $\text{BaTiO}_3$  capacitor is given in table 4.2.

#### 4.3 Scale Effects in Heterogeneous Ferroelectric Dielectrics

It was shown earlier in this section 4 that a measure of compositional heterogeneity is essential in very high  $K$  dielectrics so that the dielectric extrema at the Curie temperature is spread over a practically useful range. For most widely used  $\text{BaTiO}_3$  based formula, this heterogeneity is on a scale comparable to the grain structure and is often induced by processing to a non equilibrium phase distribution.

As the dielectric thickness gets smaller, particularly in ultra high capacitance density multilayer capacitors, it becomes difficult to control macroscopic heterogeneity because of short diffusion distances, and a finer scale composite would be desirable.

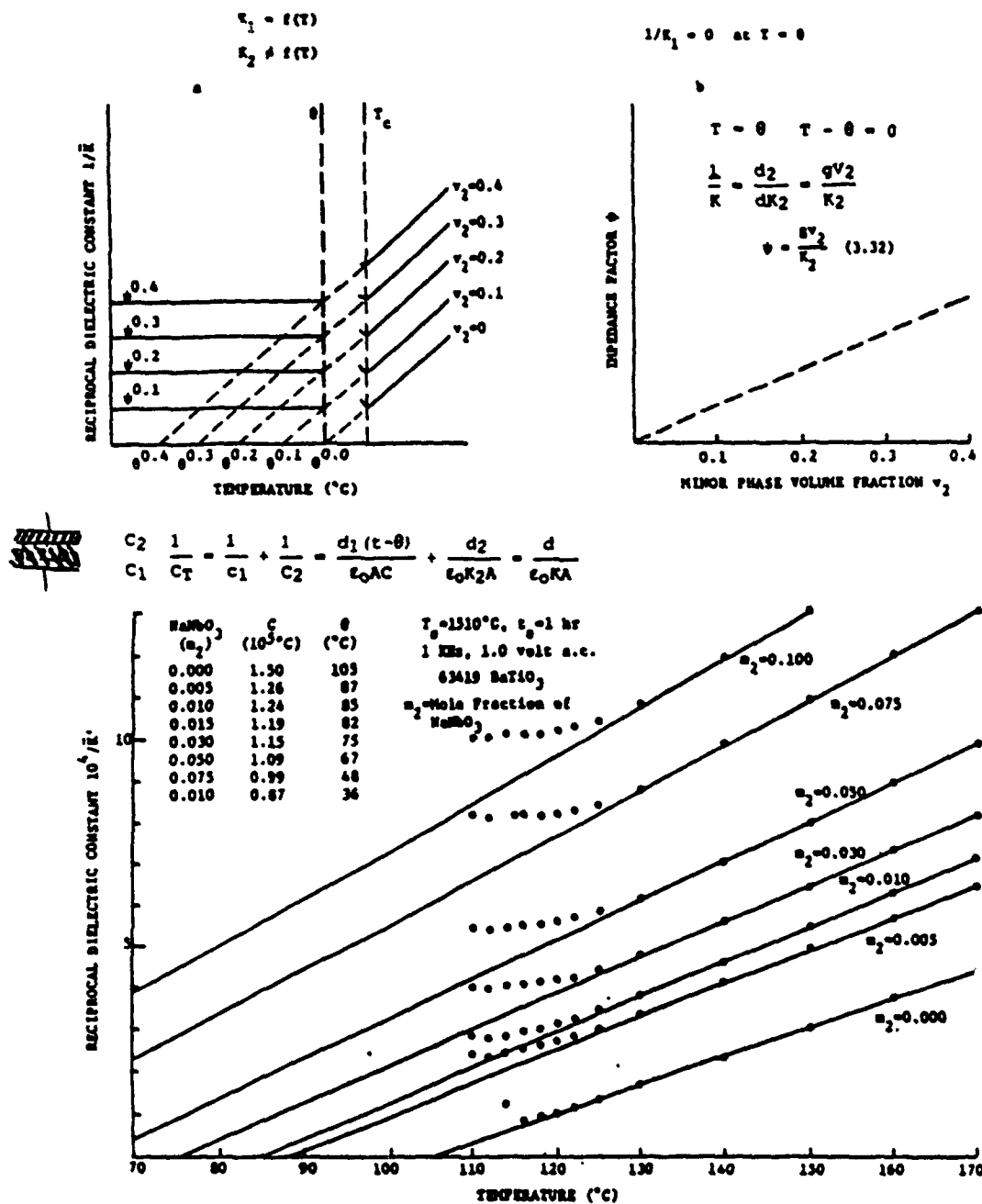


Fig. 4.17 Expection for Curie Weiss behaviour in a diphasic  $\text{BaTiO}_3$  ceramic, and confirmation of the behaviour in fast fired ceramics.

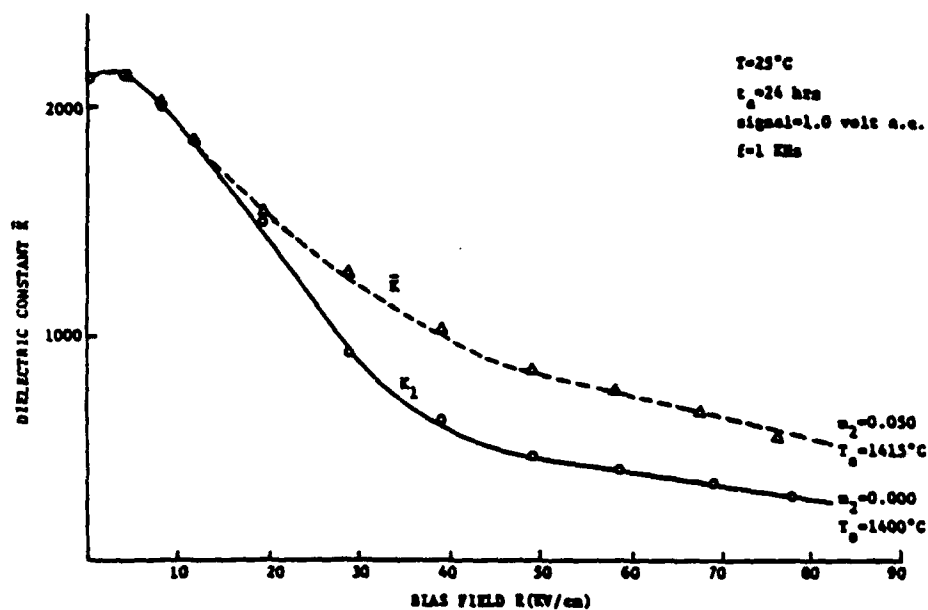
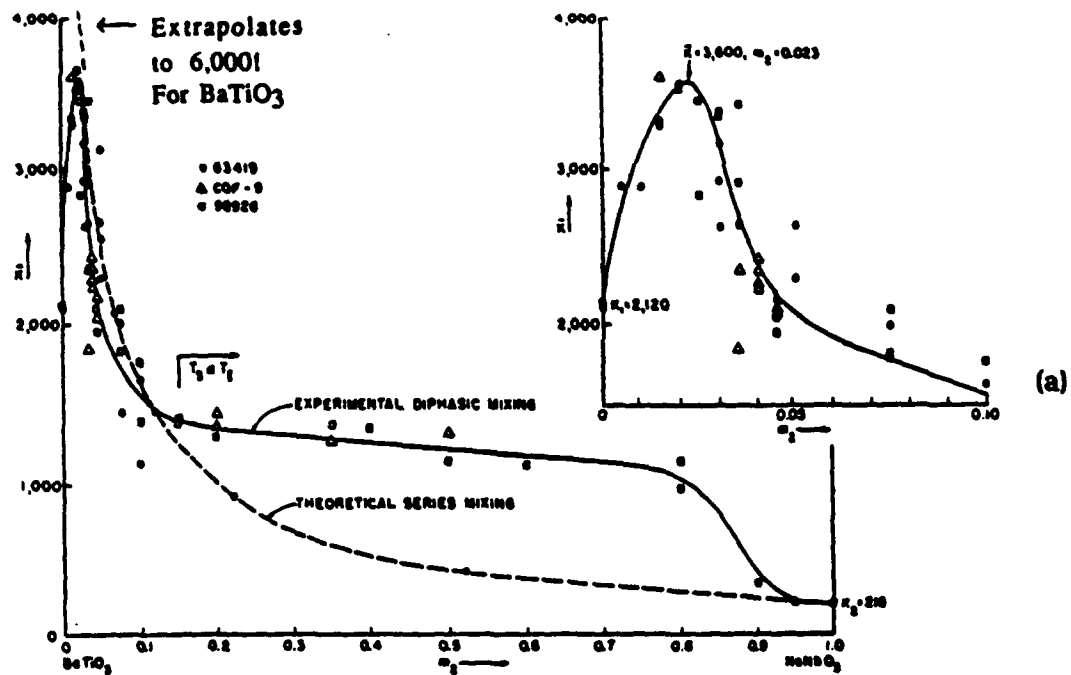


Fig. 4.18 (a) Permittivity levels as a function of  $\text{NaNbO}_3$  mole fraction in the disphasic system. (b) Improvement in the high field performance due to field splitting by the diphasic system.

TABLE 4.2

Practical advantage of a  $\text{BaTiO}_3\text{:NaNbO}_3$  composite dielectric for a high voltage capacitor.

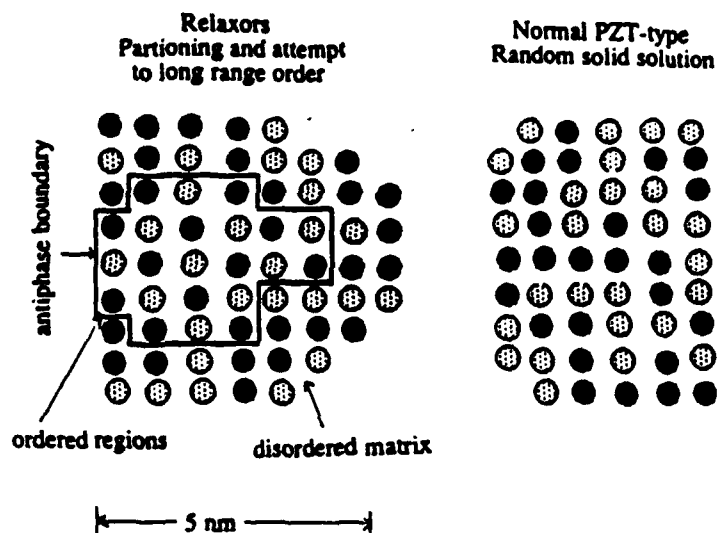
Dielectric	Permittivity K at 0 Volts	Permittivity K at 60 KV/cm	Aging %/Decade	Breakdown Strength
$\text{BaTiO}_3$	2,100	400	2.8	100 Kv/cm
$\text{BaTiO}_3$ , 5% $\text{NaNbO}_3$	2,100	750	1.25	200 Kv/cm

In the  $\text{Pb}(\text{B}_1\text{B}_2)\text{O}_3$  perovskites for which  $\text{PbMg}_{1/3}\text{Nb}_{2/3}\text{O}_3$  (PMN) is a useful prototype, it has become clear that there is a new mechanism which establishes a truly nanometer scale heterogeneity in the composition in such materials. Extensive studies by transmission electron microscopy have revealed that ordering takes place between Mg:Nb cations but not as might be expected in a 2:1 ordered sheet structure as occurs in  $\text{BaMg}_{1/3}\text{Ta}_{2/3}\text{O}_3$ , but on a local 1:1 ordering in an NaCl type lattice.<sup>54,55</sup>

A crude two dimensional picture is given in fig. 4.19 which compares the atomic arrangement in PMN with that in a conventional PZT ceramic. A feature which is immediately evident in the PMN is that the 1:1 ordering is non stoichiometric and must give rise to massive short range chemical heterogeneity. The ordered regions are highly Mg rich and must give rise to a local charge imbalance which presumably stops the ordering process at this ~5nm scale.

The ordering which is within a coherent crystal lattice occurs in both single crystal and ceramic samples and can be imaged using TEM (fig. 4.20).<sup>56</sup> This fossil chemistry which is formed at very high temperature leads to a nanoscale chemical heterogeneity which influences the manner in which these materials exhibit ferroelectricity. This family of lead based complex perovskites has been called relaxor ferroelectrics. The outstanding features of the dielectric and ferroelectric response are summarized in fig. 4.21 and the most salient features tabulated in table 4.3. Earlier studies<sup>57</sup> based on the very small scale of the polar regions in PMN had suggested a super paraelectric model for the high temperature behaviour and measurements on the SBN bronze had been adduced to demonstrate the mobility of the polar phase.<sup>58</sup> A recent natural extension has been to explore a spin glass model for the behaviour.<sup>59</sup>

## NANOSCALE CHEMISTRY



- Some type of decomposition/ partitioning on nanoscale into Nb and Mg rich regions followed by long range ordering in Mg rich regions.
- charge balance not yet satisfactorily known.
- "fossil" chemistry acts to localize polar behavior.

**Fig. 4.19** Nanoscale ordering in Lead Magnesium niobate compared to a disordered PZT solid solution.

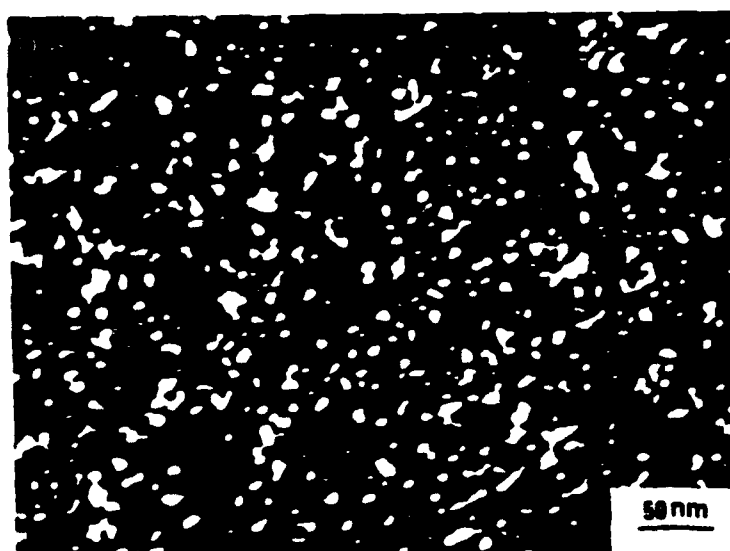


**Fig. 4.20** Dark field image of the chemically ordered domains in Lead Magnesium Niobate.

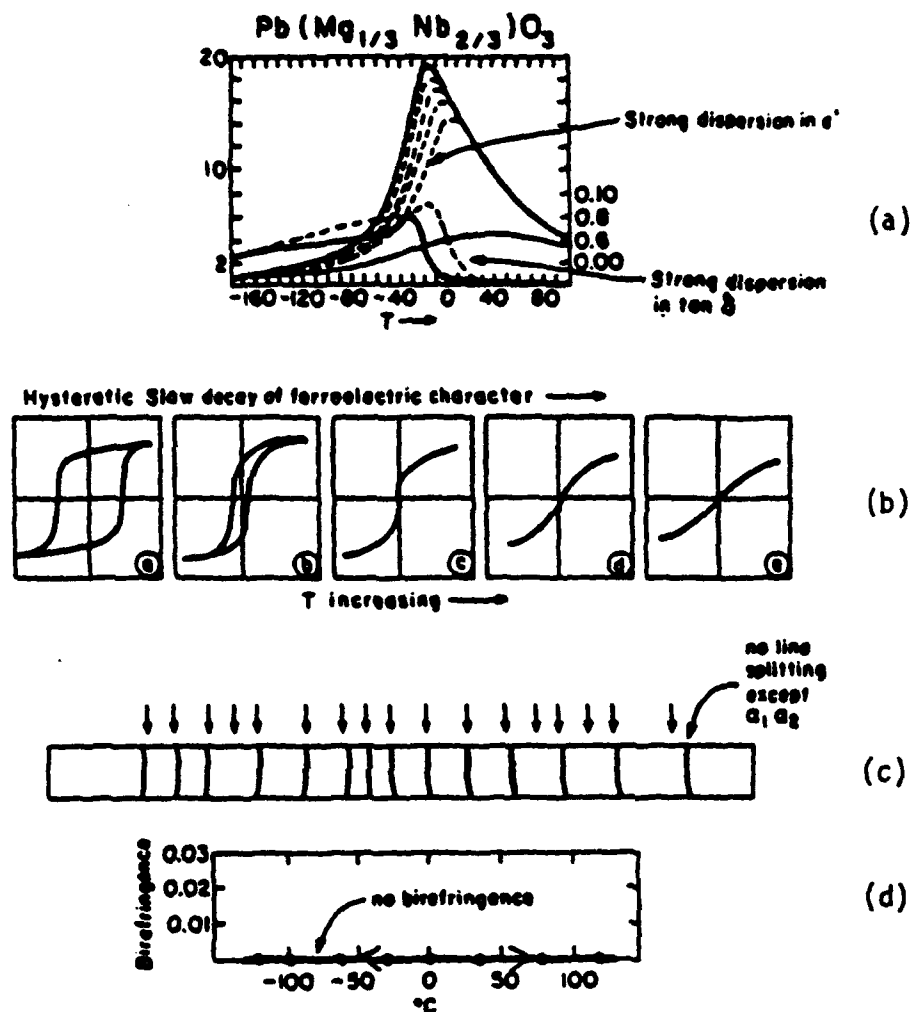


**Fig. 4.21** Special properties of the relaxor type perovskite dielectrics.  
 (a) Weak field dielectric permittivity vs  $T$ .  
 (b) High field hysteretic behaviour vs  $T$ .  
 (c) Low temperature X-ray spectrum showing no departure from cubic structure.  
 (d) Optical anisotropy in a zero field cooled single crystal of PMN.



**TABLE 4.3**

**Common features in the behaviour of relaxor ferroelectric crystals and ceramics.**

**COMMON FEATURES**

- **Compositions: Structures.**  
Common in lead containing perovskite structures of complex composition: Prototype lead magnesium niobate  $\text{Pb}(\text{Mg}_{1/3}\text{Nb}_{2/3})\text{O}_3$ .  
Occurs in many tungsten bronze compositions: Prototype strontium barium niobate  $\text{Sr}_{0.75}\text{Ba}_{0.25}\text{Nb}_2\text{O}_6$ .
- **Dielectric Response.**  
High dispersive peak permittivity  $\epsilon_R \sim 30,000$ .  
Ferroelectric response under high fields at low temperatures.
- **Compositional Heterogeneity.**  
Nano-scale heterogeneity on a coherent crystal lattice.
- **Polarization Fluctuations.**  
Large values of RMS polarization at temperatures well above that of the dielectric maximum.  
Evidence that the fluctuations are dynamical.
- **Evidence from TEM.**  
Local compositional (chemical) ordering.  
Local polar regions at low temperature nano to macro domain transitions.

Viehland<sup>60</sup> has authenticated a Vogel-Fulcher model for the dielectric relaxation (fig. 4.22) which postulates local cooperation between polar micro regions leading to a freezing temperature  $T_f$ . It was noted also, that for the field forced low temperature ferroelectric phase, the collapse of remanent polarization leads to a thawing temperature in close agreement with  $T_f$ . By looking at the manner in which different levels of DC electric field force a spin-glass to ferroelectric phase change Viehland<sup>61</sup> (fig. 4.23) was able to use the De Almeida-Thouless relation<sup>62</sup> to deduce a size for the uncoupled polar entities in close agreement with the scale of the heterogeneity observed by transmission microscopy (Fig. 4.24).

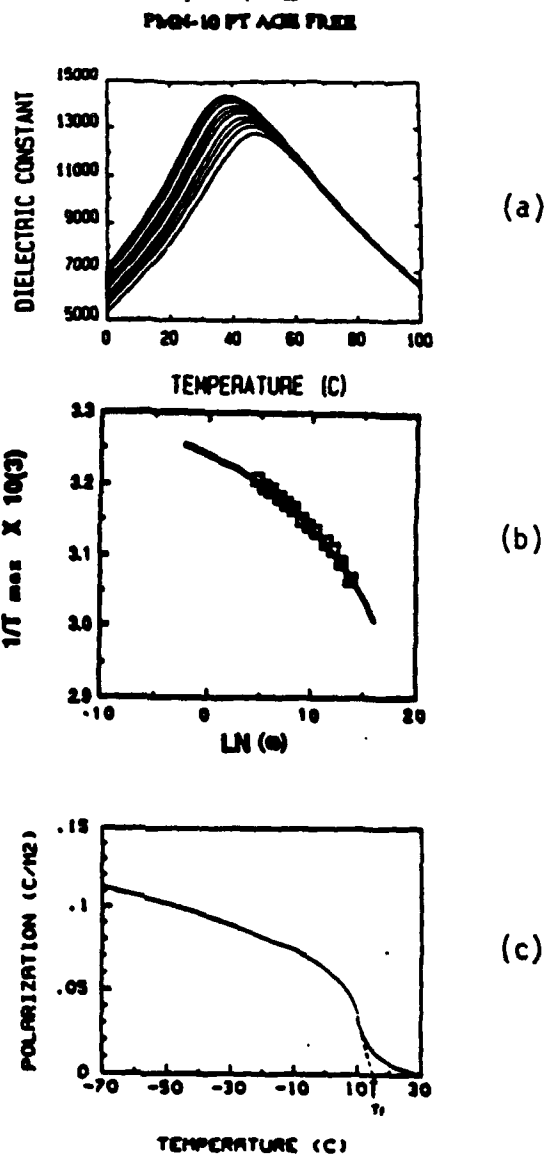
In a number of ways, the dielectric spin glass is more complex than the magnetic because of the strong electrostriction which couples nano scale polarization to nano scale distortion of the lattice. Many of the expected consequences have now been explored (fig. 4.25 to 4.30). It must be stated however that the current work has not yet proven spin glass behaviour in PMN, however the list of confirmed glass like features is indeed impressive as tabulated in table 4.4.

## 5.0 MULTILAYER CERAMIC CAPACITORS

The major sector of the high K ceramic capacitor market addresses ultra compact high capacitance miniature units which are required for power line stabilization in the packaging of silicon semiconductor integrated circuits. These units are fabricated using a co-firing technology which integrates the electrode into a monolithic multilayer ceramic. The normal construction is shown in schematic form in fig. 5.1. The alternating electrode layers which are fired into the ceramic are picked up on a modified silver termination which is added in a post firing operation.

For the early  $\text{BaTiO}_3$  formulations, the necessary high firing temperatures forced the use of platinum or gold-platinum alloy electrodes which become the major cost in the unit. Over time an essential component of the evolution has been the development of lead and bismuth oxide based fluxes which permit co-firing at temperatures down to  $1150^\circ\text{C}$  and thus the use of less expensive palladium-silver alloy electrodes.<sup>63</sup> Basic principles of the design of the dielectrics are essentially unchanged from before, and the effort has been to find fugitive fluxes or fluxes which incorporate into the dielectric with minimum damage to the permittivity properties.

Alternative to the  $\text{BaTiO}_3$  based compositions, the lead based relaxor (spin glass) compositions appear to be attracting increasing attention from the major MLC producers. A recent survey of the patent literature table 5.1 highlights some of the activity. It would be nice to report that it is the intrinsically superior dielectric properties (fig. 5.2) which are the major drawing force, however what must be also factored in is the important fact that the lead based formulation can be designed to fire at temperatures below  $900^\circ\text{C}$  so that with them there is the possibility of using high 70:30 silver palladium alloy electrodes, in some cases pure silver (Table 5.2) and with appropriate doping base metal copper electrodes.<sup>64</sup>



$$\omega = 10^{12} \exp \left[ \frac{-0.0407 \text{ eV}}{k(T-291.5)} \right]$$

Fig. 4.22 Vogel-Fulcher type freezing of the dielectric response in PMN:10%PT.

- (a) Dielectric response as a function of frequency and temperature.
- (b) Plot of  $1/T_{max}$  the temperature of maximum response vs frequency. Square dots are experimental points line is a fit to the equation: yielding pre-exponential  $\nu_0 \approx 10^{12}$  Hz.
- (c) Release of polarization on heating for a field cooled (poled) sample: the thawing temperature  $T_f = 291^\circ\text{K}$ .

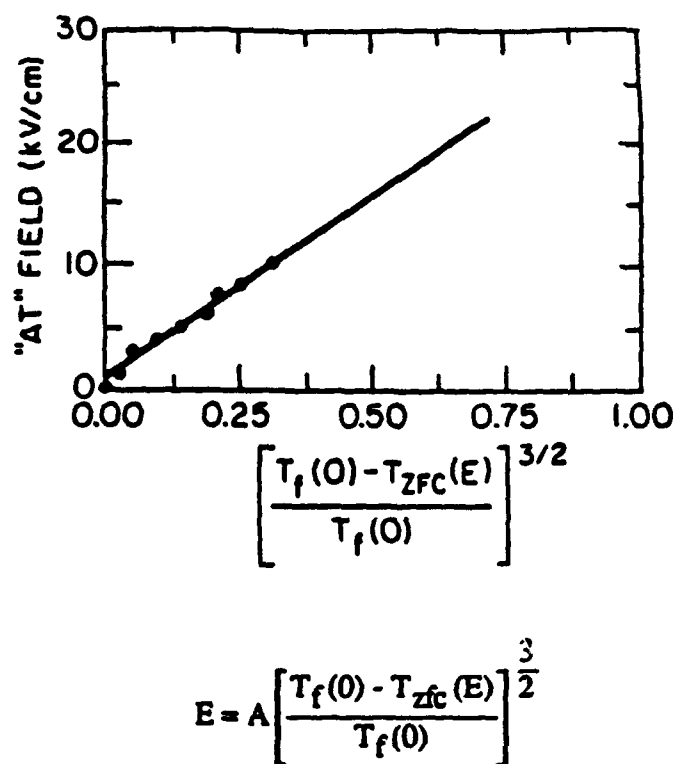
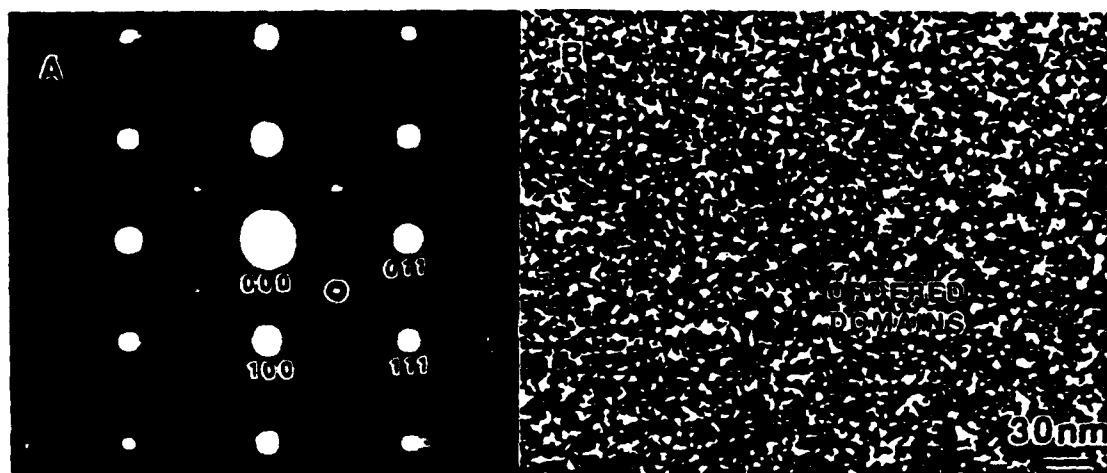
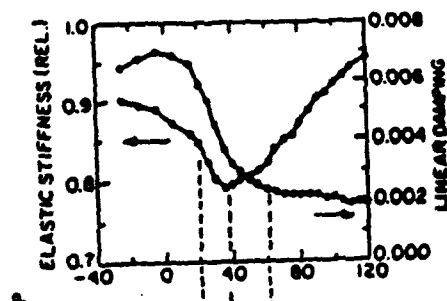


Fig. 4.23 Plot of the applied bias ("AT field") as a function of the temperature of maximum charging current, where  $T_f(0)$  is the freezing temperature of the ZFC state and the solid line is the curve fitting to the deAlmeida Thouless relationship given in equation 1.

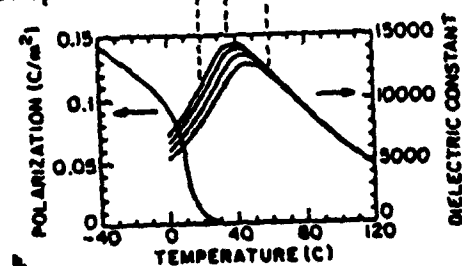


4.24 (a) Diffraction pattern of PMN showing superlattice reflections [011] zone. (b) CDF image of ordered microdomains (3-5 nm) in PMN using  $(22-2)$  reflection.

### Elastic Response



### Dielectric Response



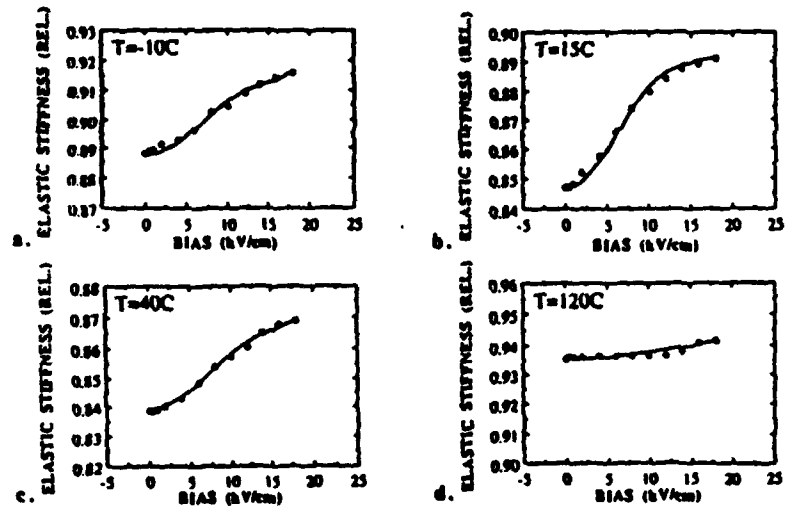
- \* Maximum softening for both responses occurs near the same temperature.

==> common origins of dielectric and anelastic relaxations.

- \* Reflects kinetics of polarization fluctuations, via the electrostriction.

**Fig. 4.25** Comparison of dielectric and elastic response in PMN. Maximum softening for both responses occurs at the same temperature - suggesting a common origin, reflecting the kinetics of polarization fluctuations coupled to the lattice via electrostriction.

## PMN-10PT



4.26 Elastic stiffness as a function of applied electric field at four temperatures.

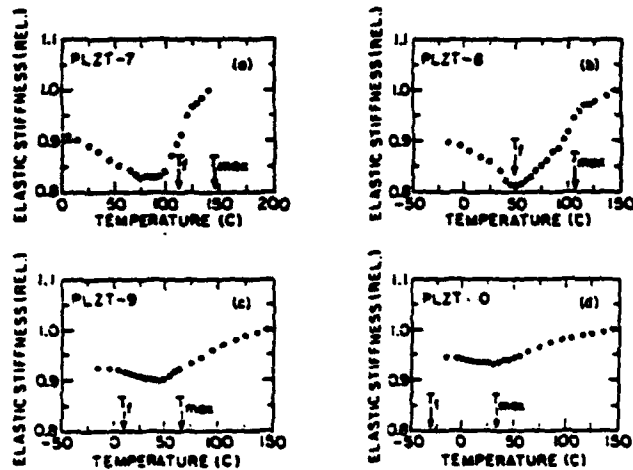
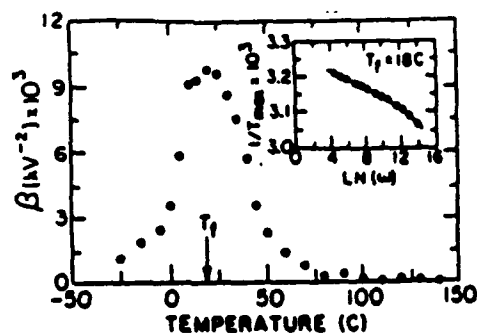


Fig. 4.27 The 100 Hz elastic stiffness as a function of temperature for various compositions of PLZT, where  $T_f$  is the freezing temperature, and  $T_{max}$  the temperature of the 100 Hz permittivity maximum. (a) PLZT-7, (b) PLZT-8, (c) PLZT-9, and (d) PLZT-10.



4.28 For the elastic constant vs electric field  $C(E) = c(0) + \beta E^2 + \eta E^4$ . Plot shows  $\beta$  as a function of temperature. Note that maximum  $\beta$  occurs near the freezing temperature  $T_f$  of the polarization fluctuations.

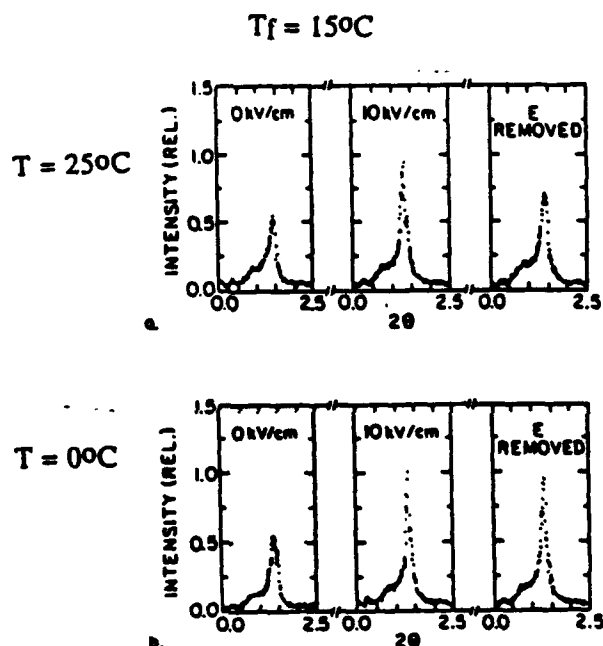


Fig. 4.29 X-ray line broadening as a function of applied electric field in PMN at a temperature above (25 °C) and below (0 °C) the freezing temperature. Note that the narrowing and peak shift is transient after field application above  $T_f$  but permists after field application below  $T_f$ .

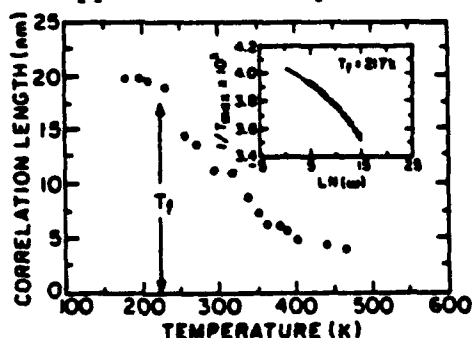


Fig. 4.30 Correlation length in single crystal PMN as a function of temperature, as deduced from neutron scattering. Correlation length saturates near  $T_f$  at 200 Å. At  $T_{\text{Burns}}$  the length ~30-40 Å close to the uncoupled cluster size.

**TABLE 4.4**

**Summary table of similarities between the relaxor ferroelectric PMN and the Magnetic spin glass. (Y in the table indicates yes that the phenomenon has been confirmed.)**

PROPERTY	RELAXOR	SPIN GLASS
Dispersion of Susceptibility	Y	Y
Dispersion of T <sub>max</sub>	Y	Y
Freezing Temperature (T <sub>f</sub> )	Y	Y
Imaginary Component Frequency Independent below T <sub>f</sub>	Y	Y
Strong Nonlinear Response	Y	Y
Maximum Nonlinearities near T <sub>f</sub>	Y	Y
Frustration	Y	Y
Susceptibility "Diffuse"	Y	Y
Deviations from Curie-Weiss Behavior	Y	Y
Analysis of Deviation for Local Order Parameter	Y	Y
Broadening of Relaxation Time Distribution on Cooling	Y	Y
Hysteresis, Irreversibility, and Remance below T <sub>f</sub>	Y	Y
Local polarization or magnetization	Y	Y
Local correlations between moments	Y	Y
Long range ordering in the Field Cooled State	Y	Y
Lack of anisotropy in the Zero Field Cooled State	Y	Y
De-Almeida Thouless Analysis	Y	Y
Polarization or Magnetization Viscosity	Y	Y
Chemical or Structural Inhomogeneity	Y	Y



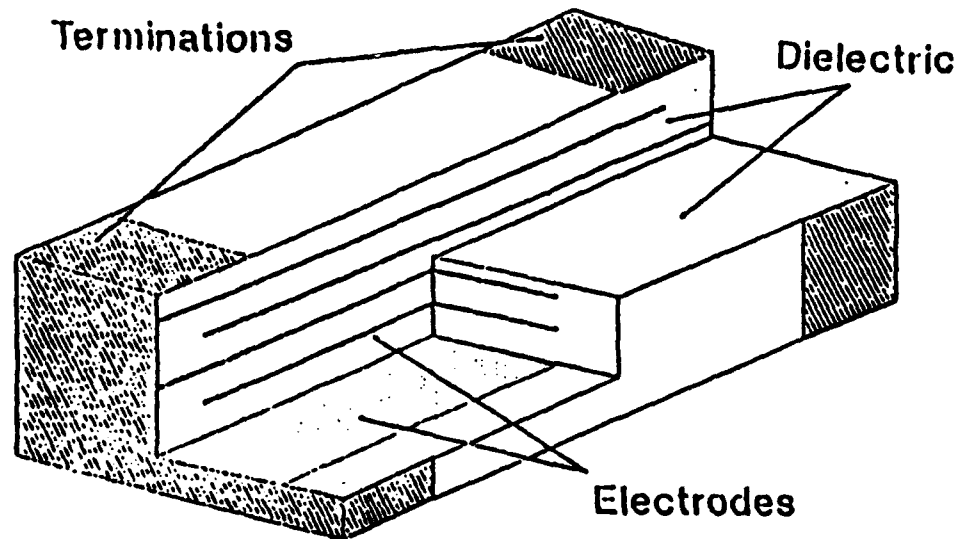


**Fig. 5.1** Construction of a typical ceramic MLC.

TABLE 5.1

Compositions being explored and recent patent filings for relaxor based dielectric formulations.

Complex Perovskites	$T_c (^{\circ}\text{C})$	** Behavior	Simple Perovskites	$T_c (^{\circ}\text{C})$	Behavior
(PMN)	-10	Relaxor-FE	PbTiO <sub>3</sub>	490	FE
(PZN)	140	Relaxor-FE	PbZrO <sub>3</sub>	230	AF
(PMN)	-120	Relaxor-FE	BaTiO <sub>3</sub>	130	FE
(PFN)	110	Normal-FE	SrTiO <sub>3</sub>	---	Para
(PFW)	-95	Relaxor-FE			
(PMW)	38	AF			
(PNW)	17	AF			

\*Transition temperatures for relaxors are averages or at 1 kHz.

\*\*FE: Ferroelectric, AF: Antiferroelectric, Para: Paraelectric.

(PMN):  $\text{Pb}(\text{Mg}_{1/3}\text{Nb}_{2/3})\text{O}_3$

(PZN):  $\text{Pb}(\text{Zn}_{1/3}\text{Nb}_{2/3})\text{O}_3$

(PMN):  $\text{Pb}(\text{Ni}_{1/3}\text{Nb}_{2/3})\text{O}_3$

(PFN):  $\text{Pb}(\text{Fe}_{1/2}\text{Nb}_{1/2})\text{O}_3$

(PFW):  $\text{Pb}(\text{Fe}_{2/3}\text{W}_{1/3})\text{O}_3$

(PMW):  $\text{Pb}(\text{Mg}_{1/2}\text{W}_{1/2})\text{O}_3$

(PNW):  $\text{Pb}(\text{Ni}_{1/2}\text{W}_{1/2})\text{O}_3$

#### Compositional Families for Relaxor-Based MLCs

Composition	EIA Temp Specification	Manufacturer (Assignee)	Patents and Refs.
PLZT-Ag	X7R	Sprague	U.S. Pat. 4,027,209 (1973) Ref. 9
PMW-PT-ST	X7R	DuPont	U.S. Pat. 4,048,546 (1973)
PFN-PFW	Y5V	NEC	U.S. Pat. 4,078,938 (1978)
PFN-PFW-PZN	Y5V	NEC	U.S. Pat. 4,236,928 (1980)
PFN-PMT	---	TDK	U.S. Pat. 4,216,103 (1980)
PMN-PT	Y5V	TDK	U.S. Pat. 4,263,668 (1981)
PMN-PFN	Y5V	TDK	U.S. Pat. 4,216,102 (1980)
PMN-PFN-PMW	Y5V	TDK	U.S. Pat. 4,287,075 (1981)
PFW-PZ	Z5U	TDK	U.S. Pat. 4,235,635 (1980)
PFW-PT-MN	Z5U	Hitachi	U.S. Pat. 4,308,571 (1981)
PMN-PZN-PT	Z5U	Murata	U.S. Pat. 4,339,544 (1982)
PFN-PFW-PbGe (MSC)	X7R		Ref. 10
PFN-PFN-PNN	Z5U, Y5V	Ferro	U.S. Pat. 4,379,319 (1983)
PMW-PT-PNN	Z5U	NEC	U.S. Pat. 4,450,240 (1984) Ref. 11
PFN-Ba Ca(CuW)-PFW	Y5V	Toshiba	U.S. Pat. 4,544,644 (1985) Ref. 12
PMN-PZN	Z5U	STL	U.K. Pat. 2,127,187A (1984)
PMN-PFN-PT	Z5U	STL	U.K. Pat. 2,126,575 (1984)
PMN-PZN-PFN	Z5U	Matsushita	Japan Pat. 59-107959 (1984)
PMN-PFW-PT	---	Matsushita	Japan Pat. 59-203759 (1984)
PNN-PFN-PFW	Y5V	Matsushita	Japan Pat. 59-111201 (1984)
PZN-PT-ST	---	Toshiba	Ref. 13
PMN-PFN-PbGe	Z5U	Union Carbide	U.S. Pat. 4,550,088 (1985)
PFN-PNN	Y5V		Ref. 14
PFW-PFN (MSC)		NTT	Refs. 15-17
PMN-PT-PNW	Z5U	Matsushita	Ref. 18
PMW-PT-PZ	X7R	NEC	Ref. 19
PZN-PMN-PT-BT-ST	Z5U	Toshiba	Japan Pat. 61-155245 (1986)
PZN-PT-BT-ST	X7R	Toshiba	Japan Pat. 61-250904 (1986)
PZN-PMN-BT	Y5U, Y5S	Toshiba	Ref. 20
PMN-PLZT	Z5U	MMC	U.S. Pat. 4,716,134 (1987)
PMN-CT, ST, BT	Z5U	Matsushita	Japan Pat. 62-115817 (1986)
PFW-PFN-PT	Y5V		Ref. 21
BT-PMN-PZN (MSC)	X7R, X7S	Toshiba	U.S. Pat. 4,767,732 (1988)
PMN-PS-PNW-Ca (Base Metal)	Z5U	Matsushita	Refs. 22-23

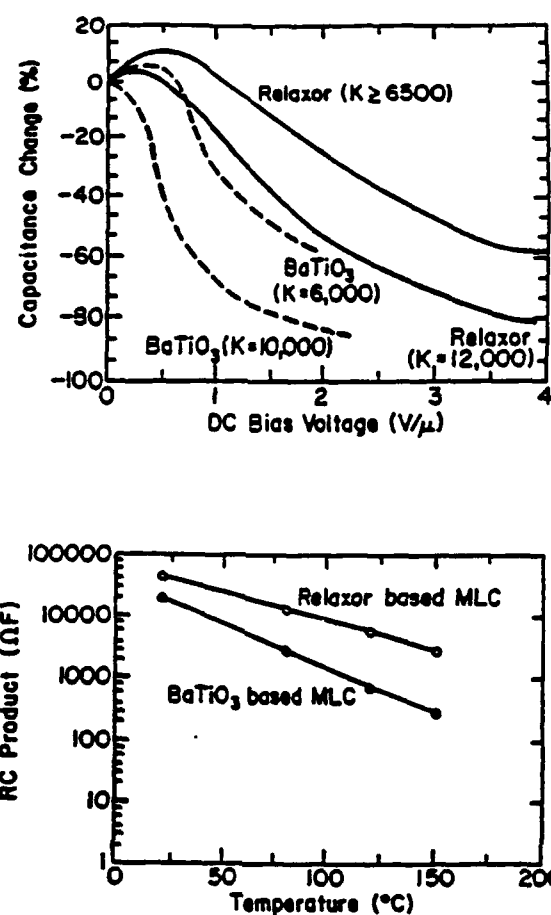


Fig. 5.2 Comparison of dielectric saturation and RC time constant behaviour between relaxor based and BaTiO<sub>3</sub> based MLC dielectrics.

TABLE 5.2

Firing conditions for and appropriate electrodes to use with BaTiO<sub>3</sub> and relaxor based formulations.

Dielectric	Firing Condition		Electrode
HF-BT	>1250°C	(air) (reducing)	Ni (100%) Ni*
MF-BT	1100-1250°C	(air) (reducing)	Ag:Pd (70/30 to 30/70) Cu, Ni
LF-BT (R&D only)	<1100°C	(air)	Ag:Pd (70/30)
HF-Relaxor	>1000°C	(air) (reducing)	Ag:Pd (70/30) Cu,
LF-Relaxor	<1000°C	(air) (reducing)	Ag:Pd (85/15), Ag (100%) Cu,

\*The partial pressure p(O<sub>2</sub>) at which Ni → NiO occurs is such that PbO → Pbmetal results, hence Ni-based electrodes are thermodynamically not feasible for relaxors.

## **6.0 FERROELECTRIC THIN FILMS**

### **6.1 Introduction**

Over the last four years (1987 to 1991) there has been a rapid increase in interest in ferroelectric thin films deposited onto semiconductor substrates for uses in nonvolatile radiation hard random access memory. The effort which has been driven in the USA primarily by major funding from the department of defense has lead to a strong revival of interest in ferroelectric switching behaviour and the evolution of a very broad range of deposition methods for a large variety of ferroelectric compositions. Since the summer school will have talks which focus upon the preparation methods for films and the switching behaviour these will only be briefly mentioned and the primary focus will be upon those properties which are likely to make the films important for more conventional capacitors and for piezoelectric transducer and sensor applications.

### **6.2 Material Systems of Interest**

The majority of studies are being carried forward upon randomly axed polycrystalline films so that it is not surprising to find major interest in the perovskite structure composition. Considerable early work on  $\text{BaTiO}_3$  films<sup>65,66</sup> never showed convincing evidence that strong ferroelectricity could be retained in sub micron thick films, and this is perhaps not surprising in the light of the very slim loops observed even in bulk  $\text{BaTiO}_3$  when the grain size approaches sub micron levels.

Most important steps in forward progress were the demonstrations of convincing dielectric hysteresis by Sayer<sup>67</sup> in sputter deposited PZT films and the confirmation of excellent hysteretic behaviour in sol-gel deposited PZT films by Payne and Budd.<sup>68</sup>

More recently the list of compositions for which useful ferroelectric behaviour has been convincingly demonstrated in thin films has increased markedly. A recent survey is given in table 6.1.

### **6.3 Preparation Techniques**

The very broad range of techniques which have already been applied to the fabrication of ferroelectric thin films are summarized in table 6.2. The majority are vapour phase methods but sol-gel and metal organic deposition are widely used. Attempts are also being made to use true metal organic chemical vapour deposition, but this approach is strongly handicapped by the low volatility and the hazardous nature of the suitable organic vehicles for the required chemical constituents

All methods currently have the common feature that they deposit an amorphous or micro crystalline ensemble of the required chemical constituents which must be architected into the required perovskite structure form by a subsequent heat treatment. These post deposition annealing treatments have received a lot of attention and it is clear that they can radically change the character of the resultant film. There appears to be a strong movement towards rapid thermal annealing methods, but again much care is needed to optimize the conditions.

In vapour phase methods substrate heating and low energy add atom assist are being used to improve quality, but the need for a sub film electrode metal precludes the possibility of precise epitaxy for perovskite type films, though topotactic grain orientation is frequently observed.

**TABLE 6.1**  
**Compositions which are under study as thin films.**

## **CHOICE OF MATERIAL SYSTEMS**

### **Non Volatile Memory**

#### **Multiaxial Ferroelectrics for Randomly Axed Films**

<b>Lead Zirconate Titanate</b>	<b>PZT</b>
<b>Lead Lanthanum Zirconate Titanate</b>	<b>PLZT</b>
<b>Lead Titanate</b>	<b>PT</b>
<b>Lead Lanthanum Titanate</b>	<b>PLT</b>
<b>Lead Bismuth Titanate</b>	<b>PBiT</b>
<b>Lead Barium Niobate</b>	<b>PBN</b>

#### **Uniaxial Ferroelectrics for Grain Orientated/ Epitaxial Films**

<b>Potassium Lithium Niobate</b>	<b>KLN</b>
<b>Strontium Barium Niobate</b>	<b>SBN</b>
<b>Lead Germanate</b>	<b>PG</b>
<b>Potassium Magnesium Fluoride</b>	<b>KMgF</b>

**TABLE 6.2**

**Growth techniques for ferroelectric thin films.**

- \* **Magnetron Sputtering from Oxide Targets.**
- \* **Multi-magnetron Sputtering (MMS).**
- \* **Multi-ion Beam Reactive Sputtering.**
- \* **Electron-Cyclotron Resonant (ECR) Plasma Assisted Growth.**
- \* **Chemical Vapor Deposition (Photo-Assist).**
- \* **Excimer Laser Ablation.**
- \* **Sol-Gel Methods.**
- \* **MOD Techniques.**

**Substrate Heating.**

**Post Deposition Annealing.**

**Rapid Thermal Annealing (RTA).**

**Low Energy Ad Atom Assist.**

There are numerous reports that the phase makeup of  $\text{PbZrO}_3\text{:PbTiO}_3$  thin films differs markedly from bulk values, however, data from S. Dey<sup>69</sup> on carefully annealed films (Fig. 6.1) suggests that the morphotropic phase boundary separating tetragonal and rhombohedral phases is close to that observed in the bulk composition.

#### 6.4 Important Properties of High K Films

In PZT films at the 52/48 Zr/Ti composition weak field dielectric permittivity  $\epsilon_w$  at room temperature as measured by many investigator on films made by different techniques is of order 1,200 and independent of thickness down to 3,500Å. Typical data from Dey<sup>70</sup> (fig. 6.2) indicates the films are dispersion free to over  $10^7$  Hz. Improper thermal annealing either at too elevated a temperature or for too long a time (fig. 6.3) indicates that massive dispersion can be induced at frequencies as low as  $10^4$  Hz. Under cyclic DC bias again films behave exactly as would be expected for proper ferroelectrics (fig. 6.4).

That the 52/48 composition is properly ferroelectric is evident from the 60 Hz hysteresis curve in fig. 6.5 with  $P_r = 30 \mu\text{C}/\text{cm}^2$  and  $E_c = 31 \text{ KV}/\text{cm}$ . That the ferroelectric polarization can be switched fast enough to be of interest in memory application is evident from the data taken by Dey (fig. 6.6) which shows switching times of ~ nano seconds in a  $30 \mu \times 30 \mu$  square capacitor.

Perhaps the most startling difference from bulk PZT comes in examination of the weak field dielectric permittivity vs temperatures (fig. 6.7). The peak is roughly at the right temperature, but the value is low and the peak is highly rounded. In all our own studies the best ratio  $\epsilon_{\text{peak}}/\epsilon_{\text{room}} < 3:1$ , where in a well prepared bulk material the peak is very sharp non dispersive and the ratio ~ 15:1.

A significant positive aspect of film behaviour is the manner in which the dielectric strength increases at low film thickness (fig. 6.8). Values of  $E_B$  as large as 4 MV/cm are not uncommon. It is interesting to note that the empirical curve predicted by Gerson and Marshall<sup>71</sup> based only on bulk measurements predicts breakdown fields for submicron thick films above 1 MV/cm.

For simple high K applications where hysteresis would be a marked disadvantage, two alternative lead based compositions are being explored. In the high lanthanum Lead Lanthanum titanates Dey has explored a 28:0:100 PLT which shows good linearity (P vs E) some dispersion with a K ~ 1,600 at 100 Hz and 1,400 at 10 MHz. Udayakumar<sup>72</sup> has explored PMN:PT compositions which show K values up to 2,800 and only weak dispersion to 10 MHz.

Clearly there are clamant needs for very compact film capacitors in high density silicon and ultra high speed Ga:As circuits and there are many options yet to explore for high K systems.

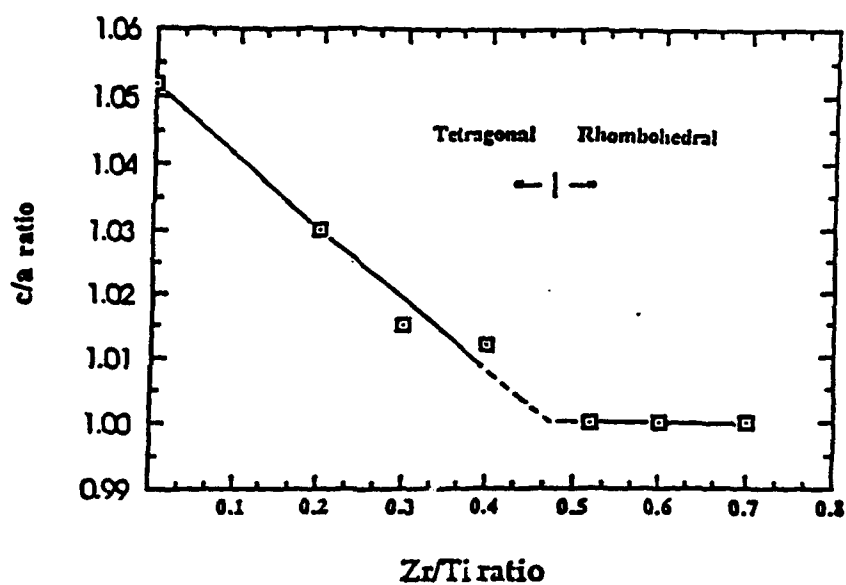


Fig. 6.1 Structure vs composition in well annealed PZT thin films (after Dey).

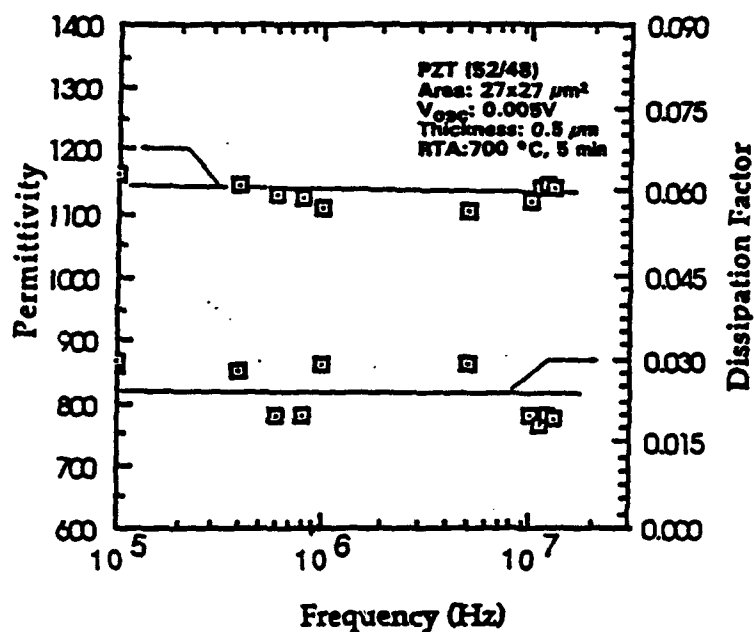


Fig. 6.2 Weak field dielectric permittivity vs frequency typical for PZT 52:48 compositions (after Dey).



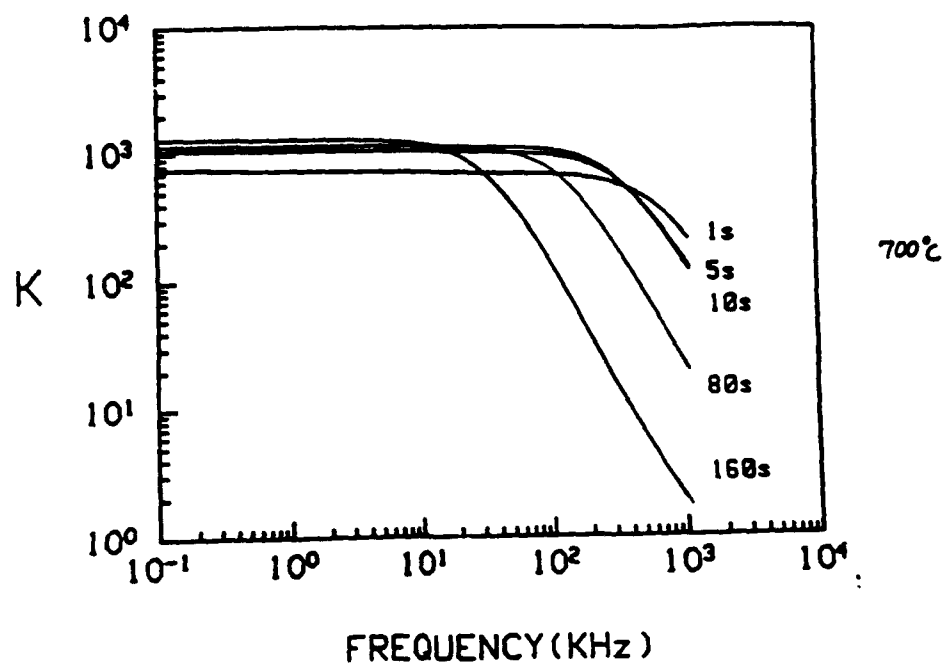


Fig. 6.3 Dielectric response vs frequency for PZT 52:48 compositions as a function of 'over' annealing.

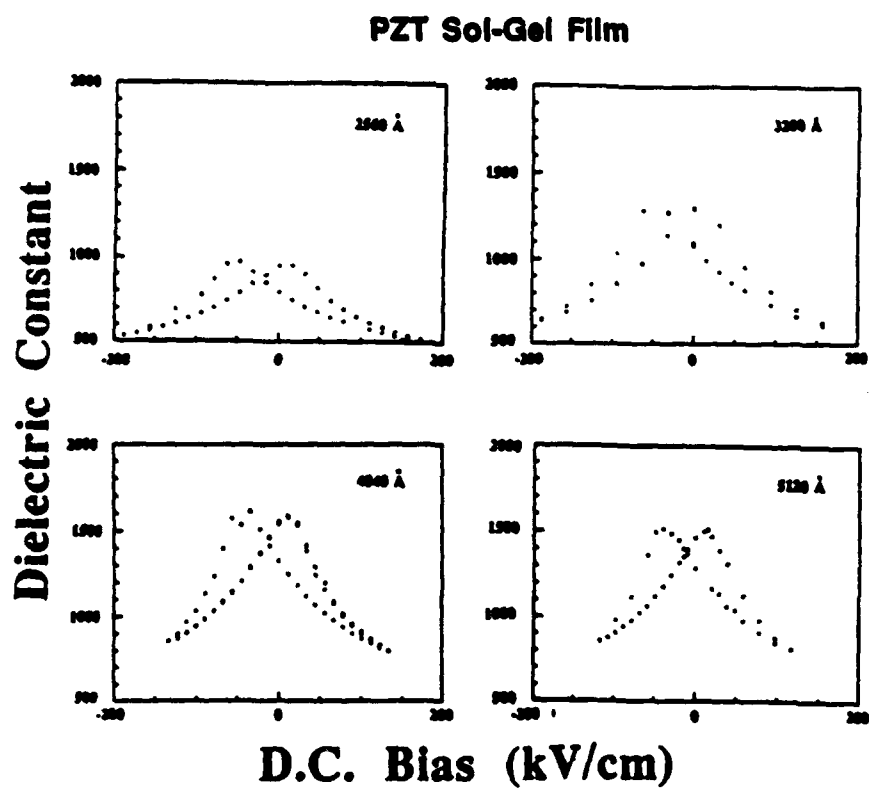
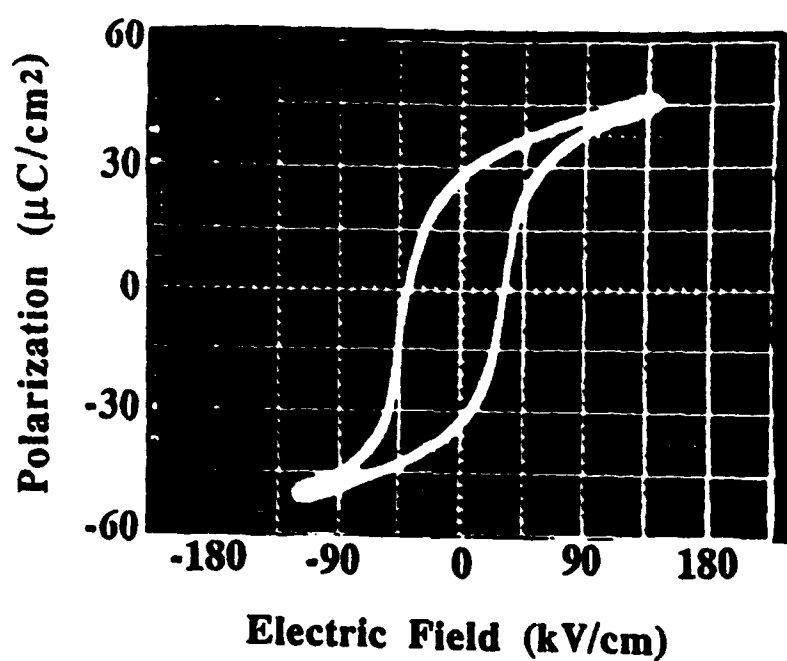


Fig. 6.4 Permittivity  $\epsilon_w$  as a function of applied electrical bias in PZT 52:45 films

### Sol-Gel PZT (52/48) Film



Thickness: 4500 Å

$P_{\text{rem}} = 30 \mu\text{C}/\text{cm}^2$

Frequency: 60 Hz

$E_{\text{coer}} \approx 31 \text{ kV/cm}$

Fig. 6.5 Polarization:field hysteresis in a PZT 52:48 film 4,500Å thick taken at 60Hz.

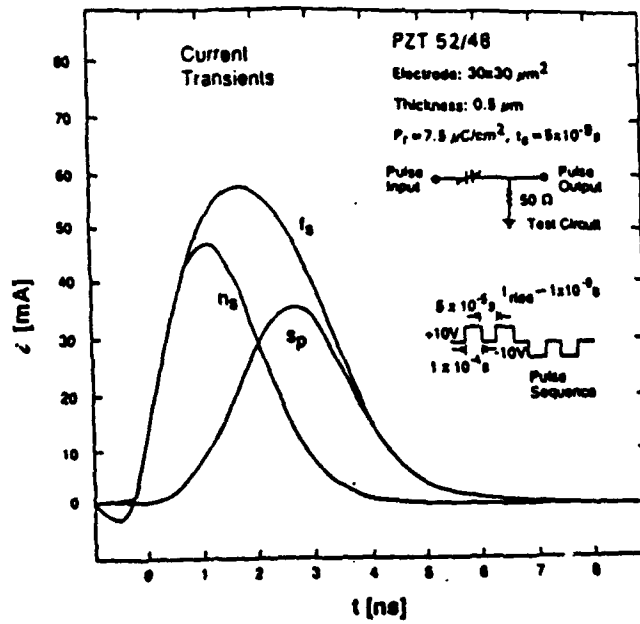


Fig. 6.6 Polarization switching using very high current pulses in PZT 52/48 (after Dey).

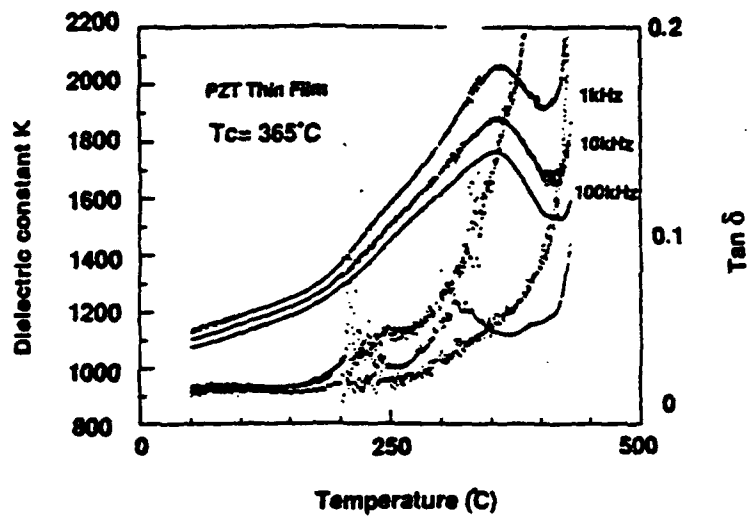


Fig. 6.7 Weak field permittivity as a function of temperature in PZT 52/48.

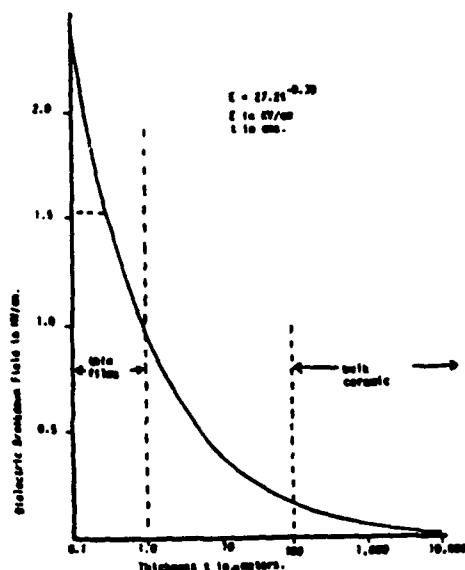


Fig. 6.8 Breakdown field  $E_b$  as a function of thickness from the empirical equation by Gerson and Marshal.

### PIEZOELECTRIC COEFFICIENTS

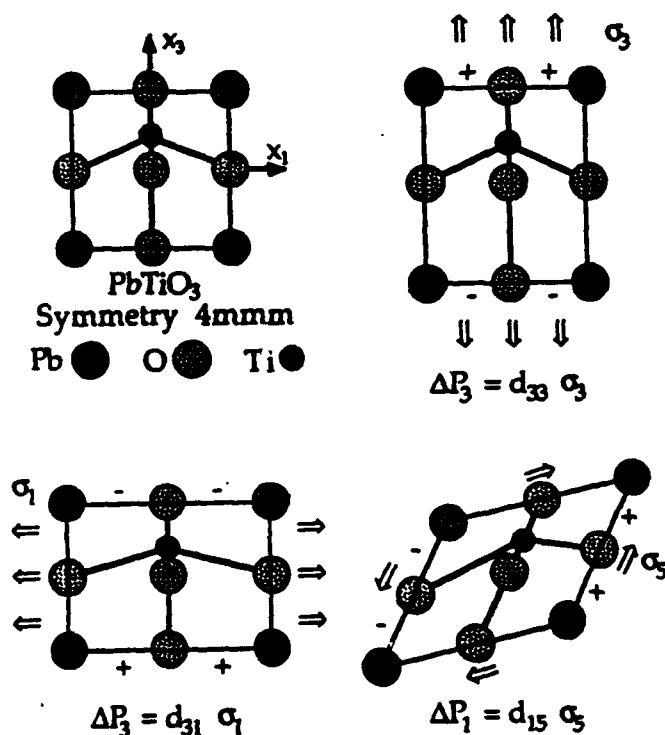


Fig. 7.1 Two dimensional description of the origin of the piezoelectric response in a single domain  $\text{PbTiO}_3$  crystal. (a) Situation under no field. (b) Shift of the Ti cation away from the equilibrium position under stress  $\tau_3$ . (c) Shift of the Ti cation back towards the cell center under stress  $\tau_1$ . (d) Tilting of the Ti position giving  $\Delta P$ , under a shear stress  $\tau_5$ .

## 7.0 PIEZOELECTRIC CERAMICS

### 7.1 Phenomenological and Pictorial Descriptions of Piezoelectricity in Crystals

The phenomenological master equation which describes the deformations of an insulating crystal subject to both elastic and electric stress takes the form

$$x_{ij} = s_{ijkl} X_{kl} + d_{mij} E_m + M_{mnnj} E_m E_n \quad (7.1)$$

where

$x_{ij}$	are the components of elastic strain
$X_{ij}$	the stress components
$s_{ijkl}$	the elastic compliance tensor
$E_m E_n$	are components of electric field
$d_{mij}$	the piezoelectric tensor components
$M_{mnnj}$	the electrostriction tensor in field notation

and the Einstein summation convention is assumed.

For crystals in which some components of the  $d_{mij}$  tensor are non zero, when  $X_{kl} = 0$  the elastic strain is given by

$$x_{ij} = d_{mij} E_m \quad (7.2)$$

which is the equation for the converse piezoelectric effects, relating induced strain directly the first power of the field, i.e.  $x_{ij}$  changes sign with  $E_m$ .

In the thermodynamically equivalent direct effect

$$P_m = d_{mij} X_{ij} . \quad (7.3)$$

Clearly 7.2 describes the actuating function of a piezoelectric, changing shape under electric field control Equation 7.3 the sensing function, a change in polarization under stress charges the capacitance of the sensing crystal giving a voltage proportional to the stress applied.

If the  $d_{mij}$  constants are zero due to symmetry as for example in a centric crystal, the residual effect is electrostrictive and at zero stress

$$x_{ij} = M_{mnnj} E_m E_n .$$

Now the strain is a quadratic function of the applied stress.

The thermodynamically converse effect is now given by

$$\eta_{mn} = M_{mnnj} X_j$$

i.e. the elastic stress dependence of the dielectric susceptibility.

Pictorially, the piezoelectric effect is illustrated by the two dimensional sketches in fig. 7.1 which models a polar crystal of the perovskite Lead titanate in its single domain ferroelectric form. To simplify the description it is assumed that the polarization resides in the  $Ti^{4+}$  ion as in  $BaTiO_3$  and the lead ion displacements are

neglected. In the base state, the titanium ion is displaced along the 3 directions a distance corresponding to the spontaneous polarization  $P_3$  and the resulting symmetry is tetragonal 4mm.

If a tensile stress  $\sigma_3$  is now applied in the  $X_3$  direction (fig. 7.1b), the upper and lower oxygen ions pull out the equatorial ions squash in forcing the  $Ti^{4+}$  farther away from the cell center and generating an enhancement of  $P_3$  by  $\Delta P$ . Since the displacement are very small  $\Delta P \propto \sigma_3$  and the constant of proportionality  $d_{33}$  is positive, i.e. a positive (tensile stress) gives a positive change in  $\Delta P$ .

For a transverse tensile stress  $\sigma_1$  however (fig. 7.1c) the equatorial oxygens are pulled out, the  $Ti^{4+}$  brought back more towards the center of the cell, giving a negative increment  $\Delta P_3$  so that

$$\Delta P_3 = d_{31} \sigma_1$$

and  $d_{31}$  must be a negative quality.

Similarly a shear stress  $\sigma_5$  ( $\sigma_{31}$ ) leads to a canting of the  $Ti^{4+}$  and a displacement direction normal to  $P_3$  i.e. a  $\Delta P_1$  so that fig. 7.1d.

$$\Delta P_1 = d_{15} \tau_5$$

For the point group 4mm clearly the action of the 4 fold axis makes 2 equivalent to 1 so that

$$d_{31} = d_{32} \quad \text{and} \quad d_{15} = d_{24}$$

and the complete piezoelectric tensor takes the form

$$\begin{pmatrix} 0 & 0 & 0 & 0 & d_{15} & 0 \\ 0 & 0 & 0 & d_{15} & 0 & 0 \\ d_{31} & d_{31} & d_{33} & 0 & 0 & 0 \end{pmatrix}$$

## 7.2 Piezoelectricity in Ceramics

In a randomly axed polycrystal ceramic, even if the grains are polar or ferroelectric as in fig. 7.2 under normal circumstance the random orientation will cancel out any anisotropy engendering a macroscopic center of symmetry which forbids piezoelectricity. For the ferroelectric ceramic however a new anisotropy can be induced since the domain polar vectors can be switched under realizable field. Thus the poling operation which develops a high remanent polarization  $P_R$  in the ceramic is essential to destroy the macro center of symmetry taking the material into the texture symmetry group  $\infty$  mm.

Theoretically it is quite straightforward to derive the possible  $P_R$  which may be induced in a ferroelectric ceramic if all domains of a given type may switch under the poling field. In a ferroelectric with only 2 antipolar domain states, only  $180^\circ$  switching would be possible and  $\bar{P}_{Rmax} = 0.25 P_s$ . In a tetragonal ferroelectric perovskite there are 6 axial orientation for the domains and  $\bar{P}_{Rmax} = .83 P_s$ , and for the rhombohedral case with 8 body diagonal orientations  $\bar{P}_{Rmax} = 0.87 P_s$ . Unfortunately the ability to

pole in practical ceramics is more restricted, so that a high count of available orientation states becomes essential. This is illustrated for  $\text{BaTiO}_3$  at room temperature in fig. 7.3 in the single domain single crystal  $P_s = 26 \mu\text{C}/\text{cm}^2$  (fig. 7.3a). Even in a very large grain ceramic  $P_r \text{ max} = 8 \mu\text{C}/\text{cm}^2$ , fig. 7.3b and in a practical fine (1  $\mu$  meter grain) ceramic  $P_r$  almost vanishes (fig. 7.3c).

### 7.3 Lead Zirconate Titanate Piezoceramics

The uniquely advantageous feature of the Lead zirconate Lead titanate ferroelectric phase diagram fig. 7.4 is the almost vertical phase boundary near the 50:50 Zr/Ti composition, the so called morphotropic phase boundary which separates a tetragonal and a rhombohedral ferroelectric phases. All ferroelectric:ferroelectric phase transitions are first order so that the boundary encompasses a finite two phase region where the 6 domain states of the tetragonal variant coexist with the 8 domain states of the rhombohedral. The advantage in terms of polability for ceramics near this composition is compared to other perovskite possibilities in fig. 7.5 showing the clear superiority of the PZT.

The maximum polability for compositions near the MPB is shown clearly in fig. 7.6, and the consequent advantage in piezoelectric constants in fig. 7.7, both taken from the book by Jaffe Cooke and Jaffe.<sup>73</sup>

#### 7.3.1 Phenomenology of Piezoelectricity in PZTs

It is clear from the earlier consideration of dielectric applications that the instability at the paraelectric:ferroelectric phase transition contributes an intrinsic compliance in the dielectric property which can be manipulated to great practical advantage. For  $\text{BaTiO}_3$ , it is easy to trace this enhanced compliance as excellent single crystals can be grown and by simple poling procedures converted into single domain states. Thus the properties of a single domain can be measured at any temperature or stress of interest and a full Landau:Ginsburg:Devonshire phenomenology developed which will *minimize* the intrinsic properties of  $\text{BaTiO}_3$  domains under any set of electric/elastic boundary conditions.<sup>74,75,76</sup>

In the lead zirconate titanate solid solution system however, the situation is significantly more complex. Different composition across the phase field exhibit antiferroelectric, oxygen octahedral tilted, and simple proper ferroelectric phases. An even more important constraint is that in spite of almost 30 years of continuous effort there are still no reputable single crystals available with compositions near to the critical 50/50 Zr/Ti ratio of the MPB and thus no direct measurements of single domain properties. Only compositions close to pure  $\text{PbZrO}_3$  and pure  $\text{PbTiO}_3$  have been grown with adequate quality and for other compositions it is necessary to use indirect methods to deduce the thermodynamic constants.

Over some 10 years the ferroelectric group at Penn State has dedicated a continuing effort to formulating an adequate phenomenology. Faculty and students involved have included B. Gadger, A. Amin, H. McKinstry, T. Halemane, M. Haun, G. Rossetti and L. E. Cross and their work is documented in a sequence of papers.<sup>77,78,79,80,81,82,83,84,85</sup> The papers 80-85 provide an excellent summary of the pure PZT work.



Fig. 7.2 Two dimension schematic of the polarization vectors in unpoled and in poled PZT. In (a) the symmetry is  $\infty \infty$  which is centric and forbids piezoelectricity. In (b) the symmetry is  $\infty mm$  which is non centric (polar) and permits piezoelectricity.

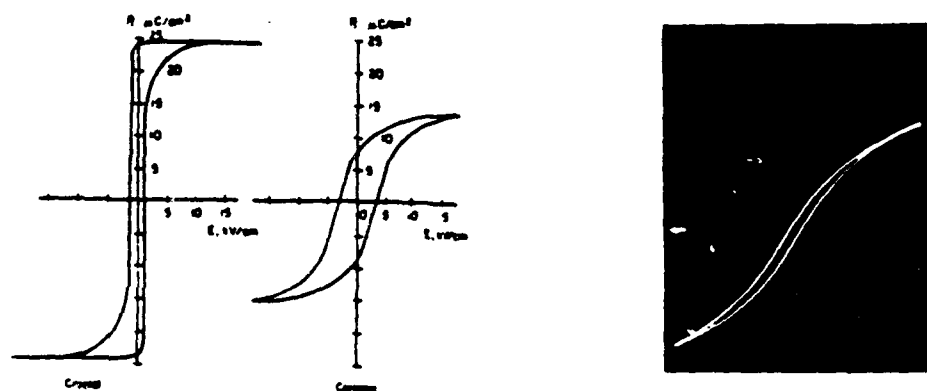


Fig. 7.3 Contrasting polarization hysteresis in (a) single crystal : (b) ceramic polycrystal : (c) fine grain ceramic  $\text{BaTiO}_3$  samples.



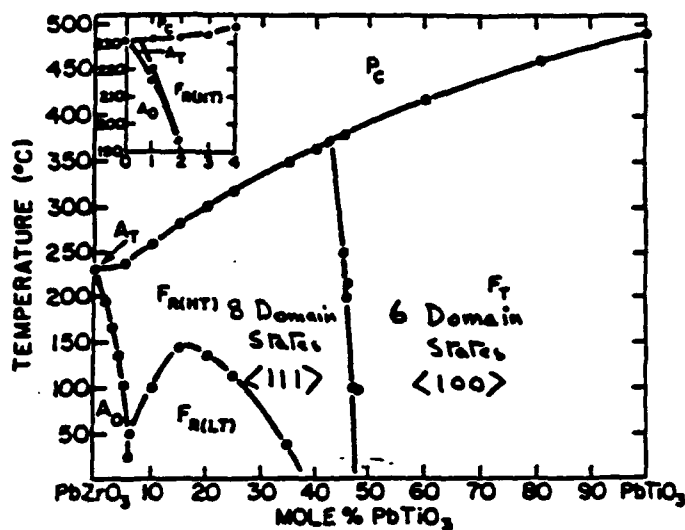


Fig. 7.4 Phase diagram of the Lead zirconate:lead titanate solid solution system, highlighting the important morphotropic phase boundary (MPB).

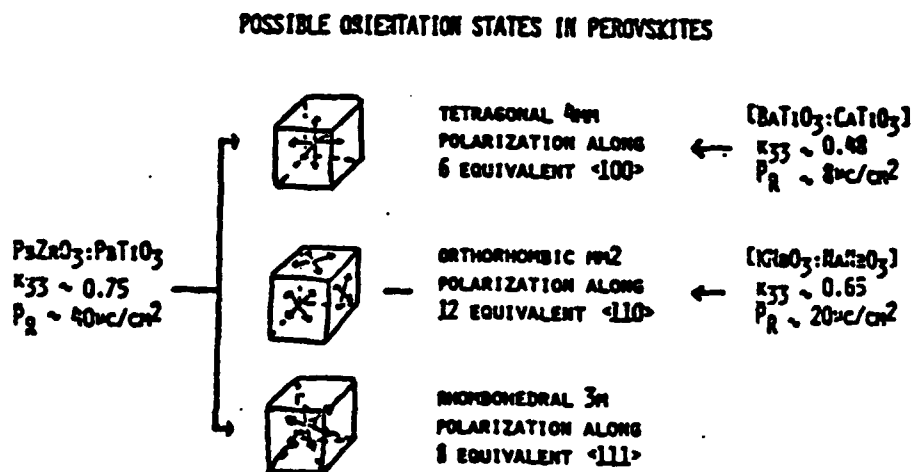


Fig. 7.5 Indicating from examples in different perovskite ceramic compositions the importance of number of equivalent domain states in realizing poling and high piezoelectric activity.

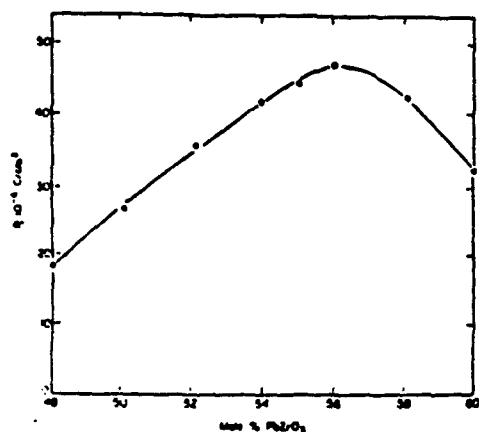


Fig. 7.6 Remanent polization in PZT ceramics of comparable grain size as a function of Zr:Ti ratio.

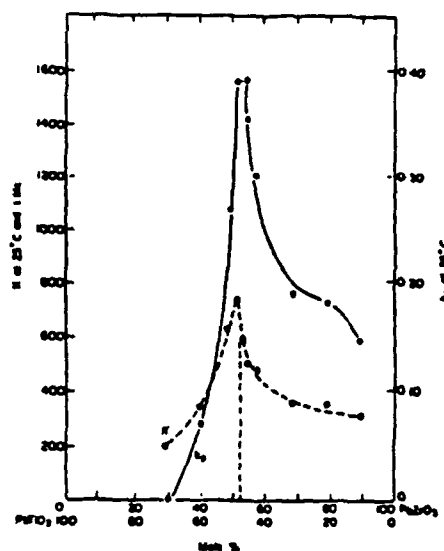


Fig. 7.7 Dielectric and piezoelectric response in poled PZT as a function of Zr:Ti ratio.

TABLE 7.1

Coefficients of the PZT Energy Function

$\alpha_i, \alpha_{ij}, \alpha_{ijk}$	ferroelectric dielectric stiffness at constant stress
$\sigma_i, \sigma_{ij}, \sigma_{ijk}$	antiferroelectric dielectric stiffness at constant stress
$\mu_{ij}$	coupling between the ferroelectric and antiferroelectric polarizations
$\beta_i, \beta_{ij}$	octahedral torsion coefficients
$\gamma_{ij}$	coupling between the ferroelectric polarization and tilt angle
$s_{ij}$	elastic compliances at constant polarization
$Q_{ij}$	electrostrictive coupling between the ferroelectric polarization and stress
$Z_{ij}$	electrostrictive coupling between the antiferroelectric polarization and stress
$R_{ij}$	rotostrictive coupling between the tilt angle and stress

In developing the "master equation" for the free energy in terms of the extensive variables, it is necessary to start with a two sub lattice model to encompass the antiferroelectric states, however, since these are confined to compositions very close to Lead zirconate it is advantageous to use linear combination of the sub lattice polarization  $P_A$  and  $P_B$  in the form

$$P = P_A + P_B \quad (7.1)$$

$$p = P_A - P_B \quad (7.2)$$

Thus when  $P_A = +P_B$   $P \neq 0$  and represents the effective ferroelectric polarization, and when  $P_A = -P_B$   $p \neq 0$  and represents the magnitude of the antipolarization in the antiferroelectric phase. Polarization and antipolarization have the axial components  $P_1 P_2 P_3$  and  $p_1 p_2 p_3$  respectively. The oxygen octahedra have tilt angle  $\theta$  with components about the axial direction  $\theta_1 \theta_2 \theta_3$ . Elastic stress and strain are designated  $X_{ij}$   $x_{ij}$ . The full family of coupling variables are delineated in table 7.1 and the resulting equation 7.3.

$$\begin{aligned} \Delta G = & \alpha_1 [P_1^2 + P_2^2 + P_3^2] + \alpha_{11} [P_1^4 + P_2^4 + P_3^4] \quad (7.3) \\ & + \alpha_{12} [P_1^2 P_2^2 + P_2^2 P_3^2 + P_3^2 P_1^2] + \alpha_{111} [P_1^6 + P_2^6 + P_3^6] \\ & + \alpha_{112} [P_1^4 (P_2^2 + P_3^2) + P_2^4 (P_1^2 + P_3^2) + P_3^4 (P_1^2 + P_2^2)] \\ & + \alpha_{123} P_1^2 P_2^2 P_3^2 + \sigma_1 [p_1^2 + p_2^2 + p_3^2] + \sigma_{11} [p_1^4 + p_2^4 + p_3^4] \\ & + \sigma_{12} [p_1^2 p_2^2 + p_2^2 p_3^2 + p_3^2 p_1^2] + \sigma_{111} [p_1^6 + p_2^6 + p_3^6] \\ & + \sigma_{112} [p_1^4 (p_2^2 + p_3^2) + p_2^4 (p_1^2 + p_3^2) + p_3^4 (p_1^2 + p_2^2)] \\ & + \sigma_{123} p_1^2 p_2^2 p_3^2 + \mu_{11} [P_1^2 p_1^2 + P_2^2 p_2^2 + P_3^2 p_3^2] \\ & + \mu_{12} [P_1^2 (p_2^2 + p_3^2) + P_2^2 (p_1^2 + p_3^2) + P_3^2 (p_1^2 + p_2^2)] \\ & + \mu_{44} [P_1 P_2 p_1 p_2 + P_2 P_3 p_2 p_3 + P_3 P_1 p_3 p_1] + \beta_1 [\theta_1^2 + \theta_2^2 + \theta_3^2] \\ & + \beta_{11} [\theta_1^4 + \theta_2^4 + \theta_3^4] + \gamma_{11} [P_1^2 \theta_1^2 + P_2^2 \theta_2^2 + P_3^2 \theta_3^2] \\ & + \gamma_{12} [P_1^2 (\theta_1^2 + \theta_3^2) + P_2^2 (\theta_1^2 + \theta_3^2) + P_3^2 (\theta_1^2 + \theta_2^2)] \\ & + \gamma_{44} [P_1 P_2 \theta_1 \theta_2 + P_2 P_3 \theta_2 \theta_3 + P_3 P_1 \theta_3 \theta_1] \\ & - \frac{1}{2} S_{11} [X_1^2 + X_2^2 + X_3^2] - S_{12} [X_1 X_2 + X_2 X_3 + X_3 X_1] \\ & - \frac{1}{2} S_{44} [X_1^2 + X_2^2 + X_3^2] - Q_{11} [X_1 P_1^2 + X_2 P_2^2 + X_3 P_3^2] \\ & - Q_{12} [X_1 (P_2^2 + P_3^2) + X_2 (P_1^2 + P_3^2) + X_3 (P_1^2 + P_2^2)] \\ & - Q_{44} [X_4 P_2 P_3 + X_5 P_1 P_3 + X_6 P_1 P_2] - Z_{11} [X_1^2 p_1 + X_2^2 p_2 + X_3^2 p_3] \\ & - Z_{12} [X_1 (p_2^2 + p_3^2) + X_2 (p_1^2 + p_3^2) + X_3 (p_1^2 + p_2^2)] \\ & - Z_{44} [X_4 p_2 p_3 + X_5 p_1 p_3 + X_6 p_1 p_2] - R_{11} [X_1 \theta_1^2 + X_2 \theta_2^2 + X_3 \theta_3^2] \\ & - R_{12} [X_1 (\theta_2^2 + \theta_3^2) + X_2 (\theta_1^2 + \theta_3^2) + X_3 (\theta_1^2 + \theta_2^2)] \\ & - R_{44} [X_4 \theta_2 \theta_3 + X_5 \theta_1 \theta_3 + X_6 \theta_1 \theta_2] \end{aligned}$$

### 7.3.2 Solutions to the Energy Function

Considering zero stress conditions the following solutions to the energy function (Equation 7.3) are of interest in the PZT system:

*Paraelectric Cubic ( $P_C$ )*

$$P_1 = P_2 = P_3 = 0, \quad p_1 = p_2 = p_3 = 0, \quad \theta_1 = \theta_2 = \theta_3 = 0 \quad (7.4)$$

*Ferroelectric Tetragonal ( $F_T$ )*

$$P_1 = P_2 = 0, \quad P_3^2 \neq 0, \quad p_1 = p_2 = p_3 = 0, \quad \theta_1 = \theta_2 = \theta_3 = 0 \quad (7.5)$$

*Ferroelectric Orthorhombic ( $F_O$ )*

$$P_1 = 0, \quad P_2^2 = P_3^2 \neq 0, \quad p_1 = p_2 = p_3 = 0, \quad \theta_1 = \theta_2 = \theta_3 = 0 \quad (7.6)$$

*Ferroelectric High-temperature Rhombohedral ( $F_{R(HT)}$ )*

$$P_1^2 = P_2^2 = P_3^2 \neq 0, \quad p_1 = p_2 = p_3 = 0, \quad \theta_1 = \theta_2 = \theta_3 = 0 \quad (7.7)$$

*Ferroelectric Low-temperature Rhombohedral ( $F_{R(LT)}$ )*

$$P_1^2 = P_2^2 = P_3^2 \neq 0, \quad p_1 = p_2 = p_3 = 0, \quad \theta_1^2 = \theta_2^2 = \theta_3^2 \neq 0 \quad (7.8)$$

*Antiferroelectric Orthorhombic ( $A_O$ )*

$$P_1 = P_2 = P_3 = 0, \quad p_1 = 0, \quad p_2^2 = p_3^2 \neq 0, \quad \theta_1 = \theta_2 = \theta_3 = 0 \quad (7.9)$$

All of these solutions, except for the ferroelectric orthorhombic solution, are stable in the PZT system. The ferroelectric orthorhombic solution was also included here, because the coefficients necessary to calculate the energy of this phase can be determined. An independent check of the calculated coefficients can then be made by confirming that this phase is metastable across the PZT system.

Applying these solutions to Equation 7.3 under zero stress conditions results in the following relations for the energies of each solution

$$P_C \quad \Delta G = 0 \quad (7.10)$$

$$F_T \quad \Delta G = \alpha_1 P_3^2 + \alpha_{11} P_3^4 + \alpha_{111} P_3^6 \quad (7.11)$$

$$F_O \quad \Delta G = 2\alpha_1 P_3^2 + (2\alpha_{11} + \alpha_{12}) P_3^4 + 2(\alpha_{111} + \alpha_{112}) P_3^6 \quad (7.12)$$

$$F_{R(HT)} \quad \Delta G = 3\alpha_1 P_3^2 + 3(\alpha_{11} + \alpha_{12}) P_3^4 + (3\alpha_{111} + 6\alpha_{112} + \alpha_{123}) P_3^6 \quad (7.13)$$

$$F_{R(LT)} \quad \Delta G = 3\alpha_1 P_3^2 + 3(\alpha_{11} + \alpha_{12}) P_3^4 + (3\alpha_{111} + 6\alpha_{112} + \alpha_{123}) P_3^6 \\ + 3\beta_1 \theta_3^2 + 3\beta_{11} \theta_3^4 + 3(\gamma_{11} + 2\gamma_{12} + \gamma_{44}) P_3^2 \theta_3^2 \quad (7.14)$$

$$A_O \quad \Delta G = 2\sigma_1 p_3^2 + (2\sigma_{11} + \sigma_{12}) p_3^4 + 2(\sigma_{111} + \sigma_{112}) p_3^6 \quad (7.15)$$

The spontaneous ferroelectric and antiferroelectric polarizations ( $P_3$  and  $p_3$ ) and tilt angle ( $\theta_3$ ) in the above equations can be found from the first partial derivative stability conditions ( $\partial\Delta G/\partial P_3$ ,  $\partial\Delta G/\partial p_3$ , and  $\partial\Delta G/\partial\theta_3$ ) as shown below.

$$F_T \quad \partial\Delta G/\partial P_3 = 0 = 3\alpha_{111}P_3^4 + 2\alpha_{11}P_3^2 + \alpha_1 \quad (7.16)$$

$$F_O \quad \partial\Delta G/\partial P_3 = 0 = 3(\alpha_{111} + \alpha_{112})P_3^4 + (2\alpha_{11} + \alpha_{112})P_3^2 + \alpha_1 \quad (7.17)$$

$$F_{R(HT)} \quad \partial\Delta G/\partial P_3 = 0 = (3\alpha_{111} + 6\alpha_{112} + \alpha_{123})P_3^4 + 2(\alpha_{11} + \alpha_{12})P_3^2 + \alpha_1 \quad (7.18)$$

$$F_{R(LT)} \quad \partial\Delta G/\partial P_3 = 0 = (3\alpha_{111} + 6\alpha_{112} + \alpha_{123})P_3^4 + 2(\alpha_{11} + \alpha_{12})P_3^2 + \alpha_1 + \gamma_{11}\theta_3^2 \quad (7.19)$$

$$\partial\Delta G/\partial\theta_3 = 0 = \beta_1 + 2\beta_{11}\theta_3^2 + \gamma_{11}P_3^2 \quad (7.20)$$

$$A_O \quad \partial\Delta G/\partial p_3 = 0 = 3(\sigma_{111} + \sigma_{112})p_3^4 + (2\sigma_{11} + \sigma_{12})p_3^2 + \sigma_1 \quad (7.21)$$

The polarizations and tilt angle can be calculated by solving these quadratic equations. Equations 7.10 - 7.15 relate the energies of each solution to the coefficients of the energy function. Thus by determining these coefficients, the energies of each phase can be calculated.

### 7.3.3 Spontaneous Elastic Strains

The spontaneous elastic strains  $x_i$  ( $\partial\Delta G/\partial x_i$ ) under zero stress conditions can be derived from Equation 7.3 as follows:

$$P_C \quad x_1 = x_2 = x_3 = x_4 = x_5 = x_6 = 0 \quad (7.22)$$

$$F_T \quad x_1 = x_2 = Q_{12}P_3^2, \quad x_3 = Q_{11}P_3^2, \quad x_4 = x_5 = x_6 = 0 \quad (7.23)$$

$$F_O \quad x_1 = 2Q_{12}P_3^2, \quad x_2 = x_3 = (Q_{11} + Q_{12})P_3^2, \quad x_4 = Q_{44}P_3^2, \quad x_5 = x_6 = 0 \quad (7.24)$$

$$F_{R(HT)} \quad x_1 = x_2 = x_3 = (Q_{11} + 2Q_{12})P_3^2, \quad x_4 = x_5 = x_6 = Q_{44}P_3^2 \quad (7.25)$$

$$F_{R(LT)} \quad x_1 = x_2 = x_3 = (Q_{11} + 2Q_{12})P_3^2 + (R_{11} + 2R_{12})\theta_3^2, \quad x_4 = x_5 = x_6 = Q_{44}P_3^2 + R_{44}\theta_3^2 \quad (7.26)$$

$$A_O \quad x_1 = 2Z_{12}p_3^2, \quad x_2 = x_3 = (Z_{11} + Z_{12})p_3^2, \quad x_4 = Z_{44}p_3^2, \quad x_5 = x_6 = 0 \quad (7.27)$$

These spontaneous strain relations can be shown to be very important in determining the coefficients of the energy function. Spontaneous strain data will be determined from x-ray diffraction of PZT powders, and used with the electrostrictive constants to calculate the spontaneous polarization, which is needed to determine coefficients of the energy function.

### 7.3.4 Intrinsic Dielectric Properties

Relations for the relative dielectric stiffness  $\chi_{ij}$  ( $= \partial^2 \Delta G / \partial P_i \partial P_j$ ) were derived from Equation 7.3 for the six solutions:

$$P_C \quad \chi_{11} = \chi_{22} = \chi_{33} = 2\epsilon_0 \alpha_1, \quad \chi_{12} = \chi_{23} = \chi_{31} = 0 \quad (7.28)$$

$$F_T \quad \chi_{11} = \chi_{22} = 2\epsilon_0 [\alpha_1 + \alpha_{12} P_3^2 + \alpha_{112} P_3^4],$$

$$\chi_{33} = 2\epsilon_0 [\alpha_1 + 6\alpha_{11} P_3^2 + 15\alpha_{111} P_3^4], \quad \chi_{12} = \chi_{23} = \chi_{31} = 0 \quad (7.29)$$

$$F_O \quad \chi_{11} = 2\epsilon_0 [\alpha_1 + 2\alpha_{12} P_3^2 + (2\alpha_{112} + \alpha_{123}) P_3^4],$$

$$\chi_{22} = \chi_{33} = 2\epsilon_0 [\alpha_1 + (6\alpha_{11} + \alpha_{12}) P_3^2 + (15\alpha_{111} + 7\alpha_{112}) P_3^4],$$

$$\chi_{12} = \chi_{31} = 0, \quad \chi_{23} = 4\epsilon_0 [\alpha_{12} P_3^2 + 4\alpha_{112} P_3^4] \quad (7.30)$$

$$F_{R(HT)} \quad \chi_{11} = \chi_{22} = \chi_{33} = 2\epsilon_0 [\alpha_1 + (6\alpha_{11} + 2\alpha_{22}) P_3^2$$

$$+ (15\alpha_{111} + 14\alpha_{112} + \alpha_{123}) P_3^4],$$

$$\chi_{12} = \chi_{23} = \chi_{31} = 4\epsilon_0 [\alpha_{12} P_3^2 + (4\alpha_{112} + \alpha_{123}) P_3^4] \quad (7.31)$$

$$F_{R(LT)} \quad \chi_{11} = \chi_{22} = \chi_{33} = 2\epsilon_0 [\alpha_1 + (6\alpha_{11} + 2\alpha_{12}) P_3^2$$

$$+ (15\alpha_{111} + 14\alpha_{112} + \alpha_{123}) P_3^4 + (\gamma_{11} + 2\gamma_{12}) \theta_3^2],$$

$$\chi_{12} = \chi_{23} = \chi_{31} = 4\epsilon_0 [\alpha_{12} P_3^2 + (4\alpha_{112} + \alpha_{123}) P_3^4 + \gamma_{44} \theta_3^2] \quad (7.32)$$

$$A_O \quad \chi_{11} = 2\epsilon_0 [\alpha_1 + 2\mu_{12} P_3^2], \quad \chi_{22} = \chi_{33} = 2\epsilon_0 [\alpha_1 + (\mu_{11} + \mu_{12}) P_3^2],$$

$$\chi_{12} = \chi_{31} = 0, \quad \chi_{23} = \epsilon_0 \mu_{44} P_3^2 \quad (7.33)$$

The multiplication by permittivity of free space  $\epsilon_0$  in these equations was required to convert from absolute to relative dielectric stiffnesses. Equations 7.28 - 7.33 can be used to calculate the relative dielectric stiffness for each phase based on the original cubic axes.

In the orthorhombic state the polarization can be along of the  $\langle 110 \rangle$  directions of the original cubic axes. The polarization of the rhombohedral state can be along any of the  $\langle 111 \rangle$  directions. By rotating these axes so that for both states the new  $x_3$  axis is along the polar directions, diagonalized matrices will result. The new dielectric stiffness coefficients (indicated by a prime) can be related to the old coefficients [defined by equations 7.28 - 7.33] with the following relations:

$$F_O \text{ and } A_O \quad \chi'_{11} = \chi_{11}, \quad \chi'_{22} = \chi_{33} - \chi_{23} \quad (7.34)$$

$$\chi'_{33} = \chi_{33} + \chi_{23}, \quad \chi'_{12} = \chi'_{23} = \chi'_{31} = 0$$

$$F_{R(HT)} \text{ and } F_{R(LT)} \quad \chi'_{11} = \chi'_{22} = \chi_{11} - \chi_{12}, \quad \chi'_{33} = \chi_{11} + 2\chi_{12}$$

$$\chi'_{12} = \chi'_{23} = \chi'_{31} = 0 \quad (7.35)$$

These equations can be used to calculate the dielectric stiffness of the orthorhombic and rhombohedral phases parallel and perpendicular to the polar axes.

The dielectric susceptibility coefficients ( $\eta_{ij}$ ) can be determined from the reciprocal of the dielectric stiffness matrices ( $\chi_{ij}$ ) using the following relation:

$$\eta_{ij} = A_{ji}/\Delta, \quad (7.36)$$

where  $A_{ji}$  and  $\Delta$  are the cofactor and determinant of the  $\chi_{ij}$  matrix. Using this relation results in the following relations for the dielectric susceptibility coefficients ( $\eta_{ij}$ ):

$$P_C \quad \eta_{11} = \eta_{22} = \eta_{33} = 1/\chi_{11}, \quad \eta_{12} = \eta_{23} = \eta_{31} = 0 \quad (7.37)$$

$$F_T \quad \eta_{11} = \eta_{22} = 1/\chi_{11}, \quad \eta_{33} = 1/\chi_{33} \quad (7.38)$$

$$F_O \text{ and } A_O \quad \eta_{11} = 1/\chi_{11}, \quad \eta_{22} = \eta_{33} = \chi_{33}/(\chi_{33}^2 - \chi_{23}^2),$$

$$\eta_{12} = \eta_{31} = 0, \quad \eta_{23} = -\chi_{23}/(\chi_{33}^2 - \chi_{23}^2) \quad (7.39)$$

$$\eta'_{11} = 1/\chi'_{11}, \quad \eta'_{22} = 1/\chi'_{22}, \quad \eta'_{33} = 1/\chi'_{33}$$

$$\eta'_{12} = \eta'_{23} = \eta'_{31} = 0 \quad (7.40)$$

$$F_{R(HT)} \text{ and } F_{R(LT)} \quad \eta_{11} = \eta_{22} = \eta_{33} = (\chi_{11}^2 - \chi_{12}^2)/(\chi_{11}^3 - 3\chi_{11}\chi_{12}^2 + 2\chi_{12}^3)$$

$$\eta_{12} = \eta_{23} = \eta_{31} = (\chi_{12}^2 - \chi_{11}\chi_{12})/(\chi_{11}^3 - 3\chi_{11}\chi_{12}^2 + 2\chi_{12}^3)$$

$$\eta'_{11} = \eta'_{22} = 1/\chi'_{11}, \quad \eta'_{33} = 1/\chi'_{33} \quad (7.41)$$

$$\eta'_{12} = \eta'_{23} = \eta'_{31} = 0 \quad (7.42)$$

These equations can be used to calculate the dielectric susceptibilities of each phase from the coefficients of the energy function.

### 7.3.5 Piezoelectric Properties

Relations for the piezoelectric  $b_{ij}$  coefficients ( $= \partial^2 \Delta G / \partial P_i \partial X_j$ ) were derived from Equation 7.3 for the tetragonal and rhombohedral states as shown below.

$$F_T \quad b_{33} = 2Q_{11}P_3, \quad b_{31} = b_{32} = 2Q_{12}P_3,$$

$$b_{15} = b_{24} = Q_{44}P_3, \quad b_{11} = b_{12} = b_{13} = b_{14} = b_{16} = 0,$$

$$b_{21} = b_{22} = b_{23} = b_{25} = b_{26} = b_{34} = b_{35} = b_{36} = 0 \quad (7.43)$$

$$F_{R(HT)} \text{ and } F_{R(LT)} \quad b_{11} = b_{22} = b_{33} = 2Q_{11}P_3, \quad b_{14} = b_{25} = b_{36} = 0$$

$$b_{12} = b_{13} = b_{21} = b_{23} = b_{31} = b_{32} = 2Q_{12}P_3,$$

$$b_{15} = b_{16} = b_{24} = b_{26} = b_{34} = b_{35} = Q_{44}P_3, \quad (7.44)$$

Since a coupling term of type  $X_i P_i \theta_i$  was not included in Equation 7.3, the  $b_{ij}$  relations [Equation 7.44] for the high and low temperature rhombohedral phases are of the same form. However, the spontaneous polarizations  $P_3$  are defined by different relations for the high and low temperature rhombohedral phases, and thus different values would result for these coefficient.

The piezoelectric  $d_{ij}$  coefficients are defined by:

$$d_{ij} = b_{kj} \eta_{ik} \quad (7.45)$$

Using this relation for the tetragonal and rhombohedral states results in the following relations:

$$\begin{aligned} F_T \quad d_{33} &= 2\epsilon_0 \eta_{33} Q_{11} P_3, \quad d_{31} = d_{32} = 2\epsilon_0 \eta_{33} Q_{12} P_3, \\ d_{15} &= d_{24} = \epsilon_0 \eta_{11} Q_{44} P_3, \quad d_{11} = d_{12} = d_{13} = d_{14} = d_{16} = 0, \\ d_{21} &= d_{22} = d_{23} = d_{25} = d_{26} = d_{34} = d_{35} = d_{36} = 0 \end{aligned} \quad (7.46)$$

$$\begin{aligned} F_{R(HT)} \text{ and } F_{R(LT)} \quad d_{11} &= d_{22} = d_{33} = 2\epsilon_0 (\eta_{11} Q_{11} + 2\eta_{12} Q_{12}) P_3, \\ d_{12} &= d_{13} = d_{21} = d_{23} = d_{31} = d_{32} \\ &= 2\epsilon_0 [\eta_{11} Q_{12} + \eta_{12} (Q_{11} + Q_{12})] P_3, \\ d_{14} &= d_{25} = d_{36} = 2\epsilon_0 \eta_{12} Q_{44} P_3, \\ d_{15} &= d_{16} = d_{24} = d_{26} = d_{34} = d_{35} = \epsilon_0 (\eta_{11} + \eta_{12}) Q_{44} P_3. \end{aligned} \quad (7.47)$$

The multiplication by the permittivity of free space  $\epsilon_0$  in these three equations was required to convert the dielectric susceptibilities from relative to absolute. Equations 7.43, 7.44, 7.45, and 7.46 can be used to calculate the piezoelectric  $b_{ij}$  and  $d_{ij}$  coefficients of the tetragonal and rhombohedral phases from the coefficients of the energy function.



### 7.3.6 Delineation of the Phenomenological Constants

The initial basic assumption applied was that all temperature dependence was carried the lowest order stiffness constants  $\alpha_1$  and  $\tau_1$  which were made linear functions of temperature. The Currie temperature  $T_c$  was taken from the phase diagram and the Curie constant  $C$  used measured values taken from high density ceramic samples. The temperature dependence of  $P_s$  required to model the higher order  $\alpha_{ij}$ . Curie was determined by assuming quadratic electrostriction and measuring the X-ray spontaneous strain in carefully prepared chemically coprecipitated powders. The MPB imposes a major constraint upon the  $\alpha$ 's since it requires that near the 50/50 Zr/Ti composition the tetragonal and rhombohedral phases have similar energies across a very wide temperature range.

Full details of the procedures, and of the most recent families of constants can be found in references 81-85. A tabulation of the room temperature values is given in table 7.2.

### 7.3.7 Intrinsic Properties of PZT

Plots of the free energy vs compositions, using the fitted parameters are given in fig. 7.8 for temperatures of 25°C, 75°C and 125°C. The resulting phase diagram deduced from the crossing points of the phase stability lines for the whole composition temperature field is given in fig. 7.9 and is shown to be in good agreement with the accepted phase diagram.

Indications of the capability to delineate single domain properties are given in fig. 7.10 for the susceptibility as a function of temperature in the PZT 60:40, and in the susceptibility as a function of composition at room temperature, given in fig. 7.11. Examples of the full family of elasto-dielectric properties which can be deduced are given in the original references.

## 7.4 Extrinsic Contributions to Response in PZT Type Piezoceramics

Even in the best poled PZT ceramic, because of the random orientation and the internal stresses generated by switching the large spontaneous strains during poling, the sample does not come to an ensemble of single domain grains. Thus in considering the polarizability of the ceramic in its ferroelectric phases, we must consider the extrinsic contributions due to changes in the polar domain structure and phase makeup brought about by the field. The type of changes occurring which could contribute to the polarizability are shown schematically in two dimensions in fig. 7.12.

For the piezoelectric response, only extrinsic actions which are shape changing will contribute so that simple 180° domain wall motion does not contribute, and is in fact deleterious to piezo response since it contributes polarization without any shape changes e.g.

$$\begin{aligned} x_3 &= Q_{11} P_3^2 & \text{and } \pm P_3 \text{ give rise to identical} \\ & & \text{strains } x_3 \text{ and } x_1 \\ x_1 &= Q_{12} P_3^2 \end{aligned}$$

Non 180° wall motion, that is motion of 90° walls in the tetragonal phase, and motion of 71° and 110° walls in the rhombohedral phases will give rise to shape change, however, the nature of the shape change will depend on the relation between

TABLE 7.2

Values of the coefficients used in the energy function (eq. 7.3) at 25°C,  
as a function of Zr:Ti ratio.

	Mole Fraction PbTiO <sub>3</sub> in PZT										
	0.0	0.1	0.2	0.3	0.4	0.5	0.6	0.7	0.8	0.9	1.0
$T_c(^{\circ}\text{C})$	231.5	256.5	300.6	334.4	364.3	392.6	418.4	440.2	459.1	477.1	492.1
$C(10^3/^{\circ}\text{C})$	2.027	2.050	2.083	2.153	2.424	4.247	2.664	1.881	1.642	1.547	1.500
$Q_{11}(10^{-12} \text{ m}^3/\text{C})$	4.620	5.080	5.574	6.175	7.260	9.660	8.116	7.587	5.142	8.544	8.940
$Q_{12}(10^{-12} \text{ m}^3/\text{C})$	-1.391	-1.540	-1.720	-1.997	-2.708	-4.600	-2.950	-2.480	-2.246	-2.507	-2.600
$Q_{13}(10^{-12} \text{ m}^3/\text{C})$	4.664	4.940	5.165	5.522	6.293	8.190	6.710	6.356	6.417	6.569	6.750
$a_1(10^3 \text{ m}^3/\text{C}^2)$ at 25°C	-4.582	-6.376	-7.470	-8.116	-7.904	-4.887	-8.340	-12.47	-14.84	-16.17	-17.08
$a_{11}(10^3 \text{ m}^3/\text{C}^2\text{F})$	52.35	41.25	31.29	22.30	13.62	4.764	3.614	0.255	-3.650	-5.845	-7.253
$a_{12}(10^3 \text{ m}^3/\text{C}^2\text{F})$	-16.71	-4.222	-0.0345	1.688	2.391	1.735	3.233	5.109	6.320	7.063	7.840
$\bar{\epsilon}(10^3 \text{ m}^3/\text{C}^2\text{F})$	-34.42	-0.2897	9.284	11.75	11.26	6.634	10.78	15.52	15.05	19.44	20.32
$a_{111}(10^3 \text{ m}^3/\text{C}^3\text{F})$	5.932	5.068	4.288	3.560	2.713	1.356	1.860	2.348	2.475	2.518	2.646
$a_{112}(10^3 \text{ m}^3/\text{C}^3\text{F})$	311.2	34.45	16.14	15.27	12.13	6.128	3.303	10.25	9.624	8.049	6.181
$a_{122}(10^3 \text{ m}^3/\text{C}^3\text{F})$	-104.1	-8.797	-7.545	-7.052	-5.690	-2.944	-4.063	-5.003	-4.901	-4.349	-3.660
$\bar{\chi}(10^3 \text{ m}^3/\text{C}^3\text{F})$	84.41	13.39	4.627	3.176	2.402	1.183	1.346	1.551	1.652	1.256	0.7518

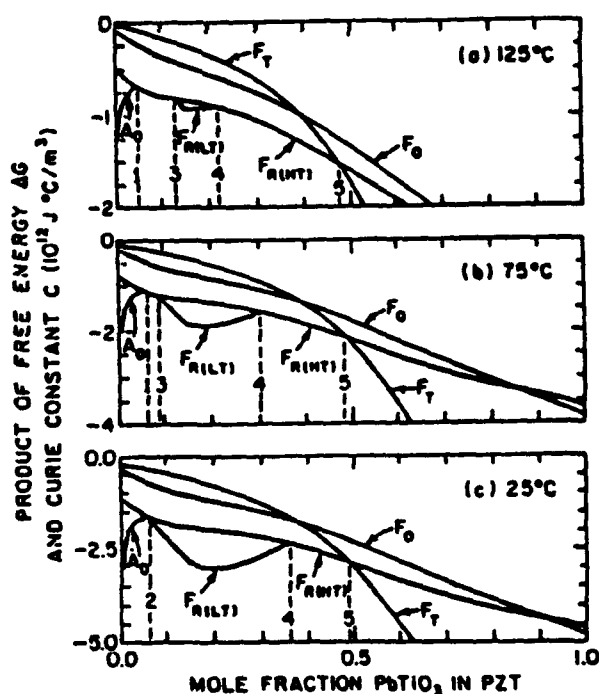


Fig. 7.8 Calculated Free Energy profiles for each realizable phase as a function of Zr:Ti ratio at (a) 25°C, (b) 75°C, (c) 125°C.

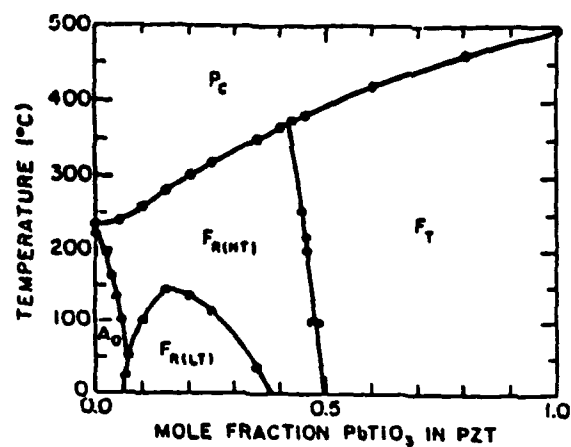


Fig. 7.9 Comparison of calculated and measured phase diagram for PZT.

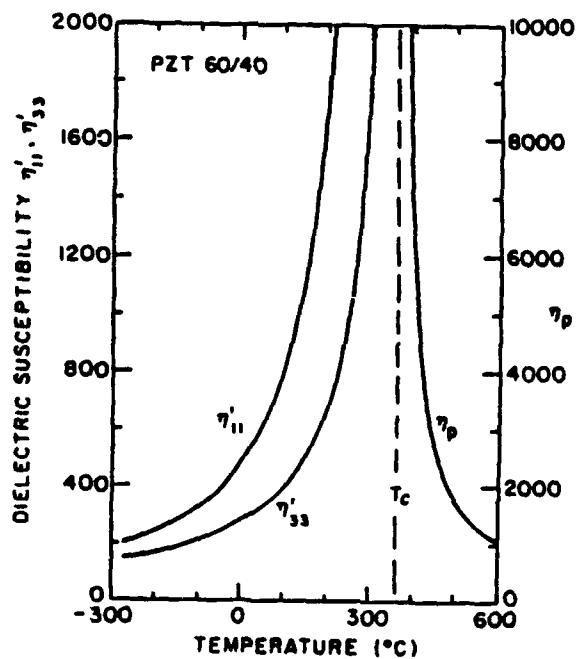


Fig. 7.10 Single domain dielectric susceptibility calculated for a PZT 60:40 composition.

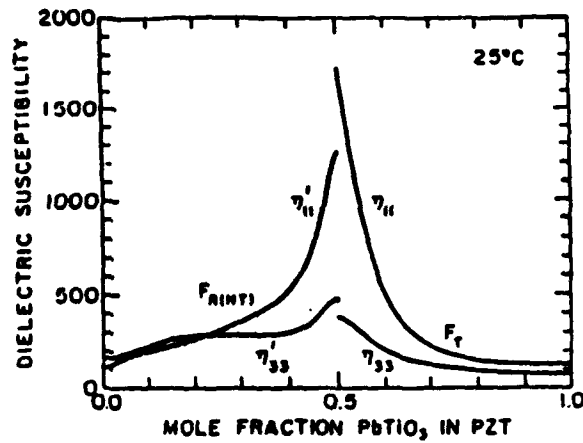


Fig. 7.11 Dielectric susceptibility of single domain states as a function of Zr:Ti ratio.

POLARIZATION MECHANISMS IN PIEZOCERAMICS

(A) HIGH FIELD

(1) INTRINSIC SINGLE DOMAIN POLARIZABILITY

$\eta_1$



(2)  $180^\circ$  DOMAIN WALL MOTION

$\eta_{(180)}$



(3) FERROELASTIC WALL MOTION

$\eta_{(90)}$



(4) FERROELECTRIC PHASE CHANGE

$\eta_F$



Fig. 7.12 Possible mechanisms which can contribute to the dielectric polarizability in a ferroelectric PZT at the MPB composition.

ferroelectric: ferroelastic wall motion and pure ferroelectric wall motion. From figure 7.13, if  $90^\circ$  motion occurs before  $180^\circ$  motion the effective shape change reverses sign with the field, if however  $180^\circ$  motion precedes  $90^\circ$  wall motion the shape change does not reverse sign with the field and is effectively electrostrictive. A similar situation exists for phase boundary motion (fig. 7.14) where again the relation to pure ferroelectric  $180^\circ$  wall switching is quite critical.

It must be stressed that in all these considerations it is that component of wall motion which is reversible with the field and which persists down to almost zero field which is of important.

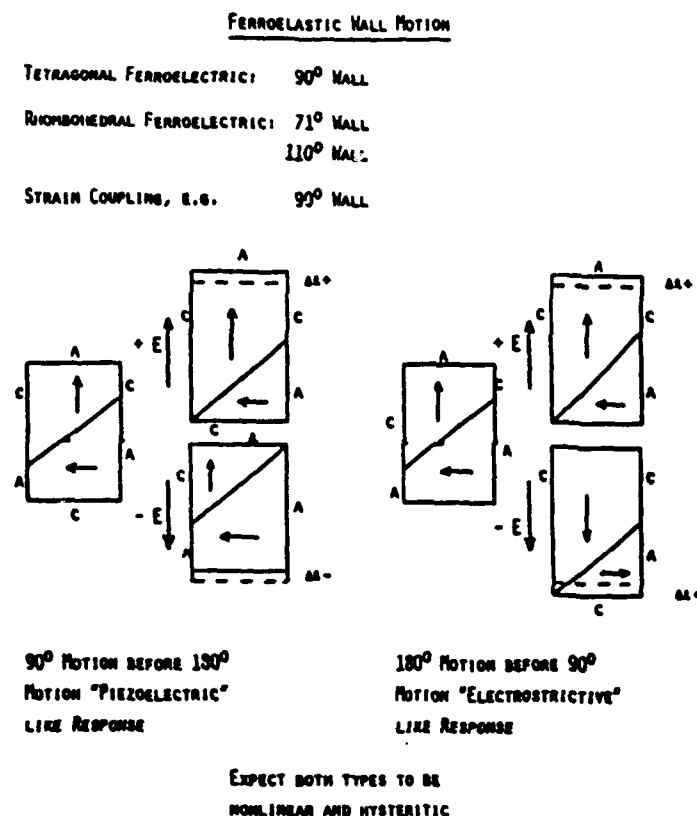


Fig. 7.13 Shape changing effects of  $180^\circ$  pure ferroelectric and ferroelectric:ferroelastic domain wall motion, depicted in schematic two dimensional models.

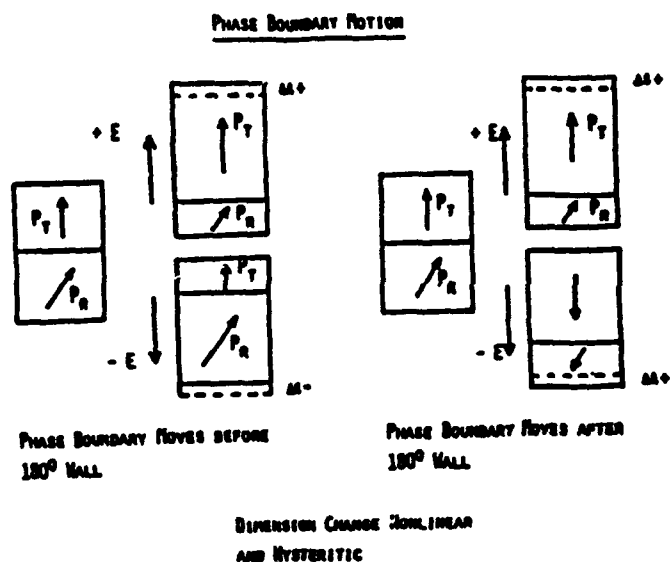


Fig. 7.14 Shape changing effects of  $180^\circ$  pure ferroelectric domain motion and of phase boundary motion in a PZT ferroelectric at a composition near the MPB.

#### 7.4.1 Control of Extrinsic Contributions to Response

During the course of many years of empirical development a wide range of low level additives (0-5 mole%) have been found to have a marked influence upon dielectric and piezoelectric properties in PZT compositions. In general, the aliovalent oxides fall into two distinct groups. Electron donor additions where the charge on the cation is larger than that which it replaces in the PZT structure and electron acceptor additives where the charge on the cation is smaller than that of the ion which it replaces (table 7)

The donor additions enhance both dielectric and piezoelectric response at room temperature and under high fields show symmetrical unbiased hysteresis loops with good "squareness" and lower coercivity.<sup>66,67</sup> The acceptor additives in general reduce both dielectric and piezoelectric responses, they give rise to highly asymmetric hysteresis response, larger coercivity and higher electrical and mechanical  $Q$ . That the effects of the dopants are mostly upon the extrinsic components of response is expected from their marked influence on the hysteresis and is confirmed by the very low temperature behaviours (fig. 7.15). For the Navy type I to V the compositions range from a strongly donor doping (type V) to a strongly acceptor doping in type III but all are at the same Zr:Ti ratio. It may be noted that the very large difference in weak field permittivity ( $\epsilon \sim 3000 \rightarrow \epsilon \sim 750$ ) is completely lost at liquid helium temperature where all extrinsic contributions are frozen out, and that the data agree quite well with the intrinsic permittivity calculated from the average of the single domain values deduced from the thermodynamic theory for that composition and temperature.

LOWER LEVEL MODIFIERS (0 to 10 MOLE %)

<u>'Donor' Additives</u>	<u>'Acceptor' Additives</u>
$\text{Nb}_2\text{O}_5$ or $\text{PbNb}_2\text{O}_6$	$\text{Fe}_2\text{O}_3$
$\text{Ta}_2\text{O}_5$ or $\text{PbTa}_2\text{O}_6$	$\text{Al}_2\text{O}_3$
$\text{WO}_3$	$\text{Cr}_2\text{O}_3$
$\text{Bi}_2\text{O}_3$	$\text{MnO}_2$
$\text{Sb}_2\text{O}_3$	$\text{MgO}$
$\text{La}_2\text{O}_3$	$\text{NiO}$
	$\text{V}_2\text{O}_5$
<u>Other Low Level Additives:</u>	
$\text{Na}_2\text{O}, \text{K}_2\text{O}, \text{Ga}_2\text{O}_3, \text{In}_2\text{O}_3, \text{IrO}_2, \text{ThO}_2$	

Fig. 7.15 Common 'dopants' used in 'soft' donor doped and 'hard' 'acceptor' doped PZT compositions.

In the acceptor doped compositions there are very good explanations of how the domain structure (not the wall) is stabilized.<sup>88,89,90</sup> In essence the charged acceptor associates with an oxygen vacancy to produce a slowly mobile defect dipole. The vacancy is the only mobile defect in the perovskite at room temperature and the defect dipole orients by vacancy migration in the dipole field associated with the domain. Thus over time the existing domain structure (poled or unpoled) is stabilized and the walls are "stiffened." Bias phenomena in both poled and unpoled ceramics can be logically explained as can some facets of the aging behaviour and the time dependence of mechanical Q.

For donor doped samples, there are only "hand waving" arguments as to how or why the domain walls should become more mobile and indeed it is not clear whether the effects are from domain walls, phase boundaries, or are defect induced. Much more work is needed to determine the physics of the softening in these materials.

A favorite pastime for empirical development has been the combination of PZTs with relaxor spin glass lead based compositions to produce improved "soft" high permittivity high coupling ceramics (fig. 7.16) and a vast range of compositions has been explored. In general the effect is to lower  $T_c$ , raise  $\epsilon$ , raise  $k_t$  and  $k_p$  and  $d_{33}$ . The typical ranges of advantage are given in 7.16. Usually the compositions used follow closely along the MPB into these 3 component phase diagrams.

## 7.5 Electrostrictive Actuators

The poled ferroelectric domain structure of the normal piezoelectric PZT provides very useful actuators with field induced strain of order  $1 - 2 \cdot 10^{-3}$  at field levels of 10kV/cm. For systems which require a fiducial zero strain position however, aging and deaging of the domain structure under high fields lead to uncomfortable changes

of the zero field dimensions which are unacceptable in precise positioning applications.

For the electrostrictor (fig. 7.17) useful strain levels require very high levels of induced polarization i.e. high dielectric permittivity.

for valence compensated additions the systems studied have included:

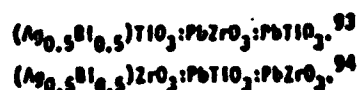
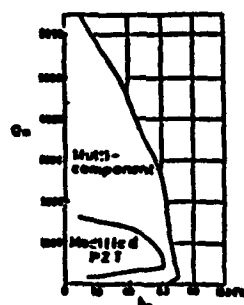
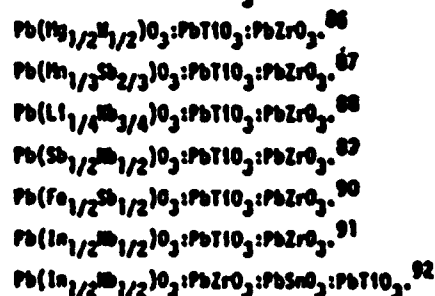
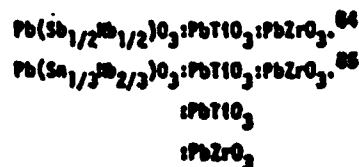
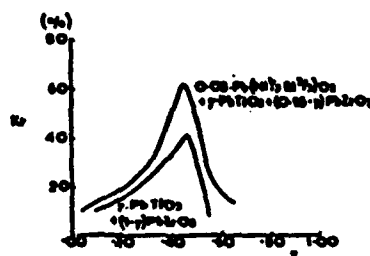
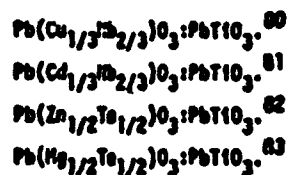
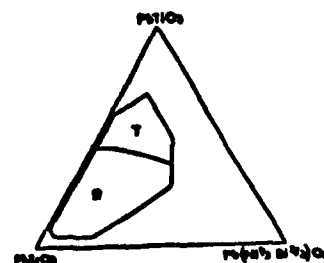
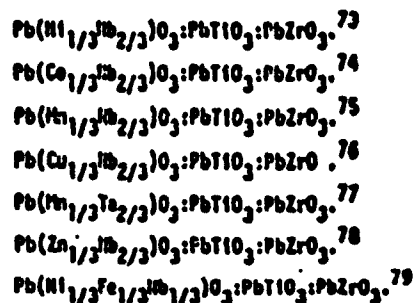


Fig. 7.16 Examples of systems using a relaxor additives to PZT.



### ELECTROSTRICTIVE ACTUATORS

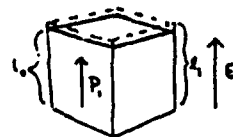
Direct Electrical Control of shape (strain) in an insulating solid.

Electrostriction.

$$u_{kl} = M_{ijkl} \epsilon_i \epsilon_j$$

$$\frac{l_j - l_0}{l_0} = M_{1111} \epsilon_1^2$$

$$u_{kl} = q_{ijkl} p_i p_j$$



M values widely scattered in different insulators.

q values - much more limited range. Systematic change with elastic behavior.

Controlling dimensions in an electrostrictive requires control of polarization.

**Fig. 7.17** Actuation using the direct electrostrictive effect in a very high K ferroelectric type perovskite.

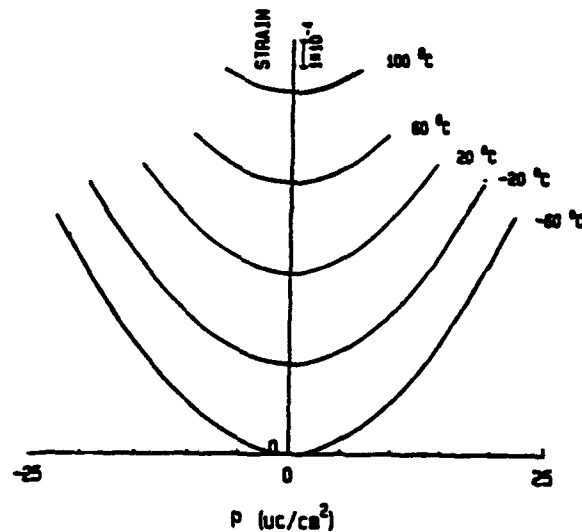


**Fig. 7.18** Typical polarization:strain curves in a PMN electrostriction actuator as a function of temperature.

In the relaxor ferroelectric spin glass compositions like lead magnesium niobate (PMN), at temperatures above the freezing temperature large levels of polarization can be induced at realizable field levels and high quadratic levels of strain are possible (fig. 7.18). Reproducibility of the strain under cyclic E field is evident in fig. 7.19, and is compared to the "walk off" which occurs in a PZT8 due to de-aging. Figure 7.20 show that the strain is truly quadratic when referenced to the polarization as would be expected in electrostrictors. It is interesting to note that the Q constants for PMN are essentially temperature independent over the range from 100 to -60°C (fig. 7.21). An unexpected bonus in the relaxors is that the steady accretion of polarization for temperatures below T Burns leads to an expansion term of the form

$$\Delta v \propto (Q_{11} + 2Q_{12})P_{\langle 111 \rangle}^2$$

which tends to compensate for the normal thermal contraction. Thus over a range of temperatures near 20°C it is possible to mate PMN:10%PT with ULE glass so that dimension can be controlled electrically but do not drift thermally.

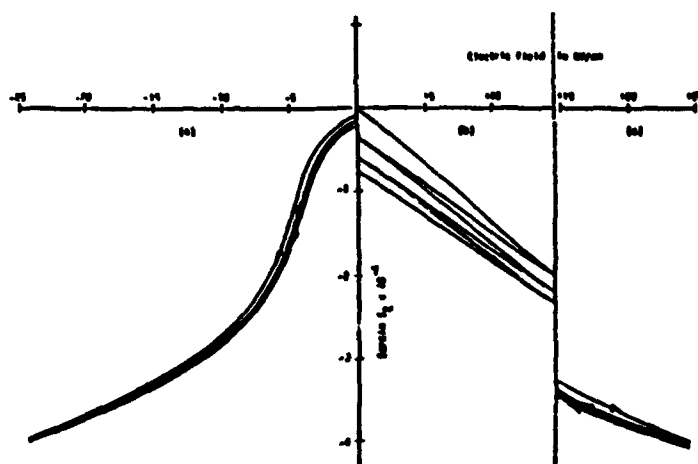


Fig. 7.19 Contrasting the non linear but repeatable strain response in a PMN:PT relaxor with the walk-off in zero field strain which occurs in a PZT 8 formulation.

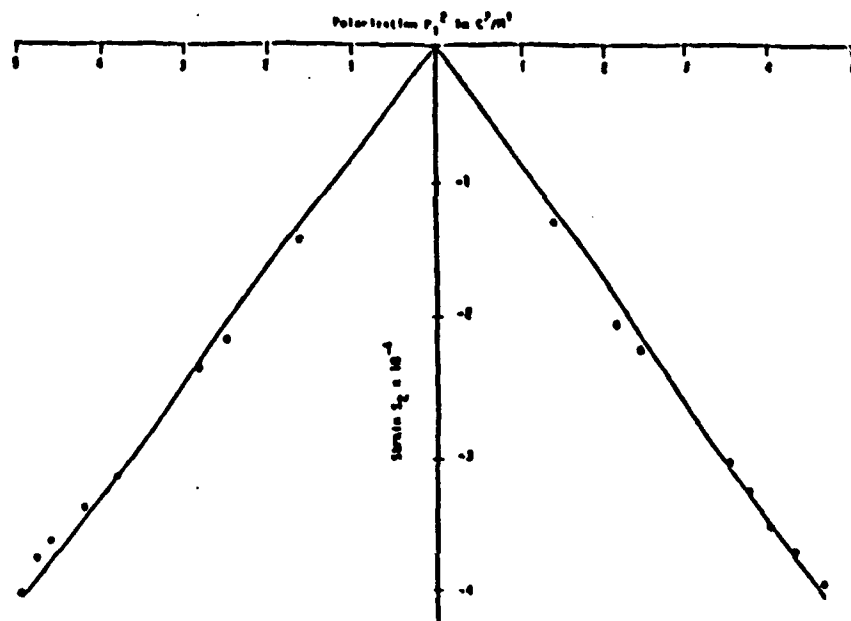


Fig. 7.20 Quadratic electrostrictive response in a PMN:10%PT actuator composition.

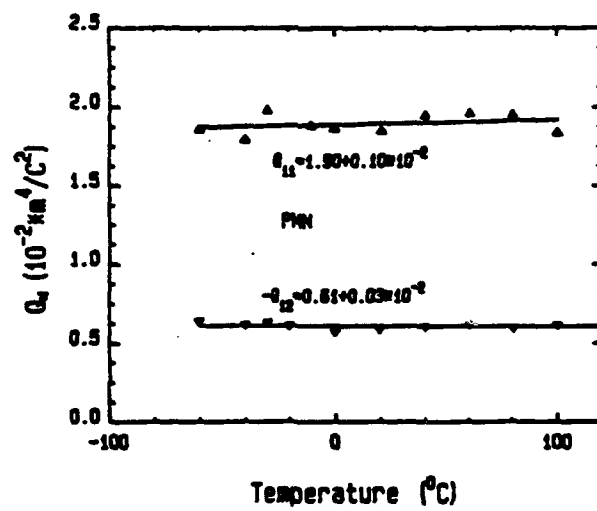


Fig. 7.21 Electrostriction constants  $Q_{11}$  and  $Q_{12}$  vs temperature in PMN:10% PT.

## 8.0 PIEZOELECTRIC COMPOSITES

Dielectric, piezoelectric and elastic properties of poled piezoelectric ceramics are tensor quantities and for many types of application it is possible to spell out a figure of merit for the material which often requires the enhancement of some of these tensor coefficients and the diminution of others.

A typical example is the requirement for sensing very weak hydrostatic pressure waves using large area sensors as in many Navy hydrophone needs (fig. 8.1). For hydrostatic pressure (fig. 8.2) the stress  $X_{11} = X_{22} = X_{33} = -p$ , so that the polarization change  $P_3$  is given by

$$\begin{aligned} P_3 &= d_{33}(-p) + d_{31}(-p) + d_{31}(-p) \\ &= (d_{33} + 2d_{31})(-p) \\ &= d_h(-p) \end{aligned}$$

where  $d_h$  is called the hydrostatic piezoelectric charge coefficient.

The voltage generated by the hydrophone, working into a very high impedance load will be given by

$$g_h = \frac{(d_{33} + 2d_{31})}{\epsilon_{33}}$$

and a figure of merit often used for hydrophone materials is the product  $d_h g_h$

$$d_h g_h = \frac{(d_{33} + 2d_{31})^2}{\epsilon_{33}}$$

For high sensitivity PZTs, there is an unfortunate near cancellation such that

$$d_{33} \approx -2d_{31}$$

so that  $d_h \ll d_{33}$  or  $d_{31}$ , and PZT alone is not a good hydrophone material.

In exploring composites for hydrophone applications it would be advantageous from the point of view of density and of flexibility to combine the ceramic with a dielectric polymer. Comparing the dielectric and elastic properties between two such phases, a fascinating juxtaposition is evident.

Dielectrically PZT is ultra soft ( $k \approx 3,000$ ) whilst the polymer is quite stiff ( $k \approx 10$ ) but in the elastic response, just the converse is true. The polymer is ultra soft ( $s_{11} \approx 30 \cdot 10^{-11} \text{M}^2/\text{N}$ ) but the ceramic is very stiff ( $s_{11} \approx 2 \cdot 10^{-11} \text{M}^2/\text{N}$ ) thus by careful control of the mode in which each phase is self-connected in the composite one can "steer" the fluxes and fields so as to enhance wanted coefficients and diminish unwanted coefficients so as to vastly improve the figure of merit.

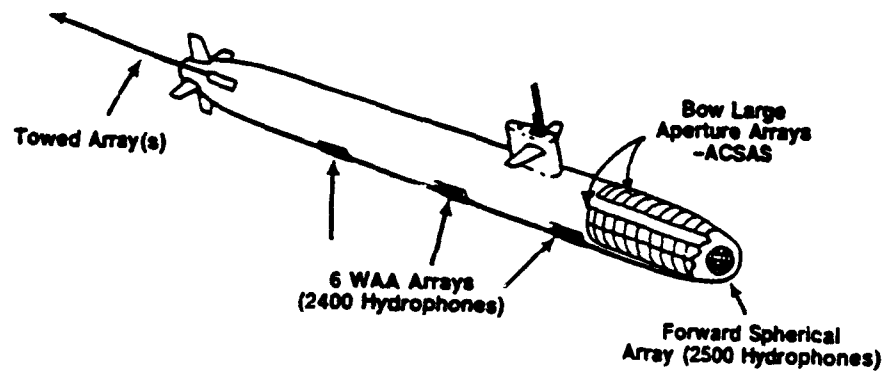


Fig. 8.1 Examples of the need for large area hydrophone sensors in submarine acoustics.

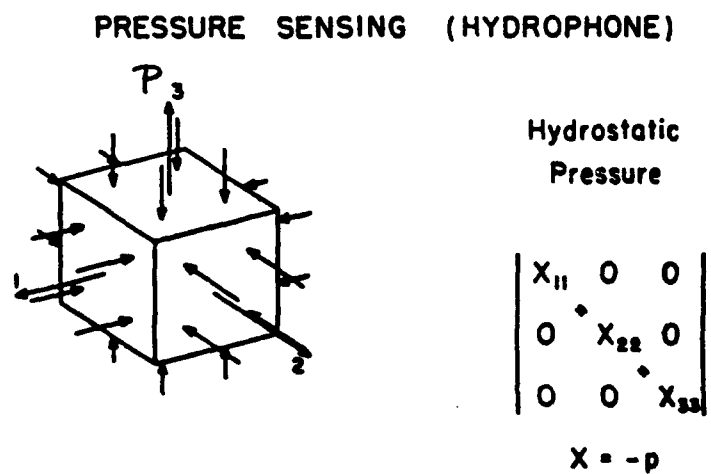
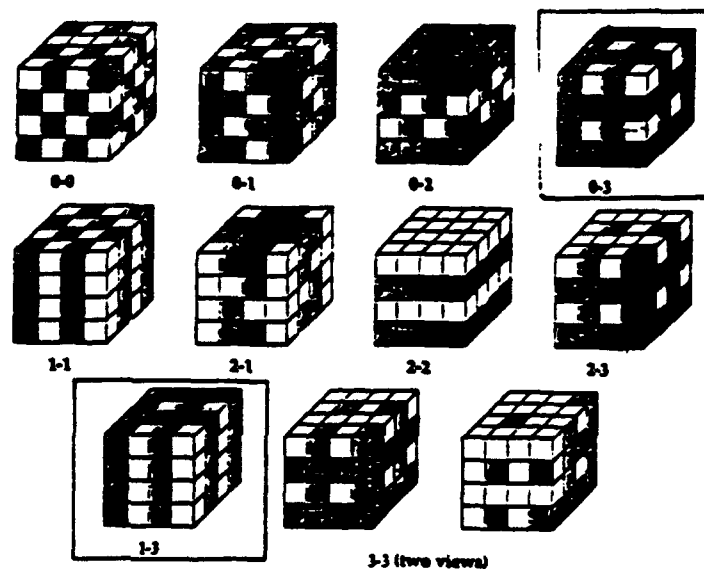


Fig. 8.2 Stress system seen by the transducer under hydrostatic conditions.

Over some 12 years of intensive effort to design effective composites three important basic principles have emerged.

- **Connectivity.** The mode of self interconnection of the phases controls the fluxes and fields in the system enabling a tailoring of the tensor coefficients.
- **Symmetry.** Both the symmetry of the individual component phases and the macro symmetry of their arrangement in the composite can be used for additional control.
- **Scale.** The mode of averaging for the property coefficients depends upon the scale of the composite phases in relation to the wavelength of excitation. Unusual resonances can occur when  $\lambda$  and  $d$  are comparable.

A major aid in thinking about the design of connectivity was the simple cubes model<sup>91</sup> (fig. 8.3) and the associated notation, now internationally accepted which describes the dimensionality of the connectivity for active and passive phases.



**Fig. 8.3** Simple 'cubes model' of connectivity patterns possible in a two phase piezoelectric ceramic polymer composite.

An indication of the many types of connectivities which have been used at Penn State for piezoceramic: polymer composites is shown in fig. 8.4 and a measure of the improvement in hydrophone figure of merit over pure PZT for some of these systems is shown in fig. 8.5.

The special case of the 1:2:3:0 composite which uses PZT rods in a foamed polymer matrix with transverse glass reinforcement is given in fig. 8.6.

For the 1:3 type composites a major impediment to evolution for large scale structures has been the problem of assembly. Recently Fiber Materials of Biddeford, Maine have applied their ultraloom (fig. 8.7) technology originally evolved for thick section carbon:carbon composites to this problem. Using the ultraloom they are able to stitch PZT posts into a template structure which contains the transverse glass fiber reinforcement (fig. 8.8) and make sections up to 4 feet in width and of almost any length.

The FMI composites are not only interesting for very large area hydrophones, but can also be used in an actuator mode. It is interesting to note that with only 5 vol% PZT and a resultant density of  $2.2 \text{ gm/cm}^3$  the transverse coupling coefficient  $k_t$  at 0.70 is larger than that of solid PZT (fig. 8.9).

The 1:3 type concept has also been applied to transducers for medical ultrasonics.<sup>92,93,94</sup> Here the required frequencies are much higher -10MHz so that the scale is very much smaller and the rod structure can be cut from solid PZT (fig. 8.10). Beam characteristics, pulse shape and coupling factor are improved over solid PZT transducers.

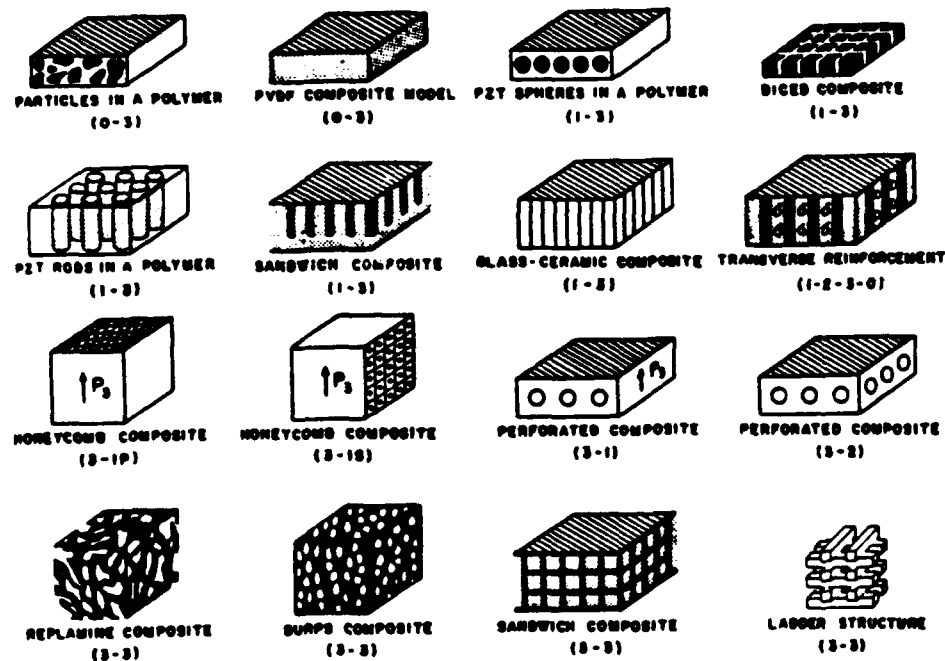


Fig. 8.4 Examples of composite structures with different engineered connectivities.

## COMPARISON OF $d_{33}$ OF VARIOUS COMPOSITES

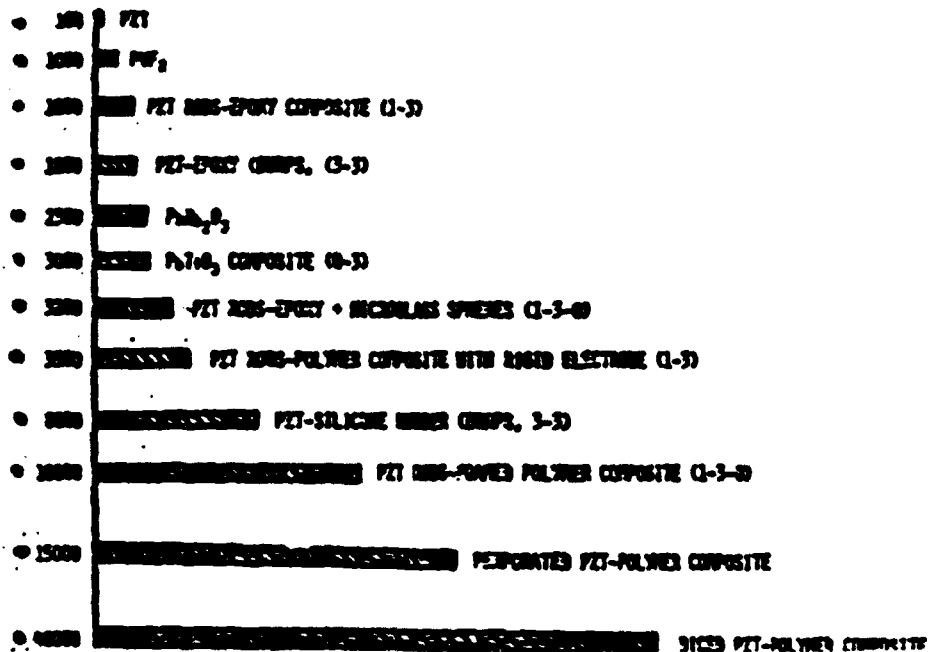


Fig. 8.5 Hydrostatic figures of merit achieved using different connectivities.

### SENSOR ENGINEERING IN ACTIVE COMPOSITES

#### NAVY HYDROPHONE

Up to 1075 Material had ultimate ultimate piezoelectric ceramic PZT

Power figure of merit  $d_{33}$

Product of hydrostatic voltage  $\times$  hydrostatic charge

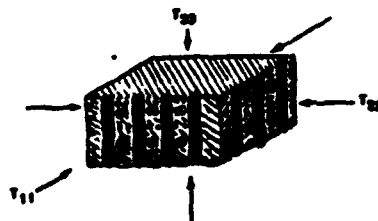
$$d_{33} \text{ in tensor form} = \frac{(d_{33} + 3d_{31})^2}{\epsilon_{33}}$$

$$d_{33} = 100 \cdot 10^{-15} \text{ m}^2/\text{N}$$

PROBLEM  $d_{33} = -3d_{31}$   $\epsilon_{33}$  very large

COMPOSITE SOLUTION

#### TRANSVERSE REINFORCEMENT (1-2-3-0)



$$\sigma = \begin{bmatrix} -T_{11} & 0 & 0 \\ 0 & -T_{22} & 0 \\ 0 & 0 & -T_{33} \end{bmatrix}$$

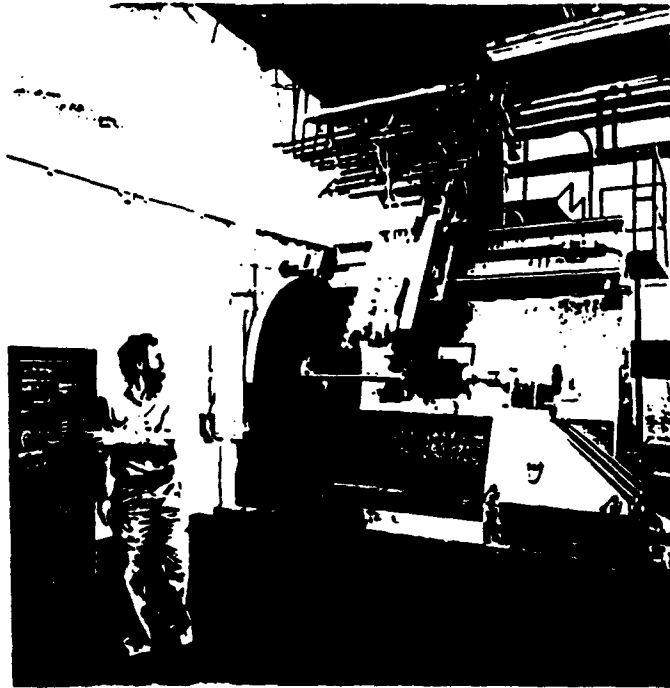
Taken up on transverse reinforcement  
Set used on PZT  
Polymer acts like a tent

$\epsilon_{33}$  much reduced by the polymer  
Composite is via PZT 60% rubber

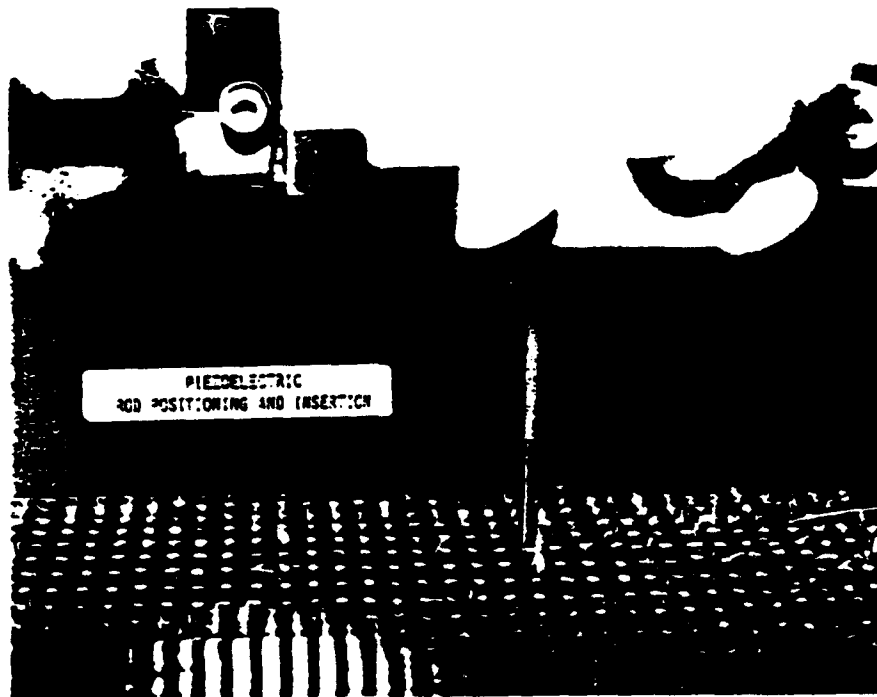
$$d_{33} = 100,000 \cdot 10^{-15} \text{ m}^2/\text{N}$$

Fig. 8.6 Figure of merit for a 1-2-3-0 transverse reinforced foamed polymer composite vs performance of pure PZT.





**Fig. 8.7** The Ultraloom three dimensional weaving machine used by FMI for 1:3 type composites.



**Fig. 8.8** PZT rod pattern in a transverse reinforced PZT:Epoxy composite undergoing fabrication of the Ultraloom at FMI Inc.

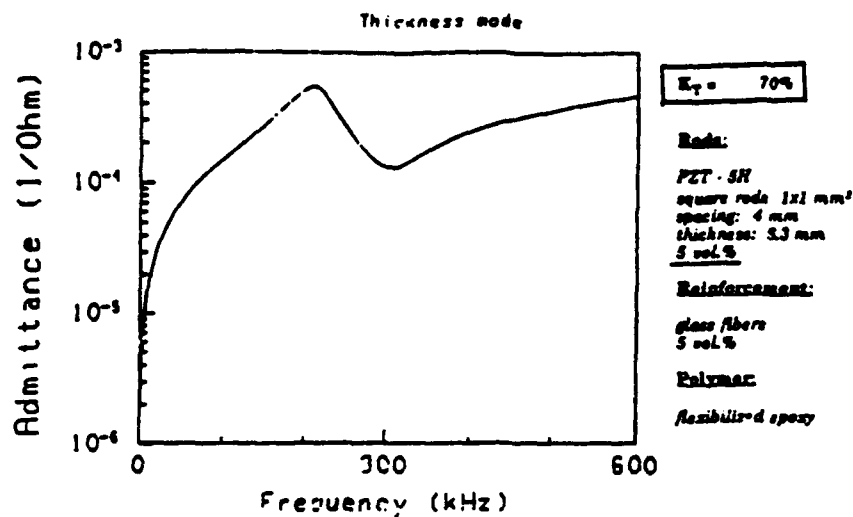


Fig. 8.9 Thickness resonance curve for an FMI 1:3 composite containing 5 vol% of PZT rods.

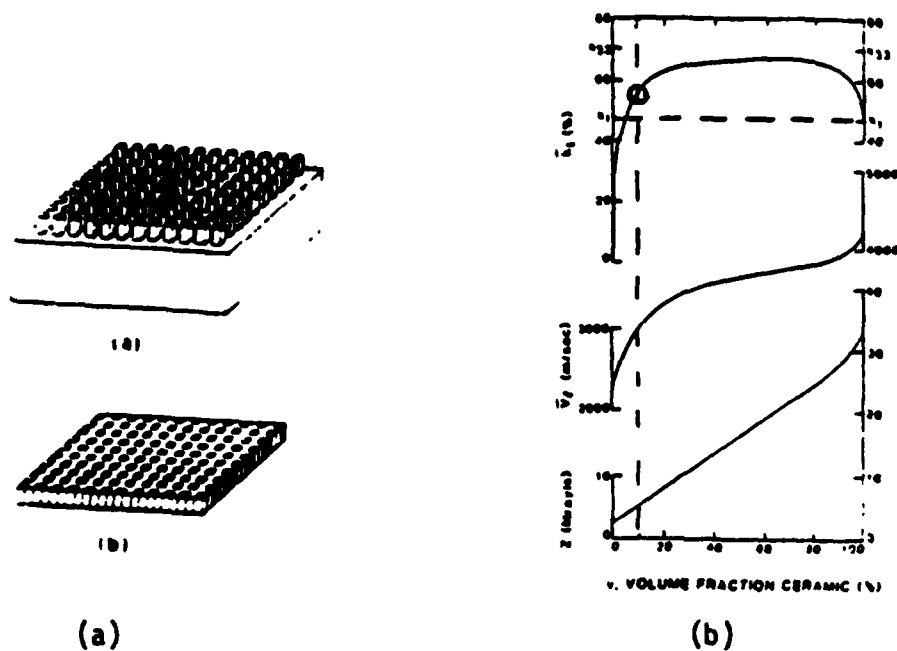


Fig. 8.10 Piezoceramic:Polymer composites applied to electromedical transduction.  
(a) The "dice and fill" method of construction.  
(b) Transverse coupling  $k_t$  of the composite as a function of volume fraction PZT.

## 9.0 PIEZOELECTRIC PROPERTIES OF THIN FILMS

In a perovskite structure ferroelectric in its tetragonal ferroelectric phase, symmetry  $4mm$ , the non zero intrinsic piezoelectric constants of the single domain are:

$$d_{31} = d_{32} = 2Q_{12}P_3\epsilon_{33}$$

$$d_{33} = 2Q_{11}P_3\epsilon_{33}$$

$$d_{15} = d_{24} = Q_{33}P_3\epsilon_{11}$$

where the  $Q_{ij}$  are the non zero electrostriction constants

$P_3$  is the spontaneous electric polarization.  
 $\epsilon_{ij}$  the components of the dielectric tensor.

For a bulk ceramic poled into conical symmetry (Curie group  $\infty mm$ ) we expect similar relations except that now the  $Q_{ij}$  are orientation averages, the  $P_3$  is now  $P_R$  and  $\epsilon_{33}$  is to be measured along the poling direction.

In the thin film it is probable that the  $Q$  constants are not significantly changed so that if we can achieve high values of  $P_R$  and of  $\epsilon_{33}$  we might expect strong piezoelectricity. Initial measurements of the change of film thickness under field, using the Penn State MRL optical ultradilatometer<sup>95,96</sup> show a clear piezoelectric effect (fig. 9.1). Measuring the slope of a sequence of strain: field curves like figure 9.1 at different DC bias levels a maximum

$$d_{33} = 217 \text{ pC/N (is recorded in fig. 9.2).}$$

For an undoped PZT of a similar 52/48 Zr:Ti composition

$$d_{33} = 223 \text{ pC/N.}$$

To measure  $d_{31}$ , since the film is firmly bonded to a platinum film on the silicon substrate, it was necessary to use a monomorph bending mode excited in a thin silicon strip. Again the measured deflections yield a value for

$$d_{31} = -88.7 \text{ pC/N (fig. 9.3).}$$

close to the value

$$d_{31} = -93.5 \text{ pC/N}$$

quoted for the 52:48 Zr:Ti undoped composition.

Taking values for the elastic constants  $s_{11}^E$ ,  $s_{33}^E$ ,  $s_{12}^E$  similar to the bulk ceramic it is then possible to derive the piezoelectric coupling coefficients

$$\begin{aligned} K_{33} &= 0.49 \\ K_{31} &= 0.22 \\ K_p &= 0.32. \end{aligned}$$

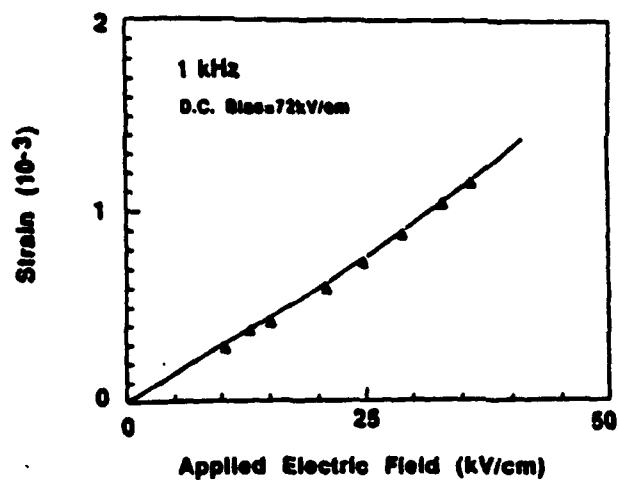


Fig. 9.1 Thickness strain  $x_3$  measured as a function of applied DC field

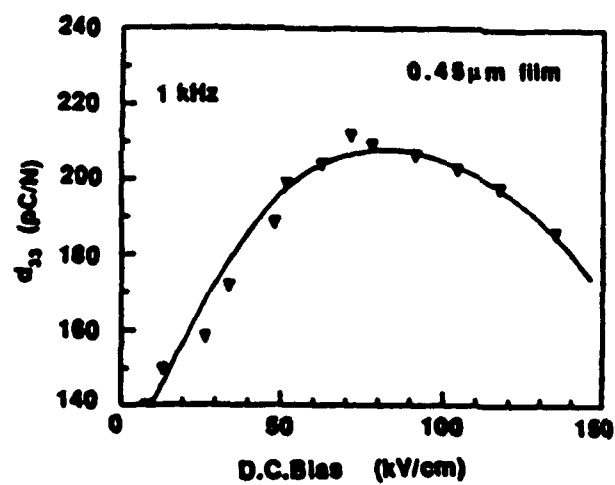
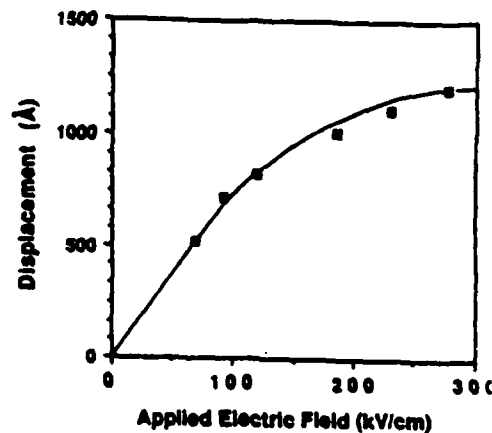


Fig. 9.2 Piezoelectric constant  $d_{33}$  as deduced from a sequence of strain:field curves such as 9.1 under different static bias field levels.



**Fig. 9.3** Strain measured from the flexure of a PZT 52/48 thin film monomorph on a silicon substrate.

As a preliminary exercise to explore the utility of the high piezoelectric constants and strong electromechanical coupling for PZT films on silicon we have cooperated with MIT and Lincoln Labs to demonstrate a piezoelectric flexure wave micro-motor.

The concept is shown schematically in fig. 9.4. The silicon wafer is coated with a thick ( $2\ \mu$  meters) silicon oxynitride film, then etched from the back side to define a window 2.5 mm square. Titanium bonded platinum electrode is deposited upon the upper surface and a 4,500 Å 52:48 PZT sol gel film is spun on and processed on the upper surface.

The upper electrode pattern 1 mm in diameter is plated onto the upper surface of the PZT using a photo-resist technique.

To examine the surface flexure wave generated by sine:cosine fields applied to the electrodes a 0.8 mm diameter glass lens was centered on the electrode pattern. With a field of 2 volts applied it was possible to generate stable rotation of the lens at a speed ~ 120 rpm. The experiment was in the nature of a proof of concept, and the system is now being redesigned to better locate the plattern and to improve the electrode geometry and dielectric perfection.

From observation of the acceleration of the glass lens on switching on the fields, we project that torques of the order  $10^{-9}$  Newton meters are realized even with this very primitive design. Such torques would not be unrealistic, given the high energy density and the strong coupling coefficient of the ferroelectric film.

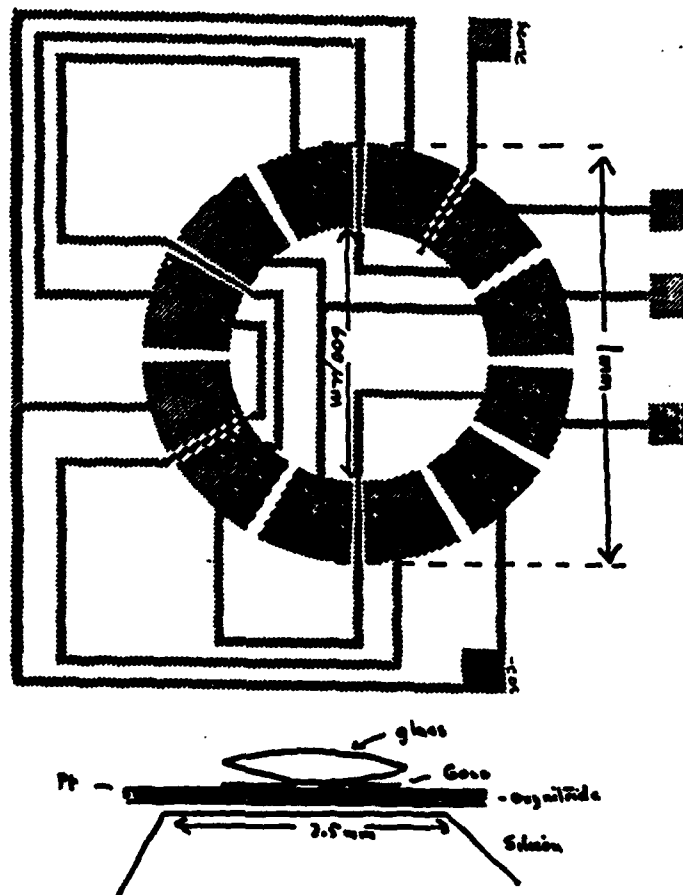


**Fig. 9.4** Schematic drawings of the electrode pattern for a PZT thin film micro-motor using a rotating flexure wave generated in a PZT film on a silicon oxy nitride diaphragm. The rotating wave has been demonstrated to rotate a small (0.8 mm) glass lens at ~120 rpm.

## REFERENCES

1. High Technology Ceramic News 2, 167, April 1990.
2. J. Herbert. **Ceramic Dielectrics and Capacitors, Electrocomponents Science Monographs**, Vol 6, Gordon Breach, London (1985).
3. E. R. Myers and Angus I. Kingon. **Ferroelectric Thin Films**, Materials Research Symposium Proceedings, San Fransisco, April 16, 20, ISSN 0272-9172, Vol. 200.
4. R. R. Tummala and E. J. Rymaszewski. **Microelectronics Packaging Handbook**, Van Nostrand, Reinhold, NY (1989).
5. L. M. Levinson. **Electronic Ceramics**, Marcel Decker, NY (1988).
6. C. A. Rosen. **Solid State Magnetic and Dielectric Devices**, chapter 5. John Wiley and Sons, NY (1959).
7. J. M. Herbert. **Ferroelectric Transducers and Sensors, Electrocomponent Science Monographs**, Vol. 3. Gordon and Breach, London (1985).
8. H. Jaffe and D. Berlincourt. *Proc. IEEE* 53, 1372 (1965).
9. R. E. Aldrich. *Ferroelectrics* 27, 19 (1980).
10. W. Y. Pan, C. Q. Dam, Q. M. Zhang and L. E. Cross. *J. Appl. Phys.* 66 (12), 6014 (1989).
11. S. G. Porter. *Ferroelectrics* 33, 193 (1981).
12. R. W. Whatmore, J. M. Herbert and F. W. Ainger. *Phys. Status Solidi A* 61, 73 (1980).
13. T. S. Liu. *Ferroelectrics* 10, 83 (1976).
14. R. Watton. *Proc. ISAF 86*, Lehigh University, 8 June 1986, p. 172.
15. B. Kazan. **Advances in Image Pickup and Display**, Academic Press, London (1977).
16. J. Daniels and K. H. Haerdil. *Philips Research Reports* 31, 489 (1976).
17. L. Hanke. *Siemens Forsch Ber.* 8.4, 209 (1979).
18. M. DiDomenico Jr. and S. H. Wemple. *J. Appl. Phys.* 40, 720 (1969).
19. P. Guenter. *Ferroelectrics* 24, 35 (1980).
20. C. J. Salvo. *IEEE Trans Electron Devices*, ED. 18, 748 (1971).
21. R. Alfness. *Proc. ISAF 86*, Lehigh University, 8 June 1986, pg. 1.
22. D. VanderLinde and A. M. Glass. *Appl. Phys.* 8, 85 (1975).
23. E. Wainer and S. Soloman. **Titanium Alloy Manufacturing Co. Reports 8-9** (September 1942).

24. S. Miyake and R. Vedral. *J. Phys. Soc. Jpn.* **1**, 32 (1946).
25. B. M. Wul and I. M. Goldman. *Dokl Akad Nauk SSSR* **46**, 154 (1945).
26. K. Wakino. *Early History of Barium Titanate Accessible through Murata Company*, Kyoto, Japan.
27. F. S. Galasso. *Structure, Properties and Preparation of Perovskite Type Compounds*, Pergamon Press, Oxford (1969).
28. Landolt Bornstein. *Ferroelectrics Oxides*, New Series III, Vol. 16a, Springer Verlag, Berlin (1981).
29. J. R. Oliver, R. R. Neurgaonkar and L. E. Cross. *J. Am. Ceram. Soc.* **72**, 202 (1989).
30. Landolt Bornstein. *Ferroelectric Oxides*, New Series III, Vol. 16a, Springer Verlag, Berlin (1981).
31. S. E. Cummins and L. E. Cross. *Appl. Phys. Lett.* **10**, 14 (1967).
32. E. C. Subbarao. *J. Phys. Chem. Solids* **23**, 665 (1962).
33. K. Aizu. *Phys. Rev.* **146**, 423 (1966).
34. K. Aizu. *Phys. Rev. B* **23**, 754 (1970).
35. K. Aizu. *J. Phys. Soc. Jpn.* **23**, 794 (1967).
36. L. A. Shuvalov. *J. Phys. Soc. Japan*, 28 Suppl, 38 (1970).
37. A. F. Devonshire. *Phil. Mag.* **740**, 1040 (1949).
38. A. F. Devonshire. *Phil. Mag.* **742**, 1065 (1951).
39. J. D. Axe. *Physics of Electronic Ceramics*, chapter 23. Marcel Dekker, NY (1972).
40. M. Glazer. *Acta Cryst* **B28**, 3384 (1972), *ibid* **A31**, 756 (1975).
41. K. Alexandrov. *Ferroelectrics* **14**, 801 (1976), *ibid* **20**, 61 (1978).
42. L. E. Cross and B. J. Nicholson. *Phil. Mag.* **46**, 452 (1955).
43. O. E. Fesenko, R. V. Kolesova and Yu G. Sindeyev. *Ferroelectrics* **20**, 177 (1978).
44. W. Merz. *Phys. Rev.* **91**, 513 (1953).
45. B. Jaffe, W. R. Cooke and H. Jaffe. *Piezoelectric Ceramics*, fig. 5.14. Academic Press, London (1971).
46. K. Kinoshita and A. Yamaji. *J. Appl. Phys.* **47**, 371 (1976).
47. J. Herbert. *Ceramic Dielectrics and Capacitors Electrocomponent Science Monographs*, Vol. 6. Gordon and Breach, London (1985).



48. A. Yamaji, Y. Enomoto, K. Kinoshita and T. Murakami. *J. Am. Ceram. Soc.* **60**, 97 (1977).
49. W. R. Buessem, L. E. Cross and A. K. Goswami. *J. Am. Ceram. Soc.* **49**, 33 (1966).
50. R. C. Pohanka, R. W. Rice and B. E. Walker, Jr. *J. Am. Ceram. Soc.* **59**, 71(1976).
51. G. Arlt, D. Hennings and G. deWith. *J. Appl. Phys.* **58**, 1619 (1985).
52. D. A. Payne. "The Role of Internal Boundaries Upon the Dielectric Properties of Polycrystalline Ferroelectric Materials." PhD Thesis, The Pennsylvania State University, March 1973.
53. D. A. Payne and L. E. Cross. *Microstructure - Property Relations for Dielectric Ceramics II*, Science Press, Beijing (1984).
54. M. P. Harmer, A. Bhalla, B. Fox and L. E. Cross. *Mat. Lett* **2** (4A), 178 (1984).
55. C. Randall, D. Barker, R. Whatmore and P. Groves. *Ferroelectrics* **76**, 277 (1987).
56. J. Chen. "Microstructure Property Relations in the Complex Perovskite Lead Magnesium Niobate," PhD Thesis, Lehigh University, March 1991.
57. L. E. Cross. *Ferroelectrics* **76**, 241 (1987).
58. P. Asadipour. "Polarization Mechanisms in Relaxor Ferroelectrics," MS Thesis, The Pennsylvania State University, May 1986.
59. D. Viehland. "The Glassy Polar Behaviour of Relaxor Ferroelectrics," PhD Thesis, The Pennsylvania State University, May 1991.
60. D. Viehland, S. J. Jang, L. E. Cross and M. Wuttig. *J. Appl. Phys.* **68** (6), 2916 (1991).
61. D. Viehland, S. J. Jang, L. E. Cross and M. Wuttig. *J. Appl. Phys.* **69** (1), 414 (1991).
62. J. DeAlmedia and D. Thouless. *J. Phys. A* **11**, 983 (1978).
63. H. J. Hagemann, D. Hennings and R. Wernicke. *Philips Tech. Rev.* **41** (3), 89 (1983).
64. J. Kato, Y. Yokotani, H. Kagata, H. Niwa. *Jpn. J. Appl. Phys.* **26**, 90 (1987).
65. H. Schwarz and A. Tourtellotte. *J. Vac. Sci. Tech.* Vol. **6**, 373 (1969).
66. V. P. Dudkevich, V. A. Bukreev, M. Mukhortov, I. Golovko, Yu G. Sindeev, M. Mukhortov, and G. Fesenko. *Phys. Stat. Sol. (a)* **65**, 463 (1981).
67. S. B. Krupanidhi, M. Maffei, M. Sayer and K. ElAssad. *J. Appl. Phys.* **54**, 6601 (1983).
68. S. K. Dey, K. D. Budd and D. A. Payne. *IEEE Trans. UFFC* **35**, 80 (1988).
69. S. Dey. Private Communication.
70. S. Dey. *Advance in Chemical Processing of Thin Films*, Arizona State University, April 1991.

71. R. Gerson and T. C. Marshall. *J. Appl. Phys.* **30**, 1650 (1959).
72. K. R. Udayakumar. To be published.
73. B. Jaffe, W. R. Cooke, Jr and H. Jaffee. *Piezoelectric Ceramics*, Academic Press, London (1971).
74. A. F. Devonshire. *Adv. in Physics* **3**, 85 (1954).
75. L. E. Cross. *Phil. Mag.*, Ser. 8 **1**, 76 (1956).
76. L. E. Cross. *J. Phys. Soc. Japan* **23**, 77 (1967).
77. A. Amin and L. E. Cross. *Ferroelectrics* **50**, 237 (1983).
78. T. R. Halemane, M. J. Haun, L. E. Cross and R. E. Newnham. *Ferroelectrics* **63**, 149 (1985).
79. A. Amin, M. J. Haun, B. Badger, H. McKinstry and L. E. Cross. *Ferroelectrics* **65**, 107 (1985).
80. M. J. Haun, T. R. Halemane, R. E. Newnham and L. E. Cross. *Japan J. Appl. Phys.* **24**, 209 (1985).
81. M. J. Haun, E. Furman, S. J. Jang and L. E. Cross. *Ferroelectrics* **99**, 13 (1989).
82. M. J. Haun, E. Furman, H. A. McKinstry and L. E. Cross. *Ferroelectrics* **99**, 27 (1989).
83. M. J. Haun, Z. Q. Zhuang, E. Furman, S. J. Jang and L. E. Cross. *Ferroelectrics* **99**, 45 (1989).
84. M. J. Haun, E. Furman, T. R. Halemane and L. E. Cross. *Ferroelectrics* **99**, 55 (1989).
85. M. J. Haun, E. Furman, S. J. Jang and L. E. Cross. *Ferroelectrics* **99**, 55 (1989).
86. R. Gerson, H. Jaffe. *J. Phys. Chem. Solids* **24**, 979 (1963).
87. R. Gerson. *J. Appl. Phys.* **31**, 188 (1960).
88. K. Carl and K. H. Hardtl. *Ferroelectrics* **17**, 472 (1978).
89. D. Dederichs and G. Arit. *Ferroelectrics* **68**, 281 (1986).
90. W. Y. Pan, T. R. Shrout and L. E. Cross. *J. Mat. Sci. Lett.* **8**, 771 (1989).
91. R. E. Newnham, D. P. Skinner and L. E. Cross. *Mat. Res. Bull.* **13**, 525 (1978).
92. A. A. Shaulov, M. E. Rosar, W. A. Smith and B. M. Singer. *Proc. ISAF 86*, Leigh University, 8 June 1986, p. 231.
93. T. R. Gururaja, W. A. Schulz, L. E. Cross and R. E. Newnham. *Proc. IEEE Ultrasonics Symp.*, 1984, pg. 523.

- 94. W. A. Smith. Proc. ISAF 86, p. 249, Lehigh University (8 June 1986).
- 95. Z. M. Zhang, W. Y. Pan and L. E. Cross. J. Appl. Phys. **63**, 2492 (1988).
- 96. W. Y. Pan and L. E. Cross. Rev. Sci. Inst. **60** (8), 2701 (1989).

## **APPENDIX 2**

## ADVANCED CERAMICS

Electronic ceramics, 601

Structural ceramics, 620

### ELECTRONIC CERAMICS

Electronic ceramics is a generic term describing a class of inorganic, nonmetallic materials utilized in the electronics industry. Although the term electronic ceramics, or electroceramics, includes amorphous glasses and single crystals, it generally pertains to polycrystalline inorganic solids comprised of randomly oriented crystallites (grains) intimately bonded together. This random orientation of small, micrometer-size crystals results in an isotropic ceramic possessing equivalent properties in all directions. The isotropic character can be modified during the sintering operation at high temperatures or upon cooling to room temperature by processing techniques such as hot pressing or poling in an electric or magnetic field (see CERAMICS AS ELECTRICAL MATERIALS).

The properties of electroceramics are related to their ceramic microstructure, ie, the grain size and shape, grain-grain orientation, and grain boundaries, as well as to the crystal structure, domain configuration, and electronic and defect structures. Electronic ceramics are often combined with metals and polymers to meet the requirements of a broad spectrum of high technology applications, computers, telecommunications, sensors (qv), and actuators. Roughly speaking, the multibillion dollar electronic ceramics market can be divided into six equal parts as shown in Figure 1. In addition to SiO<sub>2</sub>-based optical fibers and

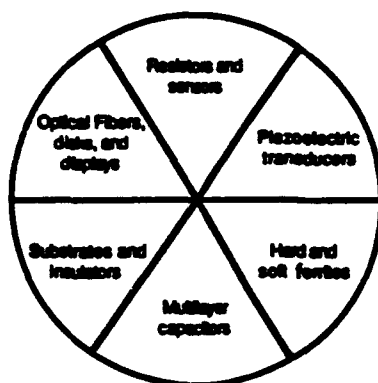


Fig. 1. Electronic ceramics market (1).

Table 1. Electronic Ceramic Functions and Products

Function	Material	Products <sup>a</sup>
insulators	porcelain, glass, steatite	high voltage insulation
packaging	Al <sub>2</sub> O <sub>3</sub> , BeO, AlN	IC substrates, packages (MMCs)
capacitors (energy storage)	BaTiO <sub>3</sub> , SrTiO <sub>3</sub> , TiO <sub>2</sub>	multilayer and barrier layer capacitors
piezoelectrics	Pb(Zr <sub>1-x</sub> Ti <sub>x</sub> )O <sub>3</sub> , SiO <sub>2</sub> (quartz)	vibrators, oscillators, filters, motors, and actuators
magnetics	Mn <sub>1-x</sub> Zn <sub>x</sub> Fe <sub>2</sub> O <sub>4</sub> , Ni <sub>1-x</sub> Zn <sub>x</sub> Fe <sub>2</sub> O <sub>4</sub>	inductors, transformers, memory devices
semiconductors	(Ba,Ln)TiO <sub>3</sub> , V <sub>2</sub> O <sub>5</sub> , Fe <sub>3-x</sub> Ti <sub>2</sub> O <sub>3</sub> , ZnO-Bi <sub>2</sub> O <sub>3</sub> , MgCr <sub>2</sub> O <sub>4</sub> -TiO <sub>2</sub> , CdS, SiC	PTC, NTC-thermistors, varistors, pH sensor, humidity sensor, solar cells, electric heater resistors (thick film), solid electrolytes, oxygen sensors, superconductors
conductors	RuO <sub>2</sub> , NaAl <sub>11</sub> O <sub>17</sub> , Zr <sub>1-2x</sub> Y <sub>2x</sub> O <sub>3-x</sub> , YBa <sub>2</sub> Cu <sub>3</sub> O <sub>7-δ</sub>	

<sup>a</sup>MMC = multicomponent components; PTC = positive temperature coefficient; NTC = negative temperature coefficient.

displays, electronic ceramics encompass a wide range of materials and crystal structure families (see Table 1) used as insulators, capacitors, piezoelectrics (qv), magnetics, semiconductor sensors, conductors, and the recently discovered high temperature superconductors. The broad scope and importance of the electronic ceramics industry is exemplified in Figure 2, which schematically displays electroceramic components utilized in the automotive industry. Currently, the growth of the electronic ceramic industry is driven by the need for large-scale integrated circuitry giving rise to new developments in materials and processes. The development of multilayer packages for the microelectronics industry, composed of multifunctional three-dimensional ceramic arrays called monolithic ceramics (MMC), continues the miniaturization process begun several decades ago to provide a new generation of robust, inexpensive products.

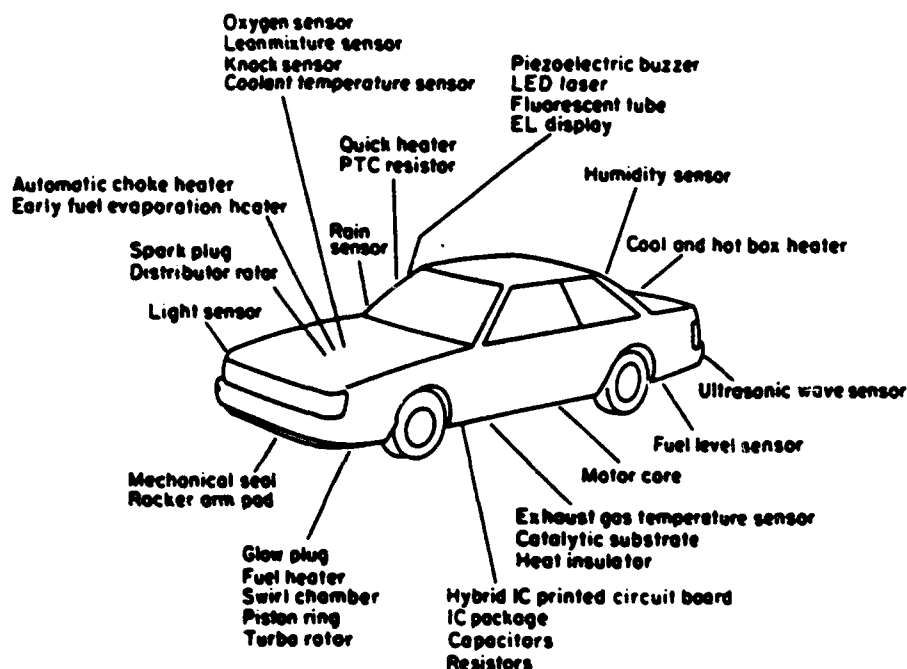


Fig. 2. Electronic ceramics for automotive applications. Courtesy of Nippon Denso, Inc.

### Structure-Property Relations

An overview of the atomistic and electronic phenomena utilized in electroceramic technology is given in Figure 3. More detailed discussions of compositional families and structure-property relationships can be found in other articles. (See, for example, FERROELECTRICS, MAGNETIC MATERIALS, and SUPERCONDUCTING MATERIALS.)

Multilayer capacitors, piezoelectric transducers, and positive temperature coefficient (PTC) thermistors make use of the ferroelectric properties of barium

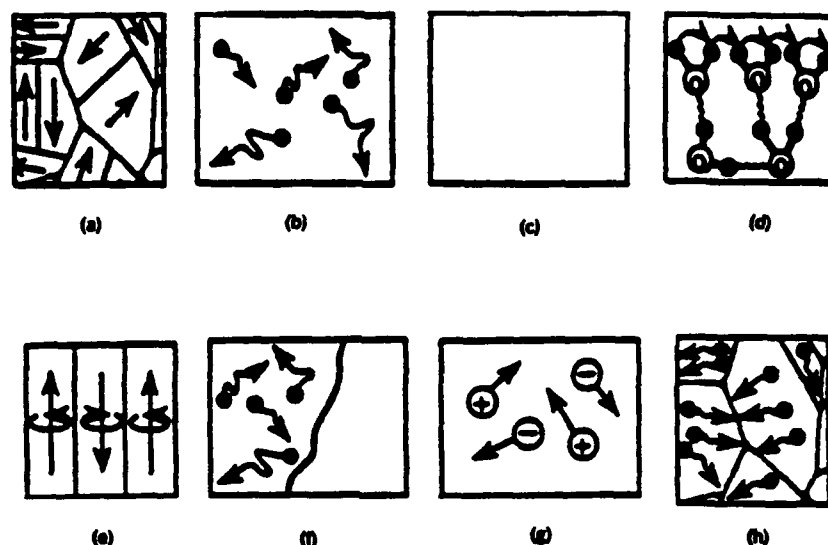


Fig. 3. An overview of atomistic mechanisms involved in electroceramic components and the corresponding uses: (a) ferroelectric domains: capacitors and piezoelectrics, PTC thermistors; (b) electronic conduction: NTC thermistor; (c) insulators and substrates; (d) surface conduction: humidity sensors; (e) ferrimagnetic domains: ferrite hard and soft magnets, magnetic tape; (f) metal-semiconductor transition: critical temperature NTC thermistor; (g) ionic conduction: gas sensors and batteries; and (h) grain boundary phenomena: varistors, boundary layer capacitors, PTC thermistors.

titanate (IV) [12047-27-7],  $\text{BaTiO}_3$ , and lead zirconate titanate [12626-81-2]. On cooling from high temperature, these ceramics undergo phase transformations to polar structures having complex domain patterns. Large peaks in the dielectric constant accompany the phase transitions where the electric dipole moments are especially responsive to electric fields. As a result, modified compositions of barium titanate (qv),  $\text{BaTiO}_3$ , are widely used in the multilayer capacitor industry and most piezoelectric transducers are made from lead zirconate titanate,  $\text{PbZr}_{1-x}\text{Ti}_x\text{O}_3$ , (PZT) ceramics. Applying a large dc field (poling) aligns the domains and makes the ceramic piezoelectric. The designation PZT is a registered trademark of Vernitron, Inc.

Similar domain phenomena are observed in ferrimagnetic oxide ceramics such as manganese ferrite [12063-10-4],  $\text{MnFe}_2\text{O}_4$ , and  $\text{BaFe}_{11}\text{O}_{17}$ , but the underlying mechanism is different. The unpaired spins of  $\text{Fe}^{3+}$  and  $\text{Mn}^{2+}$  ions give rise to magnetic dipole moments which interact via neighboring oxygen ions through a super-exchange mechanism. The magnetic dipoles are randomly oriented in the high temperature paramagnetic state, but on cooling through the Curie temperature,  $T_C$ , align to form magnetic domains within the ceramic grains. The peak in the magnetic permeability at  $T_C$  is analogous to the peak in the dielectric constant of ferroelectric ceramics. Domain walls move easily in soft ferrites (qv) like  $\text{MnFe}_2\text{O}_4$  and  $\gamma\text{-Fe}_2\text{O}_3$ , which are used in transformers and magnetic tape. In barium ferrite [11138-11-7], the spins are firmly locked to the hexagonal axis, making it useful as a permanent magnet.



Several kinds of conduction mechanisms are operative in ceramic thermistors, resistors, varistors, and chemical sensors. Negative temperature coefficient (NTC) thermistors make use of the semiconducting properties of heavily doped transition metal oxides such as  $n$ -type  $\text{Fe}_{2-x}\text{Ti}_x\text{O}_3$  and  $p$ -type  $\text{Ni}_{1-x}\text{Li}_x\text{O}$ . Thick film resistors are also made from transition-metal oxide solid solutions. Glass-bonded  $\text{Bi}_{2-2x}\text{Pb}_{2x}\text{Ru}_2\text{O}_{7-x}$  having the pyrochlore [12174-36-6] structure is typical.

Phase transitions are involved in critical temperature thermistors. Vanadium,  $\text{VO}_2$ , and vanadium trioxide [1314-34-7],  $\text{V}_2\text{O}_3$ , have semiconductor-metal transitions in which the conductivity decreases by several orders of magnitude on cooling. Electronic phase transitions are also observed in superconducting ceramics like  $\text{YBa}_2\text{Cu}_3\text{O}_{7-x}$ , but here the conductivity increases sharply on cooling through the phase transition.

Ionic conductivity is used in oxygen sensors and in batteries (qv). Stabilized zirconia,  $\text{Zr}_{1-x}\text{Ca}_x\text{O}_{2-x}$ , has a very large number of oxygen vacancies and very high  $\text{O}^{2-}$  conductivity.  $\beta$ -Alumina [12005-48-0],  $\text{NaAl}_{11}\text{O}_{17}$ , is an excellent cation conductor because of the high mobility of  $\text{Na}^+$  ions. Ceramics of  $\beta$ -alumina are used as the electrolyte in sodium-sulfur batteries.

Surface conduction is monitored in most humidity sensors through the use of porous ceramics of  $\text{MgCr}_2\text{O}_4$ - $\text{TiO}_2$  that adsorb water molecules which then dissociate and lower the electrical resistivity.

Grain boundary phenomena are involved in varistors, boundary layer capacitors, and PTC thermistors. The formation of thin insulating layers between conducting grains is crucial to the operation of all three components. The reversible electric breakdown in varistors has been traced to quantum mechanical tunneling through the thin insulating barriers. In a  $\text{BaTiO}_3$ -PTC thermistor, the electric polarization associated with the ferroelectric phase transition neutralizes the insulating barriers, causing the ceramic to lose much of its resistance below  $T_C$ . Boundary layer capacitors have somewhat thicker barriers which cannot be surmounted, and hence the ceramic remains an insulator. However, the movement of charges within the conducting ceramic grains raises the dielectric constant and increases the capacitance.

Lastly, the importance of electroceramic substrates and insulators should not be overlooked. Here one strives to raise the breakdown strength by eliminating the interesting conduction mechanisms just described. Spark plugs, high voltage insulators, and electronic substrates and packages are made from ceramics like alumina, mullite [55964-99-3], and porcelain [1332-58-7].

### Electroceramic Processing

Fabrication technologies for all electronic ceramic materials have the same basic process steps, regardless of the application: powder preparation, powder processing, green forming, and densification.

**Powder Preparation.** The goal in powder preparation is to achieve a ceramic powder which yields a product satisfying specified performance standards. Examples of the most important powder preparation methods for electronic ceramics include mixing/calcination, coprecipitation from solvents, hydro-

thermal processing, and metal organic decomposition. The trend in powder synthesis is toward powders having particle sizes less than 1  $\mu\text{m}$  and little or no hard agglomerates for enhanced reactivity and uniformity. Examples of the four basic methods are presented in Table 2 for the preparation of  $\text{BaTiO}_3$  powder. Reviews of these synthesis techniques can be found in the literature (2,5).

The mixing of components followed by calcination to the desired phase(s) and then milling is the most widely used powder preparation method (2). Mixing/calcination is straightforward, and in general, the most cost effective use of capital equipment. However, the high temperature calcination produces an agglomerated powder which requires milling. Contamination from grinding media and mill lining in the milling step can create defects in the manufactured product in the form of poorly sintered inclusions or undesirable compositional modification. Furthermore, it is difficult to achieve the desired homogeneity, stoichiometry, and phases for ceramics of complex composition.

Coprecipitation is a chemical technique in which compounds are precipitated from a precursor solution by the addition of a precipitating agent, for example, a hydroxide (5). The metal salt is then calcined to the desired phase. The advantage of this technique over mixing/calcination techniques is that more intimate mixing of the desired elements is easily achieved, thus allowing lower calcination temperatures. Limitations are that the calcination step may once again result in agglomeration of fine powder and the need for milling. An additional problem is that the ions used to provide the soluble salts (eg, chloride from metal chlorides) may linger in the powder after calcination, affecting the properties in the sintered material.

Hydrothermal processing uses hot (above 100°C) water under pressure to produce crystalline oxides (6). This technique has been widely used in the formation process of  $\text{Al}_2\text{O}_3$  (Bayer Process), but not yet for other electronic powders. The situation is expected to change, however. The major advantage of the hydrothermal technique is that crystalline powders of the desired stoichiometry and phases can be prepared at temperatures significantly below those required for calcination. Another advantage is that the solution phase can be used to keep the particles separated and thus minimize agglomeration. The major limitation of hydrothermal processing is the need for the feedstocks to react in a closed system to maintain pressure and prevent boiling of the solution.

Metal organic decomposition (MOD) is a synthesis technique in which metal-containing organic chemicals react with water in a nonaqueous solvent to produce a metal hydroxide or hydrous oxide, or in special cases, an anhydrous metal oxide (7). MOD techniques can also be used to prepare nonoxide powders (8,9). Powders may require calcination to obtain the desired phase. A major advantage of the MOD method is the control over purity and stoichiometry that can be achieved. Two limitations are atmosphere control (if required) and expense of the chemicals. However, the cost of metal organic chemicals is decreasing with greater use of MOD techniques.

**Powder Processing.** A basic guideline of powder manufacturing is to do as little processing as possible to achieve the targeted performance standards (see POWDERS, HANDLING). Ceramic powder fabrication is an iterative process during which undesirable contaminants and defects can enter into the material at any stage. Therefore, it is best to keep the powder processing scheme as simple as

Table 2. Methods Used to Prepare BaTiO<sub>3</sub> Electronic Ceramic Powders

Method	Reaction	Particle size
mixing/calcination <sup>a</sup>	$\text{BaCO}_3 + \text{TiO}_2 \xrightarrow{\Delta T} \text{BaTiO}_3 + \text{CO}_2\uparrow$	1 $\mu\text{m}$ to 100s of $\mu\text{m}$
coprecipitation <sup>b</sup>	$\text{Ba}^{2+} + \text{TiO}^{2+} + 2 \text{C}_2\text{O}_4^{2-} \xrightarrow{\text{H}_2\text{O}} \text{BaTi}(\text{C}_2\text{O}_4)_2 \cdot 4\text{H}_2\text{O} \xrightarrow{\Delta T}$ $\text{BaTiO}_3 + 4 \text{H}_2\text{O}\uparrow + 4 \text{CO}_2\uparrow$	if calcined, mean size of $\approx 0.5 \mu\text{m}$ after milling
hydrothermal <sup>c</sup>	$\text{Ba}^{2+} + \text{TiO}_2 + \text{H}_2\text{O} \xrightarrow[\Delta T, \text{pH}]{\text{OH}^-} \text{BaTiO}_3 + 2 \text{H}_2\text{O}$	nanosize to 60 $\mu\text{m}$
metal organic decomposition <sup>c</sup>	$\text{Ba}(i\text{-OC}_3\text{H}_7)_2 + \text{Ti}(\text{OC}_4\text{H}_9)_4 + 3 \text{H}_2\text{O} \rightarrow \text{BaTiO}_3 + 2 \text{C}_3\text{H}_7\text{OH} + 4 \text{C}_4\text{H}_9\text{OH}$	5.0–35.0 nm, depending upon calcination conditions

<sup>a</sup>Ref. 2.

<sup>b</sup>Ref. 3.

<sup>c</sup>Ref. 4.

possible to maintain flexibility. Uncontrollable factors such as changes in the characteristics of as-received powders must be accommodated in the processing from batch to batch of material. Keeping the processing simple is not always possible: the more complex the material system, the more complex the processing requirements.

A fundamental requirement in powder processing is characterization of the as-received powders (10-12). Many powder suppliers provide information on tap and pour densities, particle size distributions, specific surface areas, and chemical analyses. Characterization data provided by suppliers should be checked and further augmented where possible with in-house characterization. Uniaxial characterization compaction behavior, in particular, is easily measured and provides data on the nature of the agglomerates in a powder (13,14).

Milling is required for most powders, either to reduce particle size or to aid in the mixing of component powders (15). Commonly employed types of comminution include ball milling, and vibratory, attrition, and jet milling, each possessing advantages and limitations for a particular application. For example, ball milling is well-suited to powder mixing but is rather inefficient for comminution.

**Green Forming.** Green forming is one of the most critical steps in the fabrication of electronic ceramics. The choice of green forming technique depends on the ultimate geometry required for a specific application. There are many different ways to form green ceramics, several of which are summarized in Table 3. Multilayer capacitors require preparation and stacking of two-dimensional ceramic sheets to obtain a large capacitance in a small volume. Techniques used to prepare two-dimensional sheets of green ceramic, including tape casting, (16-22) are discussed later under processing of multilayer ceramics. Manufacturing methods for ceramic capacitors have been reviewed (23).

**Table 3. Green Forming Procedures for Electronic Ceramics**

Green forming method	Geometries	Applications
uniaxial pressing	disks, toroids, plates	disk capacitors, piezo transducers, magnets
cold isostatic pressing	complex and simple	spark plugs, $ZrO_2-O_2$ sensors
colloidal casting	complex shapes	crucibles, porcelain insulators
extrusion	thin sheets ( $> 80 \mu m$ ), rods, tubes, honeycomb substrates	substrates, thermocouple insulator, catalytic converters, PTC thermistor heaters
injection molding	small complex shapes ( $< 1.0$ cm)	$ZrO_2-O_2$ sensors

Uniaxial pressing is the method most widely used to impart shape to ceramic powders (24). Binders, lubricants, and other additives are often incorporated into ceramic powders prior to pressing to provide strength and assist in particle compaction (25). Simple geometries such as rectangular substrates for integrated circuit (IC) packages can be made by uniaxial pressing (see INTEGRATED CIRCUITS).

More complex shapes can be made by cold isostatic pressing (CIP). CIP uses deformable rubber molds of the required shape to contain the powder. The application of isostatic pressure to the mold suspended in a pressure transfer media, such as oil, compacts the powder. CIP is not as easily automated as uniaxial pressing, but has found wide application in the preparation of more complex shapes such as spark plug insulators (26).

Slip or colloidal casting has been used to make complex shapes in the whiteware industry for many years (24). Other work has shown that colloidal casting can be used to produce electronic ceramic materials having outstanding strength because hard agglomerates can be eliminated in the suspension processing (27-29). Colloidal casting uses a porous mold in which the fine particles in a colloidal suspension accumulate because of capillary forces at the wall surface of the mold. Relatively dense packing of the particles, to approximately 60% of theoretical density, can be achieved. More importantly, hard aggregates can be eliminated from the colloid by suitable powder selection and processing. Drying of the resulting material may not be trivial and sections greater than about ~1.25 cm thick are sometimes difficult to obtain.

In addition to being the preferred forming technique for ceramic rods and tubes, extrusion processes are used to fabricate the thick green sheets used in many electronic components (24,30,31). The smallest thickness for green sheets prepared by extrusion techniques is about 80  $\mu\text{m}$ . Organic additives similar to those used in tape casting are employed to form a high viscosity plastic mass that retains its shape when extruded. The extrusion apparatus, schematically shown in Figure 4, consists of a hopper for introduction of the plasticized mass, a de-airing chamber, and either a screw-type or plunger-type transport barrel in which the pressure is generated for passage of the plastic mass through a die of the desired geometry. The plastic mass is extruded onto a carrier belt and passed through dryers to relax the plastic strain remaining after extrusion. The green sheet can be stamped or machine diced to form disks, wafers, or other platelike shapes.

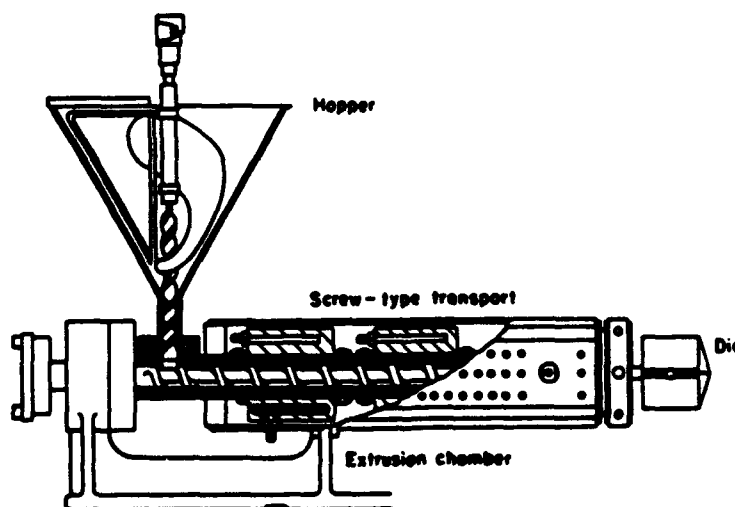


Fig. 4. Schematic of extrusion type apparatus for green sheet fabrication.

Injection molding is particularly suited to mass production of small complex shapes with relatively small ( $<1.0$  cm) cross sections (32-34). Powders are mixed using thermoplastic polymers and other organic additives. A molten mass composed of the ceramic and a thermoplastic binder system are injected via a heated extruder into a cooled mold of desired shape. The organic is burned out and the ceramic consolidated. Machining fragments from the green ceramic can be recycled because the thermoplastic polymers can be reversibly heated. Molds can be relatively expensive so injection molding is best suited to the preparation of a large number of single parts. Because of the high organic content required, organic removal is not trivial. Green sections greater than 1.0 cm thick require slow heating rates during burnout to avoid bloating and delamination of the green ceramic.

**Densification.** Densification generally requires high temperatures to eliminate the porosity in green ceramics. Techniques include pressureless sintering, hot-pressing, and hot isostatic pressing (HIP). Pressureless sintering is the most widely used because of ease of operation and economics. Hot-pressing is limited to relatively simple shapes whereas more complex shapes can be consolidated using HIP (35). Sintering is used for most oxide electronic ceramics. Hot-pressing and HIP, which employ pressure and high temperatures, are used to consolidate ceramics in which dislocation motion (leading to pore elimination) is sluggish. Both techniques are particularly useful for nonoxide materials such as silicon nitride [12033-89-5] and silicon carbide [409-21-2] (35,36) (see CARBIDES; NITRIDES).

Special precautions are often used in the sintering of electronic ceramics. Heating rates and hold times at maximum temperature are critical to microstructural development and grain size control. Sintering cycles may include intermediate temperature annealing or controlled cooling to relieve residual strains or avoid deleterious phase transformations. Atmosphere control may be important to prevent loss of volatile components or avoid reduction reactions. In continuous production, sequential burnout (organics) and sintering may take place in the same furnace, requiring complex temperature cycles even for relatively simple devices. Complex devices such as thick film circuits and monolithic multi-component ceramics may require many sequential fabrication and sintering steps.

### Processing of Multilayer Ceramics

Rapid advances in integrated circuit technology have led to improved processing and manufacturing of multilayer ceramics (MLC) especially for capacitors and microelectronic packages. The increased reliability has been the result of an enormous amount of research aimed at understanding the various microstructural-property relationships involved in the overall MLC manufacturing process. This includes powder processing, thin sheet formation, metallurgical interactions, and testing.

Presently, multilayer capacitors and packaging make up more than half the electronic ceramics market. For multilayer capacitors, more than 20 billion units are manufactured a year, outnumbering by far any other electronic ceramic component. Multilayer ceramics and hybrid packages consist of alternating layers of dielectric and metal electrodes, as shown in Figures 5 and 6, respectively.

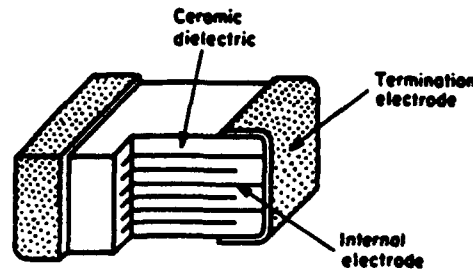


Fig. 5. Schematic cross section of a conventional MLC capacitor.

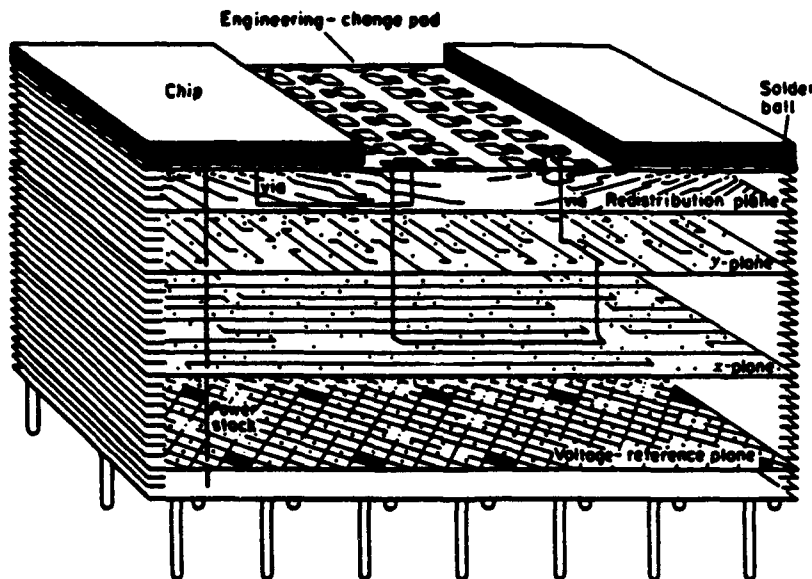


Fig. 6. Schematic of a MLC substrate for microelectronic packaging (37).

The driving force for these compact configurations is miniaturization. For capacitors, the capacitance ( $C$ ) measured in units of farads,  $F$ , is

$$C = \frac{\epsilon_0 AK}{t}$$

where  $K$  is the dielectric constant (unitless);  $\epsilon_0$  the permittivity of free space =  $8.85 \times 10^{-12} \text{ F/m}$ ;  $A$  the electrode area,  $\text{m}^2$ ; and  $t$  the thickness of dielectric layer,  $\text{m}$ . Thus  $C$  increases with increasing area and number of layers and decreasing thickness. Typical thicknesses range between 15 and 35  $\mu\text{m}$ . Similarly, for substrate packages, the multilayer configuration incorporates transversely integrated conductor lines and vertical conducting paths (vias) allowing for numerous interconnects to components throughout the device system and power distribution in a relatively small space. MLC substrates capable of providing 12,000 electrical connections containing 350,000 vias are currently manufactured (38,39).

A number of processing steps, shown in Figure 7, are used to obtain the multilayer configuration(s) for the ceramic-metal composites. The basic process steps are slip preparation, green tape fabrication, via-hole punching (packages), printing of internal electrodes or metallization, stacking and laminating, dicing or dimensional control, binder burnout, sintering, end termination, and encapsulation. After each processing step, quality control in the form of nondestructive physical and electrical tests ensures a uniform end-product.

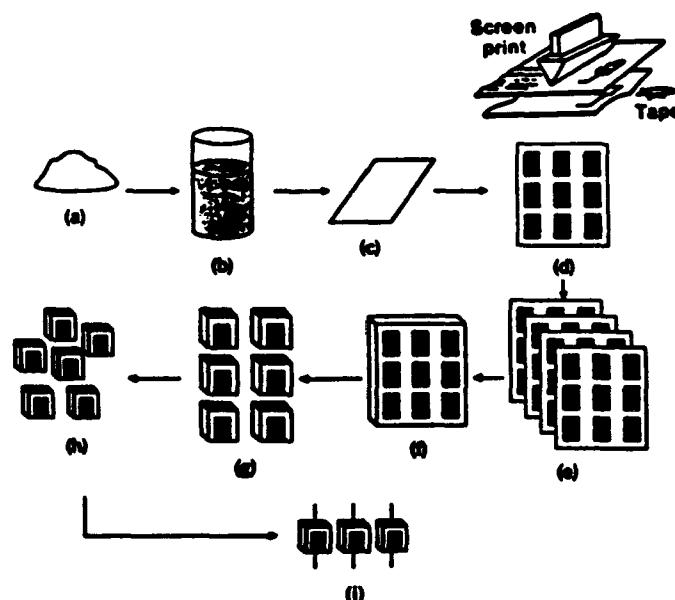


Fig. 7. Fabrication process for MLC capacitors. Steps are (a) powder; (b) slurry preparation; (c) tape preparation; (d) electroding; (e) stacking; (f) lamination; (g) dicing; (h) burnout and firing; and (i) termination and lead attachment.

The basic building block, the ceramic green sheet, starts using a mixture of dielectric powder suspended in an aqueous or nonaqueous liquid system or vehicle comprised of solvents, binders, plasticizers, and other additives to form a slip that can be cast in thin, relatively large area sheets. The purpose of the binder (20,000–30,000 molecular weight polymers) is to bind the ceramic particles together to form flexible green sheets. Electrodes are screened on the tape using an appropriate paste of metal powders. Solvents play a number of key roles, ranging from deagglomeration of ceramic particles to control the viscosity of the cast slip, to formation of microporosity in the sheet as the solvent evaporates. Plasticizers, ie, small to medium sized organic molecules, decrease cross-linking between binder molecules, imparting greater flexibility to the green sheet. Dispersants, typically 1,000 to 10,000 molecular weight polymer molecules, are added to slips to aid in the de-agglomeration of powder particles, allowing for higher green densities in the cast tape. Several review articles on the functional additives in tape cast systems are available (16,17,25,40–44). The resulting slip should have pseudoplastic rheological behavior so that the slip flows during high shear rate



casting operations, but displays little or no flow afterward, thus maintaining tape dimension (45).

There are several methods to make large ceramic sheets for MLC manufacturing (17-23). The methods include glass, belt and carrier film casting, and wet lay down techniques. The relative advantages and limitations of each technique have been reviewed (46). The two most commonly employed techniques, belt casting and doctor blading, are depicted schematically in Figure 8.

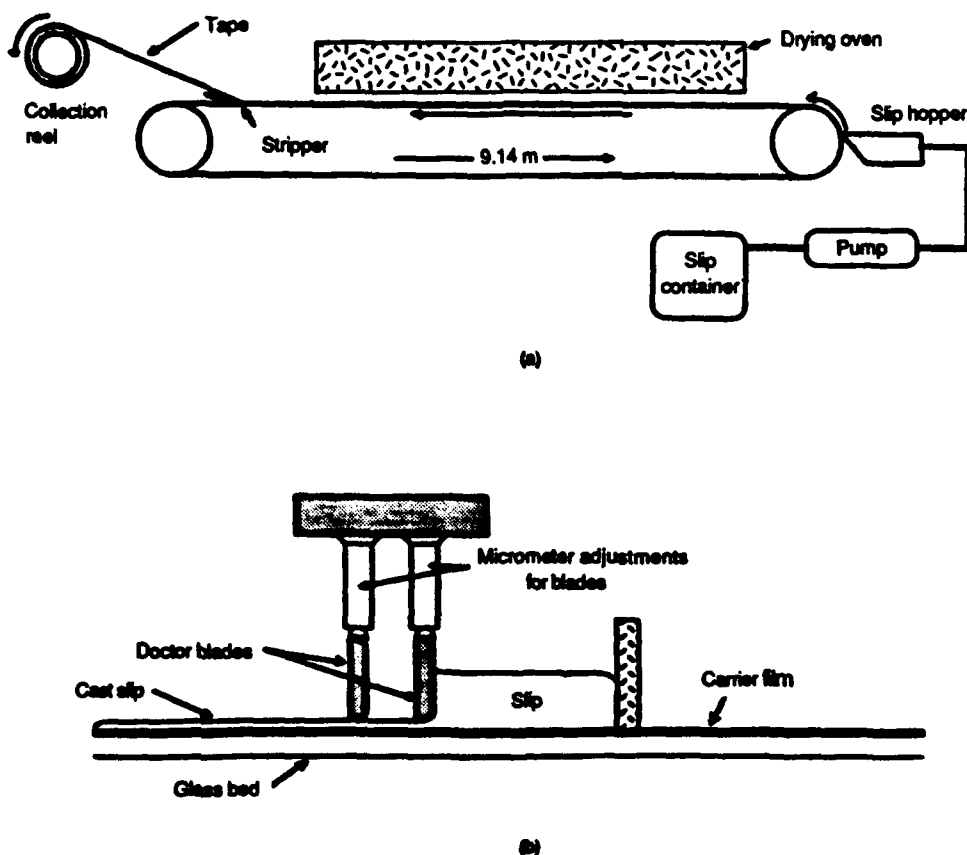


Fig. 8. Schematic of methods for MLC manufacturing; (a) belt casting; (b) carrier film casting using a doctor blade.

Metallization of the green sheets is usually carried out by screen printing, whereby a suitable metal ink consisting of metal powders dispersed in resin and solvent vehicles is forced through a patterned screen. Palladium [7440-05-3] and silver-palladium (Ag-Pd) alloys are the most common form of metallization; tungsten [7440-33-7] and molybdenum [7439-98-7] are used for high ( $>1500^{\circ}\text{C}$ ) temperature MLCs (47-52). Following screening, the metallized layers are stacked and laminated to register (align) and fuse the green sheets into a monolithic component. Proper registration is crucial to achieve and maintain capaci-

tance design (MLC capacitors) and for proper via-hole placement in MLC packages.

Sintering is the most complex process in MLC fabrication. Ideally, the binder burnout and sintering steps are performed during the same temperature cycle and in the same atmosphere. Most binders burn out by 500°C, well before pore closure in the densification of most ceramics. Sintering behavior of the many different MLC components must be reconciled to achieve a dense material. Internal metallization and the dielectric must co-fire in a single process. Firing temperatures are related to material composition and can be adjusted using additives. Densification rates are related both to the process temperature and to particle characteristics (size, size distribution, and state of agglomeration). Thus, the burnout and sintering conditions depend heavily on the system.

After densification, external electrode termination and leads are attached for MLC capacitor components, and pin module assembly and IC chip joining is carried out for MLC packages. The devices are then tested to ensure performance and overall reliability.

### Thick Film Technology

Equally important as tape casting in the fabrication of multilayer ceramics is thick film processing. Thick film technology is widely used in microelectronics for resistor networks, hybrid integrated circuitry, and discrete components, such as capacitors and inductors along with metallization of MLC capacitors and packages as mentioned above.

In principle, the process is equivalent to the silk-screening technique whereby the printable components, paste or inks, are forced through a screen with a rubber or plastic squeegee (see Fig. 7). Generally, stainless steel or nylon

**Table 4. Components of Thick Film Compositions<sup>a</sup>**

Component	Composition
functional phase	
conductor	Au, Pt/Au Ag, Pd/Ag Cu, Ni
resistor	RuO <sub>2</sub> Bi <sub>2</sub> Ru <sub>2</sub> O <sub>7</sub> LaB <sub>6</sub>
dielectric	BaTiO <sub>3</sub> glass glass-ceramic Al <sub>2</sub> O <sub>3</sub>
binder	glass: borosilicates, aluminosilicates oxides: CuO, CdO
vehicle	volatile phase: terpeneol, mineral spirits nonvolatiles: ethyl cellulose, acrylates

<sup>a</sup>Ref. 53.

filament screens are masked using a polymeric material forming the desired printed pattern in which the composition is forced through to the underlying substrate.

Thick film compositions possess three parts: (1) functional phase, (2) binder, and (3) vehicle. The functional phase includes various metal powders for conductors, electronic ceramics for resistors, and dielectrics for both capacitors and insulation. Examples of typical components for thick film compositions are given in Table 4. The binder phase, usually a low ( $<1000^{\circ}\text{C}$ ) melting glass adheres the fired film to the substrate whereas the fluid vehicle serves to temporarily hold the unfired film together and provide proper rheological behavior during screen printing. Thick film processing for hybrid integrated circuits typically takes place below  $1000^{\circ}\text{C}$  providing flexible circuit designs.

### Current and Future Developments in Multilayer Electronic Ceramics

Advances in the field of electronic ceramics are being made in new materials, novel powder synthesis methods, and in ceramic integration. Monolithic multicomponent components (MMC) take advantage of three existing technologies: (1) thick film methods and materials, (2) MLC capacitor processes, and (3) the concept of cofired packages as presented in Figure 9. Figure 10 shows an exploded view of a monolithic multicomponent ceramic substrate.

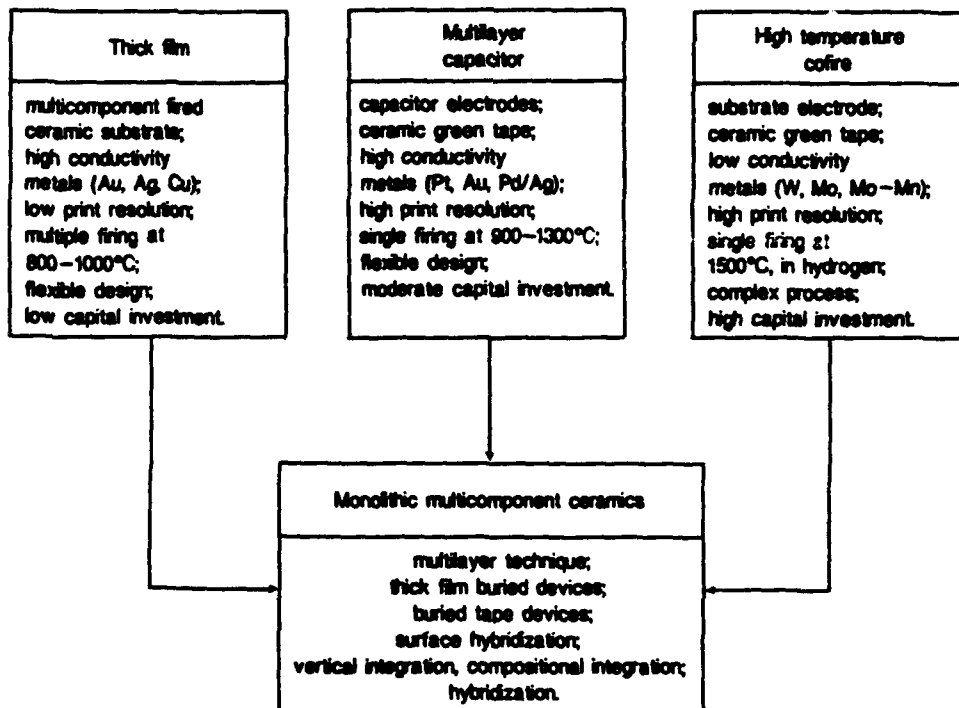


Fig. 9. Monolithic multilayer ceramics (MMCs) derived from multilayer capacitor, high temperature cofire, and thick film technologies.

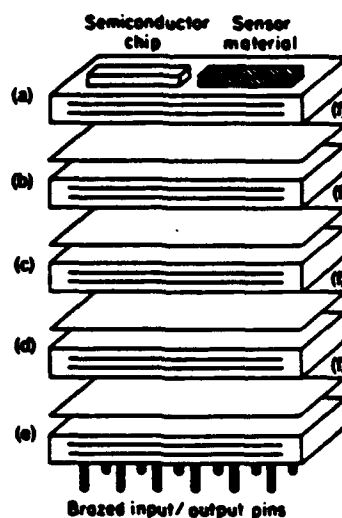


Fig. 10. Exploded view of a monolithic multicomponent ceramic substrate. Layers (a) signal distribution; (b) resistor; (c) capacitor; (d) circuit protection; and (e) power distribution are separated by (f) barrier layers.

New materials for packaging include aluminum nitride [24304-00-5], AlN, silicon carbide [409-21-2], SiC, and low thermal expansion glass-ceramics, replacing present day alumina packaging technology. As shown in Table 5, these new materials offer significant advantages to meeting the future requirements of the microelectronics industry. Properties include higher thermal conductivity,

Table 5. Properties of High Performance Ceramic Substrates<sup>a</sup>

Properties	AlN	SiC	Glass-ceramics	90% Al <sub>2</sub> O <sub>3</sub>
thermal conductivity, W/(m·K)	230	270	5	20
thermal expansion coefficient, RT - 400°C × 10 <sup>-7</sup> /°C <sup>b</sup>	43	37	30-42	67
dielectric constant at 1 MHz	8.9	42	3.9-7.8	9.4
flexural strength, kg/cm <sup>2</sup>	3500-4000	4500	1500	3000
thin film metals	Ti/Pd/Au Ni/Cr/Pd/Au	Ti/Cu	Cr/Cu, Au	Cr/Cu
thick film metals	Ag-Pd Cu	Au Ag-Pd	Au, Cu, Ag-Pd	Ag-Pd Cu, Au
cofired metals	W	Mo	Au-Cu, Ag-Pd	W, Mo
cooling capability, °C/W				
air	6	5	60	30
water <sup>c</sup>	<1	<1	<1	<1

<sup>a</sup>Ref. 30.

<sup>b</sup>RT = room temperature.

<sup>c</sup>External cooling.

lower dielectric constant, cofire compatibility, and related packaging characteristics such as thermal expansion matching of silicon and high mechanical strength as compared to  $\text{Al}_2\text{O}_3$ .

Greater dimensional control and thinner tapes in multilayer ceramics are the driving forces for techniques to prepare finer particles. Metal organic decomposition and hydrothermal processing are two synthesis methods that have the potential to produce submicrometer powders having low levels of agglomeration to meet the demand for more precise tape fabrication.

As stated above, the development of multifunctional MLCs based on existing technologies offers excellent growth potential since MMCs combine the possibilities of both the high cofire (packaged) substrates and burial of surface devices (54-57). Burial of surface devices promises gains in both circuit density and device hermeticity, leading to increased reliability. Processing trade-offs are expected since current electronic materials for multilayer applications (capacitors, transducers, sensors) are densified at very different firing temperatures. Consequently, integrated components will likely be of lower tolerance and limited range, at least in the early developmental stages. Current efforts have been directed toward incorporation of multilayer capacitor-type power planes and burial of thick film components, including resistors and capacitors. The latter processing technology offers more immediate possibilities as it is developed to cofire at conventional thick film processing temperatures for which a wide range of materials exist.

The continuing miniaturization of electronic packaging should see the replacement of components and processes using such thin film technologies developed for semiconductors as sputtering, chemical vapor deposition, and sol-gel (see SOL-GEL TECHNOLOGY; THIN FILMS) (58,59). Sputtering is the process whereby a target material is bombarded by high energy ions which liberate atomic species from the target for deposition on a substrate. Chemical vapor deposition (CVD) involves a gaseous stream of precursors containing the reactive constituents for the desired thin film material, generally reacted on a heated substrate. The more recent process for thin films, sol-gel, uses a nonaqueous solution of metal-organic precursor. Through controlled hydrolyses, a thin, adherent film is pre-

**Table 6. Current and Future Developments in Thin Film Electronic Ceramics\***

Material	Application	Methods
PT, PZT, PLZT	nonvolatile memory, ir, pyroelectric detectors, electro-optic waveguide, and spatial light modulators	sol-gel, sputtering
diamond (C)	cutting tools, high temperature semiconductors, protective optical coatings	chemical vapor deposition (CVD)
$\text{SiO}_2$ , $\text{BaTiO}_3$	capacitors	sol-gel, sputtering, chemical vapor deposition (CVD)
1:2:3 superconductors	aquids, nmr, interconnects	

\*Refs. 58 and 59.

pared by dip-coating or spin-coating. The dried "gel" film is then crystallized and densified through heat treatments. Both existing and future developments of thin film electronic ceramics and methods are presented in Table 6.

## BIBLIOGRAPHY

1. *Japan Electronics Almanac*, Dempa Publications, Inc., Tokyo, 1986, p. 412.
2. D. W. Johnson in G. Y. Chin, ed., *Advances in Powder Technology*, American Society for Metals, Metals Park, Ohio, 1982, pp. 23-37.
3. K. Osseo-Asare, F. J. Arriagada, and J. H. Adair, "Solubility Relationships in the Coprecipitation Synthesis of Barium Titanate: Heterogeneous Equilibria in the Ba-Ti-C<sub>2</sub>O<sub>4</sub>-H<sub>2</sub>O System," in G. L. Messing, E. R. Fuller, Jr., and Hans Hausin, eds., *Ceramic Powder Science*, Vol. 2, 1987, pp. 47-53.
4. D. Miller, J. H. Adair, W. Huebner, and R. E. Newnham, "A Comparative Assessment of Chemical Synthesis Techniques for Barium Titanate," Paper, 88th Annual Meeting of the American Ceramic Society, Pittsburgh, Pa., April 27-30, 1987.
5. B. J. Mulder, *Am. Ceram. Soc. Bull.* 49(11), 990-993 (1970).
6. E. P. Stambaugh and J. F. Miller, "Hydrothermal Precipitation of High Quality Inorganic Oxides," in S. Somiya, ed., *Proceedings of First International Symposium on Hydrothermal Reactions*, Gakujutsu Bunken Fukyu-kai (c/o Tokyo Institute of Technology), Tokyo, Japan, 1983, pp. 859-872.
7. K. S. Mazdidasni, C. T. Lynch, and J. S. Smith, *J. Ceram. Soc.* 48(7), 372-375 (1965).
8. R. R. Wills, R. A. Markle, and S. P. Mukherjee, *Am. Ceram. Soc. Bull.* 62(8), 904-911 (1983).
9. R. West, X.-H. Zhang, I. P. Djurovich, and H. Stuger, "Crosslinking of Polysilanes as Silicon Carbide Precursors," in L. L. Hench and D. R. Ulrich, eds., *Science of Ceramic Chemical Processing*, John Wiley & Sons, New York, 1986, pp. 337-344.
10. K. K. Verna and A. Roberts in G. Y. Onoda, Jr., and L. L. Hench, eds., *Ceramic Processing Before Firing*, John Wiley & Sons, Inc., New York, 1978, pp. 391-407.
11. J. H. Adair, A. J. Roese, and L. G. McCoy, "Particle Size Analysis of Ceramic Powders," in K. M. Nair, ed., *Advances in Ceramics*, Vol. 2, The American Ceramic Society, Columbus, Ohio, 1984.
12. J. W. McCauley, *Am. Chem. Soc. Bull.* 63(2), 263-265 (1984).
13. G. L. Messing, C. J. Markhoff, and L. G. McCoy, *Am. Ceram. Soc. Bull.* 61(8), 857-860 (1982).
14. D. E. Niesz and R. B. Bennett, in ref. 10, pp. 61-73.
15. C. Greskovich, "Milling" in F. F. Y. Wang, ed., *Treatise on Materials Science and Technology*, Vol. 9, Academic Press, New York, 1976.
16. R. E. Mistler, D. J. Shanefield, and R. B. Runk, in ref. 10, pp. 411-448.
17. J. C. Williams, "Doctor-Blade Process," in F. F. Y. Wang, ed., *Treatise on Materials Science and Technology*, Vol. 9, Academic Press, New York, 1976.
18. U.S. Pat. 3,717,487 (1973) (to Sprague Electric Company).
19. B. Schwarz and D. L. Wilcox, *Ceramic Age*, 40-44 (June 1967).
20. R. B. Runk and M. J. Andrejco, *Am. Ceram. Soc. Bull.* 54(2), 199-200 (1975).
21. C. Wentworth and G. W. Taylor, *Am. Ceram. Soc. Bull.* 46(12), 1186-1193 (1967).
22. R. E. Mistler, *Am. Ceram. Soc. Bull.* 52(11), 850-854 (1973).
23. J. M. Herbert, *Methods of Preparation, Ceramic Dielectrics and Capacitors*, Gordon and Breach Science Publishers, New York, 1985, Chapt. 3.
24. F. H. Norton, *Forming Plastic Masses, Fine Ceramics: Technology and Applications*, Robert E. Krieger Publishing, Huntington, NY, 1978, Chapt. 10.

25. T. Morse, *Handbook of Organic Additives for Use in Ceramic Body Formulation*, Montana Energy and MHD Research and Development Institute, Inc., Butte, Mont., 1979.
26. D. B. Quinn, R. E. Bedford, and F. L. Kennard, "Dry-Bag Isostatic Pressing and Contour Grinding of Technical Ceramics," in J. A. Mangels and G. L. Messing, eds., *Advances in Ceramics*, Vol. 9 (Forming of Ceramics), 1984, pp. 4-31.
27. I. A. Aksay, F. F. Lange, and B. I. Davis, *J. Am. Ceram. Soc.* **66**(10), C190-C192 (1983).
28. F. F. Lange, B. I. Davis, and E. Wright, *J. Am. Ceram. Soc.* **69**(1), 66-69 (1986).
29. I. A. Aksay and C. H. Schilling, in ref. 26, pp. 85-93.
30. G. N. Howatt, R. G. Breckenridge, and J. M. Brownlow, *J. Am. Ceram. Soc.* **30**(8), 237-242 (1947).
31. J. J. Thompson, *Am. Ceram. Soc. Bull.* **42**(9), 480-481 (1963).
32. J. A. Mangels and W. Trela, in ref. 26, pp. 85-93.
33. T. J. Whalen and C. F. Johnson, *Am. Ceram. Soc. Bull.* **60**(2), 216-220 (1981).
34. M. J. Edirisinghe and J. R. G. Evans, *Int. J. High Technol. Ceram.* **2**(1), 1-31 (1986).
35. R. R. Wills, M. C. Brockway, and L. G. McCoy, "Hot Isostatic Pressing of Ceramic Materials," in R. F. Davis, H. Palmour III, and R. L. Porter, eds., *Materials Science Research*, Vol. 17 (Emergent Process Methods for High-Technology Ceramics), Plenum Press, New York, 1984.
36. M. H. Leipold, "Hot Pressing," in F. F. Y. Wang, ed., *Treatise on Materials Science and Technology*, Vol. 9 (Ceramic Fabrication Processes), Academic Press, New York, 1976.
37. A. J. Blodgett, Jr., *Sci. Am.* **249**(1), 86-96 (1983).
38. R. R. Tummala and E. J. Rymaszewski, *Microelectronics Packaging Handbook*, Van Nostrand Reinhold, New York, 1989.
39. R. R. Tummala, *Am. Ceram. Soc. Bull.* **67**(4), 752-758 (1988).
40. D. J. Shanefield and R. S. Mistler, *Am. Ceram. Soc. Bull.* **53**(5), 416-420 (1974).
41. D. J. Shanefield and R. S. Mistler, *Am. Ceram. Soc. Bull.* **53**(8), 564-568 (1974).
42. R. A. Gardner and R. W. Nufer, *Solid State Technol.* (May 8-13, 1974).
43. A. G. Pincus and L. E. Shipley, *Ceram. Ind.* **92**(4), 106-110 (1969).
44. N. Sarkar and G. K. Greminger, Jr., *Am. Ceram. Soc. Bull.* **62**(11), 1280-1284 (1983).
45. G. Y. Onoda, Jr., in ref. 10, pp. 235-251.
46. J. H. Adair, D. A. Anderson, G. O. Dayton, and T. R. Shrout, *J. Mater. Ed.* **9**(1,2), 71-118 (1987).
47. D. A. Chance, *Met. Trans.* **1**, 685-694 (March 1970).
48. I. Burn and G. H. Maher, *J. Mater. Sci.* **10**, 633-640 (1975).
49. U.S. Pat. 4,075,681 (Feb. 1978), M. J. Popowich.
50. T. L. Rutt and J. A. Syne, "Fabrication of Multilayer Ceramic Capacitor by Metal Impregnation," *IEEE Trans. Parts Hybrids Packag.*, PHP-9, 144-147 (1973).
51. D. A. Chance and D. L. Wilcox, *Met. Trans.* **2**, 733-741 (March 1971).
52. D. A. Chance and D. L. Wilcox, *Proc. IEEE* **59**(10), 1455-1462 (1971).
53. L. M. Levinson, *Electronic Ceramics*, Marcel Dekker, Inc., New York, 1988, Chapt. 6.
54. K. Utsumi, Y. Shimada, and H. Takamizawa, "Monolithic Multicomponent Ceramic (MMC) Substrate," in K. A. Jackson, R. C. Pohanka, D. R. Uhlmann, and D. R. Ulrich, eds., *Electronic Packaging Materials Science*, Materials Research Society, Pittsburgh, Pa., 1986, pp. 15-26.
55. W. A. Vitriol and J. I. Steinberg, "Development of a Low Fire Cofired Multilayer Ceramic Technology," 1983, pp. 593-598.
56. H. T. Sawhill and co-workers, "Low Temperature Co-Firable Ceramics with Co-Fired Resistors," International Society of Hybrid Microelectronics Proceedings, 1986, pp. 473-480.
57. C. C. Shiflett, D. B. Buchholz, and C. C. Faudskar, "High-Density Multilayer Hybrid Circuits Made with Polymer Insulating Layers (Polyhic's)," Society of Hybrid Microelectronics Proceedings, 1980, pp. 481-486.

- 58. S. L. Swartz, "Topics in Electronic Ceramics," *IEEE Trans. Elect. Insul. Digest on Dielectrics* **25**, 935-987 (Oct. 1990).
- 59. C. P. Poole, Jr., T. Datta, and H. A. Farach, *Copper Oxide Superconductors*, John Wiley & Sons, New York, 1988.

*General references*

- R. C. Buchanan, ed., *Ceramic Materials for Electronics*, Marcel Dekker, Inc., New York, 1986.
- L. M. Levinson, ed., *Electronic Ceramics*, Marcel Dekker, Inc., New York, 1988.
- B. Jaffe, W. R. Cook, Jr., and H. Jaffe, *Piezoelectric Ceramics*, Academic Press, New York, 1971.

ROBERT E. NEWNHAM  
THOMAS R. SHROUT  
Pennsylvania State University



# **COMPOSITE MATERIALS**

## **APPENDIX 3**

## **TUNABLE TRANSDUCERS: NONLINEAR PHENOMENA IN ELECTROCERAMICS**

**Robert E. Newnham**  
Materials Research Laboratory  
Pennsylvania State University  
University Park, PA 16802

### **ABSTRACT**

The concept of a fully tunable transducer is developed as an example of a very smart material whose sensing and actuating functions can be tuned to optimize behavior. By constructing the composite transducer from an elastically nonlinear material (rubber) and an electrically nonlinear material (relaxor ferroelectric), most of its key properties can be adjusted over wide ranges by applying DC bias fields or mechanical prestress. These properties include resonant frequency, acoustic and electric impedance, damping factors, and electromechanical coupling coefficients.

The origins of nonlinear properties are considered briefly using electrostriction as an example. The nonlinearities usually involve phase transformations and size-dependent phenomena on the nanometer scale.

### **INTRODUCTION**

Much of the recent interest in nonlinear phenomena stems from the desire to build "smart materials" for intelligent systems. The words "smart materials" have different meanings for different people, and can be smart in either a passive sense or an active sense. Passively smart materials incorporate self-repair mechanisms or stand-by phenomena which enable the material to withstand sudden changes in the surroundings.

Ceramic varistors and PTC thermistors are passively smart materials. When struck by lightning or otherwise subjected to high voltage, a zinc oxide varistor loses its electrical resistance and the current is bypassed to ground. The resistance change is reversible and acts as a stand-by protection phenomenon. Barium titanate PTC thermistors show a large increase in electrical resistance at the ferroelectric phase transformation near 130°C. The jump in resistance enables the thermistor to arrest current surges, again acting as a protection element. The

R(V) behavior of the varistor and the R(T) behavior of the PTC thermistor are both highly nonlinear effects which act as standby protection phenomena, and make the ceramics smart in a passive mode.

A smart ceramic can also be defined with reference to sensing and actuating functions, in analogy to the human body. A smart ceramic senses a change in the environment, and using a feedback system, makes a useful response. It is both a sensor and an actuator. Examples include vibration damping systems for space structures and energy-saving windows for homes and factories. The new electronically-controlled automobile suspension systems using piezoelectric ceramic sensors and actuators constitutes an actively smart material.

By building in a learning function, the definition can be extended to a higher level of intelligence: A very smart ceramic senses a change in the environment and responds by changing one or more of its property coefficients. Such a material can tune its sensor and actuator functions in time and space to optimize behavior. The distinction between smart and very smart materials is essentially one between linear and nonlinear properties. The physical properties of nonlinear materials can be adjusted by bias fields or forces to control response.

#### TUNABLE TRANSDUCER

To illustrate the concept of a very smart material, we describe the tunable transducer recently developed in our laboratory. Electromechanical transducers are used as fish finders, gas igniters, ink jets, micropositioners, biomedical scanners, piezoelectric transformers and filters, accelerometers, and motors.

Four important properties of a transducer are the resonant frequency  $f$ , the acoustic impedance  $Z_A$ , the mechanical damping coefficient  $Q$ , the electromechanical coupling factor  $k$ , and the electrical impedance  $Z_E$ . The resonant frequency and acoustic impedance are controlled by the elastic constants and density, as discussed in the next section. The mechanical  $Q$  is governed by the damping coefficient ( $\tan \delta$ ) and is important because it controls "ringing" in the transducer. Electromechanical coupling coefficients are controlled by the piezoelectric coefficient which, in turn, can be controlled and fine-tuned using relaxor ferroelectrics with large electrostrictive effects. The dielectric "constant" of relaxor ferroelectrics depends markedly on DC bias fields, allowing the electrical impedance to be tuned over a wide range as well. In the following sections we describe the nature of nonlinearity and how it controls the properties of a tunable transducer.

#### ELASTIC NONLINEARITY: TUNING THE RESONANT FREQUENCY

Information is transmitted on electromagnetic waves in two ways: amplitude modulation (AM) and frequency modulation (FM). There are a number of advantages to FM signal processing, especially where lower noise levels are important.

Signal-to-noise ratios are also important in the ultrasonic systems used in biomedical and nondestructive testing systems, but FM-modulation is difficult because resonant frequencies are controlled by stiffness ( $c$ ) and sample dimensions ( $t$ ):

$$f = \frac{1}{2t} \sqrt{c / \rho}$$

Neither  $c$ ,  $t$ , or the density  $\rho$  can be tuned significantly in most materials, but rubber is an exception. To tune the resonant frequency of a piezoelectric transducer, we have designed and built a composite transducer incorporating thin rubber layers exhibiting nonlinear elasticity.

Rubber is a highly nonlinear elastic medium. In the unstressed compliant state, the molecules are coiled and tangled, but under stress the molecules align and the material stiffens noticeably. Experiments carried out on rubber-metal laminates demonstrate the size of the nonlinearity. Young's modulus ( $E = 1/s_{1111}$ ) was measured for a multilayer laminate consisting of alternating steel shim and soft rubber layers each 0.1 mm thick. Under compressive stresses of 200 MN/m<sup>2</sup>, the stiffness is quadrupled from about 600 to 2400 MN/m<sup>2</sup>. The resonant frequency  $f$  is therefore double, and can be modulated by applied stress.

Rubber, like most elastomers, is not piezoelectric. To take advantage of the elastic nonlinearity, it is therefore necessary to construct a composite transducer consisting of a piezoelectric ceramic (PZT) transducer, thin rubber layers, and metal head and tail masses, all held together by a stress bolt.

The resonant frequency and mechanical  $Q$  of such a triple sandwich structure was measured as a function of stress bias. Stresses ranged from 20 to 100 MPa in the experiments. Under these conditions the radial resonant frequency changed from 19 to 37 kHz, approximately doubling in frequency as predicted from the elastic nonlinearity. At the same time the mechanical  $Q$  increases from about 11 to 34 as the rubber stiffens under stress.

The changes in resonance and  $Q$  can be modeled with an equivalent circuit in which the compliance of the thin, rubber layers are represented as capacitors coupling together the larger masses (represented as inductors) of the PZT transducer and the metal head and tail masses. Under low stress bias, the rubber is very compliant and effectively isolates the PZT transducer from the head and tail masses. At very high stress, the rubber stiffens and tightly couples the metal end pieces to the resonating PZT ceramic. For intermediate stresses the rubber acts as an impedance transformer giving parallel resonance of the PZT - rubber - metal - radiation load.

It is interesting to compare the change in frequency of the tunable transducer with the transceiver systems used in the biological world. The biosonar system of the flying bat is similar in frequency and tunability to our

tunable transducer. The bat emits chirps at 30 kHz and listens for the return signal to locate flying insects. To help it differentiate the return signal from the outgoing chirp, and to help in timing the echo, the bat puts an FM signature on the pulse. This causes the resonant frequency to decrease from 30 to 20 kHz near the end of each chirp. Return signals from the insect target are detected in the ears of the bat where neural cavities tuned to this frequency range measure the time delay and flutter needed to locate and identify its prey. Extension of the bat biosonar principle to automotive, industrial, medical and entertainment systems is obvious.

#### **PIEZOELECTRIC NONLINEARITY: TUNING THE ELECTROMECHANICAL COUPLING COEFFICIENT**

The difference between a smart and a very smart material can be illustrated with piezoelectric and electrostrictive ceramics. PZT (lead zirconate titanate) is a piezoelectric ceramic in which the ferroelectric domains are aligned in a poling field. Strain is linearly proportional to electric field in a piezoelectric material which means that the piezoelectric coefficient is a constant and cannot be electrically tuned with a bias field. Nevertheless it is a smart material because it can be used both as a sensor and an actuator.

PMN (lead magnesium niobate) is not piezoelectric at room temperature because its Curie temperature lies near 0°C. Because of the proximity of the ferroelectric phase transformation, and because of its diffuse nature, PMN ceramics exhibit very large electrostrictive effects. The nature of this large nonlinear relationship between strain and electric field, and of its underlying atomistic origin, will be described later.

Electromechanical strains comparable to PZT can be obtained with electrostrictive ceramics like PMN, and without the troubling hysteretic behavior shown by PZT under high fields. The nonlinear relation between strain and electric field in electrostrictive transducers can be used to tune the piezoelectric coefficient and the dielectric constant.

The piezoelectric  $d_{33}$  coefficient is the slope of the strain-electric field curve when strain is measured in the same direction as the applied field. Its value for  $\text{Pb}(\text{Mg}_{0.3}\text{Nb}_{0.6}\text{Ti}_{0.1})\text{O}_3$  ceramics is zero at zero field and increases to a maximum value of 1300 pC/N (about three times larger than PZT) under a bias field of 3.7 kV/cm.

This means that the electromechanical coupling coefficient can be tuned over a very wide range, changing the transducer from inactive to extremely active. The dielectric constant also depends on DC bias. The polarization saturates under high fields causing decreases of 100% or more in the capacitance. In this way the electrical impedance can be controlled as well.

Electrostrictive transducers have already been used in a number of applications including adaptive optic systems, scanning tunneling microscopes, and precision micropositioners.

To summarize, two types of nonlinearity are utilized in the fully tunable transducer: elastic nonlinearity and piezoelectric nonlinearity. By incorporating thin rubber layers in an electrostrictive transducer several important properties can be optimized with bias fields and bias stresses. Electromechanical coupling coefficients and electric impedance are tuned with electric field, and mechanical damping, resonant frequency, and acoustic impedance with stress bias.

## RELAXOR FERROELECTRICS

In the three remaining sections we consider the atomistic origin of nonlinear behavior in ceramics. The magnesium - niobium distribution in PMN ceramics have been studied by transmission electron microscopy. Images formed from superlattice reflections show that the size of the regions with 1:1 ordering is approximately 3 nm ( $\approx 30\text{\AA}$ ). The ordered regions are small islands separated by narrow walls of niobium - rich PMN.

A simple energy argument explains the scale of the ordered regions. The chemical formula of PMN can be divided into 1:1 ordered regions with niobium-rich coatings as follows:



assuming all ions have their usual valence states, the ordered regions will be negatively charged and the coatings positive. The ordering must therefore be on a very fine scale in order to minimize coulomb energy.

A cubes model is adopted to estimate the size of ordered islands. Let each island be a cube  $n$  unit cells on edge. Then there will be  $n^3/2$  Mg atoms and  $n^3/2$  Nb atoms within the island. This means that  $n^3/2$  Nb atoms are excluded from the island because the Mg:Nb ration is 1:1 in the ordered island and 1:2 in the chemical formula. We assume the excluded niobiums form a thin monolayer coating on the cubes then  $n^3/2 = 3n^2$ , where  $3n^2$  is the number of surface atoms per cube, neglecting edges and corners. By keeping the coating as thin as possible, charge is neutralized on a local scale, and electrostatic energy is minimized.

Solving the equation gives  $n=6$ , or  $24\text{\AA}$ , surprisingly close to the  $30\text{\AA}$  observed by TEM. It is also interesting to compare this result with the behavior observed of small ferroelectric particles. X-ray studies of very fine-grained  $\text{PbTiO}_3$  show that the polar tetragonal phase becomes unstable below about  $200\text{\AA}$ , the so-called ferroelectric - superparaelectric transformation. Relaxor ferroelectrics like PMN exhibit many of the characteristics of superparaelectric solids where the dipole moments are strongly coupled to one another, but not to a

crystallographic axis. The coupled electric dipoles oscillate in orientation and respond readily to applied fields giving rise to large dielectric constants and massive electrostriction coefficients.

## SEVEN MISCONCEPTIONS ABOUT ELECTROSTRICTION

Perhaps the best way to describe the basic features of nonlinear physical properties is to first dispel some of the common misconceptions. Some of the key ideas are described in this section using electrostriction as an example.

---

**Misconception #1:** Electrostrictive strain is proportional to the square of the electric field.

---

When an electric field  $E$  is applied to an insulator it develops a polarization  $P$  and a strain  $\epsilon$ . In tensor notation the strain can be written as a power series in  $E$  or in  $P$ .

$$(1) \epsilon_{ij} = d_{ijk} E_k + M_{ijkl} E_k E_l + \dots$$

$$(2) \epsilon_{ij} = d_{ijk} P_k + Q_{ijkl} P_k P_l + \dots$$

The first term in both equations represents piezoelectricity, the second electrostriction. Piezoelectricity is a third rank tensor property found only in noncentrosymmetric materials. It is absent in most ceramic materials, but electrostriction is not. The electrostriction coefficients  $M_{ijkl}$  or  $Q_{ijkl}$  constitute a fourth rank tensor which, like the elastic constants, are found in all materials, regardless of symmetry. In the discussion which follows, we deal with centrosymmetric media for which the piezoelectric coefficients are zero.

Returning to equations (1) and (2), which of these equations is the correct way to describe electrostriction, or can both be used? For normal low permittivity materials, the polarization  $P$  is proportional to the applied electric field  $E$ , and therefore both expressions are correct, but for high permittivity solids only one is correct. Under high fields, the polarization saturates in high permittivity materials, especially in ferroelectric ceramics just above  $T_c$ , the Curie temperature. In capacitor dielectrics, it is not unusual to observe a decrease in dielectric constant of 100% under high electric fields. In this situation  $P$  is not proportional to  $E$ , and therefore electrostrictive strain cannot be proportional to both  $E^2$  and  $P^2$ .

When strain is plotted as a function of electric field for PMN-PT, a typical electrostrictive transducer ceramic, it is not proportional to  $E^2$  except for small fields where the shape is parabolic. When plotted as function  $P^2$ , a straight line is obtained for the  $\epsilon(P^2)$  relationship. Therefore the correct way to formulate electrostriction is



$$(3) \quad \boxed{\epsilon_{ij} = Q_{ijkl} P_k P_l} \quad (i, j, k, l = 1, 2, 3)$$

The  $M_{ijkl}$  coefficients in eq. (1) are not good constants except in linear dielectrics.

It is instructive to convert the fourth rank tensor coefficients to the more manageable matrix form

$$(4) \quad \epsilon_i = Q_{ij} P_j^2 \quad (i, j = 1-6)$$

When written out in full for cubic point group  $m\bar{3}m$ , this becomes

$$(5) \quad \begin{array}{rcll} \epsilon_1 & & Q_{11} & Q_{12} & Q_{12} & 0 & 0 & 0 & P_1^2 \\ \epsilon_2 & & Q_{12} & Q_{11} & Q_{12} & 0 & 0 & 0 & P_2^2 \\ \epsilon_3 & = & Q_{12} & Q_{12} & Q_{11} & 0 & 0 & 0 & P_3^2 \\ \epsilon_4 & & 0 & 0 & 0 & Q_{44} & 0 & 0 & P_2 P_3 \\ \epsilon_5 & & 0 & 0 & 0 & 0 & Q_{44} & 0 & P_3 P_1 \\ \epsilon_6 & & 0 & 0 & 0 & 0 & 0 & Q_{44} & P_1 P_2 \end{array}$$

In this expression  $\epsilon_1$ ,  $\epsilon_2$  and  $\epsilon_3$  represent tensile strains along the [100], [010], and [001] axes, respectively.  $\epsilon_4$ ,  $\epsilon_5$  and  $\epsilon_6$  are shear strains about the same three axes.

To understand the structure-property relationship underlying electrostriction, it is helpful to visualize the atomistic meaning of coefficients  $Q_{11}$ ,  $Q_{12}$ , and  $Q_{44}$ . The high temperature structure of  $\text{PbTiO}_3$  is pictured in Fig. 1 a. Lead ions are located at the corners of the cubic unit cell, titanium ions at the body-centered position, and oxygens at the face-center positions.

When an electric field is applied along [100], polarization component  $P_1$  develops along the same axis. This in turn causes the unit cell to elongate by an amount  $\Delta a$ , and the resulting tensile strain is  $\epsilon_1 = \Delta a/a$ . Electrostrictive coefficient  $Q_{11}$  is equal to  $\epsilon_1/P_1^2$ . The drawing in Fig. 1b makes it clear why electrostrictive strain is proportional to electric polarization rather than electric field. Polarization and strain are both controlled by atomic displacement.

The atomistic meaning of  $Q_{12}$  and  $Q_{44}$  are pictured in figs. 1 c and 1 d, respectively.

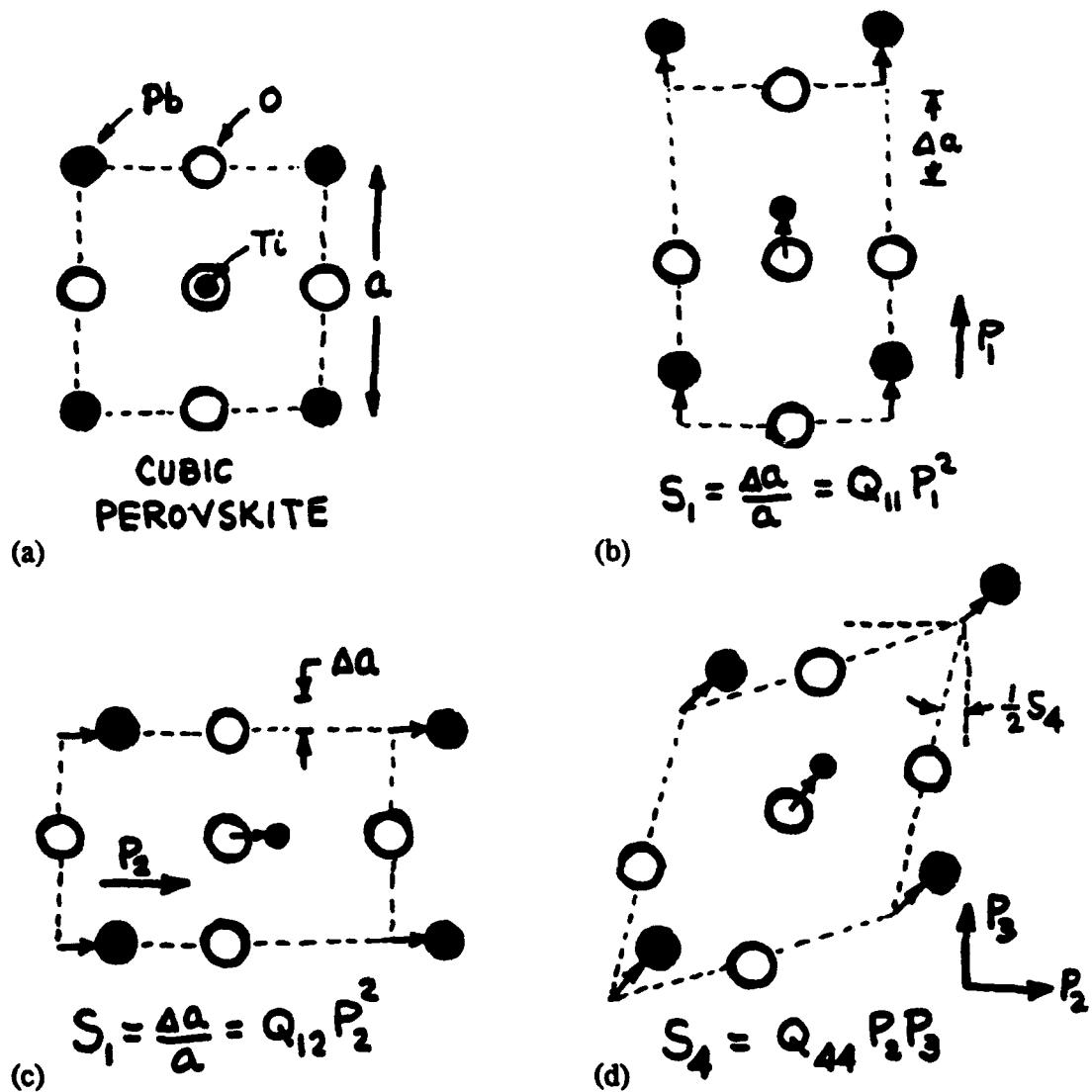


Fig. 1 Electrostriction in cubic perovskite showing the physical origin of coefficients  $Q_{11}$ ,  $Q_{12}$ , and  $Q_{44}$ .

---

**Misconception #2. Large voltages are required to observe electrostriction.**

---

This misconception arises from the fact that historically, the first electroceramics were high voltage insulators made from low permittivity oxides such as porcelain, glass, steatite, and alumina. To prevent breakdown, the insulators were fabricated in large sizes, typically with 1-10 cm separation between electrodes. Under these conditions the voltages required to induce measurable electrostriction are huge, but the picture has changed in the last decade.

Two factors have made the difference: smaller electrode separation and higher permittivity. The introduction of thin and thick film technology, together with tape-casting, has reduced the thickness of the dielectric constants to less than 50  $\mu\text{m}$  with corresponding increases in the electric field levels. Fields of megavolts/meter are common under these circumstances. At the same time, new ferroelectric ceramics with dielectric constants in excess of 10,000 have raised the polarization levels to new heights, further contributing to electrostriction strain. As a result, strains of  $10^{-3}$  to  $10^{-2}$  are observed with relatively modest voltages.

---

**Misconception #3 Electrostriction coefficients are about the same size for all materials.**

---

**Misconception #4 Electrostriction coefficients are largest in ferroelectric solids with high dielectric constants.**

---

$Q_{11}$  coefficients measured for normal oxides are several orders of magnitude or more larger than those of ferroelectrics.

	$Q_{11} (\text{m}^4/\text{C}^2)$
Silica	+12.8
Barium Titanate	+0.11
Lead Magnesium Niobate	+0.009

---

**Misconception #5 Materials with large electrostrictive coefficients produce the biggest strains.**

---

The  $Q$  coefficients are largest for non-ferroelectrics but relaxor ferroelectrics like PMN have the largest strains. The following table lists typical values of the electrostriction coefficients  $Q$ , the dielectric constant  $K$ , and electrostrictive strain  $\epsilon$  computed for a field of 1 MV/m.

	$Q$	$K$	$\epsilon$
non-ferroelectric	$\sim 10$	$\sim 10$	$\sim 10^{-7}$
normal ferroelectric	$\sim 10^{-1}$	$\sim 10^3$	$\sim 10^{-5}$
relaxor ferroelectric	$\sim 10^{-2}$	$\sim 10^4$	$\sim 10^{-4}$

Note that the product  $QK \sim 100 \text{ m}^4/\text{C}^2$  is approximately a constant for all three classes. To see why this is so, consider the following argument based on the atomistic models in Fig 1.

Under the action of an applied electric field, the cations and anions in a crystal structure are displaced in opposite directions by an amount  $\Delta r$ . It is this displacement which is responsible for electric polarization ( $P$ ), the dielectric constant  $K$ , and the electrostrictive strain  $\epsilon$ . To a first approximation, all three are proportional to  $\Delta r$ . The electrostriction coefficient  $Q$  is therefore proportional to  $1/K$ :

$$Q = \frac{E}{P^2} \sim \frac{(\Delta r)}{(\Delta r)^2} = \frac{1}{\Delta r} \sim \frac{1}{K}$$

This means then, that  $QK$  is approximately constant, as indicated earlier. Materials with high permittivity have small electrostriction coefficients but large electrostrictive strain.

---

**Misconception #6.** Unlike piezoelectricity there is no converse electrostriction effect.

---

In the direct piezoelectric effect an applied mechanical stress  $\sigma_{kl}$  produces an electric polarization  $P_i = d_{ijk} \sigma_{kl}$ . The converse effect relates mechanical strain to applied electric field,  $\epsilon_{ij} = d_{ijk} E_k$ . The piezoelectric coefficients  $d_{ijk}$  are identical in the direct and converse effect because both originate from the same term in the free energy function:

$$F = \dots + d_{ijk} P_i \sigma_{jk} + \dots$$

Electrostriction and its converse effects arise from the free energy term

$$F = \dots + Q_{ijkl} P_i P_j \sigma_{kl} + \dots$$

Taking the partial derivatives in different order leads to three equivalent effects. The first is the normal electrostriction effect, the variation of strain with polarization:

$$\frac{\partial}{\partial P_i} \left( \frac{\partial}{\partial P_j} \left( \frac{\partial F}{\partial \sigma_{kl}} \right) \right) = \frac{\partial^2 \epsilon_{kl}}{\partial P_i \partial P_j} = Q_{ijkl}$$

The second is the stress dependence of the dielectric stiffness  $\beta_{ij}$ , better known as the reciprocal electric susceptibility:

$$\frac{\partial}{\partial \sigma_{kl}} \left( \frac{\partial}{\partial P_i} \left( \frac{\partial F}{\partial P_j} \right) \right) = \frac{\partial \beta_{ij}}{\partial \sigma_{kl}} = Q_{ijk}$$

The third effect is the polarization dependence of the piezoelectric voltage coefficient  $g_{jkl}$ :

$$\frac{\partial}{\partial P_i} \left( \frac{\partial}{\partial \sigma_{kl}} \left( \frac{\partial F}{\partial P_j} \right) \right) = \frac{\partial g_{jkl}}{\partial P_i} = Q_{ijk}$$

Thus there are two converse effects for electrostriction, and there are three ways of evaluating the electrostrictive coefficients.

The three effects are used in three different applications: (1) the electrostrictive micropositioner, (2) a capacitive stress gauge, and (3) a field-tunable piezoelectric transducer.

---

**Misconception #7** Thermal expansion effects make electrostrictive micropositioners and stress gauges impractical.

---

This is true for normal oxide insulators but not for relaxor ferroelectrics. For a normal oxide such as silica, the electrostrictive coefficient  $Q \sim 10 \text{ m}^2/\text{C}^2$ , the dielectric constant  $K \sim 10$ , and the thermal expansion coefficient  $\alpha \sim 10^{-5} \text{ K}^{-1}$ . For such a material the strain produced by an electric field of 1 MV/m is about  $10^{-7}$ , which is equivalent to a temperature change of only  $10^{-2}$  degrees. This would pose severe problems in an actuator or micropositioner, but the situation is quite different for a ferroelectric.

For PMN,  $Q \sim 10^{-2}$ ,  $K \sim 10^4$  and  $\alpha \sim 10^{-6} \text{ K}^{-1}$ . Therefore the electrostrictive strain for a field of 1 MN/m is about  $10^{-3}$  which is equivalent to a temperature rise of 1000°! Relaxor ferroelectrics sometimes have an abnormally low thermal expansion coefficient near the diffuse phase transformation where the dielectric constant and the electrostrictive strain are unusually large. Micropositioners made from ferroelectric ceramics are not troubled by small variations in temperature.

## ORIGINS OF NONLINEARITY

What do nonlinear materials have in common? The passively-smart PTC thermistor and ZnO varistor have grain boundaries a few nm thick, insulating barriers that can be obliterated by the polarization charge accompanying a ferroelectric phase transformation, or, in the case of the varistor, insulating boundaries so thin they can be penetrated by quantum mechanical tunneling.

Small size is also key factor in the nonlinear behavior of semiconductors. The thin gate region in a transistor allows charge carriers to diffuse through unimpeded. The p-region in an n-p-n transistor is thin compared to the diffusion length in single crystal silicon. Similar size-related phenomena are observed in quantum well structures made from GaAs and  $\text{Ga}_{1-x}\text{Al}_x\text{As}$ . Planar structures with nm-thick layers show channeling behavior of hot electrons in clear violation of Ohm's law. Current - voltage relationships are highly nonlinear in many submicron semiconductor structures. Ohm's law is a statistical law which relies upon the assumption that the charge carriers make a sufficiently large number of collisions to enable them to reach a terminal velocity characteristic of the material. When the size of the conduction is sufficiently small, compared to the mean free path between collisions, the statistical assumption breaks down, and Ohm's law is violated.

Nonlinear behavior is also observed in thin film insulators where even a modest voltage of 1-10 volts can result in huge electric fields of 100 MV/m or more. This means that thin film dielectrics experience a far larger field than do normal insulators, and causing the polarization to saturate and electric permittivity to decline. Because of the high fields, electric breakdown becomes a greater hazard, but this is partly counteracted by an increase in breakdown strength with decreasing thickness. This comes about because the electrode equipotential surfaces on a thin film dielectric are extremely close together, thereby eliminating the asperities that lead to field concentration and breakdown.

The influence of nanometer-scale domains on the properties of relaxor ferroelectrics has already been made plain. Here the critical size parameter is the size of the polarization fluctuations arising from thermal motions near the broad ferroelectric phase transformation in PMN and similar oxides. The ordering of Mg and Nb ions in the octahedral site of the PMN structure results in a chemical inhomogeneous structure on a nm-scale, and this, in turn, influences the size of the polarization fluctuations. Tightly coupled dipoles within each Nb-rich portion of this self-assembling nanocomposite behave like a superparaelectric solid. The dipoles are strongly coupled to one another but not to the crystal lattice, and thus they reorient together under the influence of temperature or electric field. This in turn causes the large electric permittivities and large electrostrictive effects found in relaxor ferroelectrics.

The importance of nanometer-scale fluctuations and the instabilities associated with phase transformations is also apparent in the nonlinear elasticity of rubber and other polymeric materials. The thermally-assisted movement of the randomly oriented polymer chains under tensional stress results in large compliance coefficients, but rubber gradually stiffens as the chains align with the stress into pseudo-crystalline regions. The increase in stiffness with stress gives rise to sizeable third order elastic constants in many amorphous polymers. The effect depends markedly on temperature. On cooling, to lower temperatures rubber and other amorphous polymers transform from a compliant rubber-like material to a brittle glass-like phase which is of little use in nonlinear devices.

Nonlinear behavior is also observed in magnetic and optical systems. Superparamagnetic behavior, analogous to the superparaelectric behavior of relaxor ferroelectrics, is found in spin glasses, fine powder magnets, and magnetic cluster materials. As in PMN, the magnetic dipoles are strongly coupled to one another in nanometer-size complexes, but are not strongly coupled to the lattice. Superparamagnetic solids display nonlinear magnetic susceptibilities and unusual " $\Delta E$ " effects in which Young's modulus  $E$  can be controlled by magnetic field. The effect is especially large in metallic glasses made from Fe-Si-B-C alloys. The cluster size in spin glasses is in the nanometer range like those in PMN.

Lead lanthanum zirconate titanate (PLZT) perovskites can be prepared as transparent ceramics for electrooptic modulators. Quadratic nonlinear optic behavior are observed in pseudocubic regions of the phase diagram which show relaxor-like properties.

In summary, the nonlinear properties of electroceramics are often associated with nanometer-scale structure and diffuse phase transformations. Under these circumstances the structure is poised on the verge of an instability and responds readily to external influences such as electric or magnetic fields, or mechanical stress.

The ready response of nonlinear ceramics allows the properties to be tuned in space or time to optimize the behavior of the sensor-actuator systems referred to by some as "very smart ceramics."

#### ACKNOWLEDGEMENTS

Numerous discussions with Q.C. Xu, M. Blaskiewicz, L.E. Cross, K. Uchino, S.J. Jang and S. Yoshikawa are gratefully acknowledged. Carol Foster typed the manuscript with great skill.

## DISCUSSION

**P. Davies:** Concerning the relaxor ferroelectric with cation ordering in the nanodomains, the charge imbalance between the ordered and disordered regions bothers me a little bit. Are we sure there are no oxygen deficiencies in these domains? Why are the ordered domains stable?

**R. Newnham:** Well, that's a good question. If you examine various ordered configurations, say by model-building, you find the one-to-one pattern goes together very nicely because there are six unit cells around each perovskite unit cell, making it easy to pair things off. If you try, two-to-one ordering corresponding to the overall composition, you find it is necessary to position niobium ions in neighboring octahedral sites. This violates Paulings electrostatic valence rule and leads to charge imbalance on the atomic scale.

What I'm pointing out is that if you look at other possible ordering schemes there are problems with them, too, so it comes down to which is least unfavorable.

**P. Davies:** Are we sure there are no oxygen deficiencies in the domains?

**R. Newnham:** Well, I'll let Prof. Smyth comment on that, but I can tell you that these relaxors are excellent insulators which will withstand very high voltages, and I think if there were a lot of oxygen vacancies which were present we would be seeing conduction and degradation phenomena which are not observed.

**D. Smyth:** Well, that's a question of continuity. You might have some motion within the domain, but whether it would transport throughout the entire system, I don't know. I don't think we have any direct evidence on that because it is difficult to probe these very small areas.

**D. Kolar:** What is the effect of grain size?

**R. Newnham:** The samples we have prepared have normal grain sizes on the micron scale. There have been studies of small grain sizes in ferroelectric ceramics and studies of nanocomposite materials showing transitions from the multidomain regime, to single domain, and to the superparaelectric regime. You have to ask in what temperature range and in which size regime are you operating. In the high temperature regime, the electrostrictive material behaves like a normal paraelectric, then on cooling, there is a broad diffuse phase region with relaxor phenomena, and then at low temperatures it is a normal ferroelectric with normal domain structure. Then PMN behaves pretty much like other ferroelectrics, but it is this broad diffuse range which comes about because of nanometer scale structure, and which we think is analogous to similar phenomena observed when ferroelectrics are prepared in very small particle sizes. This is what is often called superparaelectricity with very large dielectric constants and very large electrostrictive effects.



## **APPENDIX 4**

# **International Encyclopedia of Composites**

**Volume 6**

**Stuart M. Lee**  
*Editor*



**VCH**  
*New York*

## Composite Electroceramics\*

Composite materials have found a number of structural applications, but their use in the electronics industry has been relatively limited. As the advantages and disadvantages of electroceramic composites are better understood, we can expect this picture to change.

In this article we review some of the basic ideas underlying composite electroceramics: sum and product properties, connectivity patterns leading to field and force concentration, the importance of periodicity and scale in resonant structures, the symmetry of composite materials and its influence on physical properties, polychromatic percolation and coupled conduction paths in composites, varistor action and other interfacial effects, coupled phase transformation phenomena in composites, and the important role that porosity and inner surface area play in many composites.

### Sum and Product Properties

The basic ideas underlying sum and product properties were introduced by Van Suchtelen (1). For a sum property, the composite property coefficient depends on the corresponding coefficients of its constituent phases. Thus the stiffness of a composite is governed by the elastic stiffnesses of its component phases.

Product properties are more complex and more interesting. The product properties of a composite involve different properties in its constituent phases, with the interactions between the phases often causing unexpected results. In a magnetoelectric composite, for instance, the magnetostrictive strain in one phase creates an electric polarization in an adjacent piezoelectric phase. Examples of sum and product phases are described in the following sections.

### Sum Properties

The dielectric constant will be used to illustrate a simple sum property. Series and parallel mixing rules for the dielectric constant are shown in Figure 1. The mixing rules involve only the dielectric constants  $K_A$  and  $K_B$  of the two phases and their volume fractions  $v_A$  and  $v_B$ . When plotted as a function of composition, the dielectric constant of the composite,  $\bar{K}$ , decreases smoothly from  $K_A$  to its minimum value at  $K_B$ .

The series and parallel models represent extremes for the mixing rules. Maximum values are obtained with parallel mixing, and minimum with the series case. There are, of course, other mixing rules that lie between these extremes.

Two examples of dielectric composites are illustrated in Figures 2 and 3. The microwave foamed glass in Figure 2 has an extremely low dielectric constant. By introducing 60 vol % porosity in a lithium aluminum silicate

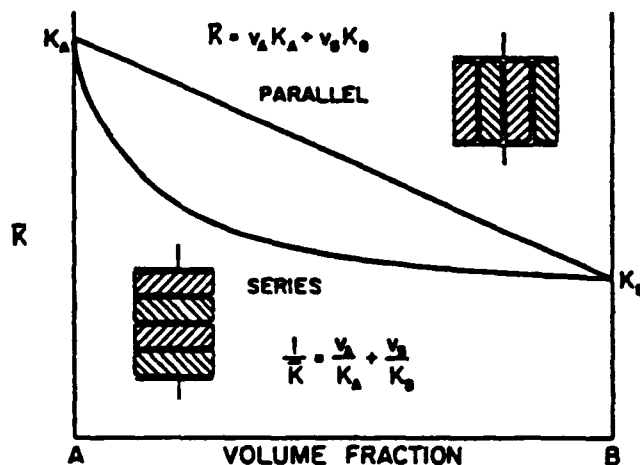


FIGURE 1 Dielectric constant plotted as a function of composition for series and parallel mixing.

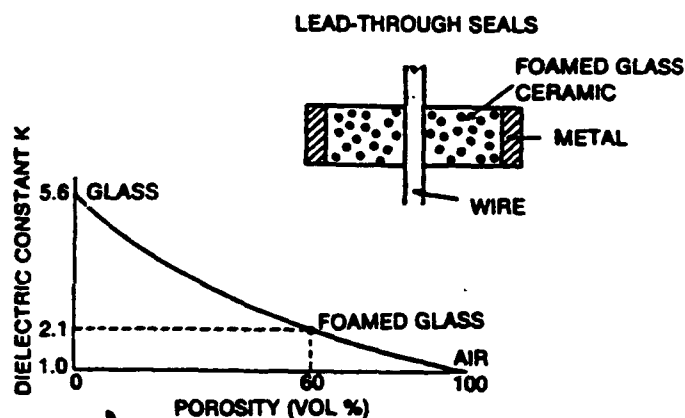


FIGURE 2 Dielectric constant of a porous glass used in microwave lead-through seals. (From Ref. 2.)

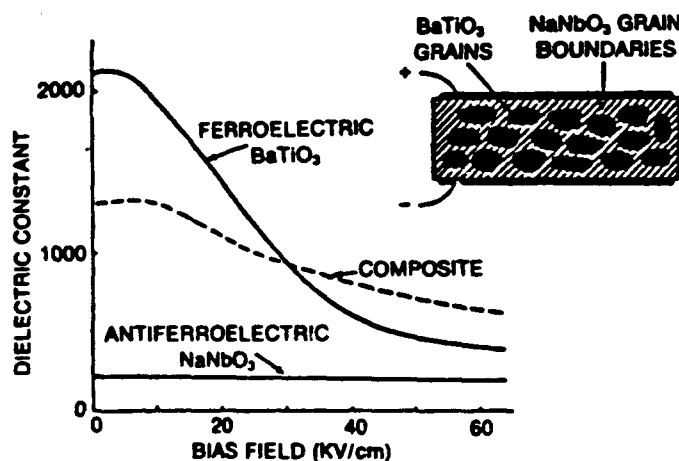


FIGURE 3 Composite capacitor dielectric consisting of  $\text{BaTiO}_3$  grains in a  $\text{NaNbO}_3$  matrix. The dielectric constant shows relatively little variation with field.

\* Reprinted from *Journal of Materials Education*, 7, 60 (1985).

glass, its dielectric constant is reduced from 5.6 to 2.1 [2]. Decreasing the dielectric constant increases the speed of electromagnetic waves traveling along conducting wires embedded in the composite. The speed is doubled by replacing alumina ( $K \sim 9$ ) with porous glass ( $K \sim 2$ ).

Composite ceramics are also useful in high voltage applications. The dielectric constant of  $\text{BaTiO}_3$  multilayer capacitors decreases substantially under high voltage fields, often by 100% or more. This is normal behavior for ferroelectric materials where the polarization saturates, but antiferroelectric substances such as  $\text{NaNbO}_3$  behave differently. The dielectric constant of sodium niobate is nearly independent of bias field (Fig. 3), as its metastable ferroelectric structure begins to influence the permittivity under high fields.

Capacitor compositions with enhanced permittivity at high fields have been manufactured from composites made from  $\text{BaTiO}_3$  and  $\text{NaNbO}_3$  [3]. Fast-firing a mixture of  $\text{BaTiO}_3$  and  $\text{NaNbO}_3$  causes the  $\text{NaNbO}_3$  to melt and coat the grains of  $\text{BaTiO}_3$ , producing a composite structure with ferroelectric grains and antiferroelectric grain boundaries. By adjusting the composition and firing schedule, a capacitor with field-independent permittivity is produced. Coating the grains with  $\text{NaNbO}_3$  prevents growth of the  $\text{BaTiO}_3$  grains, further enhancing the dielectric properties of the composite, and causing it to exceed both component phases at high voltages.

### Combination Properties

For simple mixing rules, the properties of the composite lie between those of its constituent phases. This is not true for combination properties, which involve two or more coefficients. Poisson's ratio is a good example of a combination property since it is equal to the ratio of two compliance coefficients. As is well known, some composite materials have extremely small values of Poisson's ratio, smaller than those of the materials used to make the composite.

Another example of interest in electronic applications is the acoustic wave velocity, which determines the resonant frequency of piezoelectric devices. For a long, thin rod, the velocity of waves propagating along the length of the rod is  $v = (E/\rho)^{1/2}$ , where  $E$  is Young's modulus and  $\rho$  is the density. Fiber-reinforced composites often have very anisotropic wave velocities. Consider a compliant matrix material reinforced with parallel fibers. Long, thin rods fashioned from the composite have different properties when the fibers are oriented parallel or perpendicular to the length of the rod. Much faster wave velocities are measured for longitudinal orientation than for transverse orientation of the fibers (Fig. 4). For the longitudinal case:

$$v_L = \sqrt{\frac{(E_f - E_m)v_f + E_m}{(\rho_f - \rho_m)v_f + \rho_m}}$$

and for transverse fibers:

$$v_t = \sqrt{\frac{E_m(1 + 2\nu_f)}{\rho_m + (\rho_f - \rho_m)(1 - \nu_f)}}$$

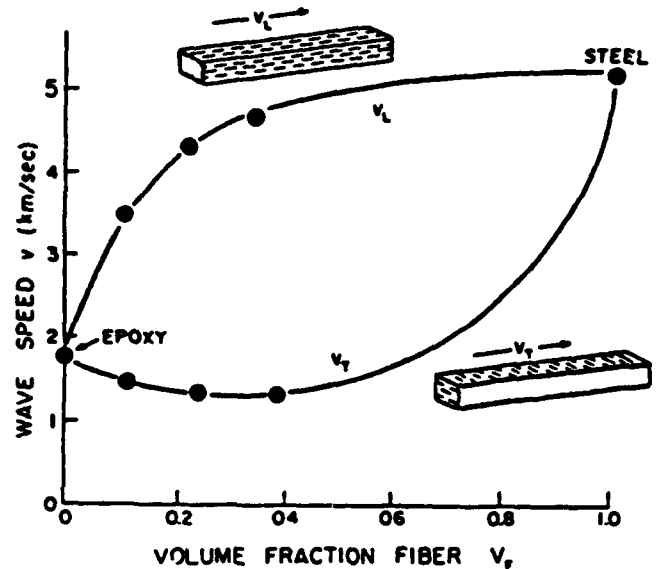


FIGURE 4 Speed of stress waves in composite materials made from steel filaments in epoxy. Waves traveling parallel to the filaments travel faster than transverse waves; the transverse waves are slower than waves in the pure epoxy matrix. (From Ref. 4.)

where  $E_f$  and  $E_m$  are the Young's modulus values for the fibers and matrix, respectively,  $\rho_f$  and  $\rho_m$  are the densities,  $v_f$  is the fiber volume fraction, and

$$n = \frac{(E_f/E_m) - 1}{(E_f/E_m) + 2}$$

Experimental data [4] for composites made from steel filaments embedded in epoxy conform closely to the equations for  $v_L$  and  $v_t$ . Note that  $v_t$ , the wave velocity for waves traveling transverse to the fibers, is less than the velocity in both epoxy and steel, the two phases that make up the composite. The slowness of this wave is caused by the fact that density and stiffness depend differently on volume fraction. This difference in mixing rules for  $E$  and  $\rho$  causes the combination property  $v_t$  to lie outside the range of the end members. The longitudinal wave  $v_L$  behaves more normally. In this case  $E$  and  $\rho$  follow the same mixing rule and the values for  $v_L$  lie between those of the end members.

Another example of unusual wave behavior occurs in composite transducers made from poled ferroelectric fibers embedded in an epoxy matrix [5]. When driven in thickness resonance, the regularly spaced fibers excite resonance modes in the polymer matrix, causing the matrix to vibrate with much larger amplitude than the piezoelectric fibers. The difference in compliance coefficients causes the nonpiezoelectric phase to respond far more than the stiff ceramic piezoelectric. Composite materials are therefore capable of mechanical amplification.

**TABLE 1**  
**Examples of Product Properties**

Property of Phase I	Property of Phase II	Composite Product Property
Thermal expansion	Electrical conductivity	Thermistor
Magnetostriction	Piezoelectricity	Magnetoelectricity
Hall effect	Electrical conductivity	Magnetoresistance
Photoconductivity	Electrostriction	Photostriction
Superconductivity	Adiabatic demagnetization	Electrothermal effect
Piezoelectricity	Thermal expansion	Pyroelectricity

### Product Properties

A product property utilizes different properties on the two phases of a composite to produce yet a third property through the interaction of the two phases. By combining different properties of two or more constituents, surprisingly large product properties are sometimes obtained with a composite. Indeed, in a few cases, product properties are found in composites that are entirely absent in the phases making up the composite. Table 1 lists a few of the hundreds of possible product properties, several of which are described in the following paragraphs.

In the magnetoresistive field plate developed by Weis [6], a composite of InSb and NiSb is directionally solidified to form parallel NiSb needles in an InSb matrix. A long rectangular segment of the composite is electroded across the ends, with the NiSb fibers parallel to the electrodes and transverse to the length of the composite (Fig. 5). InSb is a semiconductor with a large Hall effect, and NiSb is metallic with large electrical conductivity.

When an electric current flows along the length of the bar, and a magnetic field is applied perpendicular to the current and perpendicular to the NiSb needles, the current is deflected because of the Hall effect. Normally this would result in an electric field transverse to the current and the magnetic field, but the NiSb needles short out the field. Electric current continues to be deflected as long as the magnetic field is present. The resulting product property is a large magnetoresistance effect.

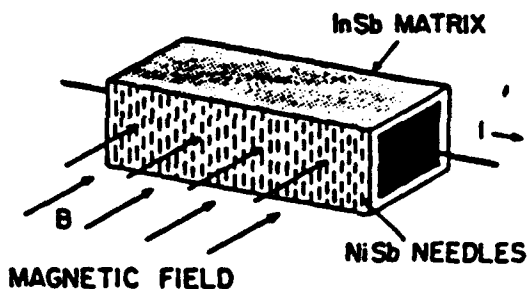


**FIGURE 5** Magnetoresistive field plate made from indium antimonide and nickel antimonide. The plate is used as a magnetic field sensor and a noncontacting variable resistor.

A second example of a product property is the superconducting stabilizer developed by W. N. Lawless [7]. The superconducting cable made of Nb<sub>3</sub>Sn is sheathed with a paramagnetic ceramic of CdCr<sub>2</sub>O<sub>4</sub>. Temperature fluctuations cause portions of the superconducting cable to revert to normal metallic behavior, thereby decreasing the superconducting electric current and the surrounding magnetic field it generates. The decrease in magnetic field demagnetizes the paramagnetic CdCr<sub>2</sub>O<sub>4</sub>, and lowers its temperature. This in turn cools the Nb<sub>3</sub>Sn cable, causing it to return to the superconducting state (Fig. 6).

A magnetoelectric composite made from ferroelectric BaTiO<sub>3</sub> and ferrimagnetic cobalt titanium ferrite has been studied by scientists from Philips Laboratory [8,9]. A dense intimate mixture of the perovskite and spinel-structure phase was obtained by directional solidification, and then electrically poled to make the BaTiO<sub>3</sub> phase piezoelectric (Fig. 7). When a magnetic field is applied to the composite, the ferrite grains change shape because of magnetostriction. The strain is passed along to the piezoelectric grains, resulting in an electrical polarization. Magnetoelectric effects a hundred times larger than those in Cr<sub>2</sub>O<sub>3</sub> are obtained this way. Subsequent research [10] has led to the development of a broadband magnetic field probe with an exceptionally flat frequency response up to 650 kHz.

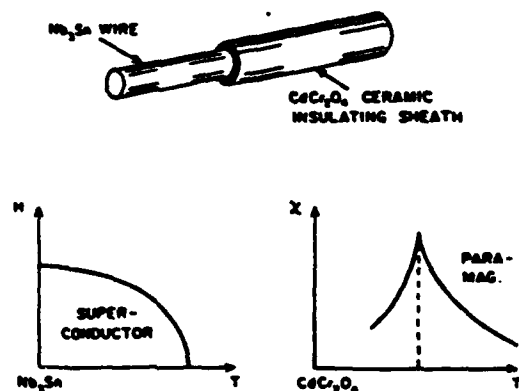
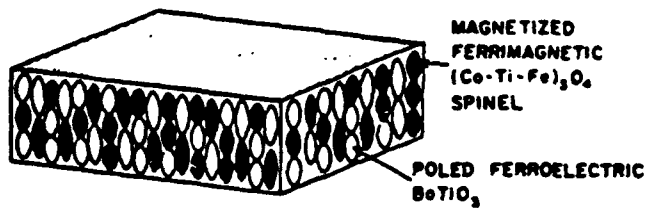


**FIGURE 6** Superconducting wire of Nb<sub>3</sub>Sn surrounded by a paramagnetic sheath of CdCr<sub>2</sub>O<sub>4</sub>.



#### PRODUCT PROPERTY

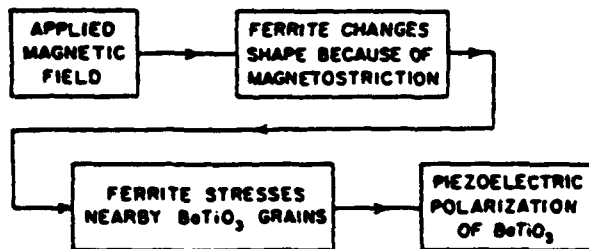


**FIGURE 7** Magnetoelectric transducer making use of the magnetostrictive effect of a ferrite mechanically coupled to piezoelectric barium titanate.

### Transport Properties of Composites

Conductor-filled composites are discussed in this section, emphasizing the importance of percolation in random and segregated mixes. Differential thermal expansion between matrix and filler sometimes leads to remarkable variations in resistance with temperature. Composite PTC thermistors and humidity sensors based on these ideas are described in this section.

#### Percolation and Segregated Mixing

Some of the principles can be illustrated with the work on wax-graphite composites carried out by Rajagopal and Satyam [11]. After melting the wax, the graphite par-

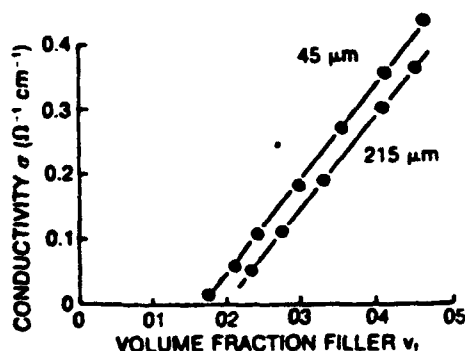


**FIGURE 8** Electrical conductivity of wax-graphite composites plotted as a function of composition. Critical volume fraction for percolation is determined by extrapolating the conductivity to zero. (From Ref. 11.)

ticles are stirred in and the composites pressed to remove porosity. Graphite grains 45 to 215  $\mu\text{m}$  in size were used in the study. A typical variation of conductivity with composition is shown in Figure 8. At approximately 20 vol % graphite, the resistance decreases rapidly as the graphite particles begin to contact one another. This critical volume fraction  $v_f$  is referred to as the percolation limit, and is evaluated by plotting conductivity on a linear scale versus volume fraction conducting filler (Fig. 8). The electrical conductivity of composites rich in filler is controlled by contacting graphite particles, whereas below the percolation limit the conductivity is controlled by the polymer. Near the percolation limit the conductivity is controlled by thin polymer layers between graphite particles. As shown in Figure 8, the critical volume fraction for 45  $\mu\text{m}$  graphite particles is smaller than that for 215  $\mu\text{m}$  particles.

The smaller particles show segregated mixing. The effect of particle size on mixing is illustrated in Figure 9, which compares the situations when the conducting particles are comparable in size to the insulating particles, and when the conducting particles are much smaller than the insulating particles. Percolation requires a larger volume fraction when the two types of particles are comparable in size. When the conducting particles are small, they are forced into interstitial regions between the insulating particles; this forces the conducting particles into contact with one another, resulting in a low percolation limit.

These ideas are borne out by experiments on copper particles embedded in a matrix of polyvinyl chloride [12]. Figure 10 shows the resistivity of Cu-PVC composites plotted as a function of volume fraction of copper. The critical volume fraction decreases markedly when the Cu particles are far smaller than the polymer particles. When the size ratio is 35:1, the critical volume percent is only 4% Cu. This highly segregated mixing establishes contact between conducting copper particles at a very low ratio of conductor to insulator.

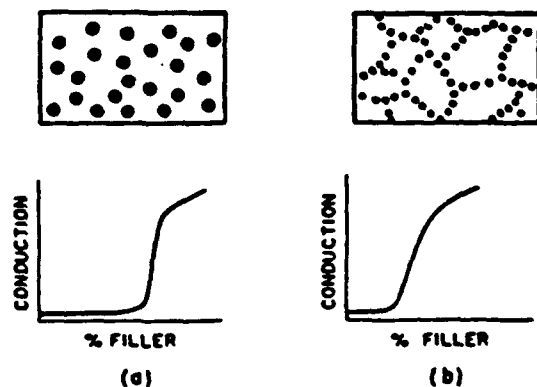


**FIGURE 9** Mixing of (a) equal-size particles and (b) large and small particles. The percolation limit is smaller when the conducting particles are segregated into interstitial sites between larger insulating particles.

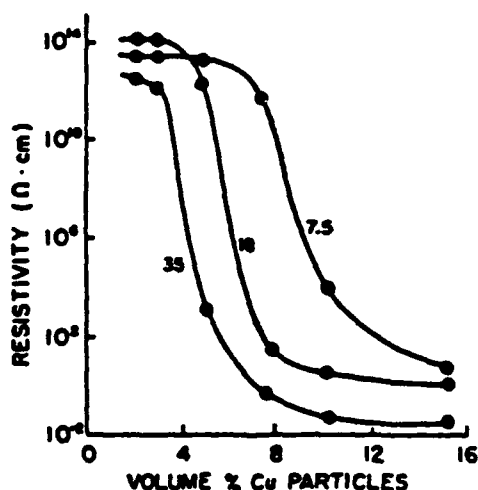


**FIGURE 10** Resistivity of Cu-PVC composites for several size ratios of PVC-Cu particles. Percolation occurs easily when the Cu particles are small and concentrated in grain boundary regions. (From Ref. 12.)

### Composite Thermistors

A second interesting effect is the dependence of electrical resistance on temperature. PTC thermistors are characterized by a positive temperature coefficient of electrical resistance. Doped barium titanate ( $\text{BaTiO}_3$ ) has a useful PTC effect in which the resistance undergoes a sudden increase of four orders of magnitude just above the ferroelectric Curie temperature ( $130^\circ\text{C}$ ). The PTC effect is caused by insulating Schottky barriers created by oxidizing the grain boundary regions between conducting grains of rare earth-doped  $\text{BaTiO}_3$ .

Similar PTC effects are observed when polymers are loaded near the percolation limit with a conducting filler. The Polyswitch overload protector (13) is made from high density polyethylene with carbon filler. At room temperature the carbon particles are in contact, giving resistivities of only  $1\ \Omega\text{-cm}$ , but on heating the polymer expands more rapidly than carbon, pulling the carbon grains apart and raising the resistivity. Polyethylene expands very rapidly near  $130^\circ\text{C}$ , resulting in a pronounced PTC effect comparable to that of  $\text{BaTiO}_3$ . A rapid increase in resistivity of six orders of magnitude occurs over a  $30^\circ$  temperature rise (Fig. 11).

As pointed out by Doljack (13), the carbon-polyethylene PTC thermistor has several advantages over  $\text{BaTiO}_3$ : (a) the room resistivity is lower, (b) it shows PTC behavior at high temperature, (c) the resistance is insensitive to voltage, and (d) the device has good thermal shock resistance. The principal drawback with Polyswitch composites seems to be the slow recovery time. Several hours are required for the resistance to return to within 10% of its initial value at room temperature. The slow recovery of base resistance is caused by polymer melting followed by secondary recrystallization and gradual reformation of the carbon black chains responsible for conduction.

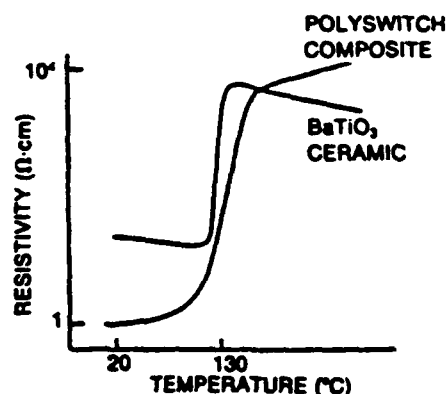


**FIGURE 11** Comparison of the PTC effects in  $\text{BaTiO}_3$  and carbon-polyethylene composites. The PTC effect is caused by the volume expansion of the polyethylene during an amorphous-crystalline phase transformation.

Similar, but less dramatic, changes in resistivity are observed in wax-graphite composites, where a threefold increase in resistivity occurs over a  $20^\circ\text{C}$  temperature rise (11). Not all composites show a PTC effect, however. Magnetite-alumina composites (14) made by arc plasma spray possess NTC behavior with a decrease of four orders of magnitude in resistivity on heating from  $100^\circ$  to  $300\ \text{K}$ . For composites containing 60 vol %  $\text{Fe}_3\text{O}_4$ , the magnetite particles remain in contact throughout the temperature range.

Combined NTC-PTC composites have also been constructed (15). Vanadium sesquioxide ( $\text{V}_2\text{O}_5$ ) has a metal-semiconductor transition near  $160\ \text{K}$  with a large increase in conductivity on heating (16). This material can be incorporated in a composite by mixing  $\text{V}_2\text{O}_5$  powder in an epoxy matrix. The filler particles are in contact at low temperatures and exhibit an NTC resistance change similar to that observed in  $\text{V}_2\text{O}_5$  crystals and single-phase ceramics. On heating above room temperature, the polymer matrix expands rapidly, pulling the  $\text{V}_2\text{O}_5$  grains apart and raising the resistance by many orders of magnitude. This produces a PTC effect similar to that in the Polyswitch composite. The net result is an NTC-PTC thermistor with a conduction "window" in the range  $-100^\circ\text{C}$  to  $+100^\circ\text{C}$ . This is a good example of the use of coupled phase transformations in composites.

Many interesting experiments remain to be done using electroceramic fillers in polymer matrices. In addition to the conductor particles just discussed, there are interesting combinations of piezoelectric (e.g., (17)), magnetic, pyroelectric, ferroelectric, varistor, thermistor, and insulator fillers to be explored.

### Porous Composites

Composite humidity sensors have been synthesized by loading lithium fluoride with alumina (18). Differential thermal contraction of the  $\text{LiF}$  matrix and  $\text{Al}_2\text{O}_3$  filler causes internal microcracks to open within the composite. The electrical resistance of this material is very sensi-

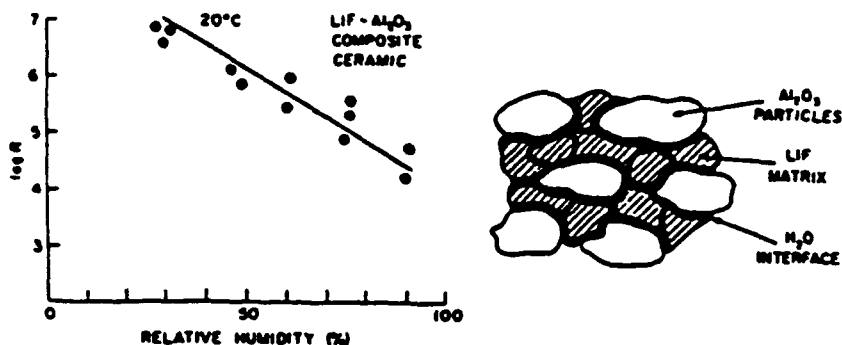


FIGURE 12 Electrical resistance of  $\text{Al}_2\text{O}_3$ -LiF composites used as humidity sensors.

tive to humidity (Fig. 12). Moisture penetrates into the microcracks, affecting the surface resistance. Conduction probably occurs by the Grothaus mechanism ( $\text{H}_3\text{O}^+ \rightleftharpoons \text{H}_2\text{O} + \text{H}^+$ ) at low humidity levels, and by  $\text{Li}^+$  ion conduction in adsorbed water layers at high humidity. In any case, the ceramic alumina particles play an interesting role in the composite: their presence initiates the microcracking responsible for increased surface conduction.

Composite gas sensors have been constructed on similar principles [19]. The addition of  $\text{Al}_2\text{O}_3$  to ZnO ceramics stabilizes a porous microstructure ideal for adsorption-desorption-type gas sensors. The porous texture enhances the electrical conductivity to such an extent that the sensitivity to flammable gases is adversely affected, but soaking the porous structure in a lithium-containing solution increases the resistivity, resulting in a reproducible gas sensor sensitive to methane, propane, and other hydrocarbon gases.

As pointed out by Yanagida [20], interactions between two different materials can give rise to very unusual phenomena. Dispersing a basic refractory ( $\text{MgCr}_2\text{O}_4$ ) in an acid refractory ( $\text{TiO}_2$ ) produces a composite humidity sensor suitable for monitoring cooking in electric ovens.

Contacts between *p*- and *n*-type ceramic grains are also sensitive to humidity [21]. The *I*-*V* characteristics of ZnO (*n*-type) and NiO (*p*-type) junctions change markedly with humidity and exposure to flammable gases.

Another interesting composite in which the ceramic filler plays an indirect role is the metal-ceramic contacts used for high current switches [22]. In one type, cadmium oxide particles are embedded in a silver metal matrix. Large switching currents sometimes cause localized melting, which welds the contact shut. When the silver grains melt in the composite, CdO grains are exposed, lowering the current flow and preventing welding. Cadmium oxide decomposes to prevent surface accumulation. This results in a blowing effect that quenches arc formation.

### Polychromatic Percolation

Transport by percolation through two or more materials can be visualized in terms of colors. Black and white

patterns (Fig. 13) illustrate percolation in a diphasic solid. Three kinds of percolation are possible: (a) percolation through an all-white path, (b) percolation through an all-black path, and (c) percolation through a combined black-white path. From a composite point of view, the third possibility is the most interesting because it offers the possibility of discovering new phenomena that are not present in either phase individually. Foremost among these effects are the interfacial phenomena, which arise by inserting a thin insulating layer between particles with high electrical conductivity. Varistors, PTC thermistors, and boundary-layer capacitors are examples. In ceramic varistors, conducting ZnO grains are surrounded by thin layers of  $\text{Bi}_2\text{O}_3$  insulation. The tunneling of electrons through this barrier gives rise to the varistor effect.

The two-color patterns in Figure 13 show how percolation depends on volume fraction for a random mix. As pointed out earlier, the percolation limit depends on connectivity. Highly connected segregated mixtures have lower percolation limits than random mixtures of low connectivity. Of the three kinds of transport paths, all three may occur in a diphasic composite with equal proportions of the two constituents. As pictured in Figure 13a, there are all-white paths, all-black paths, and black-white paths, with the last predominating. When one

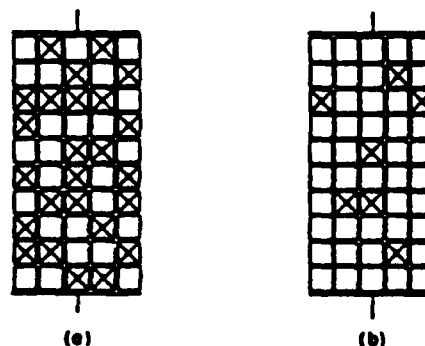
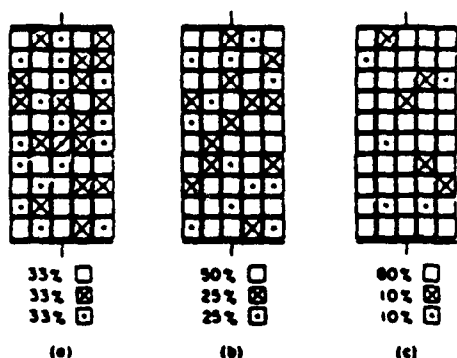


FIGURE 13 Black-and-white percolation patterns drawn for randomly mixed particles of equal size and shape. The black/white mixing ratios are 50/50 in (a) and 15/85 in (b).





**FIGURE 14** Tricolor percolation patterns drawn from randomly mixed particles of equal size and shape. Mixing ratios are (a) 33/33/33, (b) 50/25/25, and (c) 80/10/10.

color outnumbers the other (Fig. 13b), the minority phase may lose its connectivity as its volume fraction drops below the percolation limit.

Three-color percolation is illustrated in Figure 14. Seven kinds of conduction paths are possible: three monocolor, three bicolor, and one tricolor. When all three colors are present in equal amounts (Fig. 14a), it is possible that there will be no monocolor transport. In this case, bicolor and tricolor paths become important. Monocolor conduction paths become increasingly important as the volume fractions become unbalanced (Fig. 14b,c).

Ternary composition diagrams (Fig. 15) are useful in determining which types of conduction paths are to be

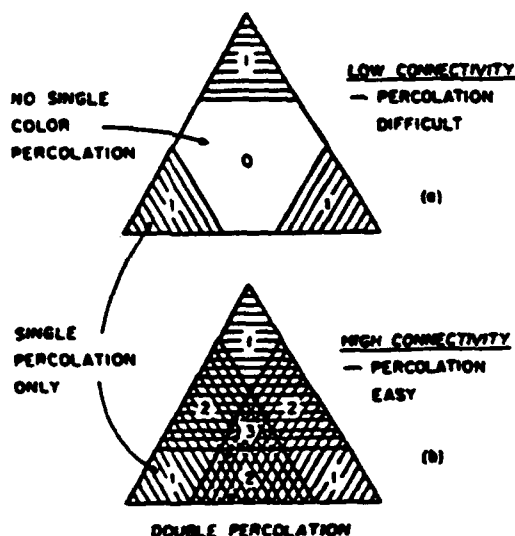


**FIGURE 15** Ternary percolation diagrams for tricolor composites. (a) A composite with low connectivity shows single-color percolation only near end-member compositions. (b) High connectivity promotes percolation throughout the diagram. All three colors can percolate simultaneously near the center of the diagram.

found in a composite. Figure 15a shows a symmetric three-phase composite with low connectivity. Only monocolor conduction composition regions are identified. Monocolor paths occur only when a high volume fraction of the color in question is present. No monocolor transport occurs for compositions near the center of the ternary system, although bicolor and tricolor paths are present.

The situation is very different for a tricolor system with high connectivity and easy percolation (Fig. 15b). In this case, the percolating limits for monocolor transport overlap to give regions in the ternary where two or three monocolor conduction paths coexist. Bicolor and tricolor paths also exist in the system. Connectivity requirements for polychromatic percolation have been discussed from a theoretical viewpoint by Zallen [23].

An example of coupled bicolor percolation is shown in Figure 16. Consider the situation where an insulating polymer matrix is partially filled with two kinds of particles. If the particles are of low connectivity, percolation occurs only when the matrix is filled to high levels. The conduction may be monocolor or bicolor, depending on the relative proportions of the two fillers.

For high connectivity fillers, conduction is much easier, and the ternary diagram possesses a region of overlap for monocolor conduction. At lower levels of filling, there is also a region where only bicolor transport is possible.

An asymmetric percolation diagram is shown in Figure 16. Here one filler has high connectivity, the other low. The high connectivity phase might be a finely divided material such as carbon; the low connectivity phase could be of coarser grain size.

An example of such a system is an easy-poling piezoelectric composite made up of two kinds of particles mixed in an insulating polymer matrix [24]. The first kind of particulate phase in a piezoelectric composite is PZT (lead zirconate titanate), a ferroelectric ceramic phase that must be poled to make it piezoelectrically active. Poling is difficult because the PZT grains are not in good electrical contact; and when shielded by a polymer, only

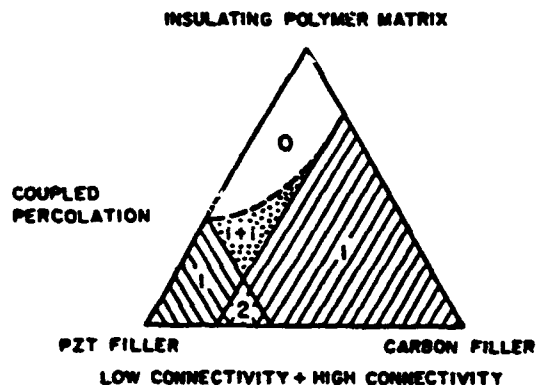


**FIGURE 16** Ternary percolation diagram for polymer-PZT-carbon composite. Composites can be poled in the 1 + 1 coupled percolation region.

a small fraction of the poling field penetrates into the ferroelectric PZT particles. To aid in poling, a small amount of a second conductive filler material is added. When a conductor is added and the composite is stressed, electrical contact is established between the ferroelectric grains, making poling possible (Fig. 17a-c). Pressure sensors of greater sensitivity can be obtained in this way [24].

Doubly filled composites are also used as backing materials for broadband piezoelectric transducers such as PZT. To efficiently couple the backing material to the transducer, it is necessary to match the acoustic impedance of the backing to that of the piezoelectric. The acoustic impedance of an isotropic solid is given by  $z = \rho v$ , where  $\rho$  is the density and  $v$  the acoustic wave velocity.

Two-phase mixtures consisting of a polymer matrix and a heavy metal filler provide the required high attenuation and a wide range of acoustic impedances. The filler particles scatter the acoustic waves efficiently, and polymers generally have high absorption coefficients; together the two provide the required high attenuation. Acoustic impedances of about  $30 \times 10^6 \text{ kg/m}^2\text{s}$  are required to match piezoelectric transducers made from PZT or  $\text{LiNbO}_3$ , but it is not easy to obtain such values with normal composite materials. In principle an epoxy-tungsten composite can provide a wide range of acoustic impedances ( $3\text{--}100 \times 10^6$ ), but in practice it is difficult to load the matrix to more than 70 vol % tungsten. It is

found that most of the change in impedance takes place at higher volume fractions. Metal matrix backing materials avoid this problem. Using lead-indium-based alloy as a matrix with copper and tungsten fillers gave impedance values closely matched to those of the transducers [25]. Three-phase backing materials such as this make excellent acoustic dampers with impedances in the range of  $20\text{--}45 \times 10^6 \text{ kg/m}^2\text{s}$ .

## Symmetry of Composite Materials

A wide variety of symmetries are found in composite materials. Examples of crystallographic groups, Curie groups, black-and-white groups, and color groups will be given, and the resulting effect on physical properties discussed.

In describing the symmetry of composite materials, the basic idea is Curie's principle of symmetry superposition: A composite material will exhibit only those symmetry elements that are common to its constituent phases and their geometrical arrangement.

The practical importance of Curie's principle rests on the resulting influence on physical properties. Generalizing Neumann's law from crystal physics: The symmetry elements of any physical property of a composite must include the symmetry elements of the point group of the composite. Applications of Neumann's law to single-crystal materials can be found in the book by Nye [26]. A discussion of more wide-ranging topics concerning the effects of symmetry has been given by Shubnikov and Koptsik [27].

## Laminate Symmetry

The laminated composites pictured in Figures 18, 19, and 20 are good illustrations of composite symmetry. In

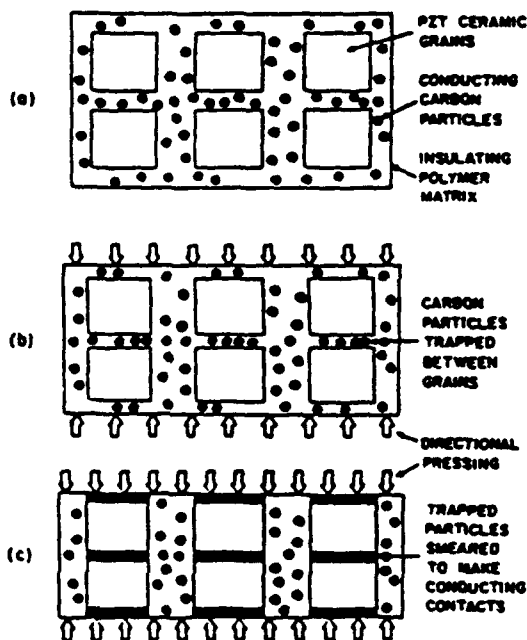


**FIGURE 17** Pressed ternary composites made by mixing PZT and carbon particles in an epoxy matrix. (a) Carbon particles are small ( $\sim 5 \mu\text{m}$ ) with low connectivity. When pressed, (b) the carbon particles are trapped between PZT grains to form conducting contacts in the poling direction (c).

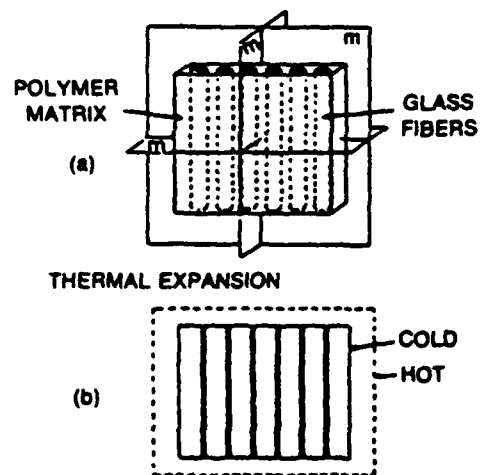


**FIGURE 18** (a) Unidirectional laminate consisting of parallel glass fibers in an epoxy matrix. (b) The orthorhombic  $mmm$  symmetry of the composite is maintained on heating.

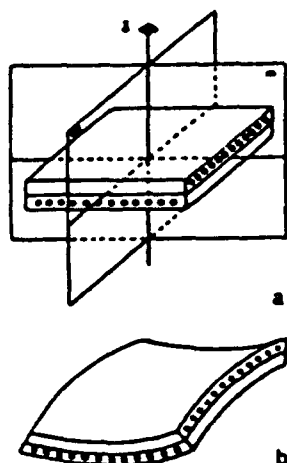


**FIGURE 19** (a) Cross-ply laminate containing orthogonal fibers in adjacent layers. (b) Double curvature occurs on heating, consistent with  $42m$  symmetry.

a unidirectional laminate (Fig. 18), the glass fibers are aligned parallel to one another, such that a laminate has orthorhombic symmetry (crystallographic point group  $mmm$ ). Mirror planes are oriented perpendicular to the laminate normal, and perpendicular to an axis formed by the intersection of the other two mirrors. The physical properties of a unidirectional laminate must therefore include the symmetry elements of point group  $mmm$ . If

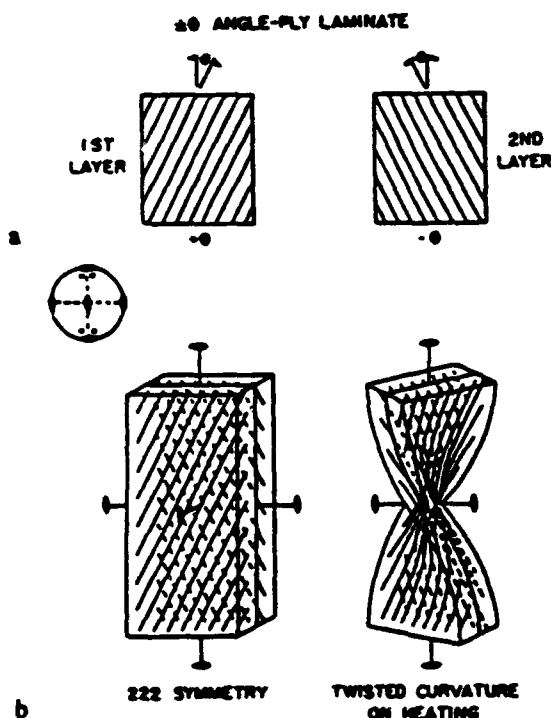


**FIGURE 20** (a)  $\pm \theta$  angle-ply laminate with  $222$  symmetry. (b) Twisted curvature develops when the temperature is raised.

the laminate is heated, it will change shape because of thermal expansion. Less expansion will take place parallel to the fiber axis because glass has a lower thermal expansion and greater stiffness than polymer. The laminate will therefore expand anisotropically, but it will not change symmetry. The heated laminate continues to conform to point group  $mmm$ .

A cross-ply laminate (Fig. 19) is made up of two unidirectional laminates bonded together with the fiber axes at  $90^\circ$ . Such a laminate belongs to tetragonal point group  $42m$ . The fourfold inversion axis is perpendicular to the laminated sheets and to both sets of glass fibers. Twofold symmetry axes are oriented perpendicular to the  $4$  axis and at  $45^\circ$  to the fiber axes. The tetragonal symmetry is maintained on heating. A double curvature distortion occurs, but the symmetry elements of point group  $42m$  are not violated.

Laminated composites with  $\pm \theta$  angle-ply alignment exhibit orthorhombic symmetry consistent with point group  $222$ . In a  $\pm \theta$  angle-ply laminate, the fibers in the first layer are oriented at an angle of  $\pm \theta$  with respect to the edge of the laminate. Fibers in the second layer form an angle of  $-\theta$  with the edge and an angle of  $2\theta$  with respect to the fibers in the first layer. Two twofold symmetry axes bisect the fiber directions, with a third perpendicular to the laminated layers. When heated, the layers twist, but the symmetry is unchanged (Fig. 20).

The thermal strains of the three laminated composites just discussed are excellent examples of Neumann's law. In all three cases the symmetry of the physical property includes that of the point group of the composite. Other properties of the composite obey Neumann's law as well. The elastic properties of an angle-ply metal matrix are graphed in Figure 21. Young's moduli are plotted as a function of the fiber angle  $\theta$ . Maximum anisotropy in Young's modulus is observed when the fibers in the adjacent layers are parallel to one another ( $\theta = 0^\circ$  or  $90^\circ$ ). In this case the symmetry of the composite is clearly orthorhombic, but as  $\theta$  approaches  $45^\circ$ , the anisotropy disappears until the symmetry becomes tetragonal at  $\theta = 45^\circ$ , corresponding to the cross-ply laminate situation.

The point groups for unidirectional laminates ( $mmm$ ), cross-ply laminates ( $42m$ ), and angle-ply laminates ( $222$ ) are examples of crystallographic symmetry in composite materials. More complicated symmetry patterns have been incorporated in three-dimensional weaves. Woven carbon-carbon composites are made from carbon fibers with infiltrated pyrolytic carbon (28). Aerospace engineers have found that weaves with cubic geometries show excellent ablation resistance. Cubic symmetry is obtained by weaving the fibers in directions corresponding to important symmetry directions in a cube. In one such pattern, the fiber axes are aligned perpendicular to one another along three nonintersecting  $\langle 100 \rangle$  directions. Another utilizes four nonintersecting  $\langle 111 \rangle$  directions as fiber directions. An even more complex weave is obtained by combining the  $\langle 100 \rangle$  and  $\langle 111 \rangle$  patterns in a seven-directional weave with faceted strands. In the carbon-carbon composites, 60–75% of the volume is occupied by carbon fibers.

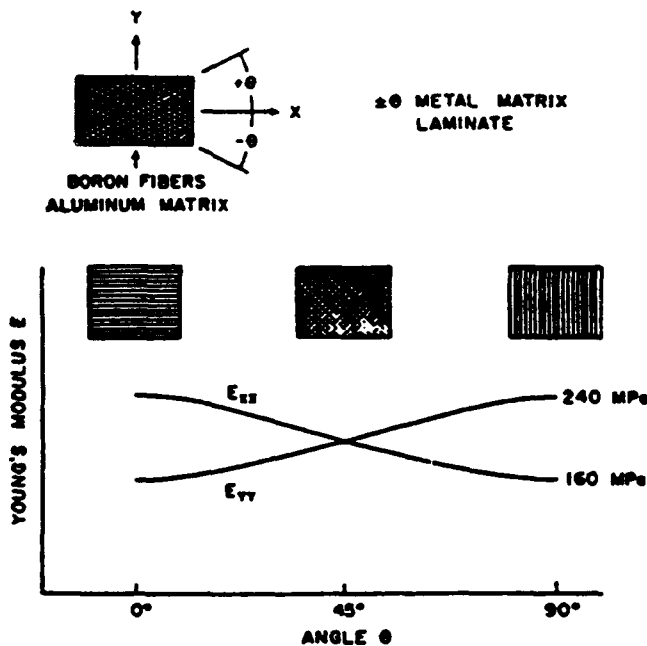


**FIGURE 21** Elastic properties of a boron fiber; aluminum matrix composite in  $\pm \theta$  angle-ply configuration. Young's moduli ( $E_{xx}$  and  $E_{yy}$ ) are plotted as a function of  $\theta$ . The symmetry changes from orthorhombic ( $E_{xx} \neq E_{yy}$ ) to tetragonal ( $E_{xx} = E_{yy}$ ) at  $\theta = 45^\circ$ , corresponding to cross-ply lamination.

### Extruded Geometries

Other types of symmetry elements can also be introduced during processing. The extruded honeycomb ceramics used as catalytic substrates are an interesting example [29]. By suitably altering the die used in extruding the ceramic slip, a large number of different symmetries can be incorporated into the composite body when the extruded form is filled with a second phase. Figure 22

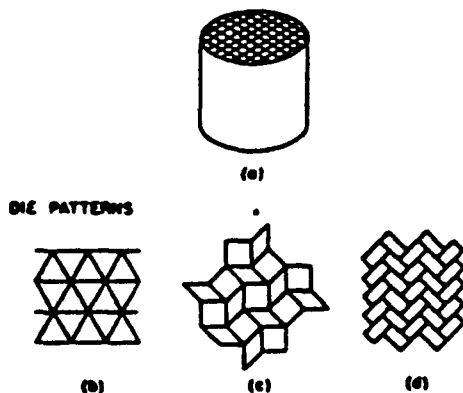


**FIGURE 22** (a) Electroceramic bodies can be extruded with many different symmetries. Monolithic honeycomb patterns with (b) hexagonal, (c) tetragonal, and (d) orthorhombic symmetries are illustrated.

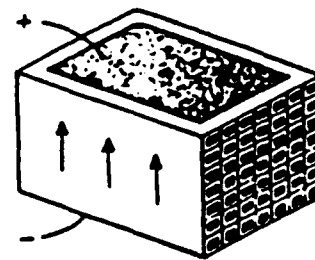


**FIGURE 23** Honeycomb pressure sensor extruded with tetragonal 4/mm symmetry and then transversely poled to give orthorhombic mm2 symmetry.

illustrates three of the extruded geometries with hexagonal, tetragonal, and orthorhombic symmetries. The orthorhombic pattern (Fig. 22d) resembles the cellular structure of wood in which cell walls terminate on adjacent transverse walls. Such a structure has excellent resistance to mechanical and thermal shock.

Lead zirconate titanate (PZT) honeycomb ceramics have been transformed into piezoelectric transducers by electroding and poling. The symmetry of the honeycomb transducers depends on the symmetry of the extruded honeycomb and also on the poling direction. For a square honeycomb pattern, the symmetry of the unpoled ceramic is tetragonal (4/mm) with fourfold axes parallel to the extrusion direction. When poled parallel to the same direction, the symmetry changes to 4mm. Longitudinally poled PZT composites have been investigated by Shrout and coworkers [30]. Transversely poled composites filled with epoxy are especially sensitive to hydrostatic pressure waves [31]. In this case the symmetry belongs to orthorhombic point group mm2 (Fig. 23).

Not all composites have crystallographic symmetry. Some belong to the seven limiting groups of  $\infty$ -fold symmetry axes (Fig. 24). The best known of the Curie groups

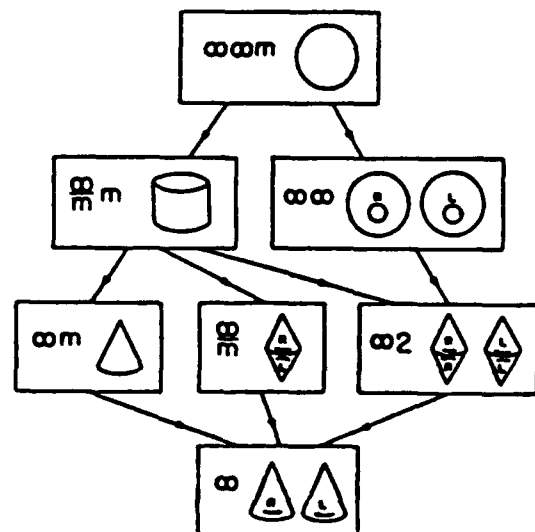


**FIGURE 24** Curie groups showing subgroup-supergroup relationships.

are those with spherical ( $\infty\infty m$ ), cylindrical ( $\infty/mm$ ), and conical ( $\infty m$ ) symmetry [27]. The remaining four groups exhibit right- and left-handed characteristics that can best be illustrated with various types of liquids.

An ordinary liquid (water or benzene) has spherical symmetry. In such a liquid, the molecules have no alignment or handedness; hence there are an infinite number of  $\infty$ -fold axes and mirror planes, corresponding to Curie group  $\infty\infty m$ . All other limiting groups are subgroups of  $\infty\infty m$ , as indicated in Figure 24.

The mirror planes are lost when the liquid possesses handedness. Dissolving sugar in water is a simple way of imparting handedness to water. Though randomly oriented in water, the sucrose molecules are all of the same handedness, thereby making the solution optically active. When dissolved in water, dextrose and levose—the right- and left-handed forms of sugar—give rise to the enantiomorphic forms of point group  $\infty\infty$ . This symmetry can be imposed on a composite material by incorporating randomly oriented molecules with a handedness within the body.

Point groups  $\infty\infty m$  and  $\infty\infty$  are consistent with random orientation of crystallites as well. A polycrystalline body of alumina (single-crystal symmetry  $3m$ ) belongs to  $\infty\infty m$ . The symmetry group of polycrystalline quartz (enantiomorphic single-crystal group  $32$ ) depends on the relative population of right- and left-handed grains. If the two were equal in population, as would normally be the case, the symmetry of a randomly oriented polycrystalline body would be  $\infty\infty m$ . If left-handed grains were systematically excluded, say by grinding up a right-handed crystal, the symmetry group would be  $\infty\infty$ .

Composite bodies with texture may belong to one of the five remaining Curie groups:  $\infty/mm$ ,  $\infty m$ ,  $\infty/m$ ,  $\infty 2$ , or  $\infty$ . All five groups have a special symmetry axis. Liquid crystals have orientational order, which conforms to Curie group symmetry. In nematic liquid crystals, the molecules are parallel to one another, giving cylindrical symmetry  $\infty/mm$ . When the molecules are parallel and polar, conical symmetry ( $\infty m$ ) is achieved. And if the liquid crystal molecules have handedness, or are stacked in helical fashion as in cholesteric liquids, then the symmetry group is  $\infty 2$ . Group  $\infty/m$  occurs in the unlikely circumstance that right- and left-handed molecules align with opposite polarity. Certain ferroelectric crystals such as  $Pb_2Ge_2O_{11}$  exhibit such ambidextrous behavior. The lowest symmetry Curie group, polar point group  $\infty$ , occurs in ferroelectric liquid crystals with handedness.

Mixed liquids can lead to some interesting symmetry changes. Mixing an enantiomorphic liquid ( $\infty\infty$ ) with a nematic liquid crystal ( $\infty/mm$ ) creates a "mixed drink" with symmetry  $\infty 2$  in accordance with the principle of symmetry superposition.

Physical forces or fields can be assigned to certain symmetry groups. As an example, consider a temperature gradient  $dT/dx$ . This is a vector that can be imposed on a composite material during processing, and if the material has a "memory," the vector nature of the temperature gradient will be retained after the temperature gradient is removed. The polar glass-ceramics developed at Penn State illustrate the idea [32]. A glass is crys-

tallized under a strong temperature gradient with polar crystals growing like icicles into the interior from the surface. Certain glass-ceramic systems such as  $Ba_2TiSi_2O_8$  and  $Li_2Si_2O_5$  show sizable pyroelectric and piezoelectric effects when prepared in this manner. Polar glass-ceramics belong to the Curie point group  $\infty m$ , the point group of a polar vector. As the glass is crystallized in a temperature gradient, it changes symmetry from spherical ( $\infty\infty m$ ) to conical ( $\infty m$ ), the same as that of a poled ferroelectric ceramic.

### Magnetic Curie Groups

Other physical forces can also be classified into Curie group symmetries. The chart in Figure 25 is helpful in relating these symmetries. To describe the magnetic fields and properties, it is necessary to introduce the black-and-white Curie groups. Magnetic fields are represented by axial vectors with symmetry  $\infty/mm'$ . The symbol  $m'$  indicates that the mirror planes parallel to the magnetic field are accompanied by time reversal. The relationship between black-and-white Curie groups is shown in Figure 25. The symbol  $l'$  is added to the Curie group symbols to indicate that in normal Curie groups all symmetry elements occur twice, both with and without time reversal.

Polar vectors such as temperature gradient or an electric field belong to Curie group  $\infty ml'$ . Tensile stress is represented by a second-rank tensor belonging to cylindrical group  $\infty/mm'l'$ .

The symmetry superposition principle applies to the point groups in Figure 25. In the magnetoelectric composites made from ferroelectric and ferromagnetic phases, the symmetry of the poling fields is retained through domain wall motion. If the electric and magnetic poling fields are applied in the same direction, the symmetry of the composite is  $\infty m'$ . When the poling fields are perpendicular to one another, the symmetry group is  $2'mm'$ . This point group also applies to the  $NiSb$ - $InSb$  field plate described earlier.

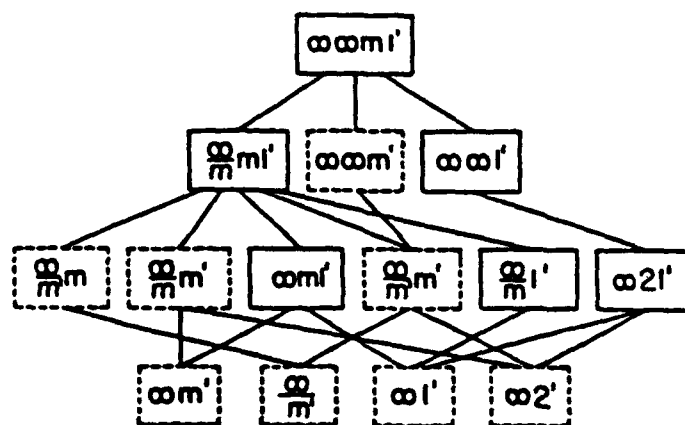
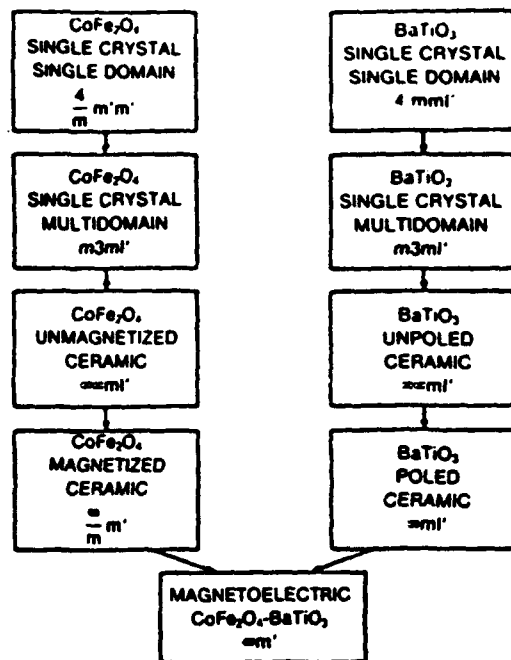


FIGURE 25 Curie groups (solid boxes) and their magnetic derivatives (dashed boxes).



**FIGURE 26** Symmetry derivation for a polycrystalline  $\text{BaTiO}_3\text{-CoFe}_2\text{O}_4$  magnetoelectric composite poled and magnetized in parallel electric and magnetic fields.

To summarize the symmetry of composites, some composites belong to crystallographic point groups (cross-ply laminate  $42m$ ), some to limiting groups (polar glass-ceramics  $mm$ ), and some to black-and-white limiting groups (magnetoelectric composite  $mm'$ ). Composites containing more than two phases can be described by color group symmetry.

The magnetoelectric composite described previously is an excellent illustration of the importance of symmetry in composite materials. Figure 26 shows the change in symmetry going from domain single crystals of  $\text{CoFe}_2\text{O}_4$  and  $\text{BaTiO}_3$  through multidomain and polycrystalline states to a polycrystalline composite that has been poled and magnetized in parallel E and H fields. In com-

**TABLE 3**  
Number of Independent Property Coefficients for the Fourteen Magnetic Curie Groups\*

Magnetic Curie Group	$i$	$\chi$	$\alpha$	$Q$
$mmm$	0	1	0	0
$mm'm'$	0	1	0	0
$mmm'$	0	1	0	0
$mm/mm'$	0	2	1	1
$mm/mm$	1	2	0	3
$mm'/m'$	0	2	1	0
$mm'/m$	0	2	2	0
$mm/m$	1	2	1	4
$mm'/m'$	0	2	3	0
$mm$	0	2	1	1
$mm'$	1	2	2	3
$mm2$	0	2	2	1
$mm2'$	1	2	1	3
$mm$	1	2	3	4

\* Axial tensors of rank 1, 3, and 4 are represented by pyromagnetism ( $i$ ), magnetoelectricity ( $\alpha$ ), and piezomagnetism ( $Q$ ). Magnetic susceptibility coefficients behave as a polar second-rank tensor.

binning a magnetized ceramic (symmetry group  $mm'/m'$ ) with a poled ferroelectric ceramic (symmetry group  $mm'$ ), the symmetry of the composite is obtained by retaining the symmetry elements common to both groups:  $mm'$ .

An interesting feature of this symmetry description is its effect on physical properties. According to Neumann's law, the symmetry of a physical property of a material must include the symmetry elements of the point group. The symmetry of a magnetized ceramic and a poled ferroelectric both forbid the occurrence of magnetoelectricity, but their combined symmetry ( $mm'$ ) allows it. By incorporating materials of suitable symmetry in a composite, new and interesting product properties can be expected to occur.

A listing of property coefficients for the Curie groups and their magnetic analogues is presented in Tables 2 and 3.

**TABLE 2**  
Number of Independent Property Coefficients for the Seven Curie Groups\*

Curie Group	$p$	$\epsilon$	$d$	$s$	$g$
$mmm'$	0	1	0	2	0
$mm'm'$	0	1	0	2	1
$mm/mm'$	0	2	0	5	0
$mm'/m'$	0	2	0	5	0
$mm'$	1	2	3	5	0
$mm2'$	0	2	1	5	2
$mm'$	1	2	4	5	2

\* Polar tensors of rank 1 through 4 are represented by pyroelectricity ( $p$ ), permittivity ( $\epsilon$ ), piezoelectricity ( $d$ ), and elastic compliance ( $s$ ). Optical activity coefficients ( $g$ ) constitute an axial second-rank tensor.

## Connectivity

Connectivity [33] is a key feature in property development in multiphase solids, since physical properties can change by many orders of magnitude depending on the manner in which connections are made. Imagine, for instance, an electric wire in which the metallic conductor and its rubber insulation were connected in series rather than in parallel. Obviously, its resistance would be far higher.

Each phase in a composite may be self-connected in zero, one, two, or three dimensions. It is natural to confine attention to three perpendicular axes because all property tensors are referred to such systems. If we limit

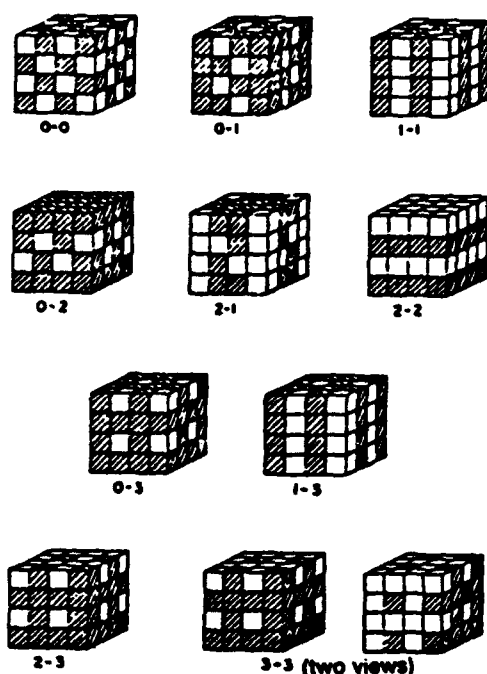


**FIGURE 27** Ten connectivity patterns used to describe the tensor properties of diphasic composites. (From Ref. 33.)

the discussion to diphasic composites,\* there are ten connectivities [33]: 0-0, 1-0, 2-0, 3-0, 1-1, 2-1, 3-1, 2-2, 2-3, and 3-3. The ten different connectivities are illustrated in Figure 27, using a cube as the basic building block. A 2-1 connectivity pattern, for example, has one phase self-connected in two-dimensional chains or fibers. The connectivity patterns are not generally unique. In the case of a 2-1 pattern, the fibers of the second phase might be perpendicular to the layers of the first phase, as in Figure 27, or they might be parallel to the layers.

During the past few years we have been developing processing techniques for making ceramic composites with different connectivities [34]. Extrusion, tape casting, and replamine methods have been especially successful. The 3-1 connectivity pattern in Figure 27 is ideally suited to extrusion processing. A ceramic slip is extruded through a die giving a three-dimensionally connected pattern with one-dimensional holes, which can later be filled with a second phase (see Fig. 23).

Another type of connectivity well suited to processing is the 2-2 pattern made up of alternating layers of the two phases. The tape casting of multilayer capacitors

\* Connectivity patterns for more than two phases are similar to the diphasic patterns, but more numerous. There are 20 three-phase patterns and 35 four-phase patterns, compared to the 10 two-phase patterns in Figure 27. For  $n$  phases the number of connectivity patterns is  $(n + 3)!/3n!$ . Triphasic connectivity patterns are important when electrode patterns are incorporated in the diphasic ceramic structures discussed later.

with alternating layers of metal and ceramic is a way of producing 2-2 connectivity. In this arrangement, both phases are self-connected in the lateral  $X$  and  $Y$  directions but not connected perpendicular to the layer along  $Z$ .

In 3-2 connectivity, one phase is three-dimensionally connected, the other two. This pattern can be considered a modified multilayer pattern with 2-2 connectivity. If holes are left in the layers of one phase, layers of the second phase can connect through the holes, giving three-dimensional connectivity.

The most complicated, and in many ways the most interesting, pattern is 3-3 connectivity in which the two phases form interpenetrating three-dimensional networks. Patterns of this type often occur in living systems such as coral, where organic tissue and an inorganic skeleton interpenetrate one another. These structures can be replicated in other materials using the lost-wax method. The replamine process, as it is called, can also be used to duplicate the connectivity patterns found in foam, wood, and other porous materials [35].

### Stress Concentration

The importance of stress concentration in composite materials is well known from structural studies, but its relevance to electroceramics is not so obvious. Stress concentration is a key feature of many of the piezoelectric composites made from polymers and ferroelectric ceramics [34]. By focusing the stress on the piezoelectric phase, some of the piezoelectric coefficients can be enhanced and others reduced [33].

As an example, consider the piezoelectric voltage coefficient  $\bar{g}_{33}$ , relating electric field to applied stress. Both the tensile stress  $\sigma_3$  and the resulting electric field  $E_3$  are parallel to the poling direction.

If the two phases of the composite are arranged in parallel, the stress acting on the more compliant phase will be transferred to the stiffer phase. Under these circumstances, the voltage coefficient is:

$$\bar{g}_{33} = \frac{E_3}{\sigma_3} = \frac{\bar{d}_{33}}{\bar{\epsilon}_{33}} = - \frac{{}^1V^1d_{33}^2s_{33} + {}^2V^2d_{33}^1s_{33}}{({}^1V^2s_{33} + {}^2V^1s_{33})({}^1V^1\epsilon_{33} + {}^2V^2\epsilon_{33})}$$

In this expression the properties of the two phases are designated with superscripts 1 and 2. Symbols  ${}^1V$ ,  ${}^1d_{33}$ ,  ${}^1\epsilon_{33}$  and  ${}^2s_{33}$  represent the volume fraction of phase 1 and its piezoelectric charge coefficient, electric permittivity, and elastic compliance. The corresponding properties of the second phase are  ${}^2V$ ,  ${}^2d_{33}$ ,  ${}^2\epsilon_{33}$ , and  ${}^2s_{33}$ .

A composite of interest here is that of a ferroelectric ceramic (phase 1) in parallel with a compliant polymer (phase 2). In this case  ${}^1d_{33} \gg {}^2d_{33}$ ,  ${}^1s_{33} \ll {}^2s_{33}$ ,  ${}^1\epsilon_{33} \gg {}^2\epsilon_{33}$ , and:

$$\bar{g}_{33} = \frac{{}^1d_{33}}{{}^1V^1\epsilon_{33}} = \frac{{}^1g_{33}}{{}^1V}$$

If 90% of the composite volume is polymer, then  ${}^1V = 0.1$  and  $\bar{g}_{33}$  is ten times larger than the voltage coefficient  $c$

the ceramic,  $\bar{g}_{33}$ . Excellent hydrophone designs are obtained in this way [34].

Advantageous internal stress transfer can also be utilized in pyroelectric coefficients. If the two phases have different thermal expansion coefficients, there is stress transfer between the phases that generates the electric polarization through the piezoelectric effect. In this way it is possible to make a composite pyroelectric in which neither phase is pyroelectric [33].

### Electric Field Concentration

The multilayer design used for ceramic capacitors is an effective configuration for concentrating electric fields. By interleaving metal electrodes and ceramic dielectrics, relatively modest voltages are capable of producing high electric fields.

Multilayer piezoelectric transducers are made in the same way as multilayer capacitors [36]. The oxide powder is mixed with an organic binder and tape-cast using a doctor blade configuration. After drying, the tape is stripped from the substrate, and electrodes are applied with a screen printer and electrode ink. A number of pieces of tape are then stacked, pressed, and fired to produce a ceramic with internal electrodes. After attaching leads, the multilayer transducer is packaged and poled. When compared to a simple piezoelectric transducer, the multilayer transducer offers a number of advantages:

1. The internal electrodes make it possible to generate larger fields for smaller voltages, eliminating the need for transformers for high power transmitters. Ten volts across a tape-cast layer 100  $\mu\text{m}$  thick produces an electric field of  $10^5$  V/m, not far from the depoling field of PZT.
2. The higher capacitance inherent in a multilayer design may also help in impedance matching.
3. Many different electrode designs can be used to shape poling patterns, which in turn control the mode of vibration and the ultrasonic beam pattern.
4. Additional design flexibility can be produced by interleaving layers of different composition. One can alternate ferroelectric and antiferroelectric layers, for instance, thereby increasing the depoling field.
5. Grain-oriented piezoelectric ceramics can also be tape cast into multilayer transducers. Enhanced piezoelectric properties are obtained by aligning the crystallites parallel to the internal electrodes [37].
6. Another advantage of the thin dielectric layers in a multilayer transducer is improved electric breakdown strength. Gerson and Marshal [38] measured the breakdown strength of PZT as a function of specimen thickness. The DC breakdown field for ceramics 1 cm thick was less than half that for 1 mm thick samples. It is likely that the trend continues to even thinner specimens, leading to improved poling and more reliable transducers.

Perhaps even more important than these factors is the enhancement of electrostrictive effects. Electrostriction is a second-order electromechanical coupling between strain and electronic field. For small fields, electrostrictive strains are small compared to piezoelectric strain, but this is not true for the high fields generated in multilayer transducers.

Multilayer electrostrictive transducers [39] made from relaxor ferroelectrics such as lead magnesium niobate (PMN) are capable of generating strains larger than PZT (Fig. 28). Since there are no domains in PMN, there are no "walk-off" effects in electrostrictive micropositioners. Moreover, poling is not required, and there are no aging effects. The concentration of electric fields makes nonlinear effects increasingly important.

### Multilayer Thermistors

For many applications it is desirable to lower the room temperature resistance because the thermistor elements are often connected in series with the circuit elements they are designed to protect. It is possible, of course, to lower the resistivity of the composite by altering the components, but the resistivity cannot be lowered indefinitely without degrading the PTC thermistor effect.

The introduction of internal electrodes offers a way to reduce the resistance per unit volume without affecting the temperature characteristics. Thermistor devices are presently being fabricated as ceramic discs or as composite wafers. Recently we developed a way of making multilayer  $\text{BaTiO}_3$  PTC thermistors [40] that greatly lowers the room temperature resistance. Barium titanate powder doped with rare-earth ions is mixed with an organic binder and tape cast on glass slides. Electrodes are then screen-printed on the tapes, followed by stack-

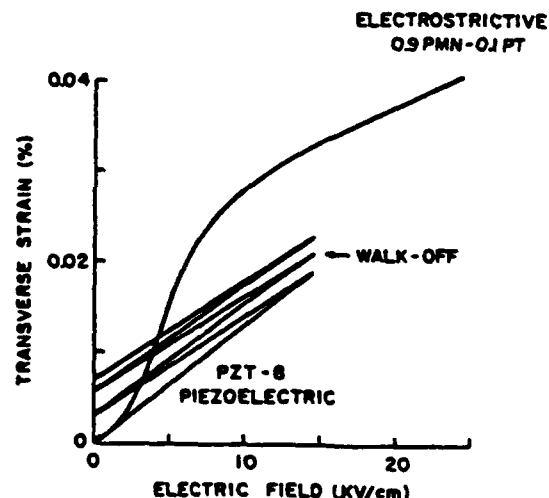


FIGURE 28 Comparison of electrostrictive and piezoelectric micropositioners. Nonlinear effects become important in multilayer composites where the electric fields are large.



ing, pressing, and firing. The internal electrode configuration is very similar to that of multilayer capacitors.

The basic idea involves comparison of a single-layer disk thermistor with a multilayer thermistor of the same external dimensions. The multilayer device is assumed to have  $n$  ceramic layers and  $n + 1$  electrodes. Let  $A$  represent the area of the single-layer disk thermistor,  $t$  its thickness, and  $\rho$  the resistivity. The resistance of the disc thermistor is:

$$R_s = \frac{\rho t}{A}$$

For the multilayer thermistor, the total electroded area is  $nA$  (neglecting margins) and the thickness is  $t/n$  (neglecting the electrode thickness). The resistance of the multilayer device is:

$$R_M = \frac{\rho(t/n)}{nA} = \frac{R_s}{n^2}$$

The resistivity of the thermistor is lowered by a factor of  $1/n^2$  with  $n - 1$  internal electrodes.

We have demonstrated the feasibility of this idea with a multilayer device containing four tape-cast layers. As predicted, the resistance of the multilayer specimen is approximately  $n^2$  ( $=16$ ) times smaller with very little change in the temperature characteristic.

## Summary

Some of the basic ideas underlying composite electroceramics have been illustrated in this module. By way of summary, we might state them as Ten Commandments:

1. *Sum properties* involve the averaging of similar properties in the component phases, with the mixing rules bounded by the series and parallel models. For a simple sum property such as the dielectric constant, the dielectric constant of the composite lies between those of the individual phases. This is not true for *combination properties* based on two or more properties. Acoustic velocity depends on stiffness and density, and since the mixing rules for these two properties are often different, the acoustic velocity of a composite can be smaller than those of its constituent phases.

2. *Product properties* are even more complex because three properties are involved: different properties in the constituent combine to yield a third property in the composite. In a magnetoelectric composite, the piezoelectric effect in barium titanate acts on the magnetostrictive effect of cobalt ferrite to produce a composite magnetoelectric effect.

3. *Connectivity patterns* are a key feature of composite electroceramics. The self-connectiveness of the phases determines whether series or parallel models apply, and thereby minimizes or maximizes the properties of the composite. The three-dimensional nature of the connectivity patterns makes it possible to minimize some tensor

components while maximizing others. Piezoelectric composites made from parallel ferroelectric fibers have large  $d_{31}$  coefficients and small  $d_{31}$  values.

4. *Concentrated field and force patterns* are possible with carefully selected connectivities. Using internal electrodes, electrostrictive ceramics are capable of producing strains comparable to the best piezoelectrics. Stress concentration is achieved by combining stiff and compliant phases in parallel. A number of different hydrophone designs are based on this principle.

5. *Periodicity and scale* are important factors when composites are to be used at high frequencies where resonance and interference effects occur. When the wavelengths are on the same scale as the component dimension, the composite no longer behaves like a uniform solid. The colorful interference phenomena observed in opal and feldspar minerals are interesting examples of natural composites. Acoustic analogues occur in the PZT-polymer composites used as biomedical transducers.

6. *Symmetry* governs the physical properties of composites just as it does in single crystals. The Curie principle of symmetry superposition and Neumann's law can be generalized to cover fine-scale composites, thereby elucidating the nature of their tensor properties. As in the case of magnetoelectric composites, sometimes the composite belongs to a symmetry group that is lower than any of its constituent phases. Unexpected product properties occur under such circumstances.

7. *Interfacial effects* can lead to interesting barrier phenomena in composites. ZnO-Bi<sub>2</sub>O<sub>3</sub> varistors and carbon-polymer PTC thermistors are important examples of Schottky barrier effects. Barrier-layer capacitors made from conducting grains separated by thin insulating grain boundaries are another example.

8. *Polychromatic percolation* is an interesting concept that has yet to be fully explored. Composites fabricated from two or more conducting phases can have several kinds of transport paths, both single-phase and mixed, depending on percolation limits and volume fractions. Carbon-PZT-polymer composites can be poled because polychromatic percolation establishes flux continuity through ferroelectric grains. The SiC-BeO composites under development as substrate ceramics are another example. These diphasic ceramics are excellent thermal conductors and poor electrical conductors at one and the same time. A thin layer of BeO-rich carbide separates the SiC grains, insulating them from one another electrically, but providing a good acoustic impedance match ensuring phonon conduction.

9. *Coupled phase transformations* in polyphasic solids introduce additional possibilities. Recently discovered NTC-PTC composites made from V<sub>2</sub>O<sub>5</sub> powder and embedded in polyethylene combine matrix and filler materials with complementary properties. At low temperatures the vanadium oxide particles are in a semiconducting state and in intimate contact with one another. On passing through a semiconductor-metal transition, the electrical conductivity increases by five orders of magnitude. Further heating brings the polymer to a phase transformation, causing a rapid expansion in vol-

ume and pulling the  $V_2O_5$  particles apart. As a consequence, the electrical conductivity decreases dramatically, by eight orders of magnitude. In addition to this "window material" with a controlled conductivity range, several other composites with coupled phase transformations were described.

10. Porosity and inner surfaces play a special role in many electroceramic composites used as sensors. Humidity sensors made from  $Al_2O_3$  and LiF have high inner surface area because of thermally induced fracture. The high surface area and hygroscopic nature of the salt result in excellent moisture sensitivity of the electrical resistance. Chemical sensors based on similar principles can be constructed in the same way.

R. E. Newnham

## References

1. J. Van Suchtelen, *Philips Res. Rep.*, 27, 28 (1972).
2. G. Partridge, *Glass Technology*, 24, 293 (1983).
3. D. Payne, Ph.D. Dissertation in Solid State Science, The Pennsylvania State University, 1973.
4. J. Ross and R. Sierakowski, *Shock and Vibration Digest*, 7, 1 (1975).
5. T. R. Gururaja, Ph.D. Thesis in Solid State Science, The Pennsylvania State University, 1984.
6. H. Weis, *Met. Trans.*, 2, 1513 (1971).
7. W. N. Lawless, private communication.
8. J. van den Boomgaard, D. R. Terrell, R. A. J. Born, and H. F. J. I. Giller, *J. Mat. Sci.*, 9, 1705 (1974).
9. A. M. J. G. van Run, D. R. Terrell, and J. H. Scholing, *J. Mat. Sci.*, 9, 1710 (1974).
10. L. P. M. Bracke and R. G. Van Vliet, *Int. J. Electronics*, 51, 255 (1981).
11. G. Rajagopal and M. Satyam, *J. Appl. Physics*, 49, 5536 (1978).
12. S. K. Bhattacharya and A. C. D. Chaklader, *Polym. Plast. Tech. Eng.*, 19, 21 (1982).
13. F. A. Doljack, *Trans. I.E.E.E. CHMT-4*, 372 (1981).
14. D. P. H. Smith and J. C. Anderson, *Phil. Mag.*, B43, 811 (1981).
15. K. A. Hu, B. V. Hiremath, T. P. Runt, and R. E. Newnham, *J. Amer. Ceramic Soc.*, 70, 583 (1987).
16. F. J. Morin, *Phys. Rev. Lett.*, 3, 34 (1959).
17. J. A. Chilton and M. T. Goosey, *Composite Polymers*, 3(2), 71 (1990).
18. B. C. Tofield and D. E. Williams, *Solid State Ionics*, 83, 1299 (1983).
19. Y. Takuma, M. Miyoyama, and H. Yanagida, *Chemistry Letters*, 1982, 345 (1982).
20. H. Yanagida, *Bull. Am. Ceram. Soc.*, 63, 1135 (1984).
21. Y. Toyoshima, S. Miyayama, and H. Yanagida, *Japan J. Appl. Phys.*, 22, 1933 (1983).
22. D. Stockel, *Proceedings of the A.I.M.E. Conference on Composites*, 1975, p. 129.
23. R. Zallen, *Phys. Rev. B* 16, 1426 (1977).
24. G. Sa-gong, A. Safari, and R. E. Newnham, *Ferroelectrics Letters*, 5, 131 (1986).
25. Y. Bar-Cohen, D. A. Stubbs, and W. C. Hopps, *J. Acoust. Soc. Amer.*, 75, 1629 (1984).
26. J. F. Nye, *Physical Properties of Crystals*, Oxford University Press, 1957.
27. A. V. Shubnikov and V. A. Koptsik, *Symmetry in Science and Art*, Plenum Press, New York, 1974.
28. J. J. Gebhardt, A. C. S. Symposium Series 21, 1976, p. 212.
29. I. M. Lachman, R. D. Bagley, and R. M. Lewis, *Bull. Amer. Ceram. Soc.*, 60, 202 (1981).
30. T. R. Shrout, L. J. Bowen, and W. A. Schulze, *Mat. Res. Bull.*, 15, 1371 (1980).
31. A. Safari, A. Halliyal, R. E. Newnham, and I. M. Lachman, *Mat. Res. Bull.*, 17, 302 (1982).
32. A. Halliyal, A. S. Bhalla, and R. E. Newnham, *Mat. Res. Bull.*, 18, 1007 (1983).
33. R. E. Newnham, D. P. Skinner, and L. E. Cross, *Mat. Res. Bull.*, 13, 525 (1978).
34. R. E. Newnham, L. J. Bowen, K. A. Klicker, and L. E. Cross, *Materials in Eng.*, 11, 93 (1980).
35. R. A. White, J. N. Weber, and E. W. White, *Science*, 176, 922 (1972).
36. G. O. Dayton, W. A. Schulze, T. R. Shrout, S. Swartz, and J. V. Biggers, *Adv. in Ceramics*, 9, 115 (1984).
37. M. Granahan, M. Holmes, W. A. Schulze, and R. E. Newnham, *J. Amer. Ceram. Soc.*, 64, C68 (1981).
38. R. Gerson and T. C. Marshall, *J. Appl. Phys.*, 30, 1650 (1959).
39. K. Uchino, S. Nomura, L. E. Cross, R. E. Newnham, and S. J. Jang, *J. Mat. Sci.*, 16, 569 (1981).
40. B. V. Hiremath, R. E. Newnham, and A. Amin, *Ferroelectrics Letters*, 8, 1 (1987).

## **APPENDIX 5**

**TUNABLE TRANSDUCERS AS SMART MATERIALS**  
Michael Blaszkiewicz, Robert E. Newnham and Q.C. Xu  
Materials Research Laboratory  
Pennsylvania State University  
University Park, PA 16802

**Abstract**

A solid-state tunable transducer has been developed by incorporating an elastically nonlinear material, silicone rubber, into an electroacoustic transducer made from piezoelectric ceramics. The resonant frequency and mechanical  $Q$  of the transducer are tuned mechanically by applying a uniaxial compressive stress to the composite. The resonant frequency is tuned electrically by placing a piezoelectric actuator into the composite and varying the magnitude of the d.c. bias.

**Introduction**

Smart materials sense a change in the environment and, using a feedback system, make a useful response with an actuator. Examples of passively smart and actively smart materials have been described in a recent review paper.(1) Passively smart materials have self repair mechanisms or standby phenomena that enable the material to withstand a sudden change in the environment. Ceramic varistors and positive temperature coefficient (PTC) thermistors are passively smart materials in which the electrical resistance changes reversibly with voltage (varistor) or temperature (thermistor). When struck by lightning, a zinc oxide varistor exhibits a large decrease in its electrical resistance, and the current is shorted to ground. This change in resistance is reversible. PTC thermistors, such as doped barium titanate ( $\text{BaTiO}_3$ ), show a large increase in electrical resistance at the ferroelectric-paraelectric phase transformation ( $\sim 130^\circ \text{C}$ ). The increase in resistance protects circuit elements against large current surges. Varistors and PTC thermistors function as passively smart materials that use standby mechanisms to prevent electrical breakdown.

Actively smart materials are used in automobile suspension systems to provide controlled compliance for the shock absorber system. The TEMS (Toyota Electronic Modulated Suspension) system (2) uses a piezoelectric sensor to monitor road roughness. The sensor produces a voltage which is amplified in magnitude and altered in phase, and then applied to a piezoelectric actuator. The actuator produces a hydrostatically enlarged displacement which adjusts the damping force in the shock absorber system. All of these functions, from sensing to hydraulic adjustment, takes place in less than 20 msec.

By introducing a learning function into smart materials, the degree of smartness is upgraded to very smart. A very smart material senses a change in the environment and responds by changing one or more of its property coefficients. Such a material

can "tune" its sensor and actuator functions in time and space to optimize behavior. With the help of memory elements and a feedback system, a very smart material becomes smarter with age.

The distinction between smart and very smart materials is essentially one between linear and nonlinear properties. This difference can be demonstrated in the behavior of strain with applied electric field in piezoelectric PZT ( $\text{PbZr}_{0.5}\text{Ti}_{0.5}\text{O}_3$ ) and electrostrictive PMN ( $\text{PbMg}_{0.33}\text{Nb}_{0.67}\text{O}_3$ ) ceramics. In hard PZT, the strain is linearly dependent to the applied electric field. Therefore, the piezoelectric  $d_{33}$  coefficient, which is equal to the slope of the strain-electric field curve, is constant and cannot be tuned with a bias field. However, PMN ceramics exhibit very large electrostrictive effects in which the strain is proportional to the square of the electric polarization. The nonlinear relation between strain and electric field can be used to tune the  $d_{33}$  coefficient. In certain modified PMN ceramics, these values range from zero at zero bias field to 1500 pC/N at a bias field of 4 kV/cm.

The tunable transducer described in this paper is an example of a very smart material. Silicone rubber, an elastically nonlinear material, has an adjustable elastic modulus, enabling the transducer to be tuned in frequency and acoustic impedance.

Electromechanical acoustic transducers which employ piezoelectric materials operating at resonance are used as fish finders, biomedical scanners, and sonar systems to search for objects of various sizes. These systems are limited in that the resonant frequency of operation,  $f_r$ , as well as the mechanical  $Q_m$ , are fixed and depend on the geometry of the transducer and its complex stiffness. The scattering power of the target depends on the frequency of the interrogating wave and the mismatch in acoustic impedance. It is maximized when the wavelength is approximately the same size as the object. Objects of various sizes can be identified using the same transducer if the resonant frequency can be changed accordingly. By creating a composite transducer whose resonant frequency and mechanical  $Q$  can be tuned over a wide range, the versatility of a transducer and its interrogation capabilities can be vastly improved.

**Tunable Transducer**

**Concept**

The resonant frequency of a thickness mode transducer is given by:

$$f_r = \frac{1}{2t} \sqrt{\frac{E}{\rho}} \quad (1)$$

where  $t$  is the thickness,  $E$  is the elastic modulus, and  $\rho$  is the density. Previous studies of tunable transducers by W.J. Fry et al. (3) and E.P. Lanina (4) concentrated on varying the resonant frequency by controlling the effective thickness of the transducer. Fry et al. (3) used a liquid backing media (mercury) which had an adjustable thickness. The object was to produce high intensity ultrasound over a relatively wide and continuous frequency range. This ultrasound was to be projected into a liquid medium. A reduction in the resonant frequency from 80 kHz to 40 kHz was observed as the length of the mercury (and, therefore, the effective thickness of the system) was varied from zero to 2.5 cm.

Lanina (4) described a tunable high-frequency, high-power piezoelectric ceramic radiator for nonlinear acoustic studies. The system was similar to that of Fry et al. (3) but instead of one piezoelectric ceramic plate and its backing material, the system consisted of two piezoelectric ceramic plates separated by a liquid matching layer, oil. The spacing of the plates was varied between 0.5 and 3 mm. The addition of the second piezo-ceramic plate increased the radiation intensity by a factor of four over that of a single plate. The resonant frequency was varied from 1.7 MHz to 1.9 MHz by changing the thickness of the oil matching layer. Shock waves were produced in a water-filled tank using this device.

According to equation 1, the resonant frequency can also be changed by varying the elastic modulus or the density of the transducer. However, neither of these properties can be easily tuned in piezoelectric ceramics or other standard transducer materials. Therefore, in our design a nonlinear elastic material (rubber) was incorporated into a multilayer composite transducer.

It has been shown that ultrathin (0.01-.05 mm) rubber-metal laminates possess more pronounced nonlinear behavior of the elastic modulus than ordinary rubber or laminates containing rubber layers 2-4 mm thick. (4) For example, with rubber layers 0.02 mm thick bonded to copper shim 0.08 mm thick, we observed a change in the effective elastic modulus from 6 MPa to 150 MPa under a uniaxial compressive stress of 43 MPa.

Fig. 1 shows a schematic of the composite multilayer transducer consisting of a rubber-metal laminate sandwiched between two PZT disks and a brass head and tailmass. A stress bolt is used to hold the composite together. In this configuration, the effective elastic modulus of the rubber, and therefore of the composite, can be controlled by tightening the stress bolt to apply a uniaxial compressive stress.

#### Rubber-Metal Laminate

In our initial attempts to control the resonant frequency with uniaxial stress, a layer of silicone rubber (0.4 mm thick) was placed in between two PZT-5 disks. However, the data were not reproducible from one run to the next because the rubber layer was squeezed out from between the PZT and did not contract back into the composite when the stress was decreased. Under high mechanical stress, the rubber was torn and permanently damaged. Similar irreproducible results were obtained with rubber-metal laminates made from silicone rubber and brass shims. The problem in both cases was the inability of the rubber layer to adhere to the PZT or the brass shim. The problem

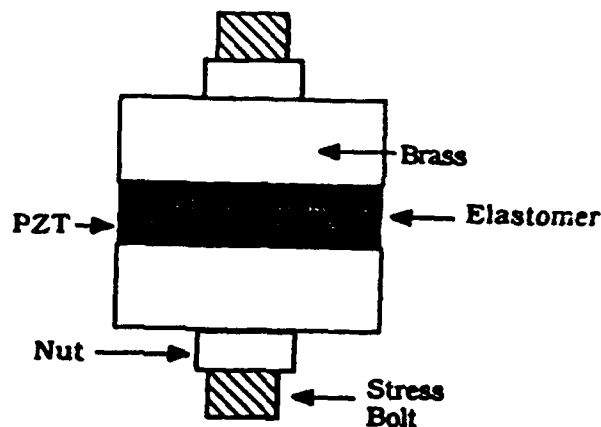


Fig. 1 The tunable transducer. the brass has an outer diameter (OD) of 22 mm, an inner diameter (ID) of 5 mm, and is 7.7 mm thick. The PZT-5 piezoelectric has an OD of 21 mm, an ID of 5 mm, and is 2.5 mm thick. The elastomer is a rubber-metal laminate and is described in the text.

was solved by making a laminate incorporating a specially treated copper shim with a thin coating of polyimide to assist the adhesion with silicone rubber.

The laminate was made in the following way. A silicone rubber-trichloroethylene solution was applied to the polyimide coated side of two pieces of the copper shim cut in the shape of a toroid. This was allowed to set for one hour to let the solvent evaporate. Then the two sides covered with silicone rubber were sandwiched together and placed in a die. This laminate was then hot-pressed at a pressure of 37 MPa and a temperature of 150° C for one hour. Reproducible behavior of the resonant frequency under applied stress was achieved with these composites.

#### Mechanical Tuning

The resonant frequency and mechanical  $Q$  of the composite transducer can be tuned by applying a mechanical bias (Fig 2.) The measurements in Fig. 2 were performed by applying a uniaxial stress to the composite by tightening the stress bolt with a torque wrench. Then, the resonant frequency of the composite was determined by measuring the conductance as a function of frequency with a Hewlett-Packard 4192A LF Impedance analyzer.

#### Modeling the Transducer

The tunable transducer can be modeled using an equivalent circuit shown in Fig. 3. The circuit shows only half the transducer since it is symmetric. The rubber layers are modeled as a spring with zero mass, and the mechanical compliance of the ceramic is neglected. The brass is modeled as having both mass and mechanical compliance. It is further assumed that only the mechanical compliance of the rubber changes appreciably with the application of stress. When the composite is at resonance the mechanical compliance of the rubber is given by:

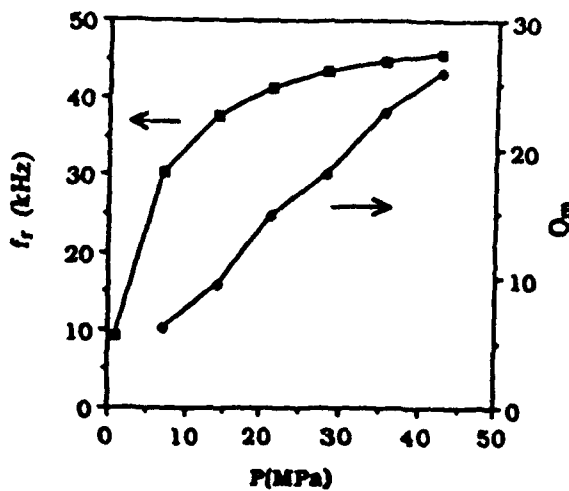


Fig. 2 The resonant frequency and mechanical  $Q$  of the tunable transducer. A rubber-metal laminate consisting of 5 rubber layers (each 0.02 mm thick) and 6 layers of copper shim (each 0.08 mm thick).

$$s_R = \left[ \omega^2 M_C + \omega^2 \frac{M_B}{2} + \frac{\omega^2 \frac{M_B}{2}}{1 - \omega^2 \frac{M_B}{2} s_B} \right]^{-1} \quad [2]$$

where  $\omega$  is  $2\pi f_r$ ,  $M_C$  is the mass of the ceramic,  $M_B$  is the mass of the brass, and  $s_B$  is the mechanical compliance of the brass.

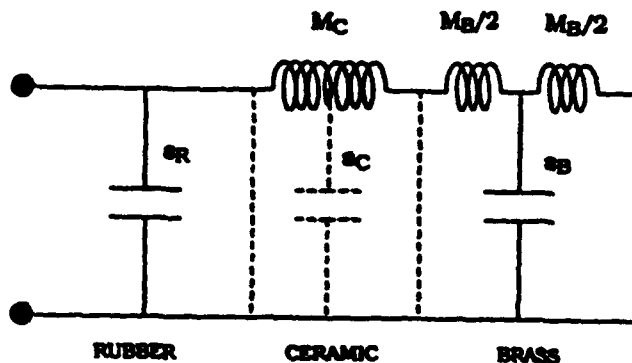


Fig. 3 The equivalent circuit of a tunable transducer.

At very low stress the rubber is very compliant and effectively isolates the upper PZT and brass from the bottom. As the stress increases, so does the mechanical stiffness of the rubber and an additional resonance appears at a frequency much lower than the usual thickness mode with a mechanical  $Q$  that is far less than that of the PZT and brass. Both of these effects are caused by the decreased compliance of the rubber and the coupling of the upper and lower parts of the composite. As the rubber stiffens, both the resonant frequency and the mechanical  $Q$

increase.

### Electrical Tuning

Besides being able to tune the frequency mechanically, it is also possible to tune it electrically. A multilayer piezoelectric actuator made of PZT was incorporated into the composite transducer to produce an additional displacement after a mechanical prestress has been applied (Fig. 4).

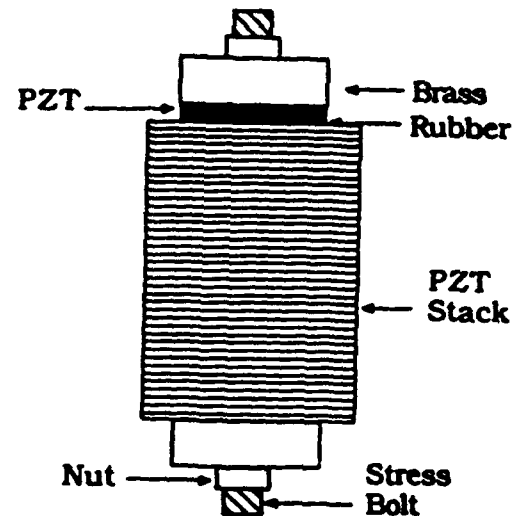


Fig. 4 The tunable transducer with the PZT actuator stack included. The stack is 45 mm thick with an OD of 32 mm and an ID of 6 mm.

The actuator will expand when a d.c. electric field is applied. A PZT stack of 42 ceramic toroids, each 1 mm thick, produces 10  $\mu$ m motions (Fig. 5) with 500 volts applied. The displacement is linear with the applied voltage with just a small hysteresis.

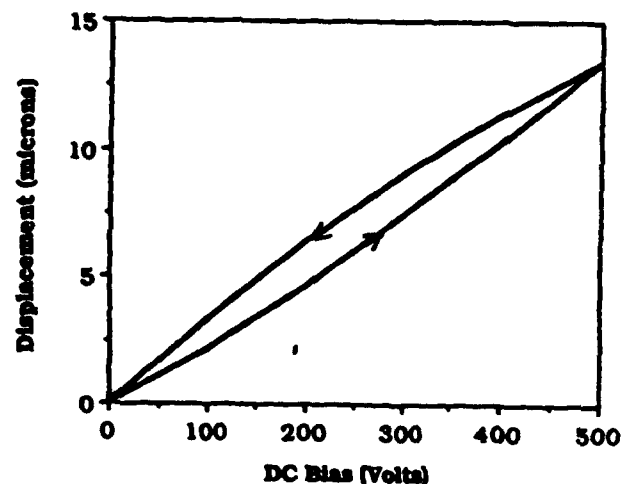


Fig. 5 The displacement produced by the 42 layer PZT actuator stack. Notice the near linear behavior and the slight hysteresis.

There is a relaxation process that occurs when a mechanical prestress is applied to this composite. It is caused by the epoxy between the toroids in the PZT stack. The epoxy is used to hold the stack together. Initially, the resonant frequency of the composite tends to increase with time because of the hardening of the epoxy in response to the increased mechanical bias. Fig. 6 shows a plot of the resonant frequency as a function of time at a prestress of 7 MPa and no d.c. voltage applied to the PZT stack. Typically, it takes about 12 hours for the resonant frequency to stabilize.

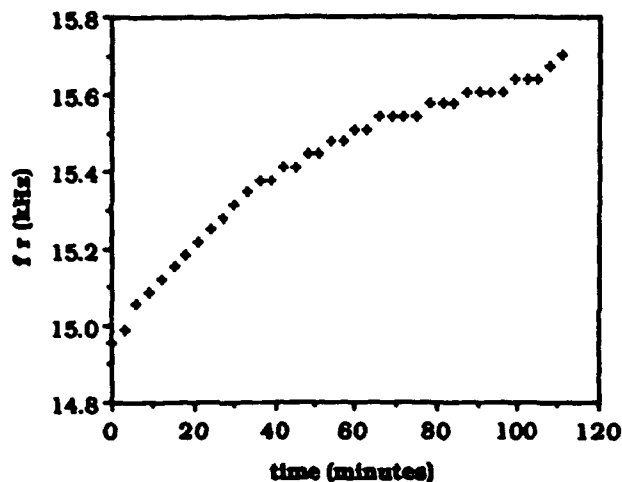


Fig. 6 The resonant frequency as a function of time after a prestress of 7 MPa was applied to the composite.

After the resonant frequency has stabilized, it is possible to tune the frequency using the converse piezoelectric property of the PZT stack. Fig. 7 shows the resonant frequency as a function of the d.c. voltage applied to the PZT stack.

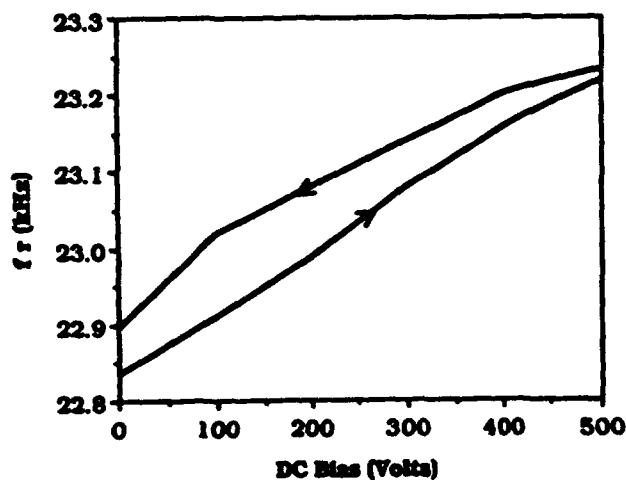


Fig. 7 The resonant frequency plotted as a function of d.c. voltage. The prestress was 7 MPa on a rubber-metal laminate with a rubber thickness of 0.02 mm.

The reason for the small change in resonant frequency (approximately 350 Hz) was thought to be due to the geometry of the system in that the maximum stress is now approximately at the center of the PZT stack rather than at the rubber-metal laminate. The transducer design was altered to place the maximum stress at the rubber-metal laminate by incorporating a large piece of brass of the same dimensions as the PZT stack. Fig. 8 shows this design.

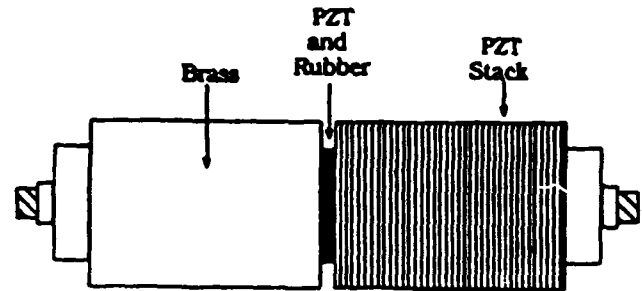


Fig. 8 The tunable transducer consisting of a PZT actuator stack and a brass cylinder of similar dimensions.

The resonant frequency of this modified transducer remained relatively small (330Hz) for the same pressure and rubber thickness as the previous measurement. The total mass and/or relative thickness of the rubber to the transducer may be the limiting factor in these cases and requires further investigation.

The tunable transducer can be compared with transceiver systems in the biological world. The bioonar system of the flying bat is similar in frequency and tunability to the tunable transducer. The bat emits chirps at 30 kHz and listens for the return signal to locate flying insects. The resonant frequency is modulated by a decrease from 30 kHz to 20 kHz near the end of each chirp.(6) Frequency modulation provides superior signal-to-noise ratios and more precise timing of the return signal. The bat modulates the frequency by adjusting the tension applied to the membrane in the larynx generating the chirps. At the beginning of a chirp the muscles apply substantial tension to the membrane. The tension is released at the end of the chirp causing a decrease in frequency. The decrease takes place in milliseconds.(7) We can mimic this frequency modulation in the tunable transducer using an electrically driven screwdriver to tighten the stress bolt. The stress is then released by reversing the operation of the screwdriver in the same way the bat relaxes the muscles that apply tension to the chirp-emitting membrane.

Additional modifications are underway to convert the next generation of very smart materials into intelligent materials. These transducers consist of ceramic thin films, acting as sensors and actuators, deposited on silicon chips. These intelligent materials incorporate sensor and actuator functions with the feedback electronics into an integrated composite transducer.

### References

- [1] R.E. Newnham and G.R. Ruschau, "Smart Electroceramics", J. Am. Ceram. Soc., Vol. 74, pp. 463-480, March, 1991.
- [2] H. Tsuka, J. Nakomo, and Y. Yokoya, "A New Electronic Controlled Suspension Using Piezoelectric Ceramics", IEEE Workshop on Electronic Applications in Transportation, 1990.
- [3] W.J. Fry, R.B. Fry, and W. Hall, "Variable Resonant Frequency Crystal Systems", The Journal of the Acoustical Society of America, Vol. 23, pp. 94-110, January, 1951.
- [4] E.P. Lanina, "Tunable High-Frequency High-Power Piezoceramic Radiator", Sov. Phys. Acoust., Vol. 24, pp. 207-209, May-June, 1978.
- [5] E.I. Rivin, "Properties and Prospective Applications of Ultra Thin Layered Rubber-Metal Laminates for Limited Travel Bearings", Tribology International, Vol. 16, pp. 17-25, February, 1983.
- [6] N. Suga, "Biosonar and Neural Computation in Bats", Scientific American, Vol. 262, pp. 60-68, June, 1990.
- [7] D.R. Griffin, Listening in the Dark: The Acoustic Orientation of Bats and Men. New Haven: Yale University Press, 1958, pp. 413.



## **APPENDIX 6**

# Piezoelectric Composites with High Sensitivity and High Capacitance for Use at High Pressures

Q. C. Xu, S. Yoshikawa, J. R. Belsick, and R. E. Newnham, *Member, IEEE*

**Abstract**—A new type of piezoelectric composite has been developed for oceanographic applications. The composites have a large figure of merit ( $d_h \cdot g_h$  or  $d_h \cdot g_h / \tan \delta$ ), a large dielectric constant ( $K$ ) and low dielectric loss, as well as great mechanical strength. A shallow cavity between the PZT ceramics and thick metallic electrode is designed to convert a portion of the  $z$ -direction stress into a large radial and tangential stress of opposite sign, thereby causing the  $d_{33}$  and  $d_{31}$  contributions to  $d_h$  to add rather than subtract, and raising the figure of merit. Theoretical stress analysis was carried out using an axisymmetric finite element method. Experimental results show that the  $d_h \cdot g_h$ ,  $K$  and withstandable pressure are extremely high.

## I. INTRODUCTION

FOR many hydrophone applications, there is a great demand for piezoelectric composites with a high hydrostatic piezoelectric charge coefficient ( $d_h$ ), high hydrostatic piezoelectric voltage coefficient ( $g_h$ ), and high dielectric constant ( $K$ ) as well as a high pressure tolerance. In the last decade, several piezoelectric ceramic-polymer composites with different connectivity patterns have been developed for hydrophone and medical transducer applications [1]–[4]. The advantages of these composites over ceramics include higher figure of merit  $d_h \cdot g_h$  to enhance the sensitivity, increased mechanical compliance, smaller acoustic impedance for matching to water or tissue, and lower transverse electromechanical coupling coefficient to reduce cross-talk noise and improve directivity of the transducer array. Disadvantages of these ceramic-polymer composite transducers however, are lower dielectric constant and lower pressure tolerance than their ceramic counterparts.

Flexensional transducers composed of a piezoelectric ceramic and a shell structure exhibit good electro-acoustic performance [5], [6] in which the extensional vibration mode of a piezoelectric ceramic is coupled to the flexural vibration mode of a metal or polymer shell. The shell is used as a mechanical transformer for transforming the high acoustic impedance of the ceramic to the low acoustic impedance of the medium and for producing large volume velocity. Or, when operated in the reverse direction, the

TABLE I  
COMPARISON OF  $g_h \cdot d_h$  PRODUCT AMONG VARIOUS  
PIEZOELECTRIC MATERIALS

Material	$d_h \cdot g_h (\times 10^{-12} \text{ m}^2/\text{N})$
PZT-brass composite	~ 50,000
PZT	~ 110
PbTiO <sub>3</sub>	~ 1,800
Voided Thick PVDF	~ 5,000

large velocity in the medium produces a high stress in the ceramic. All five types of flexensional transducers described in [5] and [6] are designed to operate in the low frequency range below 10 kHz.

This paper describes a new type of piezoelectric ceramic-metal composite based on the principle of a flexensional transducer. The basic structure is described in Section II and has some similarity to a class V flexensional transducer [7]. A computer analysis of the stress in the composite was performed using the finite element method (FEM). The stress contours are described in Section III. In Section IV, the experimental results are presented to show that this type of composite can provide very high  $d_h \cdot g_h$  or  $d_h \cdot g_h / \tan \delta$ , [8] together with a large capacitance and high withstanding pressure. Table I compares the  $d_h \cdot g_h$  values of the PZT-metal composite with other commonly used transducer materials.

## II. BASIC PRINCIPLE

As is well known, PZT ceramics have high  $d_{33}$  and  $d_{31}$ , but their  $d_h (= d_{33} + 2d_{31})$  values are only about 45 pC/N because  $d_{31}$  and  $d_{33}$  have opposite signs. To enhance  $d_h$ , we have developed a PZT-metal composite with very shallow cavities between the PZT ceramic and thick metal electrodes that convert a portion of the  $z$ -direction stress into large radial stresses of opposite signs, thereby causing the  $d_{33}$  and  $d_{31}$  contributions to  $d_h$  to add rather than subtract, leading to high  $d_h$ .

A cross section view of the disk shaped PZT-metal composite is shown in Fig. 1. The cylindrically symmetric structure is designed to obtain an extensional vibration mode of PZT, and high hydrostatic pressure tolerance. The height of the shallow cavity  $h$  is less than 150  $\mu\text{m}$ . The shallow cavity allows deformation of the metal electrode toward the ceramic disk by closing the cavity that reduces stress amplification in the PZT and prevents

Manuscript received August 15, 1990; revised February 11, 1991; accepted May 7, 1991. This work was supported in part by the Office of Naval Research and in part by the Center for the Engineering of Electronic and Acoustic Materials at the Pennsylvania State University.

The authors are with the Materials Research Laboratory, Pennsylvania State University, University Park, PA 16802.

IEEE Log Number 9102673.

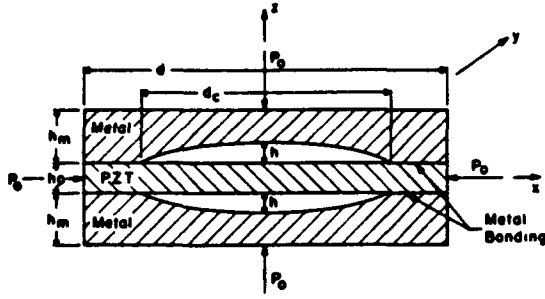


Fig. 1. Geometry of the composite.

breakdown during shockwaves or very high hydrostatic pressure. The concept of the stress transformation can be explained in a simple manner using the cross section in Fig. 2 and the following equations:

$$\frac{F_1}{F_2} = \frac{h}{\frac{d_c}{2}} = \frac{2h}{d_c} \quad (1)$$

$$F_1 = W \cdot \frac{d_c}{2} P_o, \quad F_2 = W \cdot \frac{h_p}{2} T'_x \quad (2)$$

$$T'_x = \frac{d_c}{2h} \cdot \frac{d_c}{h_p} P_o = N \frac{d_c}{h_p} P_o \quad (3)$$

$$N = \frac{d_c}{2h} \cong \frac{1}{\tan \alpha} \quad (4)$$

Similarly

$$T'_y = N \frac{d_c}{h_p} P_o \quad (5)$$

The extensional stress is considered as "negative" here. Let  $T_x$  be the  $x$ -direction stress in PZT, then

$$T_x \cong P_o - N \frac{d_c}{h_p} P_o \cong T_y \quad (6)$$

where  $P_o$  is the acoustic pressure and  $N$  is a stress amplification parameter;  $N$  is approximately equal to  $1/\tan \alpha$ , where  $\alpha$  is the shallow cavity angle shown in Fig. 2;  $T_z$  is the  $z$ -component of stress in PZT and is given by

$$T_z = P_o \quad (7)$$

The resulting polarization is  $d_{31} T_x + d_{31} T_y + d_{33} T_z S_2/S$ , where  $S$  is the surface area of the PZT and  $S_2$  is the surface area of the metal-PZT bond.

Therefore

$$(d_h)_{\max} \cong d_{33} \frac{S_2}{S} + 2d_{31} \left[ 1 - \frac{Nd_c}{h_p} \right] \quad (8)$$

This estimate of  $(d_h)_{\max}$  explains the basic principle of the composite, but the experimental result of  $d_h$  is much smaller than  $(d_h)_{\max}$ , partly because  $N$  is much less than  $1/\tan \alpha$  for a thick metal electrode.

The basic idea of the composite is to attempt to use both the  $d_{33}$  and  $d_{31}$  coefficients to obtain high  $d_h$ . Thick metal

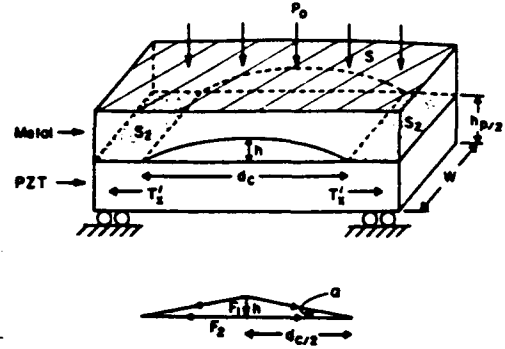


Fig. 2. Simplified model for calculating stress transformation.

plates are used as a mechanical transformer to transform the stress direction and amplitude, and also to adjust the acoustic value from a low impedance in the  $z$ -direction to a high impedance in planar direction.

The lowest vibration mode of the composite is a flex-tensional mode determined mainly by the stiffness of the PZT in a planar mode and the equivalent mass of the metal plate. This equivalent mass is much larger than the real mass of the metal plate, because the vibration velocity at the central portion of the metal is much larger than the reference velocity in the PZT. The operating frequency range of the composite is dependent on this flex-tensional mode that is controlled by the cavity diameter  $d_c$ , the height of the cavity  $h$ , the thickness of the metal  $h_m$  and the stiffness of the ceramic in planar mode.

Since the withstanding hydrostatic pressure  $P_m$  is another important parameter for the underseas application, the stress amplification coefficient  $N$  cannot be designed too high. Transducers with large cavity diameters ( $d_c$ ) have low flex-tensional resonant frequency, low  $P_m$  and high  $d_h$ .

The capacitance of the composite can be changed by adjusting the electrode area on the PZT surfaces, especially if the stress in the center portion of the PZT disk is small.

### III. STRESS ANALYSIS WITH FEM

A theoretical analysis of the PZT-brass composite was performed using the finite element analysis program, AN SYS version 4.3 [9], [10]. A one-quarter axially-symmetric model is shown in Fig. 3. The mesh contained 640 quadrilateral-shaped elements with 729 nodal points. Half of them are in the PZT. The triangular points are used to "pin" the object and allow only parallel motion on the boundary when stresses are employed.

To simplify the analysis, the metal bonding layer is neglected, and a hydrostatic reference pressure of  $P_o = 1$  is applied to the model. Fig. 4 shows the stress contours in the radial ( $R$ ) direction with a quadrupole pattern in the brass, and a stress concentration factor of about 20 at the tip point of the PZT and the brass. In the PZT, there are only extensional stresses in the radial  $R$  direction and very small stresses in the central portion of the ceramic. The

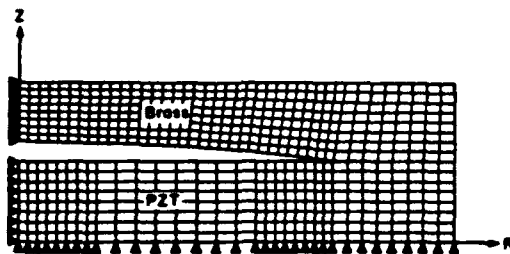


Fig. 3. Mesh used for modeling PZT-brass composites.

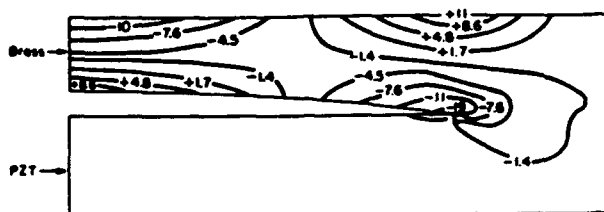


Fig. 4. Finite-element model of stress in  $R$  direction.

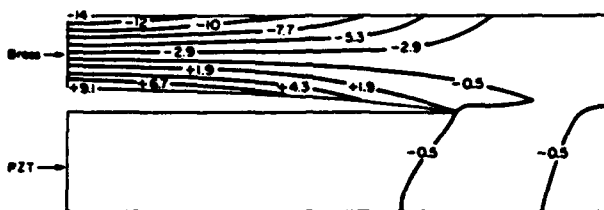


Fig. 5. Finite-element model of stress in  $\phi$  direction.

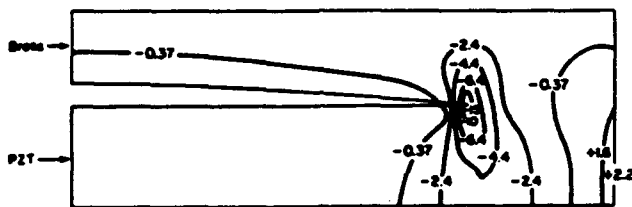


Fig. 6. Finite-element model of stress in  $z$  direction.

tangential stresses ( $\phi$  direction) in Fig. 5 shows that there are bending stresses in the brass, and extensional stresses in the PZT. The stress contours in the  $z$ -direction shown in Fig. 6 indicate that there are undesirable extensional stresses in the PZT, and the stresses are concentrated with a factor of about 15 at the tip of the cavity between the PZT and brass. The stress analysis, which neglected the PZT-brass interface layer, shows that the material used as to bond the PZT and the brass should have greater compliance than brass or PZT in order to reduce the stress concentration factor and to obtain compressive stresses in the PZT along the  $z$ -direction, thereby forming large extensional stresses in the PZT along the  $R$ - and  $\phi$ -directions. A thick bonding layer of a metal with lower elastic moduli metal leads to higher sensitivity in hydrophone applications.

#### IV. EXPERIMENTS AND RESULTS

PZT-brass composite samples with dimensions (Fig. 1):  $d = 11$  mm,  $h_m = 1.2$  mm,  $h_p = 1.1$  mm,  $h = 100$ – $150$   $\mu$ m, and four different cavity diameters  $d_c = 7.6$  mm (large cavity),  $5.8$  mm (middle cavity),  $4.1$  mm (small cavity),  $2.5$  mm (very small cavity) were fabricated for the experiments. In order to obtain a thick bonding layer, the brass plates were bonded to a PZT-5 disk with the capacitor electrode silver paste and fired at  $600^\circ\text{C}$  for 10 min. Brass was chosen for its lower thermal expansion coefficient (approximately  $15$  ppm/ $^\circ\text{C}$ ). After cooling, the composite was encapsulated around its circumference with Spurr's epoxy resin and cured at  $90^\circ\text{C}$  for more than 8 hours. The composite was poled in oil at  $150^\circ\text{C}$  with a  $2.5$  kV/mm electric field for about 15 min.

The  $g_h$  coefficient was determined using a dynamic ac technique. An electromagnetic driver was used as an ac stress generator to apply pressure waves to the sample and a PZT standard, which were kept under a static pressure (up to 1000 psi (7 MPa)) with a hydraulic press. The charge produced by the sample and the standard were buffered with an impedance converter, and the resulting voltages measured on a Hewlett-Packard 3585A Spectrum Analyzer. The ratio of the voltages is proportional to the  $g_h$  coefficients. Accounting for the geometries of the sample and PZT standard, and the stray capacitance of the holders, the  $g_h$  coefficient of the sample was calculated. Using the measured values of  $g_h$ , the hydrostatic piezoelectric coefficient,  $d_h$ , was calculated from the relation,  $d_h = \epsilon_0 K g_h$ .

A question arises in how to compare the output of this transducer with other piezoelectrics. Since  $g_h$  is obtained from the output voltage and the thickness of the composite and standard samples, we have chosen the thickness of composite sample to be the same as the thickness of PZT disk in order to retain the same dielectric constant as PZT. Otherwise,  $g_h$  will be three times less and the apparent dielectric constant will be three times higher.

The experimental results presented in Figs. 7 and 8 show that large cavity sizes lead to very large  $d_h$  and  $g_h$  values. Moreover, the dielectric constant exceeded 1500 and  $\tan \delta$  was less than 0.025. Fig. 9 shows the relationship between the  $d_{33}$  value, measured at center point of the sample with a Berlincourt  $d_{33}$  meter using the electromagnetic driver operating at a frequency of 100 Hz, and the  $d_h$  value measured by the method just described. The  $d_{33}$  value increases markedly with cavity diameter. Fig. 10 shows that the frequency of the lowest flextensional mode decreases as the cavity diameter increases. Therefore, the larger cavity diameter composites possess a lower operating range.

Because the thermal expansion coefficient of brass is larger than the PZT (approximately  $5$ – $7$  ppm/ $^\circ\text{C}$ ), compressive prestresses are applied to PZT during the bonding process in  $R$  and  $\phi$  directions perpendicular to the pol-

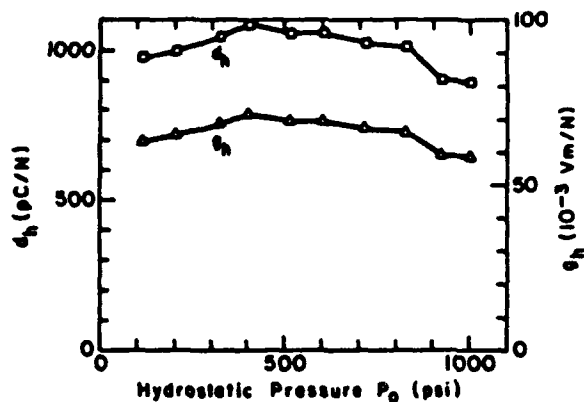


Fig. 7. Hydrostatic pressure dependence of  $d_h$  and  $g_h$ . Large cavity,  $d_c = 7.6$  mm,  $K = 1700$ .

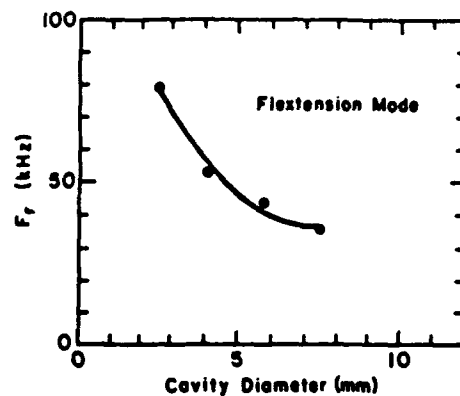


Fig. 10. First flexensional frequency dependence of cavity diameter.

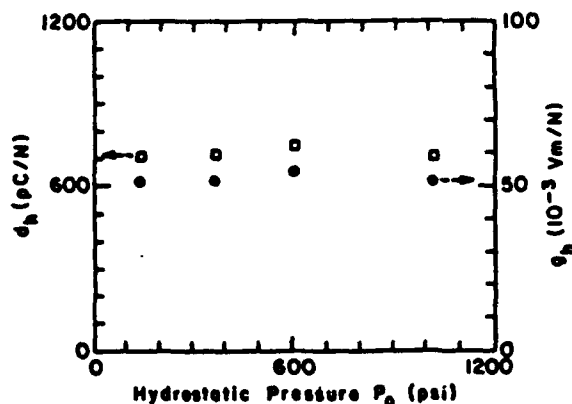


Fig. 8. Hydrostatic pressure dependence of  $d_h$  and  $g_h$ . Small cavity,  $d_c = 4.1$  mm,  $K = 1560$ .

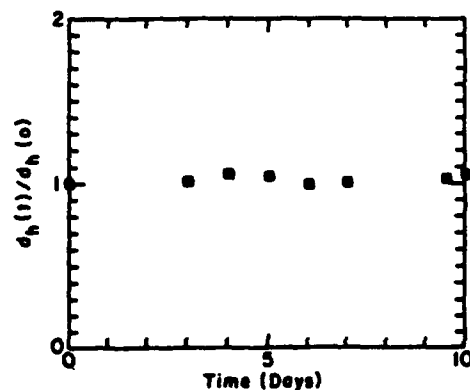


Fig. 11. Aging under hydrostatic pressure. Hydrostatic pressure  $P_m = 350$  psi.

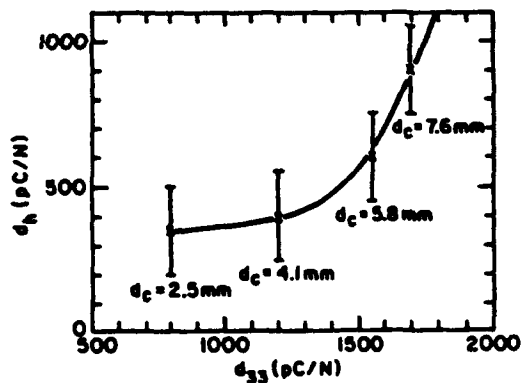


Fig. 9. The  $d_h$  dependence of  $d_{33}$  at center point of the disk.

ing direction. These prestresses help to maintain the polarization in the PZT. Fig. 11 shows that aging under hydrostatic pressure at 350 psi (about 2.5 MPa) was very small.

Lastly, a planar array was made for testing by embedding four composite samples with large cavities in epoxy resin (Eccogel 1365-25, Emerson and Cummings, Inc.) (Fig. 12). The admittance and conductance of the array

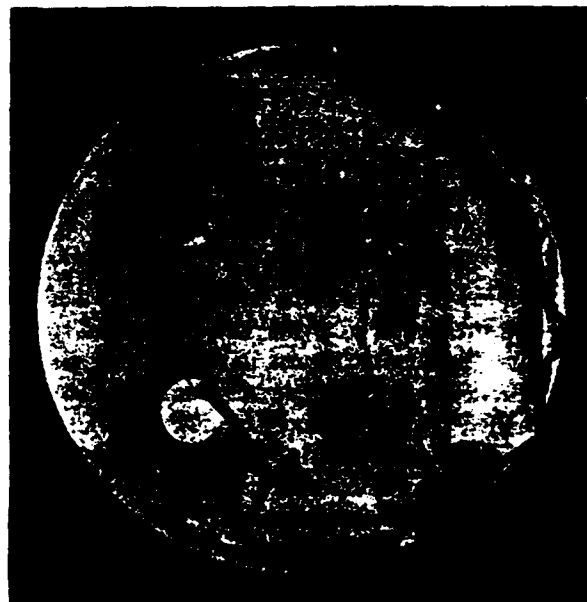


Fig. 12. Flexible array incorporating four composite transducers.

in air and in water presented in Figs. 13 and 14 show that the lowest flexensional mode was higher than 30 kHz and that the resonant peak in water was flat. Since conduct-

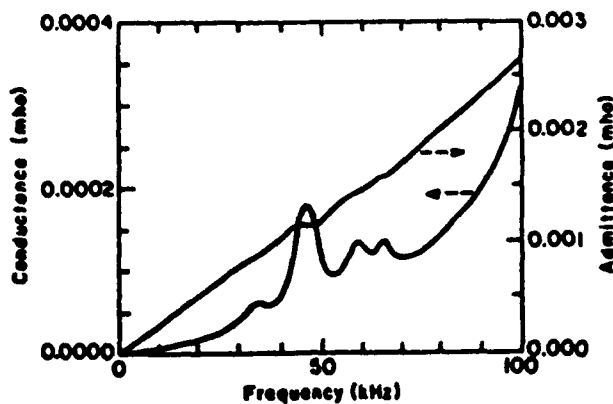


Fig. 13. Conductance and admittance of the array in air. Four elements array in air.

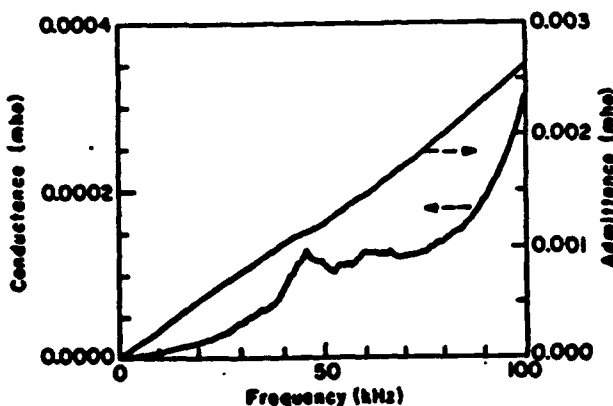


Fig. 14. Conductance and admittance of the array in water. Four elements array in water.

ance exhibit only a weak resonance peak, a flat receiving response is expected to extend to more than 20 kHz.

### V. CONCLUSION

1) PZT-brass composites with redirected stresses exhibit a very high figure of merits ( $d_h \cdot g_h$  or  $d_h \cdot g_h / \tan \delta$ ) as well as high dielectric constant  $K$ , and high with-standing pressure  $P_m$ . The composite characteristics includes values of  $d_h \cdot g_h \approx 50,000 \times 10^{-15} \text{ m}^2/\text{N}$ ,  $K > 1400$  and  $P_m > 1000$  psi. The improved transducer performance promises to be important in many naval applications, and for detectors for oil exploration and earthquake seismology.

2) Larger cavity sizes lead to large  $d_h$  and  $g_h$ , but lower operating frequencies.

3) Very little aging was observed under high hydrostatic pressure of 350 psi.

4) An experimental four-element flexible array shows that the lowest resonance frequency is higher than 30 kHz.

### ACKNOWLEDGMENT

The authors wish to thank Dr. W. Smith and Professor L. E. Cross for their advice, and P. A. Marlowe for his help with sample preparation.

### REFERENCES

- [1] R. E. Newham, "Composite electroceramics," *Ann. Rev. Mat. Sci.*, pp. 47-68, Annual Reviews, Inc. (1986).
- [2] T. R. Gururaja, A. Safari, R. E. Newham, and L. E. Cross, "Piezoelectric ceramic-polymer composites for transducer application," *Electronic Ceramics*, L. Levinson, Ed. New York: Marcel Dekker, 1987, pp. 92-128.
- [3] H. Banno, "Recent developments of piezoelectric ceramic products and composite of synthetic rubber and piezoelectric ceramic particles," *Ferroelectrics*, vol. 50, no. 1-4, pp. 329-338, 1983.
- [4] Y. Q. Zhuang, Y. G. Heu, and Q. C. Xu, "Sandwich PZT/polymer composite transducer," *Ferroelec.*, vol. 49, pp. 241-249, 1983.
- [5] G. A. Brigham and L. H. Royster, "Present status in the design of flexensional underwater acoustic transducer," *J. Acoust. Soc. Am.*, vol. 46, no. 1, Pt. 1, p. 92, 1969.
- [6] K. D. Rokh, "History of the flexensional electro-acoustic transducer," *J. Acoust. Soc. Am.*, vol. 87, no. 3, pp. 1340-1349, 1990.
- [7] R. A. Nelson Jr. and L. H. Royster, "Development of a mathematical model for the class V flexensional underwater acoustic transducer," *J. Acoust. Soc. Am.*, vol. 49, pp. 1609-1620, 1971.
- [8] A. S. Bhalla and R. Y. Ting, "Hydrophone figure of merit," *Sensors and Materials*, vol. 4, pp. 181-185, 1988.
- [9] K. L. Swain, "Crescent-shaped 3-0 piezoelectric transducers," B.S. thesis, Dept. Materials Sci. Eng., Pennsylvania State Univ., 1988.
- [10] T. J. Meyer, "3-0 crescent shaped composite hydrophones," B.S. thesis, Dept. Materials Sci. Eng., Pennsylvania State Univ., 1989.

Qi Chang Xu was born in Shanghai, China, November 11, 1936.

He is a Senior Research Associate at the Materials Research Laboratory, Pennsylvania State University, after having been a Visiting Associate Professor from 1986 to 1989. His current research interests are in acoustics and ferroelectric materials.

Shoko Yeshikawa was born in Nagao, Japan, on March 25, 1956. She received the B.S. degree in industrial chemistry from the Chubu Institute of Technology, Japan, and the M.S. degree in chemistry in 1981 from Ohio University, Athens, OH.



She has been with the Materials Research Laboratory at Pennsylvania State University, University Park, PA, where she is currently a Senior Research Assistant working on composite electronic materials. Formerly, she was Senior Chemist working on magnetic tape formulation at Ampex Corp., Magnetic Tape Division R&D, Redwood City, CA, from 1981 to 1984. She also worked on ceramic capacitor formulation at Murata-Eric North America Co., Ltd., and at Centre Engineering, Inc.



John Belsick was born in Rochester, PA, on August 20, 1964. He received the B.S. in ceramic science and engineering in 1986 and the M.S. degree in solid-state science in 1988, both from Pennsylvania State University, University Park, PA, where he is currently pursuing the Ph.D. degree.

In 1989, he was a Visiting Scientist at the Toshiba Corp., Kawasaki, Japan, where he was involved in the development of multilayer capacitors, his research interests are in the areas of

ferroelectric thin films, dielectric and piezoelectric ceramics, and composites.



Robert E. Newnham was born in Amsterdam, NY, on March 28, 1929. He received the B.S. degree in mathematics in 1950 from Hartwick College, Oneonta, NY, the M.S. degree in physics and mineralogy, from Colorado State University, Fort Collins, and the Ph.D. in crystallography in 1960 from Cambridge University, Cambridge, England.

He is ALCOA Professor of Solid-State Science at the Materials Research Laboratory at Pennsylvania State University, University Park, PA. Previously, he was a staff member of the Laboratory for Insulation Research at the Massachusetts Institute of Technology, Cambridge, MA. His research interests are in structure-property relations, electroceramics, and composite materials for electronic applications.